

A Novel Technique to Improve the Spurious-free Dynamic Range of Digital Spectrum Monitoring Receivers

Von der Fakultät 1 - MINT - Mathematik, Informatik, Physik,
Elektro- und Informationstechnik
der Brandenburgischen Technischen Universität Cottbus–Senftenberg
genehmigte Dissertation
zur Erlangung des akademischen Grades eines

Doktor der Ingenieurwissenschaften (Dr.-Ing.)

vorgelegt von

Dipl.-Ing. Manfred Fleischmann
geboren am 21.12.1952 in Windorf, Deutschland

Vorsitzender: Prof. Dr. Markus Gardill

Gutachter: Prof. Dr.-Ing. habil. Dr. h.c. mult. Ulrich Rohde

Gutachter: Prof. Dr. Matthias Rudolph

Gutachter: Univ.-Prof. Klaus Buchenrieder, Ph.D (Universität der Bundeswehr München)

Tag der mündlichen Prüfung: 02. Mai 2022

<https://doi.org/10.26127/BTUOpen-5898>

Acknowledgments

This dissertation was written as an external doctoral candidate at the Brandenburgische-Technische Universität Cottbus (BTU). Therefore, I would like to express my sincere appreciation to the Staff of Faculty 1 -MINT- who have been very kind in assisting me in carrying out my work.

The fact that I was able to write this dissertation is mainly due to Prof. Dr.-Ing. habil. Dr. h. c. mult. Ulrich Rohde who accepted me as a doctoral student. He continuously supported me with his expertise and was always available for fruitful technical discussions. His interest and participation in the progress of my work have been motivating and inspiring at all times.

I am also very grateful to Prof. Dr.-Ing. Matthias Rudolph who was always approachable and gave me timely and useful recommendations in all matters of my work.

I would also like to thank Prof. Dr. Markus Gardill for his cooperation in my examination board.

Finally, I would like to thank Univ.-Prof. Klaus Buchenrieder Ph.D. M.S. (Universität der Bundeswehr München) for his many valuable suggestions. His expertise and competence have always been a yardstick for my work and have kept my ambition high.

Abstract

This dissertation presents a novel technique for enhancing the spurious-free dynamic range (SFDR) of radio monitoring receivers with a bandwidth of several gigahertz. The improvement is based on the suppression of the discrete spurious signals that occur at higher drive levels in the output spectrum of the required broadband analog-to-digital converter (ADC). The achievable improvement of the SFDR is typically more than 20 dB, allowing better, gap-free monitoring of very wide frequency ranges. The attenuation of the spurious signals is achieved by a unique combination of two separate ADCs working in parallel and subsequent digital signal processing. The developed solution is not limited to broadband radio monitoring receivers but can generally suppress the spurious signals generated during an A/D conversion.

The elaboration starts with an analysis of the current radio receiver technology and shows the advantages and disadvantages of the most common reception principles. In order to find starting points for improving the bandwidth and dynamic range, the A/D conversion process and the performance of modern broadband A/D converters are examined. The result shows that direct sampling of the radio signals with giga samples per second (GSPS) ADCs has the potential to increase the real-time bandwidth of a receiver up to several gigahertz, but the dynamic range is severely limited by discrete spurious signals generated during A/D conversion. These various spurious signals and the mechanisms of their generation are examined, and known solutions for their suppression described in the literature are presented.

The main part of this dissertation focuses on developing a novel technique for suppressing discrete spurious signals generated by broadband A/D conversion. The analysis of the A/D conversion process shows that the frequencies and amplitudes of spurious signals are affected by the chosen A/D conversion parameters in a different way than those of the desired signals. This effect is used to detect and remove spurious signals. For this purpose, the desired signal is simultaneously sampled with two separate ADCs, one of which operates with a different conversion parameter such as the sampling frequency, the signal frequency, or the signal amplitude. When the signals are transferred to the frequency domain using a fast Fourier transform (FFT), the desired signals retain the frequencies and amplitudes in both spectra, but the interfering signals usually do not because these have a different mechanism of origin.

By comparing the spectra, the spurious signals are revealed and eventually removed from the spectrum by subtraction. The result is a purged set of spectral data with improved spurious-free dynamic range.

By using a variable sampling frequency, signal frequency, and signal amplitude, three different methods for suppressing spurious signals are developed. The mode of operation is first worked out and exemplified based on theoretical considerations. A sample implementation of the methods for MATLAB and computer simulations with different radio signals and waveforms conclude the theoretical part.

Next, a suitable hardware and software test environment is set up, and the functionality of the methods is demonstrated with measurements on A/D converters working in the hundred megahertz range. The effectiveness and limitations of the developed methods are examined in detail using test scenarios with signal generators and an antenna.

The dissertation concludes with a final discussion and evaluation of the developed spurious mitigation methods and gives an outlook on possible future developments.

Kurzfassung

In dieser Dissertation wird eine neuartige Technik zur Verbesserung des störungsfreien Dynamikbereichs (SFDR) von Funküberwachungsempfängern mit einer Bandbreite von mehreren Gigahertz vorgestellt. Die Verbesserung basiert auf der Unterdrückung der diskreten Störsignale, die bei höherer Aussteuerung im Ausgangsspektrum des benötigten, breitbandigen Analog-Digital-Wandlers (ADC) auftreten. Die erzielbare Verbesserung des SFDR beträgt typischerweise mehr als 20 dB und ermöglicht damit eine bessere, lückenlose Überwachung sehr großer Frequenzbereiche. Die Unterdrückung der Störsignale wird durch eine spezielle Anordnung von zwei parallel arbeitenden ADCs und anschließender digitaler Signalverarbeitung erreicht. Die entwickelte Lösung ist nicht auf breitbandige Funkempfänger beschränkt, sondern kann generell die bei einer A/D-Wandlung erzeugten Störsignale unterdrücken.

Die Ausarbeitung beginnt mit einer Analyse der aktuellen Funkempfängertechnologie und zeigt die Vor- und Nachteile der gängigsten Empfangsprinzipien auf. Um Ansatzpunkte für eine Verbesserung der Bandbreite und des Dynamikbereichs zu finden, werden der Analog-Digital-Wandlungsprozess und die Eigenschaften moderner Breitband-A/D Wandler untersucht. Es zeigt sich, dass die direkte Digitalisierung der Radiosignale mit geeigneten, schnellen ADCs die Echtzeitbandbreite auf mehrere Gigahertz erhöhen kann, der Dynamikbereich aber durch die bei der A/D-Wandlung entstehenden diskreten Störsignale stark eingeschränkt wird. Die verschiedenen Arten derartiger Störungen und ihre Entstehungsmechanismen werden untersucht und bekannte, in der Literatur beschriebene Lösungen zu ihrer Unterdrückung vorgestellt.

Der zentrale Teil dieser Dissertation befasst sich mit der Entwicklung einer neuartigen Technik zur Unterdrückung von diskreten Störsignalen, die bei einer breitbandigen A/D-Wandlung entstehen. Die Analyse des A/D-Wandlungsprozesses ergibt, dass die Frequenzen und Amplituden von Störsignalen durch die gewählten Wandlungsparameter in anderer Weise beeinflusst werden als die der Nutzsignale. Dieser Effekt wird genutzt, um Störsignale zu erkennen und zu entfernen. Dazu wird das Nutzsignal gleichzeitig mit zwei Analog-Digital-Wandlern abgetastet, wobei ein Wandler mit einem unterschiedlichen Wandlungsparameter wie beispielsweise der Abtastfrequenz, der Signalfrequenz oder der Signalamplitude arbeitet. Überführt man die gewonnenen Zeitsignale mittels einer schnellen Fourier Transformation (FFT) in den Frequenzbereich, behalten die Nutzsignale in beiden Spektren ihre ursprünglichen Frequenzen und Amplituden bei, die Störsignale aufgrund ihres anderen Entstehungsmechanismus jedoch nicht. Vergleicht man die gewonnenen Spektren mithilfe digitaler Signalverarbeitung, treten die

Störsignale zutage und können durch Subtraktion entfernt werden. Als Ergebnis erhält man einen bereinigten Satz spektraler Daten mit verbessertem, störungsfreiem Dynamikbereich.

Aufbauend auf den Parametern Abtastfrequenz, Signalfrequenz und Signalamplitude werden im Verlauf dieser Arbeit drei unterschiedliche Verfahren zur Störunterdrückung entwickelt und vorgestellt. Das Funktionsprinzip wird auf der Grundlage theoretischer Überlegungen ausgearbeitet und dargelegt. Eine beispielhafte Implementierung der Verfahren mit MATLAB[®] und Computersimulationen mit verschiedenen Hochfrequenzsignalen und Wellenformen schließen den theoretischen Teil ab.

Daran anschließend wird eine geeignete Hard- und Software Testumgebung aufgebaut und die Funktionsfähigkeit der Verfahren mithilfe von Messungen an A/D-Wandlern im einhundert Megahertz Bereich gezeigt. Die Wirksamkeit und die Grenzen der verschiedenen Methoden werden anhand von Testszenarien mit Signalgeneratoren und einer Antenne ausführlich untersucht.

Die Arbeit schließt mit einer Bewertung der Wirksamkeit der vorgestellten Methoden zur Störungsunterdrückung und gibt Hinweise zu deren möglichen Weiterentwicklung.

Contents

- Title Page I**
- Acknowledgments.....III**
- Abstract V**
- Kurzfassung..... VII**
- Contents.....IX**

- 1 Introduction 1**
- 1.1 Problem Description..... 2
- 1.2 Thesis Objectives..... 4
- 1.3 The Solution Concept 5
- 1.4 Development Methodology..... 6

- 2 Radio Receiver Architectures and State of the Art 7**
- 2.1 The Frequency-Conversion Process..... 8
- 2.2 Superheterodyne Receivers 11
- 2.2.1 Example Data for a High-Performance Superhet Receiver 13
- 2.2.2 Performance Evaluation of the Superheterodyne Receiver..... 13
- 2.3 Direct-Conversion Receivers 14
- 2.3.1 Example Data for a Direct-Conversion Receiver 17
- 2.3.2 Performance Evaluation for the Direct-Conversion Receiver 18
- 2.4 Direct RF-sampling Receivers..... 19
- 2.4.1 Example Data for a Direct RF-sampling Receiver 20
- 2.4.2 Performance Evaluation for the Direct RF-sampling Receiver 21
- 2.5 Broadband Radio Monitoring Receivers 22
- 2.5.1 Communication Intelligence Receivers 23

2.5.2	Electronic Intelligence Receivers	24
2.5.3	Performance Evaluation for Broadband Monitoring Receivers	25
2.5.4	Summary Conclusions on Receiver Architectures	26
3	ADC Distortion and Dynamic Range	29
3.1	ADC Imperfections	29
3.1.1	The Spurious-Free Dynamic Range of an ADC.....	30
3.1.2	Intermodulation and Harmonic Distortion.....	31
3.1.3	Quantization Errors.....	33
3.1.4	Quantization Noise	38
3.1.5	Aperture Clock Jitter	42
3.1.6	Thermal Noise.....	45
3.1.7	Noise Figure and Noise Spectral Density.....	47
3.1.8	Summary Conclusions on ADC Imperfections	48
3.2	Performance of Modern RF-sampling ADCs.....	49
3.2.1	SFDR Measurement of a Commercial ADC.....	52
3.2.2	Summary Conclusions on Modern RF-sampling ADCs	53
3.3	Known Methods for Reducing ADC Spurious Signals	54
3.3.1	Hardware Related Methods	54
3.3.2	The Frequency-Planning Approach	55
3.3.3	Spurious Mitigation Through Digital Signal Processing.....	57
3.3.4	Summary Conclusions on Known Spurious Reduction Methods	58
4	Theoretical Analysis of the A/D Conversion Process	59
4.1	The Ideal Time Discrete Sampling Process.....	59
4.2	Non-Ideal Pulse Sampling	62
4.3	The Aliasing Effect	64
4.4	Summary Conclusions on the A/D Conversion Process	67

5	Spectrum Analysis Using the FFT.....	69
5.1	Scalloping Error	69
5.2	Spectral Leakage	70
5.3	Windowing the Sampled Data	71
5.3.1	Selecting a Window Function	74
5.4	Summary Conclusions on Errors in FFT Measurements.....	75
6	A New Spurious Suppression Technique	77
6.1	Data Acquisition with one or two ADCs.....	78
6.2	The Different Sampling Frequency Method (DSF-method).....	79
6.2.1	Signal Flow of the DSF-Method	81
6.2.2	Sampling Frequency Offset for the DSF-Method	83
6.2.3	Effectiveness and Limitations of the DSF-Method	84
6.3	The Different Input Frequency Method (DIF-method)	85
6.3.1	Signal Flow of the DIF-Method	88
6.3.2	Choosing the Frequency Offset for the DIF-Method.....	89
6.3.3	Effectiveness and Limitations of the DIF-Method.....	90
6.4	The Different Input Amplitude Method (DIA-method).....	91
6.4.1	Signal Flow of the DIA-method.....	93
6.4.2	Amplitude Difference for the DIA-Method	95
6.4.3	Effectiveness and Limitations of the DIA-Method	95
6.5	Boundary Conditions for Spurious Mitigation.....	97
7	Evaluation of the Spurious Suppression Methods	99
7.1	Computer Simulations	99
7.1.1	Signal Generation	99
7.1.2	Simulation of the DSF-Method	101

7.1.3	Simulation of the DIF-Method	104
7.1.4	Simulation of the DIA-Method	107
7.1.5	Dense Spectrum Simulation	110
7.2	Laboratory Tests.....	112
7.2.1	Laboratory Test of the DSF-Method.....	114
7.2.2	Laboratory Test of the DIF-Method.....	121
7.2.3	Laboratory Test of the DIA-Method	124
7.3	Measurements With Antenna Signals	133
7.3.1	Setup for the Antenna Measurements.....	135
7.3.2	Antenna Measurements With the DSF-Method	136
7.3.3	Antenna Measurements With the DIA-method	139
7.4	Effects of Spurious Suppression on Noise and Distortion	141
7.4.1	Effect on the System Noise Level	142
8	Technical Results and Key Findings	147
9	Summary Conclusions and Future Work	149
10	Appendix	153
10.1	The ADC Test Setup	153
10.2	Test Signal Generation.....	154
10.3	Test Accessories	155
11	Abbreviations	157
12	References.....	159

1 Introduction

Digital technology has introduced an unprecedented demand for wireless message transmission combined with a continuing trend towards higher data rates and higher bandwidths. This circumstance is reflected in current broadband radio technologies such as LTE, WiGig, or 5G mobile communication systems, which now use several wide frequency bands of the frequency spectrum up to the microwave range. A similar demand for more bandwidth is observed in the military sector, where direct-sequence spread-spectrum, frequency-hopping transmissions, and sophisticated multi-mode radars are gaining ground, resulting in increasing competition for bandwidth [1]. At a coarse level, the radio frequency (RF) spectrum allocation from 3 kHz to 300 GHz in the United States of America is shown in Fig. 1.1.

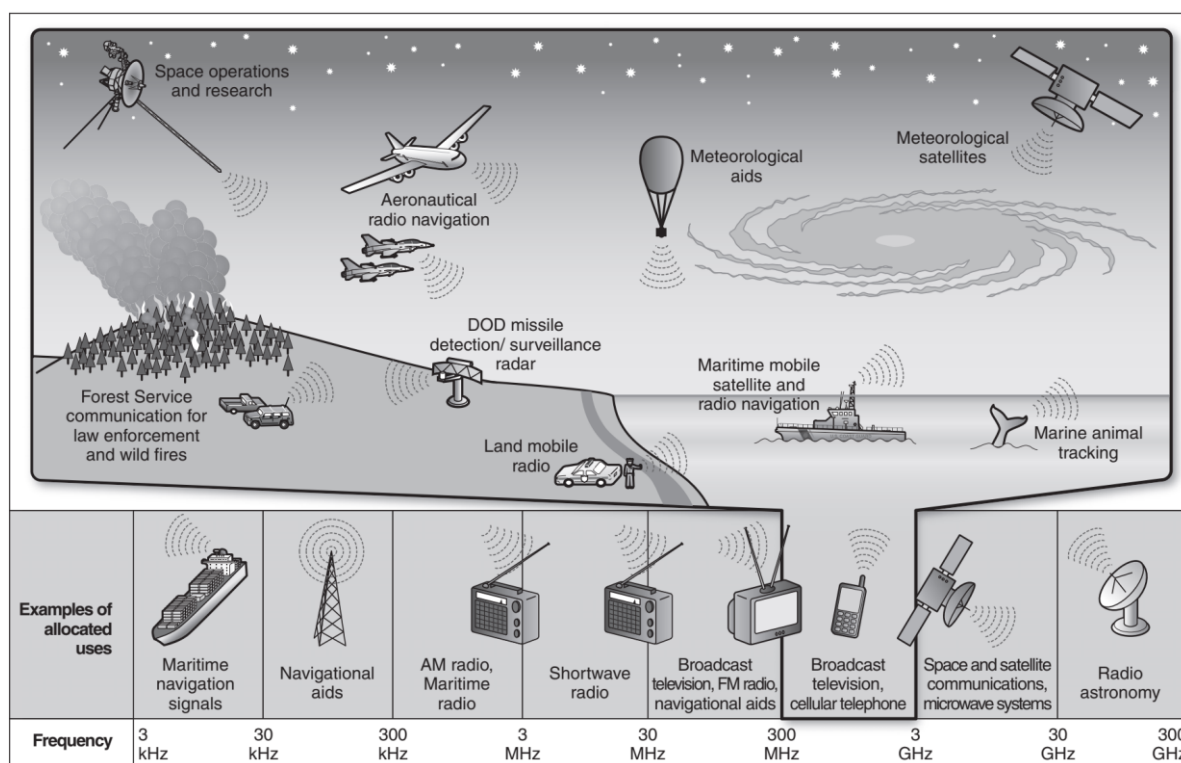


Fig. 1.1: Examples of allocated RF spectrum use in the USA in 2011. Source: GAO analysis of NTIA, federal agencies, and industry information [2].

Since wireless communication is now used virtually everywhere, spectrum allocation authorities and other government agencies need radio monitoring receivers with high real-time bandwidth (RTBW) and a high probability of intercept (POI) to perform their tasks [3]. Similar requirements for high bandwidth arise in the field of industrial measurements, e.g., in spectrum

analyzers [4], [5], or mobile radio base stations. The resulting technical challenges cannot be mastered with conventional analog receivers. That is why software-defined radios (SDR) with direct RF-sampling architectures are rapidly gaining ground. These enable higher bandwidth and improved spectrum monitoring capabilities using a fast analog-to-digital converter (ADC) and digital signal processing (DSP) algorithms. This dissertation work contributes to the improvement of such receiver architectures.

1.1 Problem Description

This Thesis was initiated with the goal of defining a high-performance software-defined radio monitoring receiver architecture that provides a real-time bandwidth of more than 2 GHz. At such high bandwidths, all current receivers must compromise on spurious-free dynamic range (SFDR), which is a measure of how well small signals can be distinguished from noise or unwanted artifacts when strong signals are present. Most broadband receivers get around this problem by using a narrowband design and periodically sweeping the RF band of interest over a wide tuning range. This concept is proven and frequently found in spectrum monitoring receivers and spectrum analyzers. It can achieve an SFDR of more than 100 dB [5], but the working principle significantly limits the RTBW to several tens of kilohertz. In addition, the sweeping principle also limits the POI for short, unknown signals. One way to achieve much higher RTBW and a simplified receiver design is to digitize the RF signals coming from the antenna directly with a giga sample per second (GSPS) ADC. However, the dynamic range of such a broadband direct RF-sampling architecture is still limited today, especially if the bandwidth exceeds several hundred megahertz. Due to the sampling process and unavoidable imperfections of the GSPS ADC, not only noise but also various discrete unwanted signals (spurious) occur in the output frequency spectrum. These phantom signals inevitably degrade the receiver's ability to distinguish an actual signal from self-generated interference. Since the A/D conversion stage is an essential part of the signal chain of a digital receiver, the SFDR of the ADC is crucial for the overall achievable dynamic range [6].

The problem of discrete spurious signals (spurs) in broadband A/D conversion is briefly demonstrated by digitizing a 3 GHz sinusoidal signal with a 10 GSPS ADC. The measurement was performed using the web-based "Remote Hardware Evaluation Tool" from Analog Devices,

Inc. [7]. The tool provides access to a laboratory test setup for evaluating products without purchasing the integrated circuit or an evaluation board. The frequency spectrum obtained from the AD9213, a state-of-the-art RF Analog-to-Digital Converter [8], is depicted in Fig. 1.2. In order to avoid saturation effects, the signal amplitude is set to -1 dB below the ADC's maximum full-scale input level (dBFS). The spectrum plot shows that the resulting SFDR of ≈ 62 dB is not limited by the ADC's broadband noise floor of approximately -90 dBFS but by a spurious signal at 4 GHz with a level of ≈ -63 dBFS. Thus, it can be concluded that eliminating the discrete spurious signals would significantly improve the SFDR to about 90 dB.

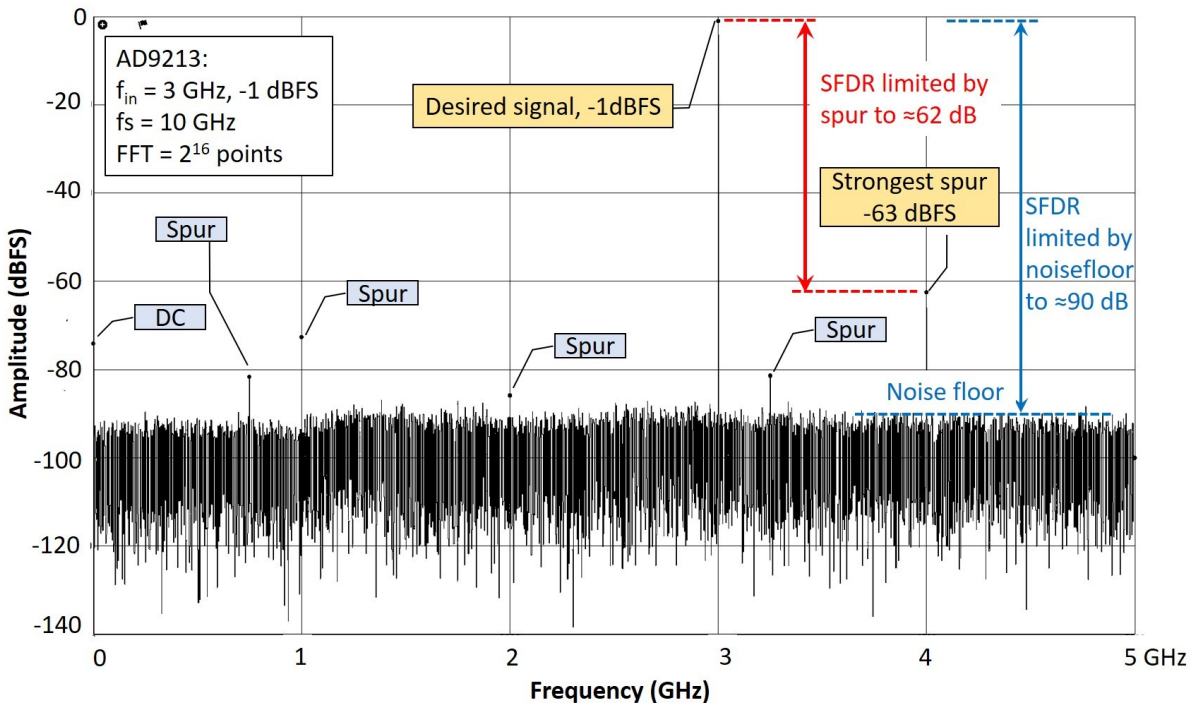


Fig. 1.2: The frequency spectrum of a 3 GHz sinusoidal signal digitized with an AD9213 [8]. The SFDR is limited by a discrete spurious signal (red arrow) rather than broadband noise (blue arrow). Measurements were made with the remote hardware evaluation tool from Analog Devices Inc. [7].

The presence of such spurious is not uncommon, especially at higher drive levels, and any RF-sampling ADC will exhibit similar distortion characteristics. Manufacturers of GPS ADCs are well aware of this problem and have implemented several on-chip technologies to improve the dynamic range of their products. These range from dithering the input signal to proprietary randomization and calibration techniques [8, p. 1]. Despite these efforts, a review of the datasheets from reputable manufacturers shows that the SFDR of GPS ADCs is still limited

to typically less than 70 dB, depending on the operating conditions [9], [10]. Therefore, the overall dynamic range of a receiver with a bandwidth of several hundred megahertz using an ADC to digitize the RF band is primarily limited by the SFDR of the ADC. A recent market survey published by B. Mantz in [11] confirms that current digital broadband receivers have a limited dynamic range of only 60 dB to 70 dB. The limited SFDR of the required GPS ADC is responsible for this. Therefore, to improve the dynamic range of a receiver with a bandwidth in the gigahertz range, new ADCs with better SFDR specifications are needed and may be available sometime in the future. With the technology available today, a different approach is required to address the dilemma of GPS ADC spurious signals. Contributing a new technique to overcome this limitation is the main motivation for this Thesis.

1.2 Thesis Objectives

This dissertation work aims to improve the spurious-free dynamic range of spectrum displays in broadband radio monitoring receivers by reducing phantom signals created by the ADC. The intention is to use the properties of the A/D conversion process to eliminate spurious signals in the output spectrum by digitally post-processing the data in the frequency domain.

The intended technical goals are:

1. An SFDR improvement of more than 20 dB by suppressing spurious signals
2. Functional across the entire Nyquist bandwidth of an ADC
3. Applicable with commercial-off-the-shelf A/D converters

The development approach of this work is practice-oriented and has a broadband radio receiver in mind. However, the results should apply to any A/D conversion process, regardless of a particular application or ADC technology. Since the focus is mainly on reducing spurious signals caused by broadband A/D conversion, a complete receiver architecture is not presented. Space requirements, weight, power consumption, processing power, and cost are also not considered.

1.3 The Solution Concept

The working hypothesis for mitigating spurious signals is that these can be detected in the output frequency spectrum of an ADC by varying its A/D conversion parameters. This is because a digitally sampled signal contains information not only about the signal itself but also about the characteristics of the sampling process and the distortion mechanisms. The A/D conversion parameters considered are the sampling frequency, the signal frequency, and the signal amplitude. If the A/D conversion parameters are known, the analog signal information can be mathematically recovered because there is a known unique relationship. Internally generated spurious signals follow a different pattern as these are related to the sampling frequency or possible ADC nonlinearities, which are immediately visible in the frequency domain. Parallel, synchronous digitization of a signal with two separate ADCs and operating with different A/D conversion parameters results in two different data sets representing the same analog signal. By performing discrete Fourier transforms (DFT) and comparing the two power spectra, spurious signals can be detected and eventually removed by post-processing the DFT data. By suppressing the unwanted signals, a set of purged frequency domain data with improved SFDR is obtained.

The same principle can be realized with only one ADC and sequential acquisition of the different data sets. A rough analogy to this method from photography is as follows: The CCD chip of a camera has a pixel error that represents the imperfection of the ADC. Now two snapshots are taken with different settings of a zoom lens. When both images are scaled to the same size and superimposed, the pixel error appears at a different location on the resulting image. The pixel error can be identified and possibly eliminated by superimposing and comparing the photos.

The following Section 1.4 describes the development methodology and the performance verification approach used in this work.

1.4 Development Methodology

The development of the spurious reduction method is carried out in three phases corresponding to the Chapter organization of this Thesis.

Phase 1: Data collection and analysis (Chapter 2 through Chapter 5), with emphasis on:

1. A review of common receiver architectures
2. ADC performance analysis and sources of ADC errors
3. A literature review of known ADC distortion reduction methods
4. An analysis of the time-discrete sampling process
5. An analysis of the DFT focusing on amplitude and frequency measurements

Phase 2: Design of a spurious mitigation method (Chapter 6) that includes:

1. The principle of operation
2. An analysis of the boundary conditions
3. The implementation of a DSP algorithm

Phase 3: Performance verification of the design (Chapter 7) by:

1. Programming a MATLAB[®] prototype and simulating the method
2. Building a test setup using commercial A/D conversion boards
3. Experimental evaluation with signal generators and antenna signals

In order to provide an overview of the capabilities and possible technical improvements of the various existing receiver architectures, a related analysis is presented in the following Chapter.

2 Radio Receiver Architectures and State of the Art

As a starting point, the operating principles of the most common radio receiver architectures are examined. The advantages and disadvantages are shown, starting with a brief review of the history of radio receivers.

After the experimental proof that electromagnetic waves can travel through free space by Heinrich Hertz in 1888, the potential of this discovery for wireless communication was exploited not by him but by Guglielmo Marconi. In 1897 Marconi was granted a British patent for "Improvements in transmitting electrical impulses and signals, and in apparatus therefor" [11, pp. 316-340]. In 1901, he had already made the first successful radio contact across the Atlantic Ocean. Since then, there has been continuous and sometimes even stormy development in radio transmitters and receivers for wireless communication. Besides the challenge of generating and radiating enough electromagnetic energy, the detection of invisible radiation was difficult too. The use of coherers and later crystals as a receiving method suffered from limited sensitivity, lack of selectivity, and unstable reception [12]. This situation improved around 1920 when vacuum tubes became available, allowing the design of amplifying receivers with more sensitive detectors. Regenerative and super-regenerative receivers were very popular at that time. A breakthrough was the invention of the superheterodyne (superhet) receiver by Lucien Lévy in 1917 [13], which improved the ability to discriminate among several nearby signals. Edward H. Armstrong was granted a US patent in 1920 [14] for this reception principle. The heterodyne or frequency-conversion principle used by these receivers had already been patented for the Canadian Reginald A. Fessenden in 1902 [15], and remarkably, it had not been used earlier. However, at a later stage, various aspects of this architecture were improved, and since then, it has been widely used until today.

The next Section provides an insight into radio receiver technology, starting with the frequency conversion process, which is the basis for understanding how almost all analog and digital radio receivers work.

2.1 The Frequency-Conversion Process

Frequency conversion is a widely used technique in nearly all communication systems. It is performed with a three-port device called a mixer, which converts a specific frequency band with a defined bandwidth into a higher or lower frequency band. In addition to the mixer, a local oscillator signal $LO(t)$ is required for frequency conversion, as shown schematically in Fig. 2.1. An ideal mixer performs a time domain multiplication of two applied signals, where $RF(t)$ is the radio frequency signal to be converted, and $LO(t)$ is the local oscillator signal (LO).

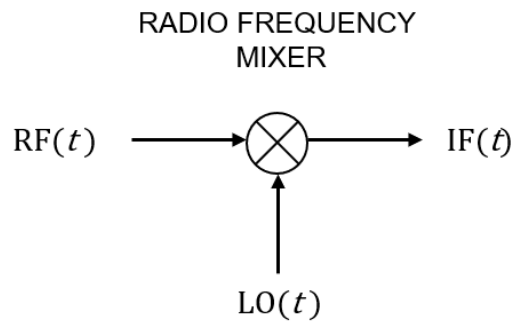


Fig. 2.1: Schematic of a radio frequency mixer and its signals in the time domain.

The resulting signal $IF(t)$ is called the intermediate frequency (IF). The mathematical relationship follows the simple equation:

$$IF(t) = RF(t) LO(t) . \quad (2.1)$$

With two sinusoidal signals $RF(t) = \cos(\omega_{RF}t)$ and $LO(t) = \cos(\omega_{LO}t)$ the multiplication results in an intermediate signal consisting of the sum and difference of both signals, while the fundamental signals $\cos(\omega_{LO}t)$ and $\cos(\omega_{RF}t)$ are suppressed [16, p. 157]:

$$IF(t) = \cos(\omega_{RF}t) \cos(\omega_{LO}t) = \frac{1}{2} \cos[(\omega_{RF} - \omega_{LO})t] + \frac{1}{2} \cos[(\omega_{RF} + \omega_{LO})t]. \quad (2.2)$$

The sum and difference frequencies are usually called the upper and lower sidebands and contain all the RF energy fed into the mixer. If only the frequencies of the mixing products are of interest, disregarding the amplitude and the phase information, these can be calculated by:

$$f_{IF} = |f_{RF} \pm f_{LO}|. \quad (2.3)$$

Fig. 2.2 (a) depicts the mixing process of two sinusoidal signals with frequencies ω_{RF} and ω_{LO} . As ω_{LO} is below ω_{RF} this technique is called low-side mixing. Both sidebands are centered around ω_{RF} and fall into the positive side of the frequency axis. Fig. 2.2 (b) shows an example of high side mixing with one sideband mathematically falling into the negative frequency axis. This sideband is mirrored over the zero-frequency axis to the positive side and shows up physically as a sideband with mirrored spectral orientation.

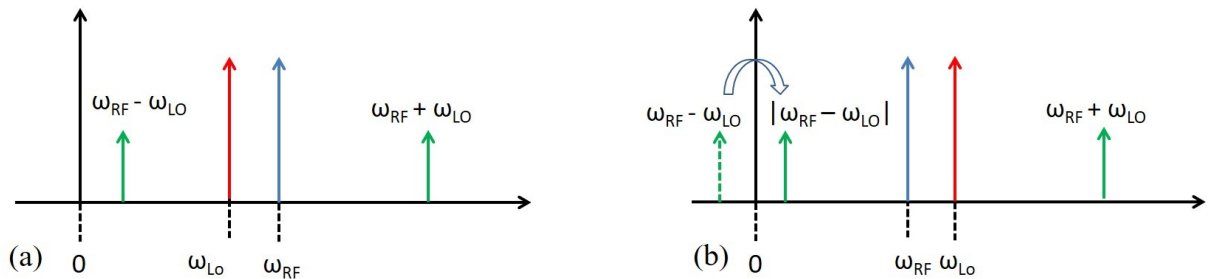


Fig. 2.2: Frequency spectrum of an ideal mixer; (a) low side mixing and (b) high side mixing.

In technical applications, most of the time, only one of the two signals is desired. The unwanted sideband is called the image frequency, which must be suppressed by adequate filtering. Besides filtering, the image problem can also be addressed by using an image-rejection mixer. It consists of an I/Q demodulator, followed by a phase shifter and a summer stage. Fig. 2.3 shows an analog and a digital implementation of this concept.

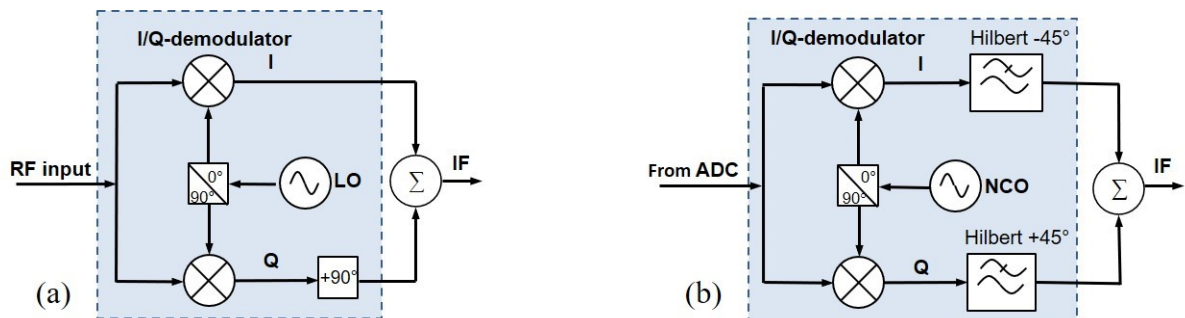


Fig. 2.3: Examples for the image-rejection mixer concept; (a) analog and (b) digital implementation.

By adding another 90-degree phase shift in the Q path of (a), the phase of the image sideband is shifted by 180 degrees overall and cancels out in the summation stage. Such integrated analog I/Q mixers are available from various manufacturers. The digital implementation, shown in Fig. 2.3 (b) is called quadrature sampling with digital mixing [17, pp. 462,463]. The local oscillator is a numerically controlled oscillator (NCO) implemented in software. The 90-degree phase shift is achieved by two ± 45 -degree low-pass Hilbert transforms in each channel. Using two identical structures guarantees the same signal processing delay and phase shift in each channel. Fig. 2.4 shows the LMX8410L, a high-performance integrated I/Q demodulator from Texas Instruments with an RF input from 4 GHz to 10 GHz with an integrated LO and an IF amplifier [18]. The IF bandwidth ranges from DC to 1350 MHz, and the image rejection ratio achieves 36 dB to 44 dB if gain and phase are calibrated. These values reflect the current state of the art and indicate what can be expected from this technology. The additional 90-degree phase shift at the IF output must be implemented in analog or digital form.

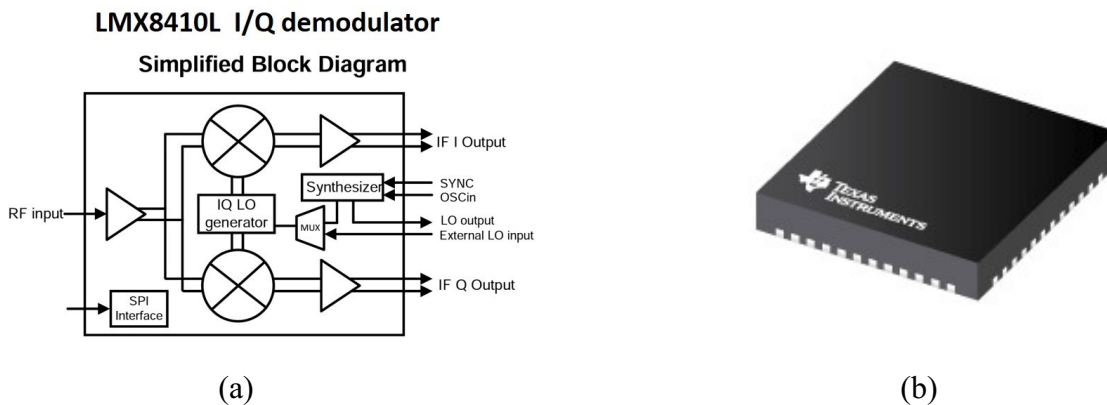


Fig. 2.4: Integrated I/Q demodulator LMX8410L from Texas Instruments [18];
(a) Simplified block diagram and (b) Picture of the 7×7 mm package.

There are no ideal mixers, regardless of whether these are implemented in digital or analog form. Hardware mixers typically consist of one or more nonlinear elements such as diodes or semiconductor switches, which have imperfect multiplication characteristics. The nonlinearities can be expressed as a Taylor series expansion that contains quadratic and higher-order terms. By multiplying the LO and RF signal with the higher-order terms, all these mixers produce additional frequency combinations at the output [19, p. 159], which can be calculated by:

$$f_{IF} = |mf_{RF} \pm nf_{LO}| \quad \text{where } m, n = 1, 2, 3 \dots, \text{ and } m + n \geq 3. \quad (2.4)$$

As these nonlinearities can, to some extent, be found in almost every electronic component, A/D converters are also subject to this kind of distortion. Even digital mixers implemented in software have some imperfections resulting from the multiplication of numerical values with limited accuracy representing the signals [20, pp. 3-3].

2.2 Superheterodyne Receivers

Frequency conversion using mixers described in the previous Section is the fundamental idea of the superheterodyne receiver, commonly abbreviated as superhet. It converts the radio signal to a fixed, often lower IF, which can be processed more easily. According to (2.3), the multiplication process delivers two intermediate frequencies along with other undesired mixing products (2.4). The desired intermediate frequency can be filtered out and processed further in the IF channel. Fig. 2.5 shows the simplified block diagram of a classic superhet design with a single frequency conversion stage.

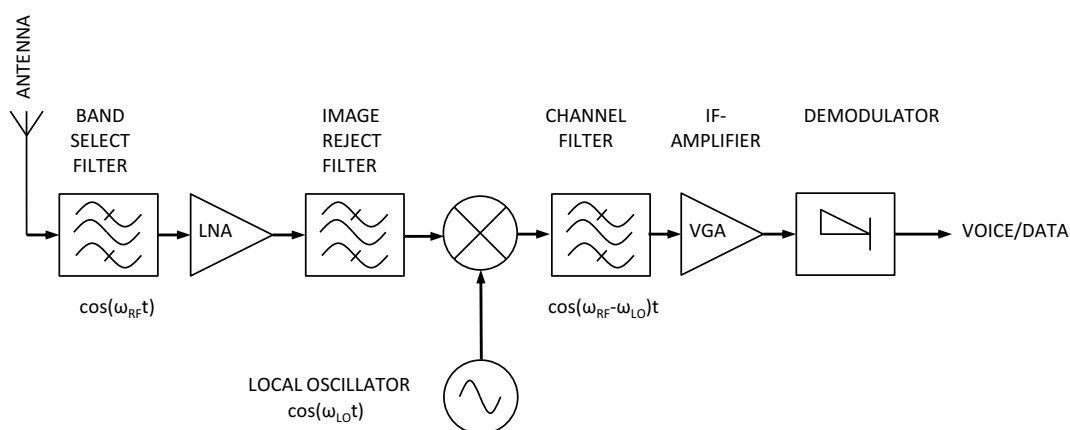


Fig. 2.5: Block diagram of a superhet receiver with a single frequency conversion stage.

The RF spectrum of interest from the antenna is bandlimited with a band select filter and amplified with a low-noise amplifier stage (LNA). The following image-reject filter prevents unwanted RF energy at the image frequency from entering the mixer. The mixer converts the RF signal to a fixed intermediate frequency. This signal is filtered with a channel filter, whose characteristics match the modulation content of the RF signal and suppress adjacent channels. The IF signal is further amplified by a variable gain amplifier (VGA), and the following demodulation stage recovers the information content of the RF signal. Equation (2.3) shows that

there are always two RF frequencies $f_{RF} = |f_{LO} \pm f_{IF}|$, which fall into the desired IF channel. Therefore, the image band must be suppressed to the required value by an adequate band-select and image-rejection filter design. Converting a very high-frequency input signal to a low-frequency signal in just one conversion stage can cause problems. In this case, the image band is close to the wanted RF band and, therefore, difficult to suppress with filtering. A dual-conversion architecture can improve this situation. By using two conversion stages, the frequency spacing between the image frequency bands and the desired input frequency is increased. An innovative, double superhet up-conversion scheme, with the first IF centered at 40 MHz, was already introduced by Racal Engineering Ltd. in a shortwave receiver in the middle of the 1950s. Fig. 2.6 shows the block diagram of a modern, widely used double superhet configuration with digital signal processing in the last IF stage.

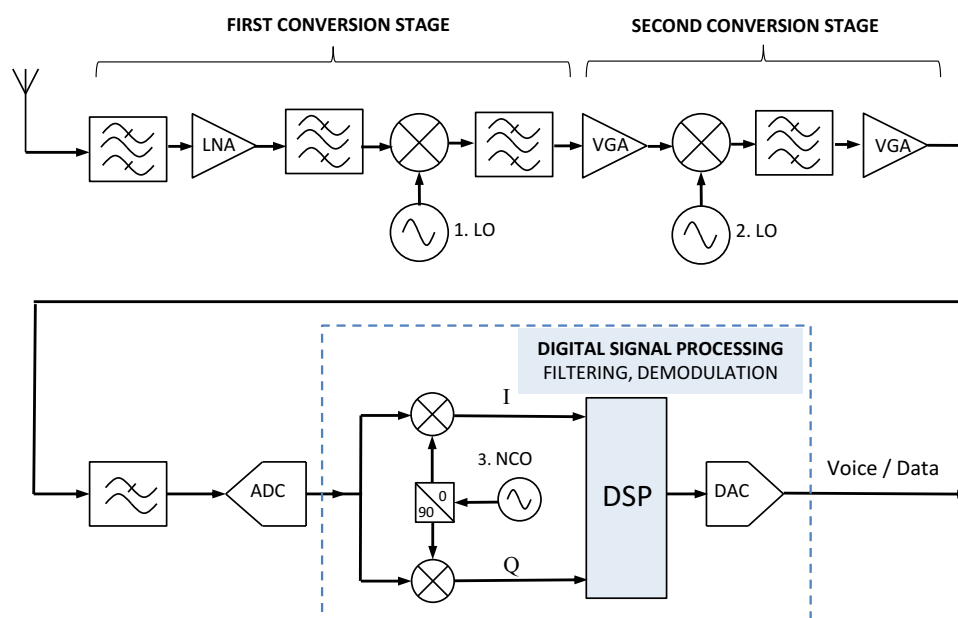


Fig. 2.6: Block diagram of a double superhet receiver with digital signal processing after the second conversion stage.

The building blocks are like the single conversion superhet in Fig. 2.5, but two analog conversion stages are used here. By sampling the narrowband second IF with an ADC, digital filtering and demodulation techniques can be used. This example uses digital I/Q mixing, as shown in Fig. 2.3 (b). DACs are used to bring the digital signals back to the analog domain. The second IF can be low so that ADCs with excellent performance can be employed. This architecture is often referred to as a low IF sampling receiver. The following Subsection provides some RF-performance data for such a receiver.

2.2.1 Example Data for a High-Performance Superhet Receiver

The key performance data of a state-of-the-art superhet, the R&S M3SR Series 4100 receiver [21], are listed in Table 2.1 below. As can be seen, the dynamic range achieves a value of more than 100 dB in single sideband (SSB) mode. However, the maximal channel bandwidth (IF-bandwidth) is limited to less than 20 kHz.

Table 2.1: RF performance of the Rohde & Schwarz M3SR Series 4100 receiver [21].

Parameter	Value	Units	Notes
RF frequency	0-30	MHz	Tuning range
IF bandwidth	<20	kHz	
Dynamic range (SSB)	>100	dB	Single sideband mode

2.2.2 Performance Evaluation of the Superheterodyne Receiver

The traditional superhet receiver architecture achieves excellent results based on a highly optimized analog down conversion architecture followed by a narrowband digital signal processing stage. Today the best available communication receivers use this architecture [22]. The sensitivity, selectivity, and dynamic range of such receivers are outstanding and are, for example, the first choice for naval communication when several transmitters and antennas are closely spaced on board a ship [23]. The price for this performance is high cost and complicated construction. Moreover, this architecture is not easy to implement, as it is prone to image problems and spurious reception due to several frequency conversion stages. It requires multiple bulky filters to suppress unwanted signals, adequate shielding, and several computer-controlled, low-phase noise synthesized local oscillators. The architecture is therefore inflexible, power-hungry, and difficult to integrate on a chip. Despite excellent RF data, the main disadvantage of such receivers is the low bandwidth and limitation to only one communication channel at a time.

2.3 Direct-Conversion Receivers

The direct-conversion receiver, also called the zero-IF receiver, does not need IF stages that limit the bandwidth. Although this architecture was invented as early as 1924, it has only become popular in the last two decades with the advent of better components, especially integrated circuits most suitable for this receiver topology. Here, the incoming RF signal $\cos(\omega_{RF}t)$ is amplified and mixed with an LO signal $\cos(\omega_{LO}t)$ of the same frequency. It is directly down-converted to baseband and, after low-pass filtering, available for further processing. The working principle is depicted in Fig. 2.7 below.

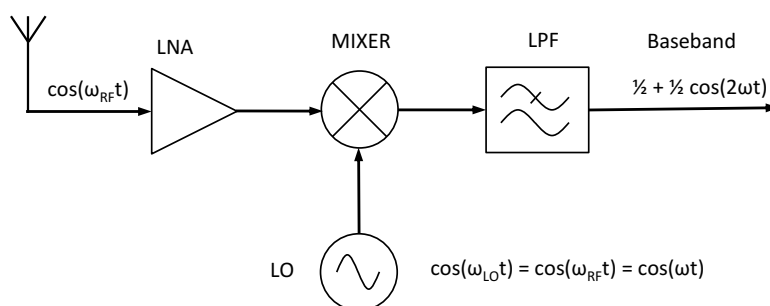


Fig. 2.7: Simple direct-conversion receiver circuit.

According to (2.2) and with $\cos(\omega_{RF}t) = \cos(\omega_{LO}t) = \cos(\omega t)$ the result of the mixing process is:

$$\cos(\omega t) \cos(\omega t) = \frac{1}{2} \cos(0) + \frac{1}{2} \cos(2\omega t) = \frac{1}{2} + \frac{1}{2} \cos(2\omega t) . \quad (2.5)$$

The incoming signal is transformed into two intermediate frequency components: A baseband component and a harmonic component with $2\omega t$, which can be easily suppressed by a simple low-pass filter (LPF). Figure 2.8 illustrates this down-conversion process for a radio frequency band before (a) and after (b) mixing it with ω_{LO} . In this example, the spectrum of the RF band is asymmetrical and not centered around ω_{LO} .

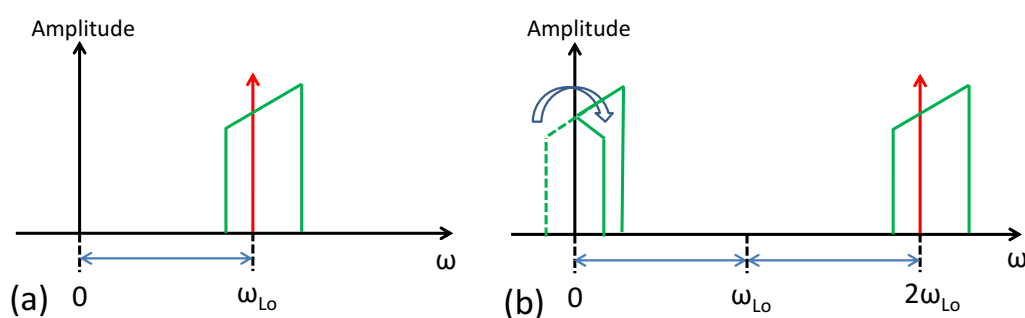


Fig. 2.8: Spectrum of a broadband RF signal (green) and the LO signal (red); (a) before and (b) after the mixing process.

The resulting RF signal components on the negative side of the frequency axis fold back at the zero-frequency axis, and both sidebands overlap. If the RF signal's modulation sidebands are symmetrical and ω_{Lo} is precisely in the middle of the band, no information content is lost. For example, this is the case for amplitude modulation or simple on-off-keying modulation schemes, where the LO and carrier of the RF signal can be synchronized. However, for most modern digital modulation schemes that use phase or frequency modulation, the two sidebands may contain different information. In this case, the overlap of the sidebands results in irreversible corruption of the information content, as is indicated in Fig. 2.8 (b). For this reason, this down-conversion scheme is only suitable for most simple devices, for example, wireless thermometers and the like, which rely on simple modulation methods.

A much more capable and frequently used concept is the so-called quadrature mixing architecture depicted in Fig. 2.9. This variant of the direct-conversion receiver converts the signal down to the baseband with an I/Q demodulator and samples the resulting signals with two separate ADCs. As the input frequency to the ADCs is from DC upwards, only half the bandwidth of the original signal needs to be supported. Therefore, good performance of the ADC stages can be expected [24, p. 12], [25, pp. 5,6].

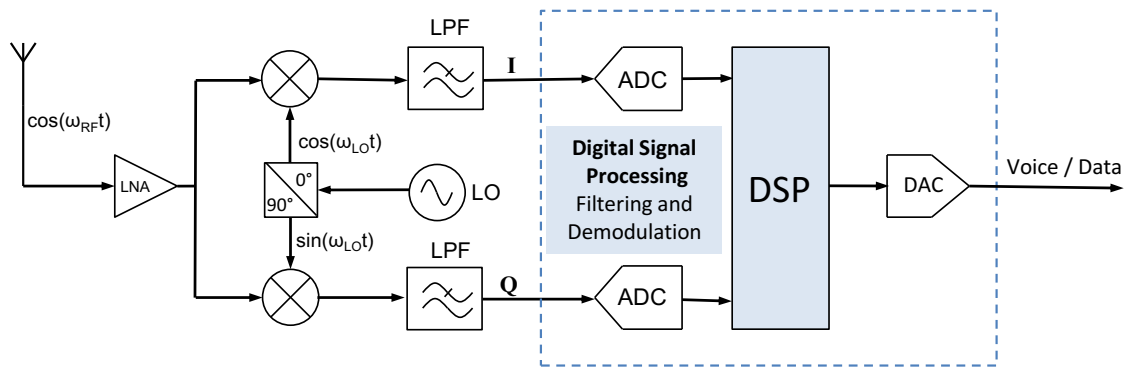


Fig. 2.9: Quadrature mixing scheme with two separate ADCs and DSP for processing the I and Q channels.

The receiver's quality depends on the performance of the I/Q demodulator, the precision of the quadrature LO signals, and how well the ADCs are matched. Any phase error or amplitude imbalance results in the degradation of the demodulated signal. Various monolithic integrated solutions for applications like the cell phone market or global positioning systems (GPS) are readily available. A typical example of this technology is depicted in Figure 2.10. It shows a Section of the receiver path of the AD9371, an integrated broadband dual 300 MHz to 6 GHz RF transceiver from Analog Devices [26]. It consists of a broadband direct-conversion I/Q path followed by a low-pass filter and two 12-bit ADCs. The RX bandwidth is specified from 8 MHz to 100 MHz, and the power consumption in transceiver mode is less than 5 W.

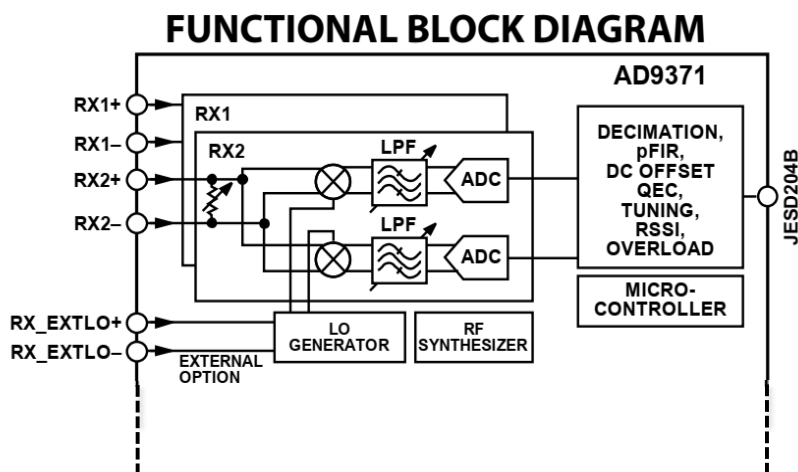


Fig. 2.10: Example for the I/Q mixing scheme; Functional diagram of the integrated dual RF-Transceiver AD9371 from Analog Devices. Only one RX path is shown. The picture is taken from [26].

A common problem of the direct-conversion architecture is self-mixing with the LO signal, also called LO-leakage. When the LO signal couples back to the mixer's RF port, the two LO signal components will heterodyne, and depending on the phase angle, a DC signal will result at the output. This DC offset, if not removed, affects the signal integrity of the baseband signal. Figure 2.11 shows three different mechanisms of how self-reception of the LO frequency can occur [27].

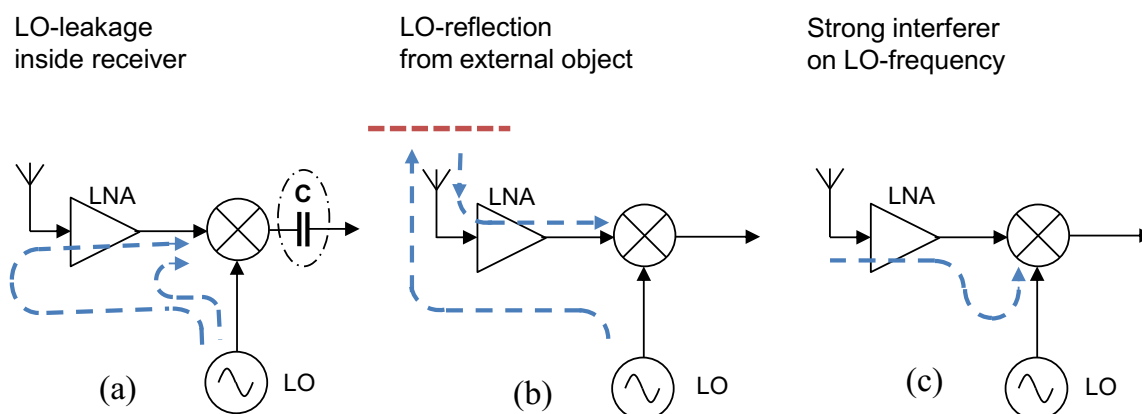


Fig. 2.11: The leakage mechanisms in a direct-conversion receiver; (a) Internal LO leakage into the mixer, (b) LO re-radiation, (c) strong interference on LO frequency. Drawing inspired by [27].

Removing the DC component with a simple coupling capacitor C , as depicted in Fig. 2.11 (a), seems obvious but has its problems. Removing the DC component from a modulation scheme that contains a DC component can compromise signal integrity and increase the bit error rate [28]. Therefore, several more elaborate methods to reduce the DC offset have been developed and published in the literature [29].

2.3.1 Example Data for a Direct-Conversion Receiver

For the high-performance I/Q demodulator shown in Fig. 2.4, the manufacturer has published the block diagram of a direct-conversion receiver design [30, p. 13]. The signal flow is depicted in Fig. 2.12. The I and Q channel are sampled by the ADS54J60, a dual-channel ADC from the same manufacturer.

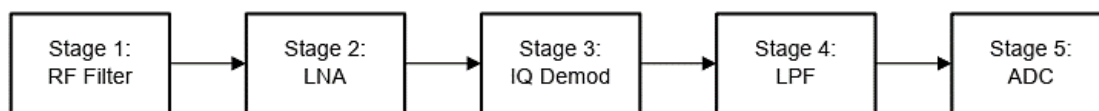


Fig. 2.12: The signal flow of a direct-conversion receiver using the LMX8410 I/Q demodulator in stage 3. Drawing taken from a Texas Instruments Application Note [30].

The performance of this architecture, according to the manufacturer, is summarized in Table 2.2. For an RF frequency of 6 GHz and an IF bandwidth from DC to 100 MHz, an SFDR of 44.1 dB was published in [30]. Compared to the characteristics of the superhet listed in Table 2.1, the real-time bandwidth has considerably improved from 20 kHz to 100 MHz, but the SFDR is about 56 dB lower, which is significantly worse. A major advantage of this design is that it is fully integrated except for two small RF filters, has a small footprint, and consumes only 5.5W.

Table 2.2: RF performance of a direct-conversion receiver design presented in [30].

Parameter	Value	Units	Notes
RF frequency	6000	MHz	Tuning range
IF band	0 -100	MHz	Real-time bandwidth
Receiver SFDR	44.1	dB	

2.3.2 Performance Evaluation for the Direct-Conversion Receiver

Compared to the superheterodyne architecture, a direct down-conversion receiver has many benefits, such as higher bandwidth, hardware simplicity, smaller size, and lower power consumption. The ADCs operate at baseband, where the performance is usually better, and filtering is much easier. This architecture is, in principle, free of mixing spurs and image signals. It works well provided the amplitudes in the I and Q channels are identical, and the phase shift is precisely 90 degrees. Modern implementations use digital and analog correction techniques to improve the amplitude and phase accuracy of the I/Q channels. Examples are given in [25] and [31]. In this way, customized solutions with good performance are possible. Billions of highly integrated receivers based on direct I/Q conversion are produced and successfully deployed for the cell phone market.

2.4 Direct RF-sampling Receivers

A well-designed superhetro receiver has superior RF performance, and the direct-conversion receiver also has many benefits. These architectures are very successful and have been steadily improved over several decades. Today there are more future-oriented alternatives such as those outlined by U. Rohde as early as 1985 [32] and J. Mitola in [33]. The basic idea is to digitize the incoming RF signal as close to the antenna as possible with a high-resolution, high sample rate ADC. All frequency conversion, filtering, and demodulation can be carried out in the digital domain. This approach significantly simplifies the overall receiver design and enables digital signal processing of an entire RF band. The architecture does not require any analog mixers, local oscillators, or IF stages that cause additional noise and distortion. If the numerical representation of the digital values is precise enough, e.g., 32-bit, the added noise and distortion due to signal processing can usually be neglected. A 32-bit word can represent a dynamic range of about $32 \times 6 \text{ dB} \approx 192 \text{ dB}$ [17, p. 634], much more than can be achieved with analog stages. Figure 2.13 shows the block diagram of a direct RF-sampling receiver. The RF signal is bandlimited by an RF filter, amplified by an LNA, followed by a low-pass filter. This filter is often called an anti-aliasing filter (AAF) and, with its sharp roll-off characteristic, keeps unwanted frequencies away from the ADC. A more detailed description of the aliasing effect can be found in Subsection 4.3. The digital signal processing routines are typically implemented in fast field-programmable gate arrays (FPGAs), standard DSP processors, or both.

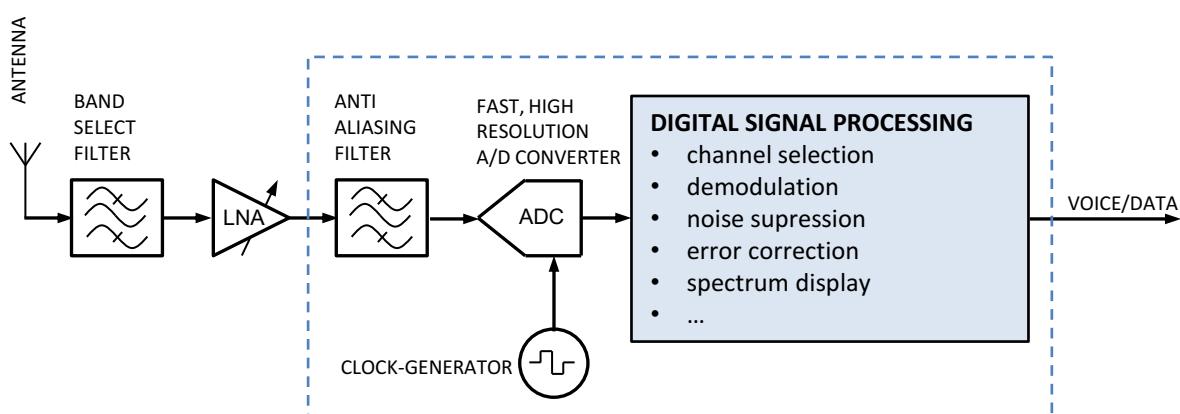


Fig. 2.13: The simplified block diagram of a direct RF-sampling receiver, where many traditional receiver functions are purely implemented in software.

At first glance, this simple, straightforward architecture seems convincing but has its challenges. The most performance-critical component is the ADC, with its imperfect conversion characteristics. Since there are no frequency-selective components apart from the RF- and the anti-aliasing filter, all signals within the band of interest reach the ADC without attenuation. Therefore, the ADC must provide a wide dynamic range to handle interfering signals. One of the first commercially available broadband monitoring receivers to use this direct RF-sampling concept was the R&S[®] EB500, which covers a frequency range from 8 kHz to 6 GHz. It was introduced in 2010 [34] and achieved an RTBW of 20 MHz. From 30 MHz downwards, it works with a direct RF-sampling architecture, using commercially available ADCs for demodulation and a panorama spectrum display. Meanwhile, many receivers with similar architectures are available on the professional and amateur radio markets. [35], [36], [37], [38].

2.4.1 Example Data for a Direct RF-sampling Receiver

An RF-sampling receiver's performance depends not only on the data of its ADC but also on other implementation details. Critical is good preselection, a high dynamic range of the LNA, and a gain control ahead of the ADC. Up to 30 MHz, the sensitivity and the SFDR are comparable to the high-performance superhet receiver presented in Subsection 2.2.1 but with a much improved real-time bandwidth. Fig.2.14 shows an example of such a receiver. It uses a direct RF-sampling architecture from 0.01 MHz to 30 MHz and a superhet architecture from 20 MHz to 6 GHz. The RTBW of the spectrum display is 20 MHz.

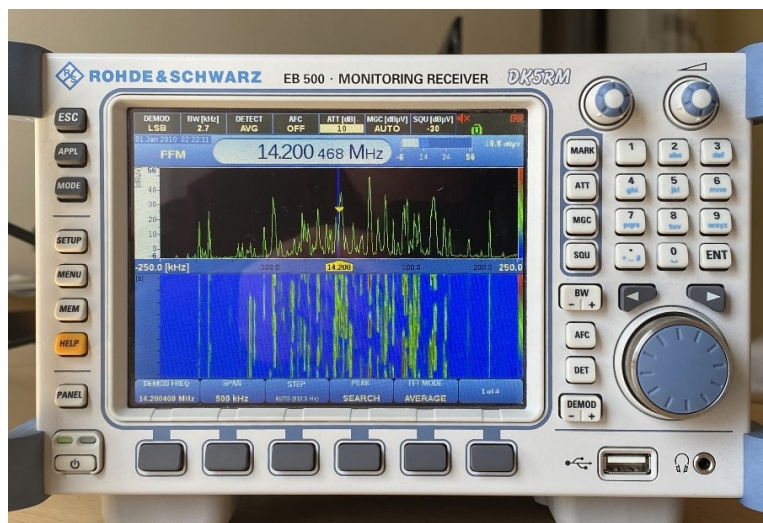


Fig.2.14: The Rohde & Schwarz EB500[®] Radio Monitoring Receiver. (Own photograph).

The tuning range, the bandwidth, and the dynamic range of this receiver are listed in Table 2.3. The RF performance data are typical for a modern radio monitoring receiver with digital signal processing.

Table 2.3: RF performance data of the Rohde & Schwarz ®EB500 Monitoring Receiver [34].

Parameter	Value	Value	Units
RF frequency	0.01 - 30	20 - 6000	MHz
Panorama bandwidth	20	20	MHz
Dynamic range (SSB)	>100	>100	dB

2.4.2 Performance Evaluation for the Direct RF-sampling Receiver

Direct RF-sampling offers many advantages over other architectures. No hardware mixers or local oscillators are necessary except for the ADC's clock oscillator. The theoretical bandwidth can be up to half the ADC sampling rate, and thus the RTBW is several orders of magnitude higher than traditional narrowband superhets. Once the RF signals are digitized, Multi-mode / multi-channel reception in parallel is possible and only limited by the computing power after the ADC. Due to the primarily digital implementation, these receivers are hardly affected by component tolerances and aging. The manufacturing process requires less effort as the parts count is reduced, and not many alignment steps or measurements are necessary. In addition, these receivers can be flexibly reconfigured with software updates.

Although ADCs continue to improve steadily, dynamic range performance is still a limiting factor in direct RF-sampling receivers when designed for sampling rates in the gigahertz range [9], [10]. High sampling rates also result in high power consumption by the ADC and the subsequent signal processing stages, which creates additional power supply and cooling challenges. In order to achieve the best possible dynamic range of the ADC, the clock oscillator must meet demanding jitter specifications in the sub-picosecond range [39]. Any direct RF-sampling receiver needs an antenna amplifier to drive the ADC. This amplifier must have a low noise figure, high gain, and excellent distortion characteristics to best use the ADC's dynamic range. These requirements make a direct RF-sampling receiver design more complicated and less attractive than the simple block diagram in Fig. 2.13 suggests.

2.5 Broadband Radio Monitoring Receivers

Civil, military, and public safety communication takes place in frequencies up to the millimeter-wave range. Broadband radio monitoring receivers are used to detect and analyze unknown signals for government and intelligence purposes. Fig. 2.15 illustrates the many frequencies used for aerospace and defense applications. Since signals can occur from the lower end of the radio spectrum into the gigahertz range, receivers with correspondingly comprehensive frequency coverage are required.

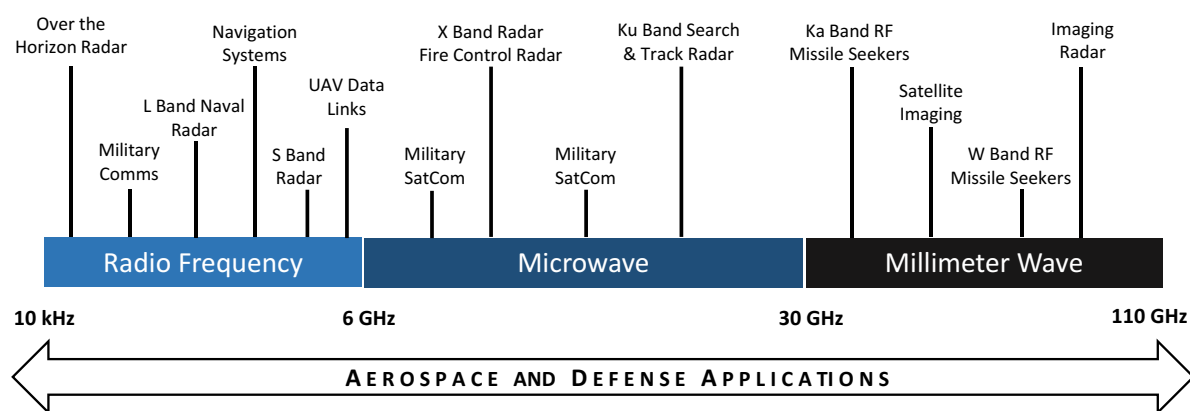


Fig. 2.15: Example of the wide range and various radio frequencies used for aerospace and defense applications. The graphic is redrawn from [40].

These receivers are designed to meet the specific requirements of government agencies or security organizations that use their own terminology to describe their mission. Strategic signal intelligence (SIGINT) generally refers to gathering information by intercepting and analyzing electronic signals of interest [41]. A distinction is made between two different types of signals. Communication Intelligence (COMINT) aims at traffic and signals that carry information, such as voice or data. Electronic Intelligence (ELINT) does not aim at the content of the transmission but instead focuses on the technical and operational parameters of the signals, e.g., radars, weapons, or beacons. Therefore, COMINT receivers must have good demodulation capabilities, while ELINT receivers are characterized by high real-time bandwidth and a good probability of intercept. Since these requirements are difficult to meet with a single architecture, two different types of receivers are typically used. These are presented in the following two Subsections.

2.5.1 Communication Intelligence Receivers

The current architecture for COMINT broadband monitoring receivers is usually based on the superheterodyne principle described in Section 2.2. Many products are implemented as fast-tuning narrowband receivers that repeatedly sweep the frequency range of interest. Due to the sweeping principle, the probability of intercept (POI) decreases when the search range is extended. A graphical spectrum display is often found in manually operated systems, while unmanned systems use fast data interfaces and computer remote control. Fig. 2.16 shows the signal flow of a radio monitoring receiver with a tuning range from 8 kHz to 40 GHz. The VHF-UHF-SHF reception path ① offers a bandwidth of 20 MHz with a dynamic range of approximately 100 dB. Path ② is an optional broadband path with an instantaneous bandwidth of up to 80 MHz for applications requiring higher bandwidth [42]. Path ③ is a direct RF-sampling architecture used for the reception of the HF band. Digital down converters (DDC) for five individual software-defined receivers and a spectrum display are implemented as digital signal processing functions.

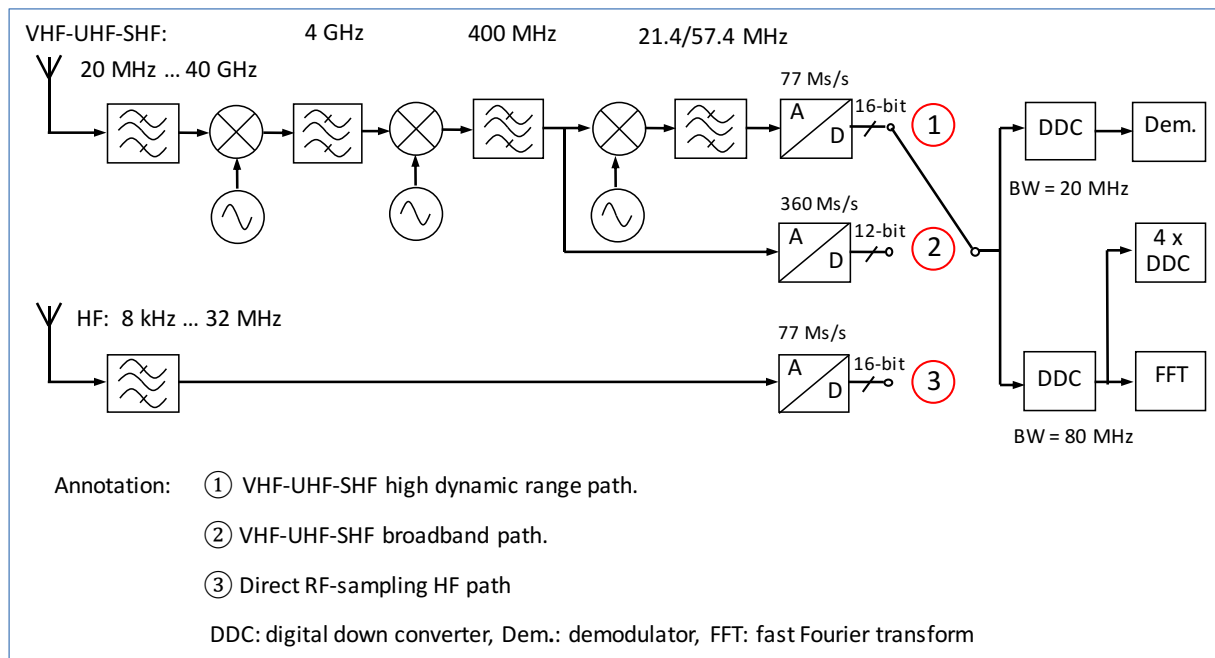


Fig. 2.16: Simplified RF signal flow of the Rohde & Schwarz [®]ESMD Monitoring Receiver. The schematic is taken from [43], redrawn, and annotated.

2.5.2 Electronic Intelligence Receivers

Receivers of this class are designed for surveillance systems to immediately intercept unknown RF signals and identify a radar platform or weapon. High receiver sensitivity and POI are essential for rapidly detecting time-limited events and frequency-agile signals. Often these are multi-mode, multi-frequency radars, or frequency-hopping transmitters. Since the signals need to be classified, the signal's signature is often analyzed and provided via data interfaces for further analysis and storage. Due to the high probability of intercept and RTBW requirements needed for analysis, the direct RF-sampling architecture presented in Section 2.4 offers many advantages for such applications. Fig. 2.17 and Fig. 2.18 show simplified block diagrams of modern, digital ELINT receivers with RF-sampling. Both approaches use multiple ADCs to overcome the bandwidth limitations of a single ADC stage.

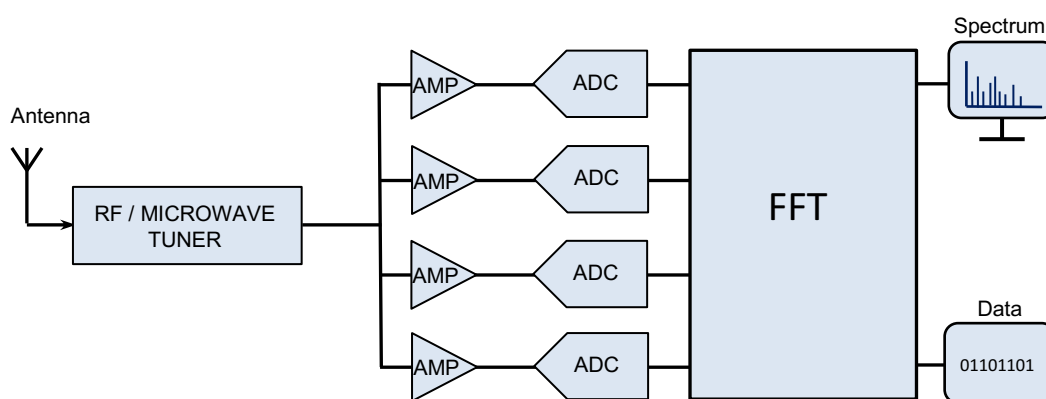


Fig. 2.17: Broadband ELINT receiver using a single RF tuner and four interleaved ADCs [40].

The architecture shown in Fig. 2.17 uses a single microwave tuner as an RF down-conversion stage, followed by four individual driver amplifiers and broadband ADCs. Using the time-interleaved technique [44] and sampling the input signal with a phase shift of 90 degrees to each other, four times the sampling rate of a single ADC is achieved. However, the ADCs must support the required RF bandwidth. This broadband solution needs only one microwave tuner, but the dynamic range suffers from the spurious signals generated by the interleaving technique [45]. A superior architecture with an enhanced dynamic range is shown in Fig. 2.18.

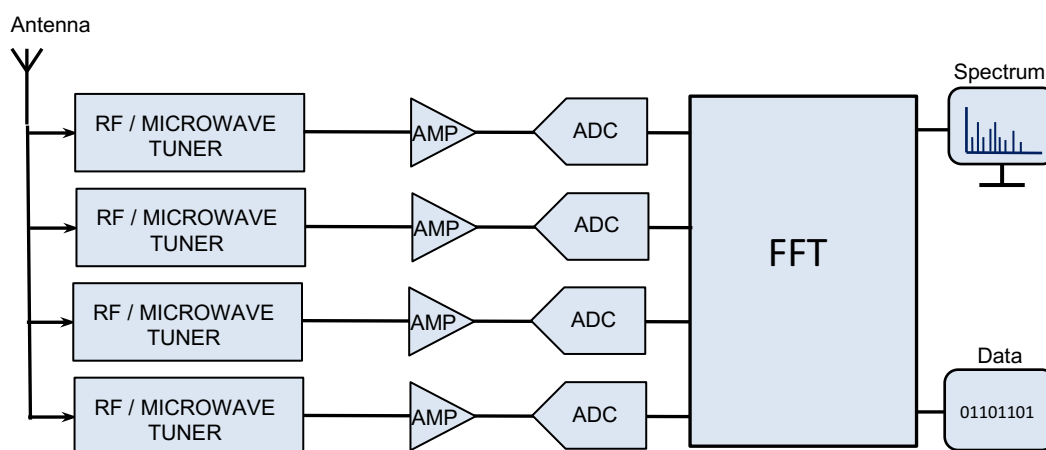


Fig. 2.18: Improved broadband ELINT Receiver with the antenna signal partitioned between four individual sets of RF tuners and ADCs [40].

Here, four microwave tuners split the analog input signal into four channels which are digitized in parallel by four individual ADCs. By recombining the frequency bands, four times the bandwidth of a single ADC is achieved. This way, the dynamic range drawbacks of an interleaving ADC architecture can be avoided. Since four independent microwave tuners are needed, the technical and financial effort is much higher than for the solution shown in Fig. 2.17.

2.5.3 Performance Evaluation for Broadband Monitoring Receivers

Not many technical details and performance data of such receivers are publicly available because these are primarily intended for defense applications and are kept confidential. According to [46], the R&S WPU2000 has a maximum tuning range of 8 kHz to 40 GHz and a maximum RTBW of 2 GHz. The spectral sampling speed is up to 2500 GHz per second. No SFDR data have been published yet. For the Keysight UXA, an RTBW of 510 MHz and an SFDR of 78 dBc are reported. The signal duration for a 100% POI is 3.51 μ s. [47].

A compilation of 40 actual radar and ELINT receivers is presented by B. Manz in [48]. According to this survey, even advanced digital architectures show significantly less dynamic range than narrowband superhets. Most products are specified with an instantaneous dynamic range of only 60 dB to 70 dB. Due to the extensive bandwidth of such receivers, it is more likely that

many strong signals will reach the A/D conversion stage unattenuated. The resulting high sum signal levels may cause ADC distortion and interference signals in the reception passband.

2.5.4 Summary Conclusions on Receiver Architectures

The optimal architecture of a radio receiver in terms of performance and cost depends primarily on the intended application. A keyless car entry has different requirements than a deep-space radio link to a remote vehicle on Mars. Both concepts work as intended but use very different architectures and technical solutions. From this perspective, there is no ideal receiver architecture per se; all of them have weak and strong aspects, as is listed in the following Table 2.4. This qualitative overview is based on Sections 2.2 to 2.5 and typical performance data of real receiver implementations.

Table 2.4: Qualitative performance benchmark of different receiver architectures.

Receiver Architecture	Tuning range	Sensitivity	Selectivity	SFDR	Detect. speed, RTBW	Blocking immunity	Size, weight	Power efficiency	Cost
Direct conversion	+	++	++	+	++	+	+++	+++	++
IF sampling superhet	+++	+++	+++	+++	-	+++	o	+	o
Sweeping monitoring	+++	+++	+++	+++	o	++	-	-	-
Direct RF-sampling	++	o	+++	-	+++	-	o	o	o

Indicators mean: excellent (++++) good (++) fair (o) poor (-)

In summary, the state of the art of radio receiver architectures can be characterized as follows:

1. Superhet receivers with low IF sampling architecture are the first choice for demanding RF environments with relatively narrow bandwidths and tuning ranges up to the microwave region. A well-designed receiver will achieve an excellent dynamic range of more than 100 dB.

2. The direct-conversion architecture finds its place where size, bandwidth, cost, and power consumption are more critical than outstanding receiver performance, e.g., in cell phones or special applications such as small, lightweight power-saving systems.
3. For spectrum monitoring receivers, sweeping superhet concepts are prevalent. This approach often combines a broadband path for spectrum monitoring with a narrowband, high dynamic range demodulation path in one instrument. The drawback is a reduced search speed due to the sweeping principle.
4. Direct RF-sampling receivers with a tuning range up to 30 MHz can achieve a similarly good dynamic range as superhets since high dynamic range ADCs with sampling rates up to 130 MSPS are available [49]. Broadband RF-sampling with GSPS ADCs offers a way to achieve exceptionally high bandwidth. However, with current ADC technology, the dynamic range is noticeably worse than narrowband concepts because the broadband A/D stage creates spurious signals when the bandwidth exceeds several hundred megahertz [50], [51]. Unlike external signals, these internally generated false signals cannot be removed by analog filtering [52]. Therefore, radio designers rely on better ADCs with a higher sampling rate and improved SFDR to make direct RF-sampling receivers more broadband and achieve a higher dynamic range [6].

In conclusion, there is currently no radio receiver architecture that combines a high RTBW of more than several hundred megahertz with the high dynamic range of a well-designed narrow-band superhet. Except for direct RF-sampling, all receiver architectures have been known and optimized for a long time; therefore, significant advances in bandwidth are not to be expected. In contrast, direct RF-sampling is a relatively new concept that will become increasingly attractive as A/D converter technology advances. For this reason, RF-sampling as close to the antenna as possible is a promising, forward-looking architecture for the next generation of broadband monitoring receivers. An essential prerequisite for this step forward is mitigating the problem of limited SFDR caused by the A/D converter stage. Therefore, improving SFDR by reducing spurious signals will be pursued in the further course of this work.

3 ADC Distortion and Dynamic Range

The following Chapter examines the key features and specifications of analog-to-digital converters that are critical for broadband receiver applications. Particular attention is paid to the dynamic range and the ADC distortion mechanisms. Moreover, the state of the art and performance examples of a modern GPS ADC are provided. The Chapter concludes with a literature review of known methods for improving the dynamic range of receiver ADC stages.

3.1 ADC Imperfections

Before a weak radio signal is sampled, it must be amplified by a low-noise, highly linear driver stage to provide a sufficient input level to the ADC. After sampling, the acquired values will still represent an infinite number of analog values. The amplitudes of the analog values must be encoded to some digital number format to complete the A/D conversion. Encoding is usually accomplished by a quantizer that rounds the analog values to 2^N discrete values and maps them to 2^N numerical values. Figure 3.1 shows the basic building blocks of an A/D converter model along with its main noise and distortion sources, which will be investigated in this Section.

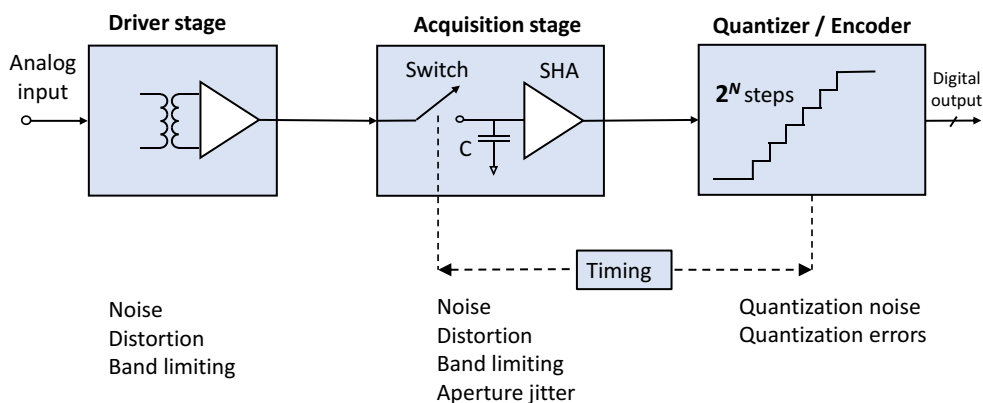


Fig. 3.1: Simplified A/D converter block diagram with error sources and a resolution of 2^N steps.

After amplification, the signal enters the acquisition stage, where it is sampled by a switch. The acquired energy is integrated with the capacitor C , stored in a sample and hold amplifier (SHA), and then transferred to the quantizer [53, p. 75]. The ideal quantizer is a stair-step function with uniform step sizes, following precisely the applied input voltage. Due to unavoidable

imperfections, all stages will add noise and distortion to the input signal. The digital output data, therefore, contains not only the desired signal but also noise and spurious components. It is, therefore, common to characterize an ADC by, among other things, how well it can suppress such unwanted signals relative to the desired ones. The following Subsection provides more details on ADC distortion.

3.1.1 The Spurious-Free Dynamic Range of an ADC

One of the most important performance specifications for an ADC intended for software-defined radio applications is the spurious-free dynamic range (SFDR) over its input bandwidth. It defines the ADC's capability to distinguish the signal of interest from noise and other unwanted signals. A common definition of the SFDR is given in [53, p. 93]: "*SFDR of an ADC is defined as the ratio of the RMS signal amplitude to the RMS value of the peak spurious spectral content measured over the bandwidth of interest. Unless otherwise stated, the bandwidth is assumed to be the Nyquist bandwidth from DC to $f_s/2$* ". The SFDR can be visualized as shown in Figure 3.2. It is either specified in decibels relative to the carrier signal (dBc) or the ADC's maximum full scale (FS) input level (dBFS). By its definition, SFDR is a quality measure that considers all sources of distortion. It is, therefore, a good indicator of the usable dynamic range in a radio communication system.

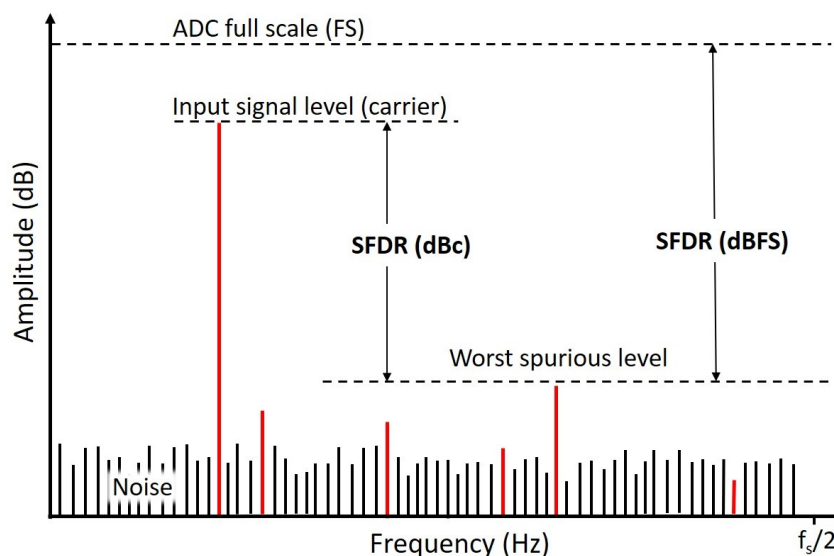


Fig. 3.2: Definition of the spurious-free dynamic range SFDR (dBc) and SFDR (dBFS) in the output spectrum of an ADC. The graphic is redrawn from [53].

3.1.2 Intermodulation and Harmonic Distortion

Amplifiers and ADCs do not have a perfectly linear transfer characteristic and will therefore create unwanted signals originating from harmonic and intermodulation distortion. Harmonic distortion components (HD) are integer multiples of a fundamental frequency, whereas intermodulation distortion (IMD) is caused by two or more frequencies mixing in a nonlinear system. These form additional spectral components at frequencies that are not only at harmonics but also at the sum and difference or multiples of these frequencies Fig. 3.3 illustrates the IMD amplitude levels in an analog, nonlinear system. When excited with two sinusoidal signals f_1 and f_2 , the output amplitude will follow the input amplitude along the transfer curve until the 1 dB compression point is reached. With increasing drive level, the amplifier will start soft-limiting and finally saturate at its maximum output.

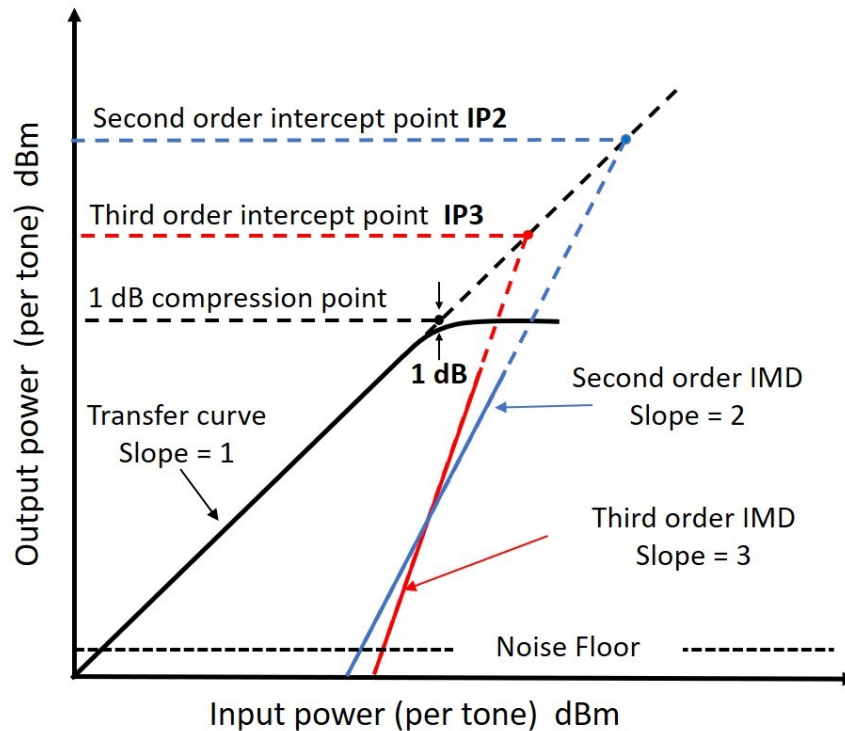


Fig. 3.3: Definition of the intercept points two and three (IP2, IP3) and the 1 dB compression point in a nonlinear, analog system.

The transfer curve of a real amplifier is not perfectly linear and can be approximated by a power series expansion. The quadratic and cubic terms cause second (IMD2) and third-order (IMD3) intermodulation products. Usually, the IMD2 products will increase by 2dB for every 1 dB increase in input power (slope = 2). The third-order intermodulation products will follow the

slope = 3 curve and therefore increase by 3 dB for every 1 dB increase of the input signal. According to [19, p. 633], the input intercept points $IP_{n,IN}$ of the order n are defined as:

$$IP_{n,IN} = \frac{P_{Out} - P_{IMn}}{n-1} + P_{IN} . \quad (3.1)$$

The level of the intermodulation products P_{IMn} of the order n is then given by:

$$P_{IMn} = P_{Out} - (n - 1)(IP_{n,IN} - P_{IN}) . \quad (3.2)$$

As IMD is a function of the signal level, higher input results in stronger IMD products at the output. Usually, at a certain point, third-order IMD3 starts to dominate over second-order IMD2. It is common that IP_2 , IP_3 , and the 1dB compression point are a function of the frequency, and that distortion gets worse with higher frequencies. Fig. 3.4 illustrates the output spectrum of a nonlinear amplifier with two tones, f_1 and f_2 applied at the input. Besides the fundamental frequencies, a number of spurious frequencies exist. The harmonic signals are characterized by an integer multiple of the input frequency and can be calculated as:

$$f_{HD} = nf, \text{ with } n = 2, 3, 4, \dots , \quad (3.3)$$

where n equals the number of the harmonic distortion. An Intermodulation product is generated by at least two signals, and the frequency can be calculated using the equation:

$$f_{IMD} = |nf_1 \pm mf_2| , \text{ with } n, m = 1, 2, 3, \dots , \quad (3.4)$$

where $m + n$ equals the order of the intermodulation distortion. If the sum of n and m is odd, the intermodulation products are called *odd-order* products. These spurious are close to the original frequencies [54, p. 12.20] and, therefore, are difficult to suppress with filters. The IMD frequencies depicted in Figure 3.4 are calculated using (3.4) and obeying $n + m \leq 3$. Thus, only IMD2 and IMD3 are present. Harmonics of the fundamentals HD2 and HD3 are calculated using (3.3) with n running from 2 to 3.

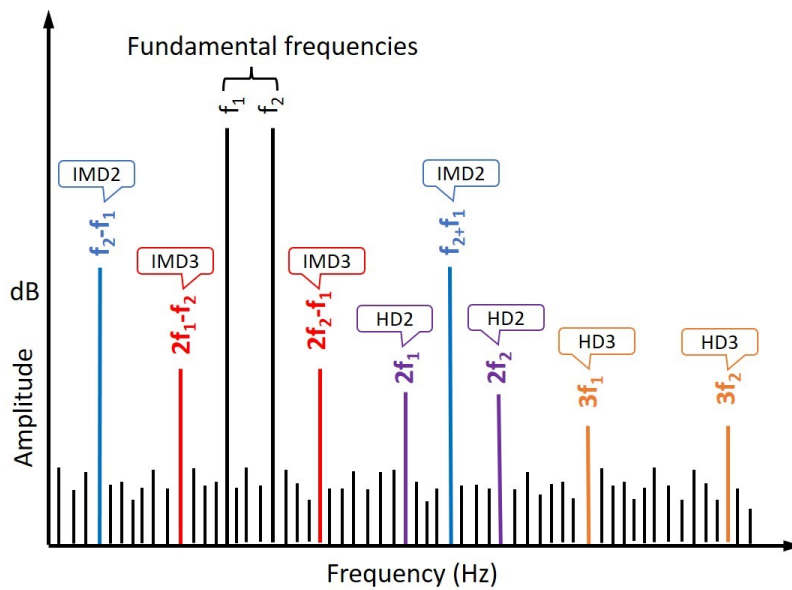


Fig. 3.4: Distortion products of a two-tone signal in the frequency spectrum of a non-linear analog amplifier. The small spectral lines indicate the amplifier's noise floor.

The distortions and errors described so far refer to analog building blocks with a monotonic transfer function. Such building blocks are also contained in an ADC, for example, in the form of a driver stage. However, A/D conversion is a non-linear process and introduces additional distortion not known from analog systems. These errors are investigated in the following Sub-section.

3.1.3 Quantization Errors

Because of the quantization stage, the transfer function of an ADC is fundamentally different from an ordinary amplifier. Quantization is an inherently nonlinear operation, as many analog input values are mapped to the same digital output value. The quantizer will therefore add additional noise and distortion to the output signal. The following graphs illustrate five common errors for a 3-bit quantizer with eight levels, driven by a linear voltage ramp from 0 to 2 V (Full Scale). The step height is determined by the least significant bit (LSB), here corresponding to a voltage of 0.25 V. Fig. 3.5 (a) shows the transfer function of an ideal quantizer, which is not achievable in practice. The offset error, a constant, linear deviation of all code steps by the same amount, is illustrated in Fig. 3.5 (b).

Since this error is constant in nature, it can be easily compensated by calibration techniques in hardware or software.

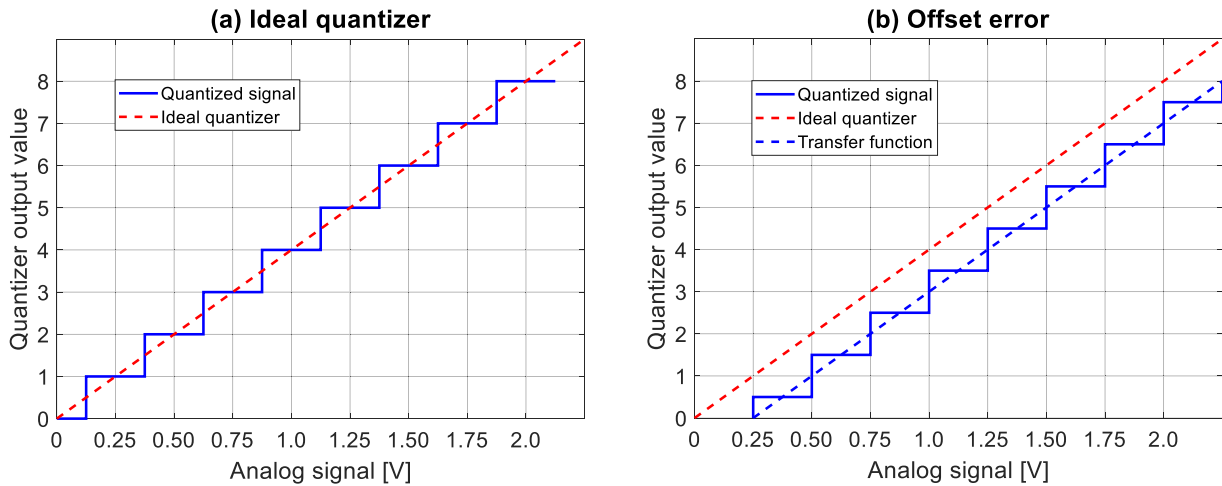


Fig. 3.5: Quantizer errors; (a) Ideal quantizer with no error, (b) Offset error of -0.5 LSB.

Figure 3.6 (a) illustrates the scale error, also called linear gain error. The output codes follow the input voltage linearly but are not correctly mapped to the output code range. Error correction is possible, but the quantizer's operating range may be degraded. The differential nonlinearity (DNL) error is depicted in Figure 3.6 (b).

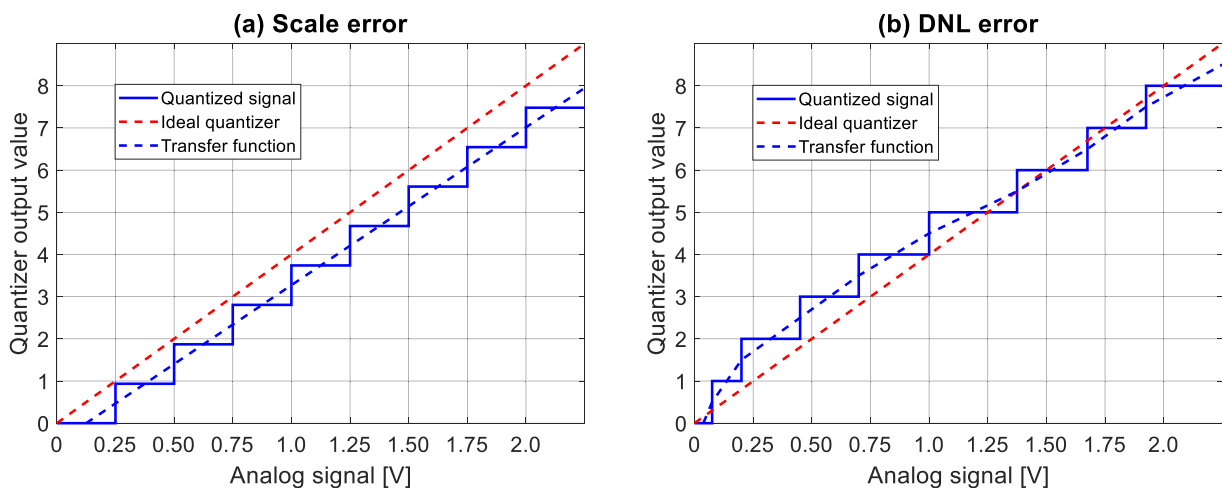


Fig. 3.6: Quantizer errors; (a) Scale error of -0.5 LSB and (b) Differential nonlinearity (DNL) error.

According to [55], the differential Non-Linearity (DNL) is defined as: "... the maximum and minimum difference in the step width between the actual transfer function and the perfect

transfer function". For an ideal quantizer, the step width should be 1 LSB, with all steps linear and monotonically distributed over the input range. DNL error is the difference between the maximum and minimum difference between the actual step width and is usually expressed in LSB. Distortion products depend on the amplitude and positioning of the input signal along the transfer curve and are therefore difficult to predict.

Fig. 3.7 (a) illustrates the missing code error. This is a special case of a large DNL error. The eight quantization levels are not correctly distributed over the input voltage range. In the example given, the quantizer will never output code 4. With such non-monotonic behavior, the quantizer may produce lower digital output codes with rising input voltage and deliver unreliable output data. Fig. 3.7 (b) shows the integral nonlinearity (INL) error. The integral nonlinearity is a kind of offset error. The transfer function is a curved line and deviates from the ideal straight line by some amount. According to [56, p. 2], "*INL error is described as the deviation, in LSB or percent of full-scale range (FSR), of an actual transfer function from a straight line*". Therefore, distortion products caused by INL vary with the level of the input signal.

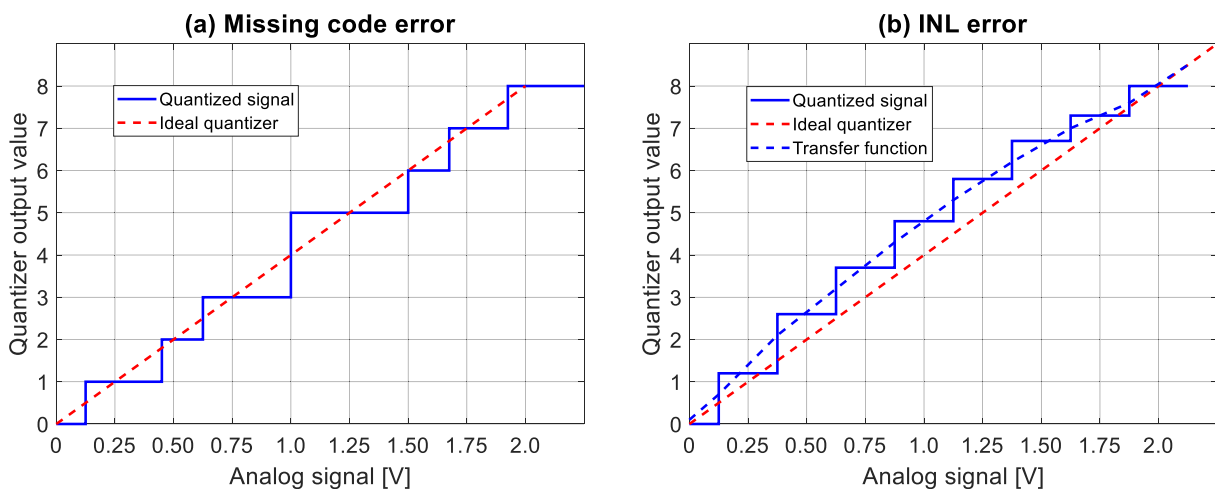


Fig. 3.7: Quantizer errors; (a) missing code error and (b) integral nonlinearity (INL) error.

As illustrated in Figure 3.6 (b) and Figure 3.7 (b), ADCs with DNL and INL errors have a nonlinear transfer function (refer to the dashed blue lines). Such troubled ADCs generate harmonics and intermodulation products that add to the output signal. The DNL and INL errors are unpredictably distributed along with the transfer function and are fundamentally different from the monotonic transfer functions seen in standard linear amplifiers.

In general, distortion for large signals close to full-scale ADC input is dominated by INL. For signals much lower than full scale, DNL keeps the distortion floor more or less constant and independent of the input level [53].

Furthermore, ADCs have no 1 dB compression point. As soon as the most significant bit (MSB) is reached, hard clipping and saturation of the output data occur. This situation produces extreme amounts of distortion and a nonlinear transfer characteristic, as illustrated in Fig. 3.8. It is evident that IP2, IP3, and the 1 dB compression point specifications are of little value for characterizing ADC distortion.

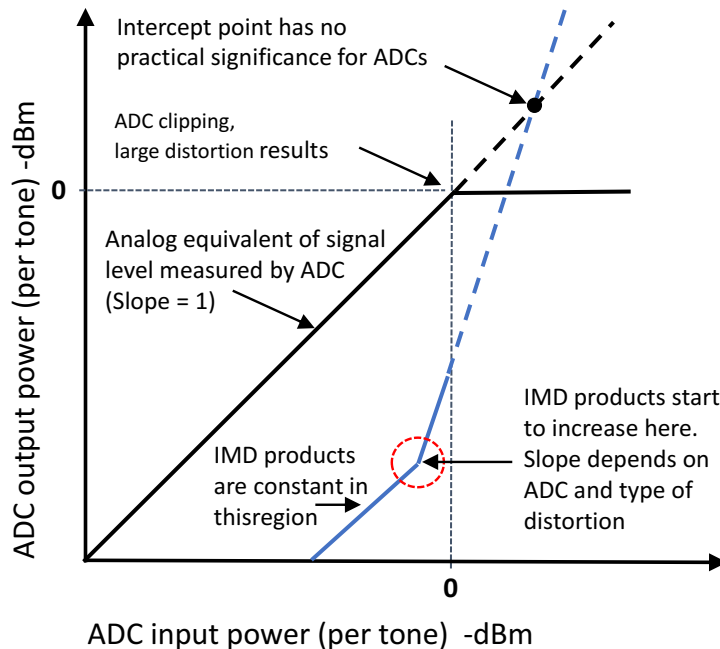


Fig. 3.8: Output of an ADC vs. input power. Intercept point specifications are not helpful. Graphic is redrawn after [53].

Instead, most manufacturers nowadays provide SFDR and signal-to-noise ratio (SNR) data. An example is depicted in Figure 3.9.

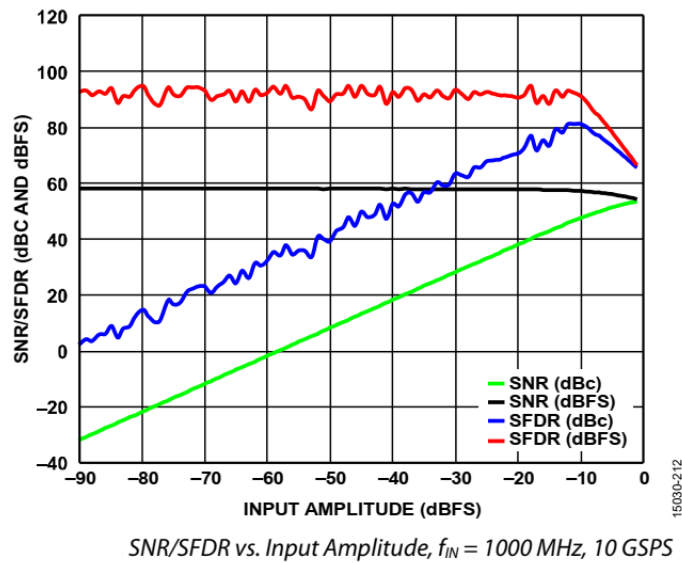


Fig. 3.9: SNR/SFDR vs. input amplitude from the datasheet of the AD9213 [8].

The data are taken from the datasheet of a state-of-the-art 12-bit, 10.25 GSPS ADC from Analog Devices. The blue line shows a roughly linear degradation of the SFDR (dBc) with decreasing input power and a maximum at around -10 dBm .

The following two graphs show the intermodulation distortion characteristics for this specific ADC. IMD3 suppression is generally better at lower input levels, Fig. 3.10 (a), and degrades with increasing frequency, Fig. 3.10 (b).

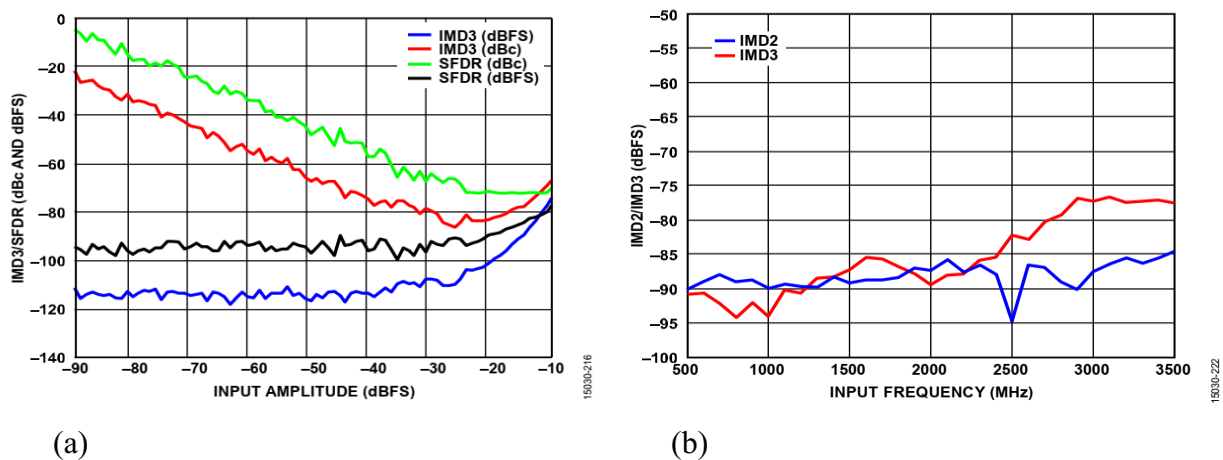


Fig. 3.10: Intermodulation distortion of the AD9213. $f_{IN1} = 2137.5 \text{ MHz}$, $f_{IN2} = 2142.5 \text{ MHz}$, 10 GSPS; (a) IMD3/SFDR vs. input amplitude, (b) IMD2/IMD3 vs. input frequency. Graphics from [8].

3.1.4 Quantization Noise

Because of the limited number of quantization steps and other imperfections, the digital representation of the signal is inherently afflicted by quantization errors. These errors manifest themselves as additional noise at the output of the ADC. The quantization process, depicted in Fig. 3.11 uses $2^4 = 16$ quantization levels and its output is in binary format. To better illustrate the error mechanism, a continuous sinusoidal signal instead of time-discrete pulses is shown as an input signal. The input signal is given by:

$$v(t) = A \sin 2\pi f t . \quad (3.5)$$

The quantization error is the difference between the input signal and the quantized value of this signal. The error function is similar to a sinusoidal, quasi sawtooth curve with a peak-to-peak amplitude of q oscillating around zero. For most practical input signals, this error can be assumed to be either positive or negative in a pseudo-random manner. The error appears as quantization noise added to the output signal. The error will become smaller with a higher quantizer resolution but will never disappear because of its systematical nature. Fig. 3.11 illustrates the situation. For 2^N quantization steps and a sinusoidal signal with amplitude A , the step width q is:

$$q = \frac{2A}{2^N} . \quad (3.6)$$

The step width q corresponds to 1 LSB, and the error voltage e has a range of:

$$-\frac{1}{2} q \leq e \leq +q \frac{1}{2} . \quad (3.7)$$

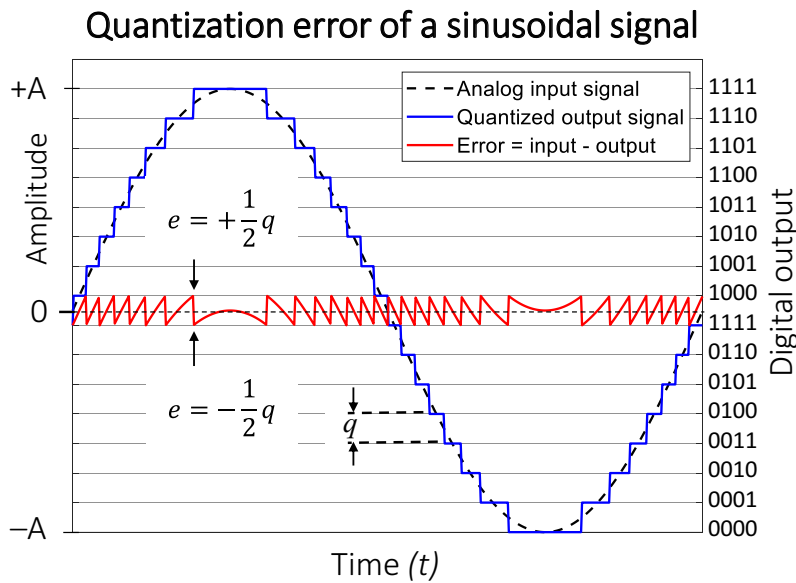


Fig. 3.11: Illustration of the quantization error with a sinusoidal signal.

As an approximation, one can assume: If the number of quantization steps is large (q is small) and the input signal is not static, all errors within the range between $\pm \frac{1}{2}q$ are equally likely. Under the further assumption that the noise amplitude is a random variable and uniformly distributed between $\pm \frac{1}{2}q$ the probability density function $p(e)$ is constant in this range and integrates to one, as shown in Fig. 3.12.

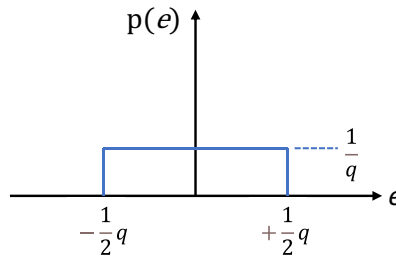


Fig. 3.12: Error probability density function $p(e)$. Drawing inspired by [57].

The integral of the probability density function is the area under the curve and equal to one [57]. Therefore, its value calculates as:

$$p(e) = \frac{1}{q} \text{ for } -\frac{1}{2}q \leq e \leq +q \frac{1}{2}. \tag{3.8}$$

Now the quantization noise power P_{Nq} normalized to 1-Ohm can be calculated by integrating

the square of the error voltages e and then substituting q^2 using (3.6):

$$P_{Nq} = p(e) \int_{-\frac{1}{q}}^{+\frac{1}{q}} e^2 de = \frac{1}{q} \left[\frac{e^3}{3} \right]_{-\frac{1}{2q}}^{+\frac{1}{2q}} = \frac{1}{q} \left[\frac{q^3}{24} + \frac{q^3}{24} \right] = \frac{q^2}{12} = \frac{A^2}{3 \times 2^{2N}} . \quad (3.9)$$

Knowing the quantization noise power P_{Nq} the quantization signal-to-noise ratio SNR_q can be calculated as well. The power of the sinusoidal input signal in a 1-Ohm load is by definition [58, p. 216]:

$$P_{\sin} = \frac{A^2}{2} . \quad (3.10)$$

The theoretical SNR_q in the Nyquist bandwidth of an ideal N -bit ADC driven by a full-scale sinusoidal voltage can be calculated using (3.9) and (3.10):

$$\begin{aligned} SNR_q &= 10 \log \left(\frac{P_{\sin}}{P_{Nq}} \right) = 10 \log \left(2^{2N} \frac{3}{2} \right) = \\ &20 \log \left(2^N \sqrt{\frac{3}{2}} \right) \cong 6.02N + 1.76 \text{ dB} . \end{aligned} \quad (3.11)$$

For example, for an ADC with $N = 12$ -bit resolution, the theoretical limit for the signal to noise ratio due to quantization noise in the Nyquist band is:

$$SNR_q \cong 6.02 \times 12 + 1.76 \text{ dB} \cong 74.01 \text{ dB} .$$

It can only be improved by a higher resolution of the ADC. Bennett derived in [59] that the power spectrum of the quantization noise is typically Gaussian distributed and can be regarded to be flat within the Nyquist bandwidth from DC to $\frac{f_s}{2}$. Therefore with (3.9), the noise power in the Nyquist bandwidth $B_{Ny} = \frac{f_s}{2}$ in a 1-Ohm load is:

$$P_{NqNy} = \frac{P_{Nq}}{B_{Ny}} = \frac{q^2}{12 \left(\frac{f_s}{2} \right)} = \frac{q^2}{6f_s} . \quad (3.12)$$

Equation (3.12) indicates that the spectral noise power will decrease with higher resolution (smaller q) or higher sampling frequency f_s of the ADC. In other words, better resolution produces smaller quantization errors, and higher sampling rates will spread the noise over a wider frequency range. Narrowband radio applications often use only a small part of the Nyquist band. In this case, the noise outside the band of interest can be filtered out, and a correction factor usually called "process gain" can be applied to the SNR equation [17, pp. 102-105]. With B_{sig} being the signal bandwidth, this gives the equation:

$$SNR_q \cong 6.02N + 1.76 \text{ dB} + 10 \log \frac{f_s}{2B_{\text{sig}}} . \quad (3.13)$$

The process gain increases by 3 dB whenever the signal bandwidth is halved, or the sampling frequency is doubled. For this reason, weak signals below the ADCs broadband noise level can be successfully processed using a narrowband, high-resolution FFT.

So far, it is assumed that quantization noise is uncorrelated to the input signal and evenly distributed (3.12). With a sufficient number of ADC resolution bits, or quantization steps, and a varying signal, this is a good approximation for most practical cases. In reality, however, the quantization error function is a deterministic signal with its many harmonics creating a noise-like spectrum. Thus, if the sampling clock and the signal are correlated, e.g., being a harmonic of each other, the noise becomes correlated, and more of the energy is concentrated at the harmonic frequencies of the signal. This noise might be misinterpreted as harmonics of the signal [53, p. 87].

To better assess the impact of this effect, a computer simulation is performed using the VisualAnalog™ Converter Evaluation Tool [60] from Analog Devices Inc. The software package models and analyzes ADC performance with user-selectable input frequencies and sampling rates. Device models are available for many of the vendor's ADC products. The AD9608, a 10-bit ADC operating at a clock frequency of 125 MHz is selected for the following simulation. This device is selected because it is later used for the experiments carried out in Section 7.2. Fig. 3.13 (a) shows the simulated frequency spectrum of an uncorrelated -3 dBFS sinusoidal signal at 12.57 MHz. The noise is randomly distributed over the entire Nyquist band.

Fig. 3.13 (b) shows the same signal moved to 12.5 MHz, precisely one-tenth of the sampling frequency. Under otherwise identical conditions, part of the noise is now concentrated at harmonics of 12.5 MHz.

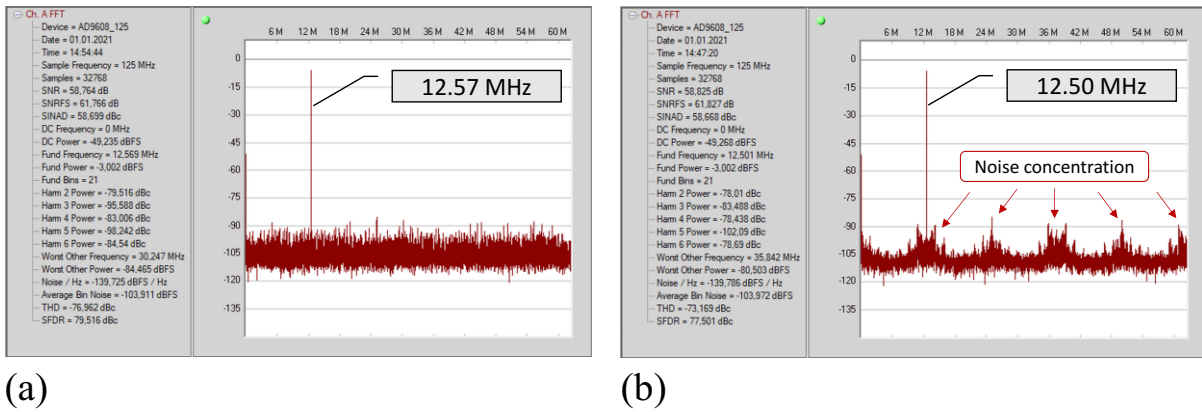


Fig. 3.13: Simulation of correlated quantization noise;
 (a) Spectrum of an uncorrelated input signal at 12.57 MHz,
 (b) correlated input signal at $f_s/10 = 12.5$ MHz,
 Data generated with VisualAnalog [60]. The device model is the AD9608. $F_s = 125$ MHz.

Such noise concentration of correlated signals can be problematic as it can be misinterpreted as spurious signals and affect the accuracy of amplitude measurements in spectral analysis applications.

3.1.5 Aperture Clock Jitter

Quantization is not the only source of noise in ADCs. Due to imperfections of the sample-and-hold-amplifier (SHA) stage and the phase noise of the external sample clock, the time from one sample to the next is subject to uncertainty. This so-called aperture jitter is an ADC phenomenon and will result in an error, as illustrated in Fig. 3.14. The error is proportional to the magnitude of the jitter amplitude and the slew rate of the input signal. Thus, higher signal frequencies are increasingly sensitive to more jitter.

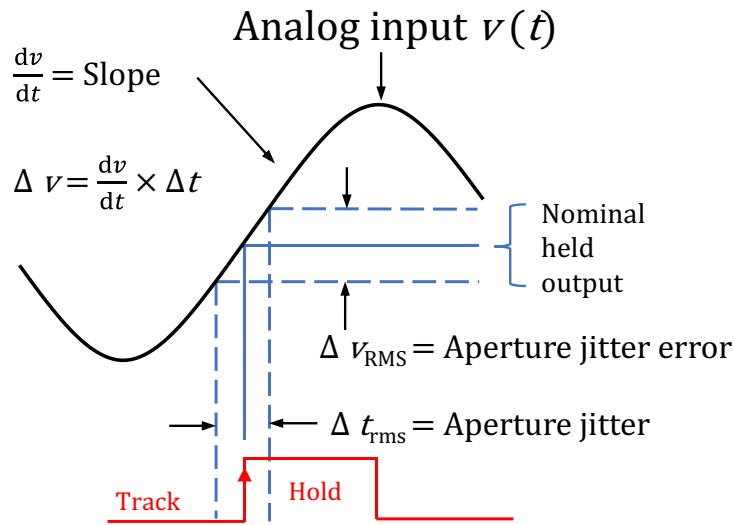


Fig. 3.14: Illustration of sample clock jitter, drawing inspired by [53, p. 107].

To determine the jitter noise, we assume that $v(t)$ is a sinusoidal signal with the frequency f , as shown in Fig. 3.14.

$$v(t) = A \sin(2\pi ft) . \quad (3.14)$$

The steepness of the slope is the first derivative of the sine function and is:

$$\frac{dv(t)}{dt} = 2\pi f A \cos(2\pi ft) . \quad (3.15)$$

By definition, the RMS value of this cosine function is the amplitude $2\pi f A$ divided by $\sqrt{2}$:

$$\left. \frac{dv(t)}{dt} \right|_{\text{RMS}} = \frac{2\pi f A}{\sqrt{2}} . \quad (3.16)$$

For any variation in the sampling instant Δt , the input signal changes by an amount of Δv , based on the steepness of the slope. With Δv_{RMS} being the RMS voltage error and t_j being the RMS aperture jitter Δt_{RMS} , we substitute in (3.16) and get:

$$\frac{\Delta v_{\text{RMS}}}{t_j} = \frac{2\pi f A}{\sqrt{2}} . \quad (3.17)$$

Now the RMS error voltage can be calculated as:

$$\Delta v_{\text{RMS}} = \frac{2\pi f A t_j}{\sqrt{2}}. \quad (3.18)$$

The power of the aperture jitter noise P_{Nj} into a 1-Ohm load is:

$$P_{Nj} = \left(\frac{2\pi f A t_j}{\sqrt{2}} \right)^2. \quad (3.19)$$

The RMS value of the full-scale sinusoidal wave is $\frac{A}{\sqrt{2}}$ and therefore, the jitter related signal to noise ratio is:

$$SNR_{jit} = 20\log\left(\frac{\frac{A}{\sqrt{2}}}{\Delta V_{\text{RMS}}}\right) = 20\log\left(\frac{\frac{A}{\sqrt{2}}}{\frac{2\pi f A t_j}{\sqrt{2}}}\right) = 20\log\left(\frac{1}{2\pi f t_j}\right) \text{ in dBFS.} \quad (3.20)$$

The contribution of the aperture jitter noise cannot be neglected. For example, an aperture jitter of 50 fs and a signal frequency of 1000 MHz calculates to an SNR_{jit} of:

$$SNR_{jit} = 20\log\left(\frac{1}{2\pi \times 10^9 \times 50 \times 10^{-15}}\right) \cong 70.06 \text{ dBFS.} \quad (3.21)$$

Fig. 3.15 shows a graph from the datasheet of a fast, modern 12-bit ADC [8] where the ideal SNR vs. input frequency and aperture jitter is depicted in agreement with (3.21). This part is specified to have an aperture jitter t_j of 50 fs (RMS). The non-ideal external clock oscillator will also add some jitter, and therefore, the SNR for a 1000 MHz full-scale sinusoidal input signal will be degraded to less than 70 dB.

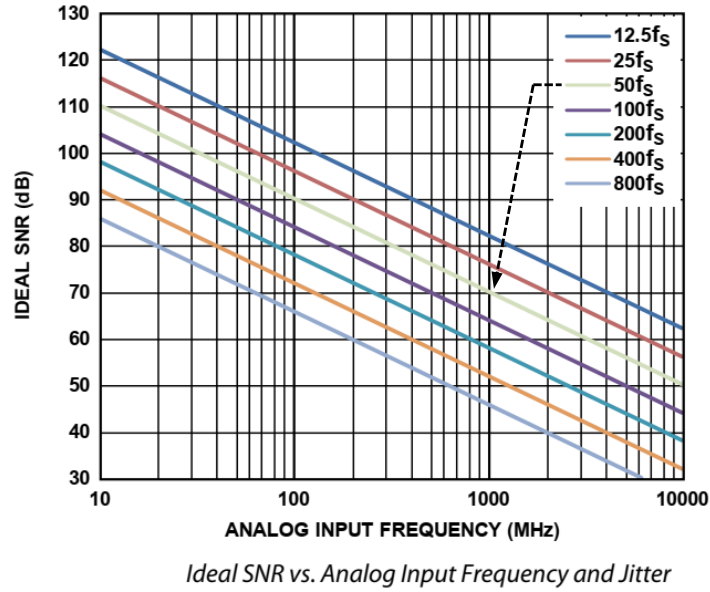


Fig. 3.15: Ideal SNR vs. input frequency and aperture jitter. The picture is taken from the datasheet [8] of the AD 9213, a 12-bit, 10.25 GSPS, RF Analog-to-Digital Converter from Analog Devices, Inc. The arrow was added to the original image to indicate the data point mentioned in the text.

As can be concluded from (3.20), aperture jitter primarily affects an ADC's SNR at high input frequencies. It does not directly depend on the sampling frequency or the ADC input level.

3.1.6 Thermal Noise

Like all other electronic circuits, A/D converters suffer from thermal noise, also called Johnson noise [61, p. 71]. Assuming that all thermal noise voltage at the input of an ADC comes from an *unloaded* source resistor R , the RMS noise voltage $v_{RMS\ noise}$ generated in the bandwidth B can be expressed as [62, p. 474]:

$$v_{RMS\ noise} = \sqrt{4kTRB} \quad , \quad (3.22)$$

where k is Boltzmann's constant = 1.380658×10^{-23} J/K and T = temperature in K.

The total thermal noise power P_{Nt} generated by the source resistor R can be calculated as:

$$P_{Nt} = \frac{v_{RMS\ noise}^2}{R} = 4kTB \ , \quad (3.23)$$

which is independent of the value of the resistor. If we substitute $B = \frac{f_s}{2}$ in (3.22), we get the thermal noise power in the Nyquist bandwidth of an ADC as:

$$P_{NtNy} = 2kTf_s \ . \quad (3.24)$$

Assuming that the full-scale input voltage of an ADC is a sinusoidal signal with a peak-to-peak amplitude of v_{FS} across its input resistance R , the full-scale input power P_{FS} is given by:

$$P_{FS} = \frac{v_{FS}^2}{8R} \ . \quad (3.25)$$

By using (3.24) and (3.25), the ideal thermal signal to noise ratio can be calculated as:

$$SNR_{therm} = 10 \log \left(\frac{P_{FS}}{P_{NtNy}} \right) = 10 \log \left(\frac{v_{FS}^2}{16RkTf_s} \right) \text{ in dBFS} \ . \quad (3.26)$$

The theoretical thermal SNR for the AD9213 with 1.4 Vpp full-scale input and 50-Ohm input impedance sampling with 10 GHz at a temperature of 290 Kelvin is only:

$$\begin{aligned} SNR_{therm} &= 10 \log \left(\frac{v_{FS}^2}{16kTRf_s} \right) = \\ &10 \log \left(\frac{1.4^2}{16 \times 1.38^{-23} \times 290 \times 50 \times 10^{10}} \right) \cong 77.87 \text{ dBFS} \ . \end{aligned}$$

The maximum theoretical SNR resulting from quantization noise, aperture jitter, and thermal noise can be used to determine which one will be the dominant limiting factor. By combining (3.9), (3.19), (3.24), and (3.25), the total SNR_{total} can be calculated as:

$$SNR_{total} = 10 \log \left(\frac{P_{FS}}{P_{Nq} + P_{Nj} + P_{NtNy}} \right) \text{ dBFS} \ . \quad (3.27)$$

Fig. 3.16 shows a plot of the noise contributors and the total SNR vs. input frequency of a theoretical ADC using (3.27).

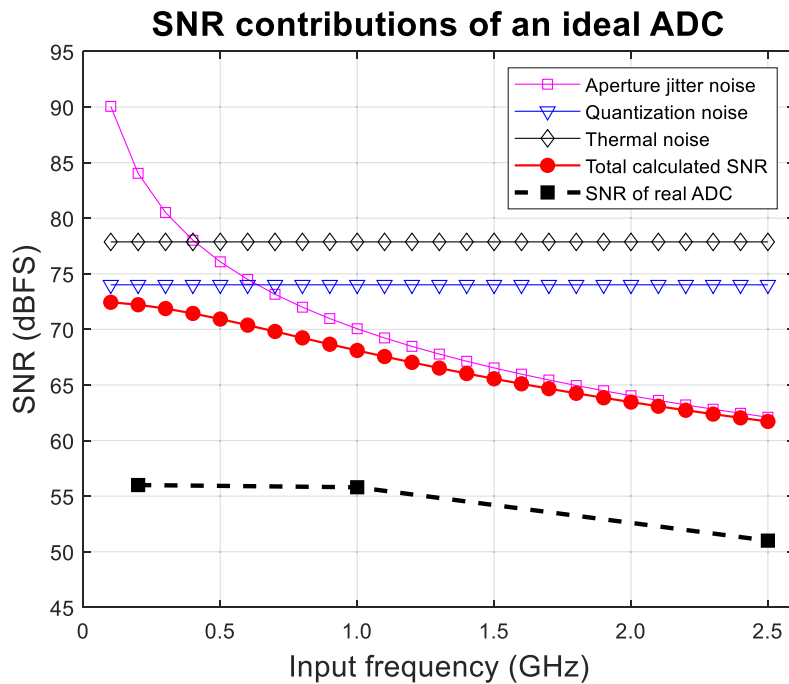


Fig. 3.16: Calculated SNR vs. input frequency for an ideal ADC with 12-bit resolution, 50 fs (RMS) aperture jitter, and a 10-GHz sampling rate. The dotted red line (-●-) represents the total theoretical SNR originating from quantization noise, aperture jitter, and thermal noise. The dashed black line (-■-) shows SNR data from the datasheet of the AD9213, a commercial 12-bit, 10.25 GSPS ADC [8].

The theoretical values are too optimistic by approximately 10 dB to 15 dB. Additional noise contributions, e.g., from the driver amplifier, the sampling stage, and the quantizer's imperfections, are not considered in this calculation. The contribution of the individual stages depends on the technical implementation of the specific ADC. Such errors within the design itself cannot be precisely calculated and are best determined by measurements. Nevertheless, (3.27) can help to estimate the theoretical limits for a particular ADC.

In summary, SNR at low input frequencies and low signal levels is more a function of thermal and quantization noise, while aperture jitter dominates the SNR at higher frequencies.

3.1.7 Noise Figure and Noise Spectral Density

An essential specification for receiver applications is the noise figure (NF) of the A/D converter, which is helpful for calculating the overall noise figure of a system. If the noise is limited to a bandwidth B, the noise figure is calculated using the equation from [53, p. 102]:

$$NF = P_{FS(dBm)} + 174 \text{ dBm} - SNR - 10 \log\left(\frac{f_s}{2B}\right) - 10\log(B) , \quad (3.28)$$

where SNR is in dB, and B and f_s are in Hz. For easier comparison of an ADC's noise performance, manufacturers usually specify a Noise Spectral Density (NSD) parameter in the datasheets. NSD is defined as the noise power spread across the Nyquist band normalized to a 1 Hz bandwidth. Knowing the converter's SNR and the sample rate, it can be calculated according to [63] as follows:

$$NSD = -SNR - 10 \log\left(\frac{f_s}{2}\right) \text{ in dBFS/Hz} . \quad (3.29)$$

Typical values for the NSD of commercial ADCs range anywhere from -165 dBFS to -140 dBFS. NSD allows comparing ADCs with different SNR and sampling rates to determine which one might have the lowest noise in a particular application.

3.1.8 Summary Conclusions on ADC Imperfections

1. Amplitude-related distortion like noise, harmonics, and intermodulation products of an ADC are functions of the input amplitude and the input frequency. Such distortion depends on the individual ADC implementation and is therefore difficult to predict.
2. At low input levels, the SNR is dominated by thermal and quantization noise.
3. The concentration of quantization noise is not a problem in receiver applications, as the sampling and signal frequencies are typically not correlated.
4. At higher frequencies, aperture jitter will dominate the overall SNR. Especially for very high-frequency applications, a sampling clock with a low jitter in the sub-picoseconds range is necessary to preserve the SNR.
5. For a useful dynamic range of >70 dB, the ADC should have a resolution of 12 bits or more.

6. Because of the high intrinsic noise of the broadband ADC, a highly linear, low-noise driver stage is mandatory for receiver applications.
7. An RF-sampling ADC should be operated with an input voltage close to its full-scale value to achieve the best spurious-free dynamic range.

3.2 Performance of Modern RF-sampling ADCs

The ADC for a digital RADAR or ELINT receiver must have a sampling rate, bandwidth, and spurious-free dynamic range as high as possible. Currently, the Fujitsu MB8AC2070 ADC is at the leading edge of performance regarding the sample rate and bandwidth [64]. This 8-bit converter has a 3-dB bandwidth of >15 GHz and a sample rate of 56 GSPS. Its target market is optical transport designs, and its signal-to-noise and distortion ratio (SNDR) is 40 dB at 1 GHz. Despite its impressive bandwidth and sampling rate, the limited SNDR specification makes it unattractive for applications such as broadband radio receivers.

As a starting point from what to expect from the latest RF-sampling ADCs, a longtime regularly updated performance survey is available from B. Murmann [65]. It provides, among other data, a ranking based on two standardized figures of merit. For this work, Schreier's figure of merit (FOMs) [66] is selected, which is well accepted for high-speed data converters. It considers three technical characteristics: The dynamic range DR, the Nyquist sampling rate f_{snyq} and the power consumption P of the device. With the bandwidth $BW = \frac{f_{snyq}}{2}$, Schreier's figure of merit [66, p. 357] is defined as:

$$FOM_s = DR + 10\log\left(\frac{BW}{P}\right) \text{ in dB} . \quad (3.30)$$

The survey result is available in a graphical form [65] and provides an overview of state-of-the-art A/D converters, as shown in Figure 3.17. The sample rate is plotted on the horizontal axis with the figure of merit on the vertical axis. The dashed black envelope line shows the performance limit of currently available ADCs.

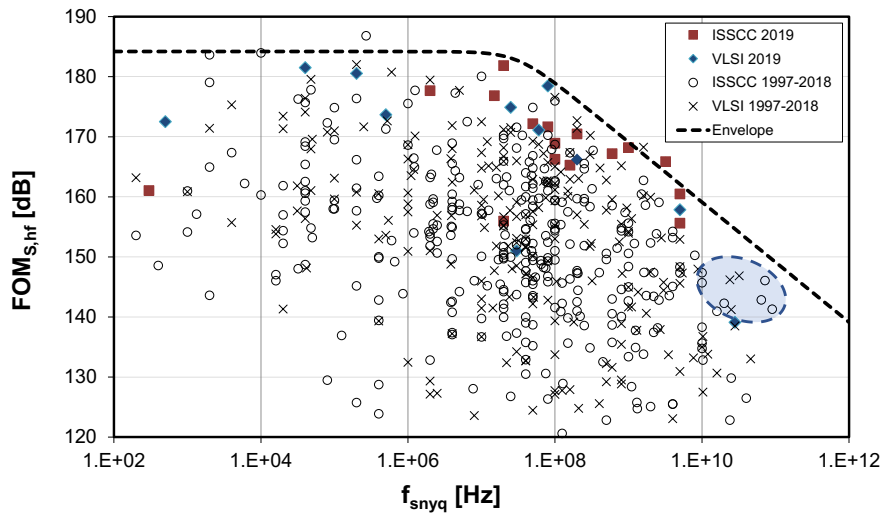


Fig. 3.17: The FOMs figure of merit vs. sample rate of data converters. Data published by B. Murman in 2020 [65]. For this dissertation, the dashed blue ellipse was added to the original diagram, indicating ADCs with a sampling rate >10 GHz and a high dynamic range.

Some of the products listed in the survey are technology demonstrators and are not commercially available. In this dissertation research work, a pragmatic approach is chosen to select a representative ADC. Since a maximum bandwidth is a target, the focus is on ADCs with a high sampling rate and good SFDR. Power consumption, cost, and other criteria were not in focus. Also, single-core designs were preferred over interleaving ADCs, because such architectures are less prone to spurious signals in broadband applications [52]. A search for commercial-off-the-shelf (COTS) high-speed ADCs on reputable manufacturers' websites revealed that the offerings for high-speed ADCs with >8 GSPS and a resolution of 12 bits or more are limited. It must also be noted that an exact performance comparison of such products is difficult. High-speed ADCs in this domain are quite complex, with many functions spanning a huge frequency and amplitude range. Specifications are not fully standardized, and manufacturers use different criteria to characterize the devices. Nevertheless, an attempt is made to compare several commercially available products with a direct RF-sampling application in mind. Fig. 3.18 is compiled using the parametric search on the data converter websites of Texas Instruments Inc. [10] and Analog Devices Inc. [9]. The selection criteria are the highest possible sampling rate, bandwidth, and SFDR. The devices shown on the chart are in good agreement with the latest performance survey from B. Murmann [65].

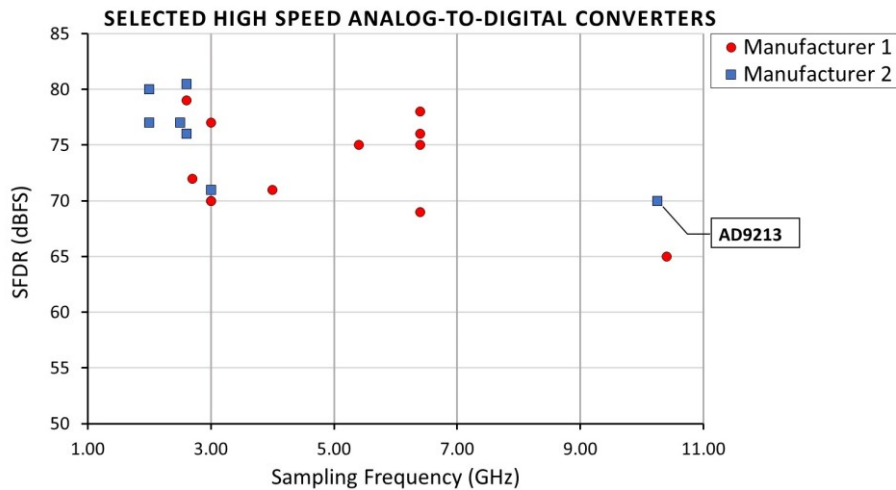


Fig. 3.18: Spurious-free dynamic range vs. sampling frequency of some commercially available ADCs. Data were extracted from the manufacturer's websites [9] and [10].

The AD9213, a 12-bit, 10.25 GSPS, RF analog-to-digital converter [8], is selected as an example of a state-of-the-art high-speed ADC because it offers a high RF bandwidth of up to 6.5 GHz and a sampling rate of 10.25 GSPS. The SFDR is in the range of 70 dB depending on the operating conditions. A simplified functional diagram and a photo of the device are depicted in Fig. 3.19.

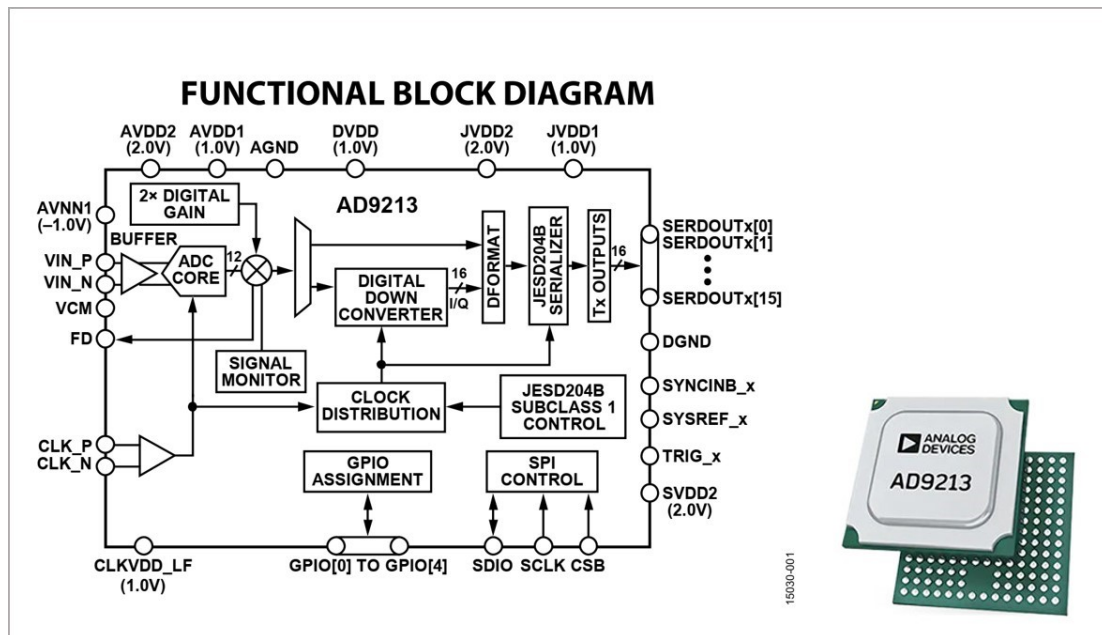


Fig. 3.19: Functional block diagram of the high-speed AD9213 taken from [8]. Images taken from [67] (left) and [68] (right).

3.2.1 SFDR Measurement of a Commercial ADC

For the AD9213, a remote hardware evaluation tool is available on the manufacturer's website [7]. It allows single-tone measurements via a web interface. After selecting the device configuration, the signal amplitude and the sampling frequency can be set. The application performs a 2^{16} -point FFT and returns the spectrum along with a numerical analysis. The main instrument in the test setup is a CXA Signal Analyzer N9000A [68]. Fig 3.20 shows the result obtained with a 10-GHz sampling rate and a 1500 MHz signal at -1 dBFS. The built-in digital post-processing options of the ADC are turned off.

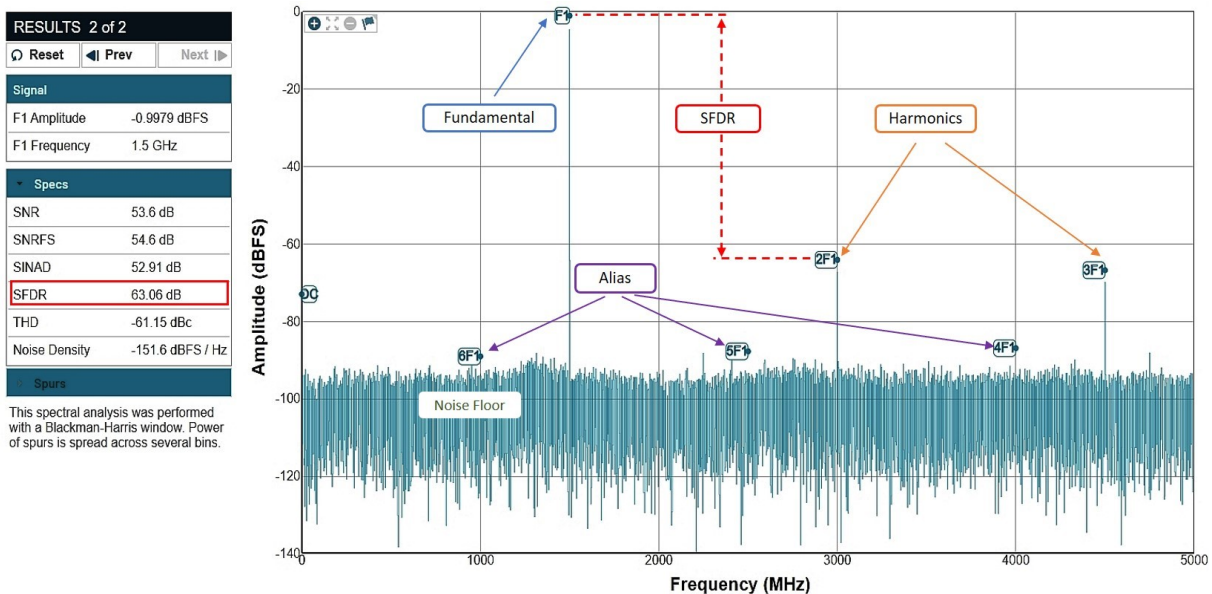


Fig 3.20: FFT of the AD9213 data converter. Single-tone measurement, performed with the tool from [7]. $F_1 = 1.5$ GHz, amplitude = -1 dBFS, FFT length = 2^{16} points, sampling frequency = 10 GSPS, Blackman-Harris window.

As expected, some harmonics and alias signals are visible in the first Nyquist zone from DC to 5 GHz. The noise floor is well below -90 dB, but the spurious-free dynamic range is limited to ≈ 63 dB by a high amplitude harmonic at 3 GHz ($2F_1$). Under these conditions, approximately 30 dB of the ADC's noise-limited dynamic range is spoiled due to spurious signals. These measurement results are in good agreement with the datasheet [8, p. 19]. Many other measurements and the manufacturer's specifications reveal that the SFDR is not constant but depends on several variables. These are the signal frequency, the input level, the sampling frequency, and even the chip temperature. The device achieves its maximal SFDR of 80 dBc at input amplitudes of approximately -10 dBFS when clocked with 6 GHz. Raising the input frequency

from 0.1 GHz to >5 GHz results in significant degradation of the SFDR by about 30 dB. The overall performance of the converter is achieved through sophisticated architecture and a careful internal design.

The datasheet [8] states: “*The device is based on an interleaved pipeline architecture and features a proprietary calibration and randomization technique that suppresses interleaving spurious artifacts into its noise floor. The linearity performance of the AD9213 is preserved by a combination of on-chip dithering and calibration, which results in excellent spurious-free performance over a wide range of input signal conditions*”. The message here is that much effort has been put into internal correction techniques which affect the relationship between input and output signals. Thus, it is difficult to predict the exact distortion characteristics of the device from the outside.

3.2.2 Summary Conclusions on Modern RF-sampling ADCs

1. Current COTS ADCs for broadband RF applications can achieve a 10-GHz sampling rate and 6-GHz bandwidth.
2. The resolution of such ADCs is currently limited to 12 bits. Depending on the operation conditions, one can expect an SFDR of approximately 70 dBFS.
3. The main reason for the limited dynamic range of high-speed ADCs is not broadband noise but the high amplitude of discrete, spurious signals at higher drive levels.
4. Single-core ADCs are superior to interleaving designs because these have fewer spurs and, therefore, better SFDR.
5. Modern fast ADCs use sophisticated spurious reduction techniques. Therefore, the distortion characteristics are fundamentally different from analog building blocks and difficult to predict.

3.3 Known Methods for Reducing ADC Spurious Signals

In the previous Section, it was shown that discrete ADC spurious signals reduce the SFDR in broadband applications and limit the dynamic range of a digital receiver. Therefore, different attempts have already been made to mitigate this problem.

3.3.1 Hardware Related Methods

Many concepts for reducing spurious signals found in the literature are related to improved ADC architectures and internal error correction mechanisms. An example is given in [69]. As this Thesis concentrates on improving the SFDR of commercially available ADCs, these hardware-related efforts are not investigated further.

Other research focuses on optimizing the A/D conversion by reducing negative influences in a particular application. Examples include a cleaner power supply, a higher quality sampling clock, or the reduction of harmful environmental influences [70].

A frequently used and effective technique to improve an ADC's performance in the frequency domain is dithering. Dithering adds a small amount of uncorrelated noise to the input signal, randomizing the ADC's encoder transfer function. This way, small-signal components will be spread out in frequency and pushed into the noise floor. Dithering also de-correlates the quantization noise from the input signal, but it cannot reduce distortion caused by the ADC driver stage or the sample and hold amplifier. In broadband receivers, a narrowband dithering signal can be introduced outside the band of interest [53, pp. 649-653] so that no degradation of the signal to noise ratio will occur. Many state-of-the-art ADCs provide on-chip dither circuits which can be accessed from outside. The internal dither circuit of the LTC2208, a widely used ADC for direct RF-sampling receivers in the HF-band, can improve the SFDR for low-level signals by up to 10 dB [71].

3.3.2 The Frequency-Planning Approach

In recent years, the concept of frequency planning has become very popular for high-speed digital sampling systems. Many spurious signals can be avoided by carefully selecting the center frequency for the RX band and the ADC's sampling frequency.

For broadband systems, a good planning approach is:

1. Using a sampling frequency as high as possible to keep the alias signals away from the band of interest,
2. Finding the optimal position for the RX band to minimize harmonics and aliasing spurs,
3. Avoiding HD2 and HD3 spurs, as these are the most dominant ones.

Several useful frequency-planning tools are available from various sources [72], [73], [74]. These computer programs help avoid in-band spurs by optimizing input frequency and sampling rate. The optimum positioning of the RX band on the frequency axis is not intuitive. Harmonics and alias signals move up and down in frequency and frequently overlap with the RX band. An additional frequency conversion stage is needed to shift the RX band to the desired position. The diagrams from Fig. 3.21 to Fig. 3.23 illustrate how the RX-band position affects in-band interference signals. All diagrams are created using the tool from [73], assuming a fixed sampling frequency of 10 GHz. The vertical dark blue lines mark the position of the RX band. Colored horizontal lines indicate the range of possible spurious frequencies and the order of distortion. Fig. 3.21 shows an unfavorable example for a 700 MHz wide reception (RX) band.

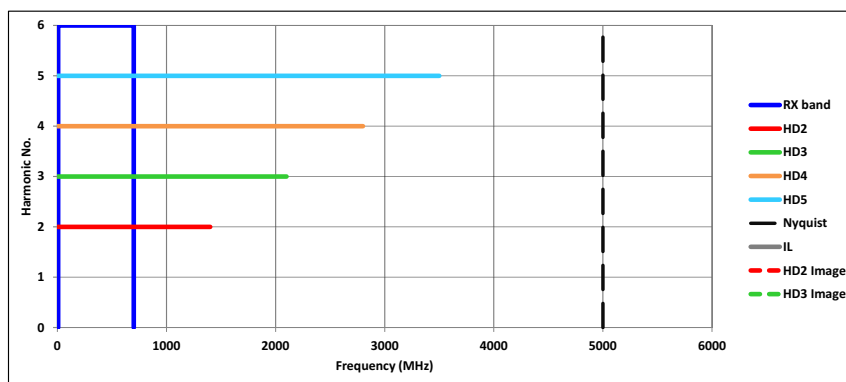


Fig. 3.21: Frequency planning; A 700-MHz wide RX band from DC to 700 MHz sampled with 10 GSPS. Although the RX band is not particularly wide, this configuration is unfavorable because all ADC harmonics fall into the RX band.

The situation can be improved considerably by positioning the receive band so that all interfering signals in the RX band are avoided, as shown in Fig. 3.22.

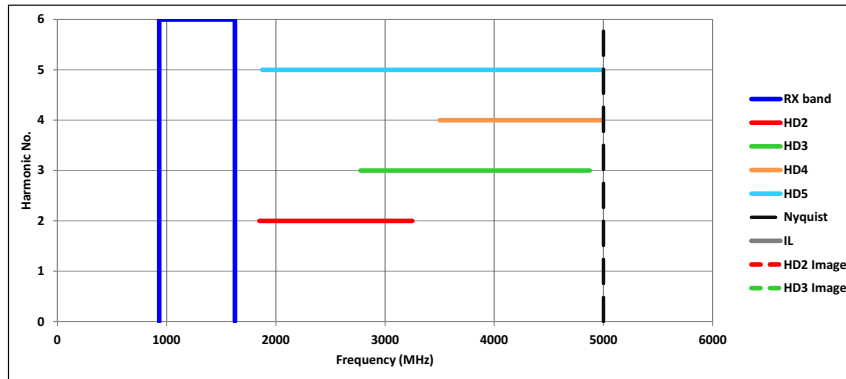


Fig. 3.22: Frequency planning; A 700-MHz wide RX band, now positioned from 925 MHz to 1625 MHz. This configuration is much better; no spurs fall into the RX band.

The example in Fig. 3.23 shows a 2 GHz wide RX band positioned from 1.5 GHz to 3.5 GHz. No position can be found that keeps it free from spurious signals. The example is optimized for minimum HD2 overlap. Nevertheless, this configuration suffers from HD2 to HD5 distortion.

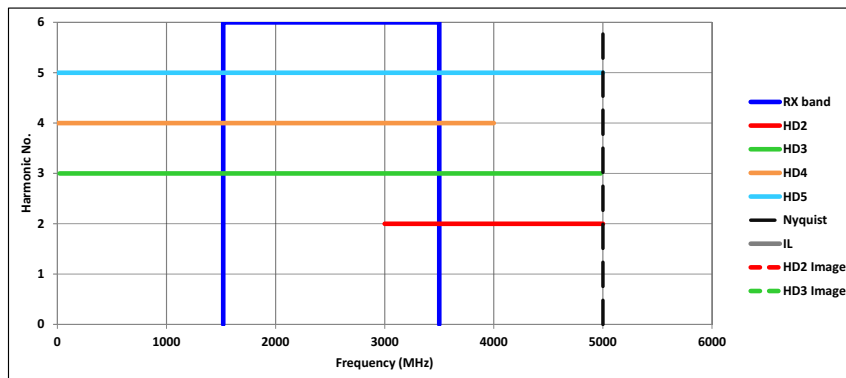


Fig. 3.23: Frequency planning; A 2 GHz wide RX band from 1.5 GHz to 3.5 GHz. Since the RX band is too wide, no position free of spurious signals can be found.

In summary, the frequency planning approach is an effective method for reducing spurious signals when the center of the reception band and the sampling frequency can be freely chosen. In general, the wider the RX band, the more difficult it is to keep it free of spurious signals. Therefore, frequency planning works best with narrow frequency bands.

3.3.3 Spurious Mitigation Through Digital Signal Processing

Several approaches to mitigating spurious signals caused by A/D conversion with digital signal processing can be found in the literature. Some examples are given below:

Compensation of nonlinear distortions in wideband receivers utilizing digital signal processing was first proposed by Valkama et al. in [75]. The idea is to split the I or Q component of the signal into two channels, of which one is fitted with a reference nonlinearity and a band limitation. The two signals are then digitally processed by an adaptive interference canceller to mitigate distortion effects from the desired signal.

The key idea of M. Valkama et al. [75] was further developed and implemented in a Thesis submitted by M. Grimm [76]. Simulation and RF measurements show that the concept can, to a certain degree, enhance the RF performance of a receiver.

Another method based on adaptive digital post-processing to reduce ADC and receiver nonlinearities was described by M. Allen in [77]. His work contributes to the modeling and digital suppression of nonlinear distortion introduced by receiver stages and the ADC.

A concept proposed by C. J. Kikkert and A. Bigdeli in [78] manipulates the input signal to reduce harmonic distortion and has some similarities to the DIF-method described in Section 6.2 of this Thesis. It applies a frequency modulation on the input signal before A/D conversion. The frequency modulation spreads the energy of the higher-order harmonics over a wider frequency range. The frequency modulation on the original signal can later be removed by signal processing techniques to restore the original signal. The authors call this technique “*Frequency Shift Dither*”.

Precision Receivers Inc. has recently published a paper describing a method for spurious reduction called high dynamic range receiver (HDRR) technology. According to the company, it is based on non-uniform sampling. The SFDR improvement is said to be 9 to >12 dBc [79]. Technical details of the working principle have not been published.

3.3.4 Summary Conclusions on Known Spurious Reduction Methods

1. The frequency planning method is very effective, mainly when the RX band is limited to a few hundred megahertz. If the goal is a bandwidth of more than 1 GHz, the method reaches its limits with today's GPS ADCs. Then, in-band spurious signals can no longer be avoided and will inevitably compromise the dynamic range.
2. Additive dithering is a proven concept and is successfully used in many digitizing applications. An SFDR improvement of 10 dB is possible.
3. DSP-based postprocessing methods can improve the spurious-free dynamic range. However, the lack of a standardized measurement method makes it difficult to compare the effectiveness of the different published approaches. Furthermore, RF signal levels and waveforms considerably impact how well the methods can suppress different types of spurious signals. In this respect, not many detailed measurement results have been made available.

4 Theoretical Analysis of the A/D Conversion Process

In order to successfully mitigate unwanted signals resulting from A/D conversion, the origin and mechanisms of their generation must first be clarified. Therefore, the following Chapter analyzes the analog-to-digital conversion process in detail and shows the achievable performance data of some commercially available RF-sampling ADCs

4.1 The Ideal Time Discrete Sampling Process

In the context of this work, sampling means the process of periodically taking measurements from a time-continuous signal with a rate f_s . The original signal can be accurately reconstructed from the time-discrete samples when the Nyquist-Shannon sampling theorem is obeyed. The sampling theorem states: “For any baseband signal that is bandlimited to a frequency f_m , the sampling rate f_s must be selected to be greater or equal to twice the highest frequency f_m in order for the original baseband signal to be recovered without distortion, using an ideal low-pass filter with a cut-off frequency f_c such that $f_m \leq f_c \leq f_s - f_m$ ” [80, p. 8].

Ideal sampling can be mathematically expressed as a multiplication of a time-continuous signal $x(t)$ with a sampling function $c(t)$. The sampled, time-discrete signal $y(t)$ can be defined as:

$$y(t) = x(t) c(t) . \quad (4.1)$$

An ideal sampling function is made up of an infinite number of δ -functions which are either zero or one with a period of $T_s = \frac{1}{f_s}$. The resulting unit impulse train $c(t)$, also called the Dirac-comb, can be written as:

$$c(t) = \sum_{n=-\infty}^{\infty} \delta(t - nT_s) , \quad \text{for } n = 0, \pm 1, \pm 2, \pm 3, \dots . \quad (4.2)$$

At time instants nT_s we have $c(t) = 1$ and zero otherwise [81].

Substitution of (4.2) into (4.1) gives:

$$y(t) = x(t) \sum_{n=-\infty}^{\infty} \delta(t - nT_s) , \quad \text{for } n = 0, \pm 1, \pm 2, \pm 3, \dots \quad (4.3)$$

The following graph illustrates the sampling process and the involved signals in the time domain. The analog, continuous-time signal $x(t)$ is sampled at equidistant intervals of T_s by multiplication with the Dirac comb $c(t)$, which has the values zero and one. The amplitude information of $x(t)$ is taken only at times when $c(t)$ has a value of one. The resulting time signal $y(t)$ consists of discrete values spaced at intervals T_s , representing the amplitudes of $x(t)$ at the sampling instances and are zero otherwise.

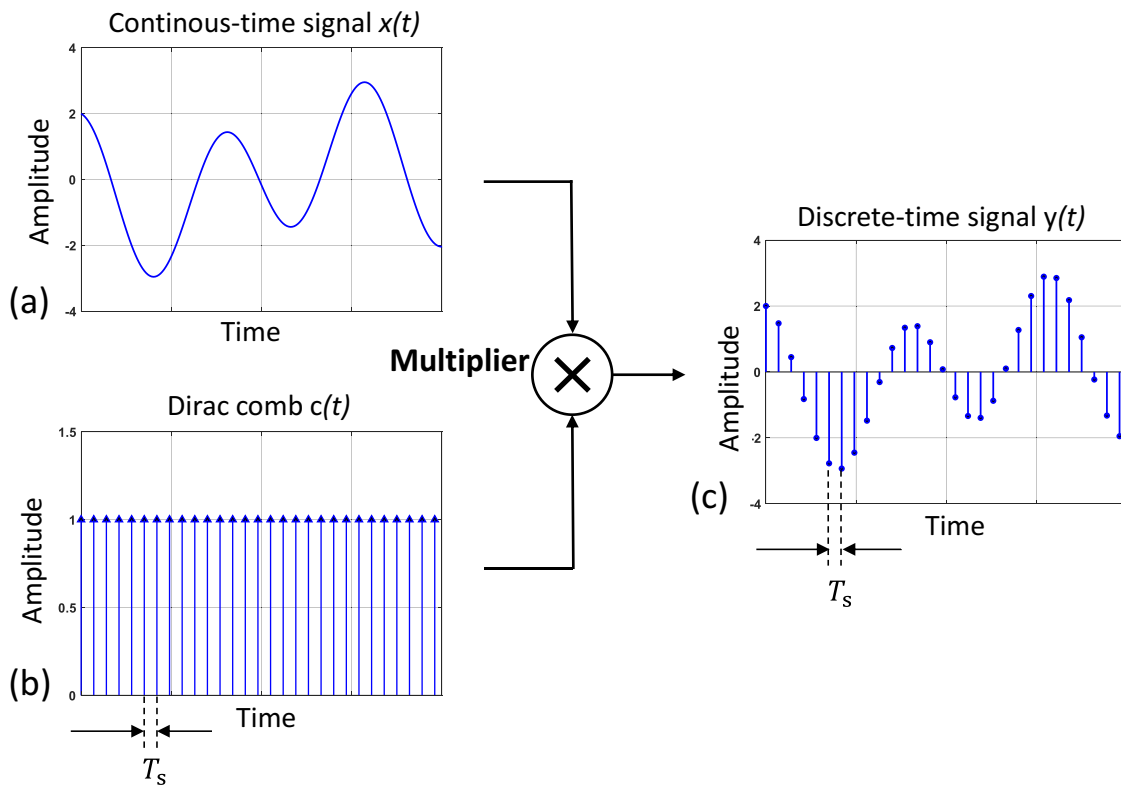


Fig. 4.1: Signals of the equidistant sampling process; (a) continuous-time signal, (b) sampling function (Dirac comb), (c) discrete-time signal.

Sampling has an impact on the spectral content of the discrete-time signal. The resulting spectrum can be calculated by folding the spectra of $x(t)$ and $c(t)$. The ideal sampling function $c(t)$, depicted in Fig. 4.2 (a), shows a flat, distributed, periodic frequency spectrum $C(f)$, Fig. 4.2 (b).

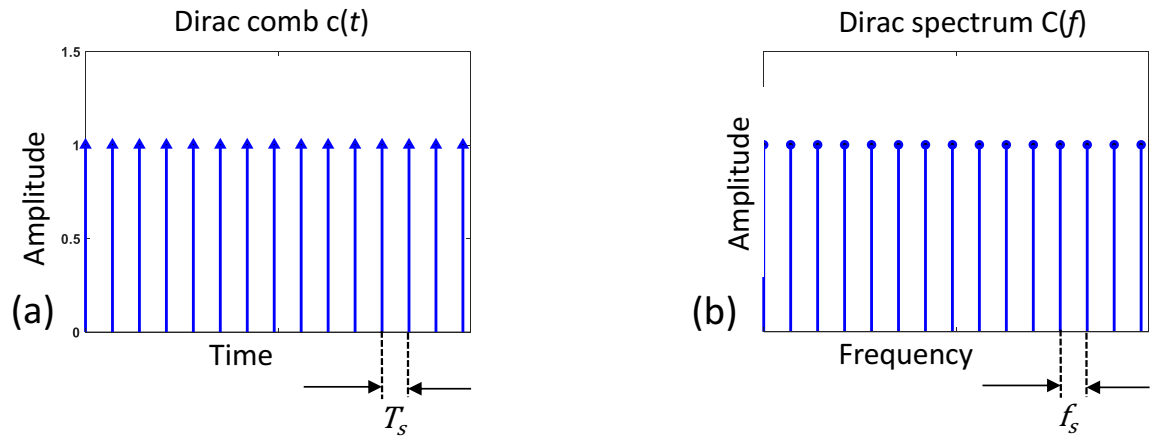


Fig. 4.2: The ideal sampling function (Dirac comb); (a) in the time domain, (b) in the frequency domain.

With the sampling frequency $f_s = \frac{1}{T_s}$ the spectrum of the sampling function can be written as:

$$C(f) = \frac{1}{T_s} \sum_{n=-\infty}^{\infty} \delta\left(f - n \frac{1}{T_s}\right) = f_s \sum_{n=-\infty}^{\infty} \delta(f - n f_s), \quad n = 0, \pm 1, \pm 2, \dots \quad (4.4)$$

As a multiplication of two signals in the time domain is equivalent to a convolution in the frequency domain, we can calculate the resulting spectrum by folding the spectra of $x(t)$ and $c(t)$. With $X(f)$ being the Fourier transform of $x(t)$, the spectrum $Y(f)$ can be calculated as the convolution of $X(f)$ with $C(f)$ and written as:

$$Y(f) = X(f) \circledast C(f). \quad (4.5)$$

After substituting (4.4) into (4.5), we get according to [82]:

$$Y(f) = X(f) \circledast f_s \sum_{n=-\infty}^{\infty} \delta(f - n f_s) = f_s \sum_{n=-\infty}^{\infty} \underbrace{X(f - n f_s)}_{\text{“spectrum replication”}}. \quad (4.6)$$

Equation (4.6) contains a term labeled “spectrum replication”. This means that the sampling process has created n copies of the input spectrum $X(f)$. These additional spectral components replicate every $n f_s$. This property of the sampling process is essential when the discrete-time

samples of an A/D conversion are transferred to the frequency domain, i. e. using a discrete Fourier transform (DFT). All additional frequencies that are now represented in the sampled signal must be considered when using this data. The sampled signal also contains information about the sampling process itself, such as the sampling frequency. This property is used later in Chapter 6 to detect unwanted signals introduced during the sampling process.

4.2 Non-Ideal Pulse Sampling

Up to this point, the description of the sampling process has assumed an ideal sampling model based on a multiplier to describe the basic mechanisms of time discrete sampling. Multiplying the input signal $x(t)$ by the ones and zeros of the impulse train with a frequency of $f_s = \frac{1}{T_s}$ is technically equivalent to switching the continuous-time signal on and off at equidistant time intervals of T_s . Practical ADCs use a switch instead of a multiplier and sampling pulses with a length T_p as depicted in Fig. 4.3.

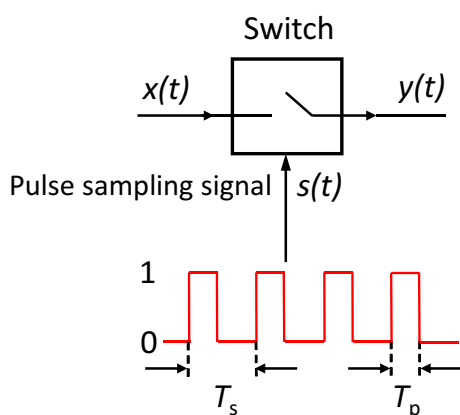


Fig. 4.3: Sampling the input signal $x(t)$ with a switch to obtain a time discrete signal $y(t)$.

In the real world, there is neither an ideal switch nor a sampling function with an ideal waveform. In practice, any pulse sampling signal will consist of pulses of a finite length T_p . Moreover, practical A/D converters have a sample and hold stage that integrates and stores the signal's energy to make it available for quantization. This stretches the total acquisition time so that the practical sampling process results in a signal more like the one shown in Fig. 4.4 (c).

The frequency spectrum of the pulse sampling signal, shown in Fig. 4.4 (a), is not as flat as that of the ideal sampling function shown in Fig. 4.2 (b). Instead, its amplitude follows a sinc-shaped function with a period of $\frac{1}{T_p}$ which is depicted in Fig. 4.4 (d) and can be calculated as:

$$S(f) = \left| \frac{\sin(\pi f T_p)}{\pi f T_p} \right|. \quad (4.7)$$

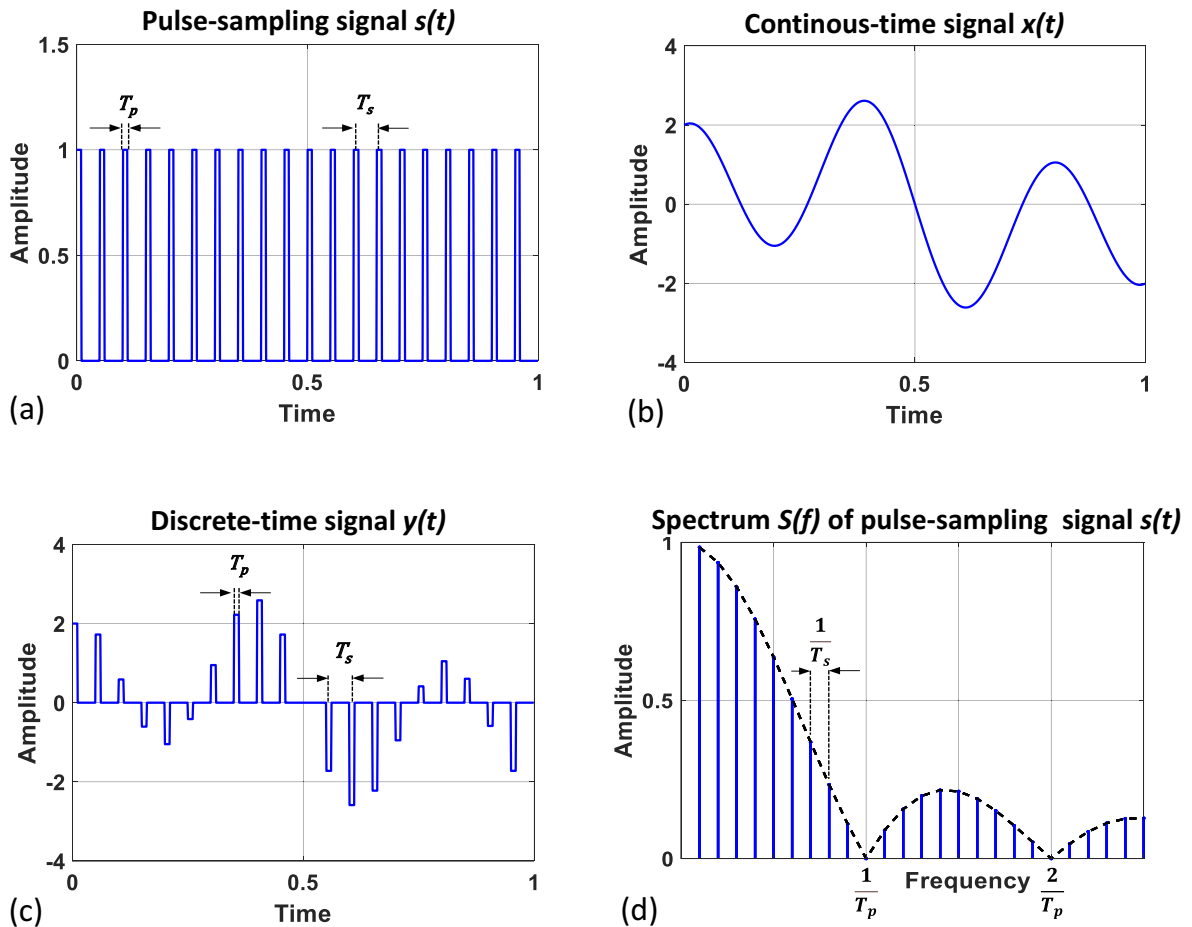


Fig. 4.4: Illustration of non-ideal sampling;
 (a) Pulse-sampling signal,
 (b) Continuous-time signal,
 (c) Sampled, discrete-time signal,
 (d) Sinc-shaped frequency spectrum of the pulse-sampling signal depicted in (a).

By the convolution of $S(f)$ with the signal spectrum $X(f)$, the amplitude variations of $S(f)$ are translated to the resulting signal $Y'(f)$ with T_p being $\frac{1}{f_s}$ [83, p. 46].

$$Y'(f) = X(f) \circledast S(f) = X(f) \left| \frac{\sin(\pi f T_p)}{\pi f T_p} \right|. \quad (4.8)$$

Therefore, non-ideal sampling introduces a systematic, sinc-shaped aperture distortion caused by the sampling stage's pulse characteristic. This amplitude error is deterministic and can be mitigated by suitable correction mechanisms implemented in hardware or software. The frequency relationship between the original signal and the sampled signal is not affected.

4.3 The Aliasing Effect

The sampling theorem states that there must be no spectral components beyond a frequency of $\frac{f_s}{2}$ when sampling a signal. This restriction is also known as the Nyquist criterion and is a prerequisite for reconstructing a sampled signal. When the Nyquist criterion is violated, a phenomenon called aliasing occurs. Fig. 4.5 and Fig. 4.6 illustrate different cases of aliasing. The spectrum is divided into so-called Nyquist zones (NZ), each with a bandwidth of $\frac{f_s}{2}$. Fig. 4.5 (a) shows the original signal with the bandwidth f_{bw} , located in the first Nyquist zone and no spectral components beyond $\frac{f_s}{2}$. According to (4.6), after sampling, multiple copies of the original frequencies and their images exist every $n f_s$. In this case, the replicated spectra shown in Fig. 4.5 (b) are well separated and do not overlap. This scenario is known as oversampling, and the original signal can be recovered using an LPF with a cut-off frequency of $\frac{f_s}{2}$.

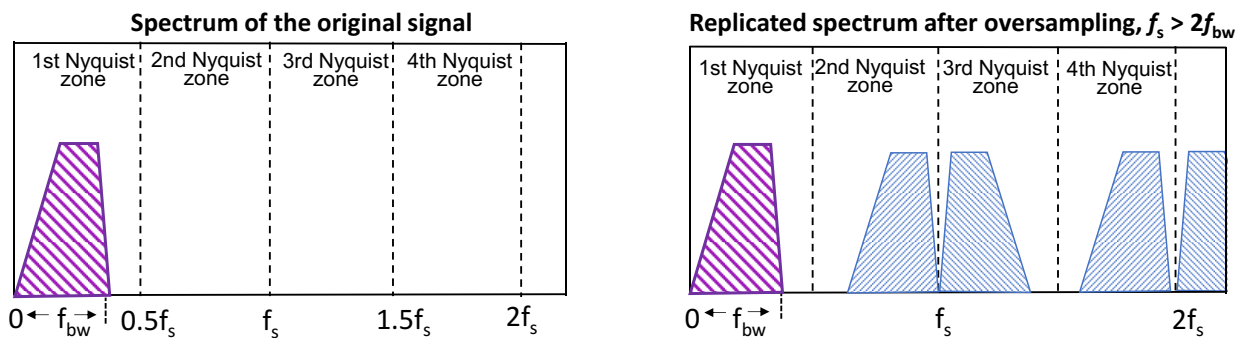


Fig. 4.5: (a) Spectrum of the original signal,

(b) Oversampling with $f_s > 2f_{bw}$.

In Figure 4.6 (a), the sampling frequency is too low, the sampling theorem is violated, and the replicated spectra overlap. This effect destroys information, and the original signal cannot be recovered. To avoid aliasing, either the sampling frequency must be high enough so that $f_s \geq 2f_{bw}$ or the input signal's bandwidth must be strictly bandlimited to $f_{bw} \leq \frac{f_s}{2}$.

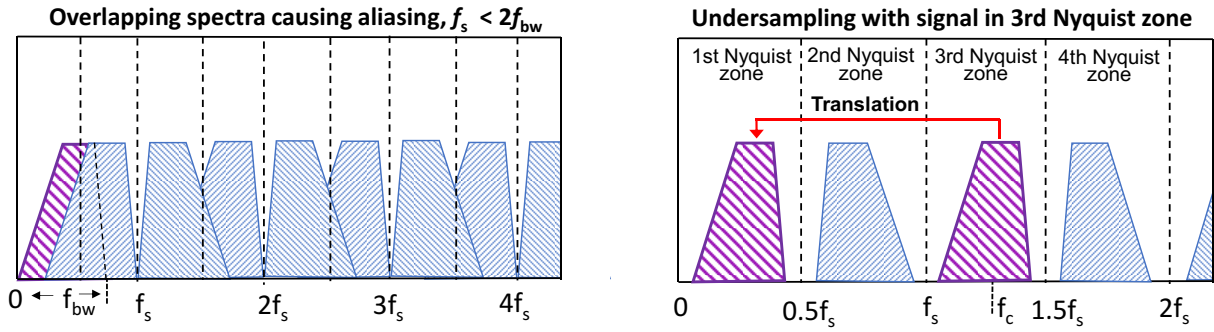


Fig. 4.6: (a) Improper sampling with $f_s < 2f_{bw}$,

(b) Undersampling with $f_s > 2f_{bw}$ and $f_c = 1.25f_s$.

When aliasing occurs, frequency components f_{alias} fold back into the first Nyquist zone. With f being the signal frequency and f_s being the sampling frequency, f_{alias} can be calculated as follows:

$$f_{alias} \leq \frac{f_s}{2} \leq |nf - mf_s|, \quad \text{with } n, m = 1, 2, 3, \dots \quad (4.9)$$

In a nonlinear system, this equation is more valuable than the usual, e.g., in [54, p. 15.7], since it will also calculate the alias of the harmonics of a signal by introducing the factor n . The order of the distortion products falling into the first Nyquist zone is given by n .

According to the sampling theorem, the sampling frequency must be equal to or greater than the signal's bandwidth. It makes no statement about the signal's location on the frequency axis relative to the sampling frequency. That is, as long as the signal bandwidth f_{bw} is not greater than $\frac{f_s}{2}$ it can be placed in any single Nyquist zone on the frequency axis. This approach is known as undersampling and makes intelligent use of aliasing. Figure 4.6 (b) shows a signal in the third Nyquist zone centered around $f_c = 1.25f_s$ which is translated down into the first Nyquist zone. The sampling theorem is not violated, and no spectral overlap occurs.

The ADC only needs to sample with at least twice the signal bandwidth. Thus, the sampling speed requirement of the ADC can be reduced despite the much higher signal frequency. However, the signal must be strictly bandlimited to one of the Nyquist zones. According to [53, p. 81], the relationship between the center frequency f_c , the sampling frequency f_s and the Nyquist zone NZ is given by:

$$f_s = \frac{4f_c}{2NZ - 1}, \quad NZ = 1, 2, 3, \dots \quad (4.10)$$

as long as the Nyquist criterion $f_{bw} \leq \frac{f_s}{2}$ is satisfied, NZ can be chosen to minimize the sampling rate or to place f_c in the desired Nyquist zone. If NZ is odd, then the image signal falling into the first Nyquist zone is not reversed, Fig. 4.6 (b). Thus, the signal can be recovered without additional signal processing effort for sideband reversal. However, the analog bandwidth of the ADC must be high enough to allow the processing of the signals in the higher NZ, which can be much higher than the sampling frequency.

Without calculations, the effect of bandpass sampling and aliasing can be illustrated with a transparent computer fan-fold paper shown in Fig. 4.7.

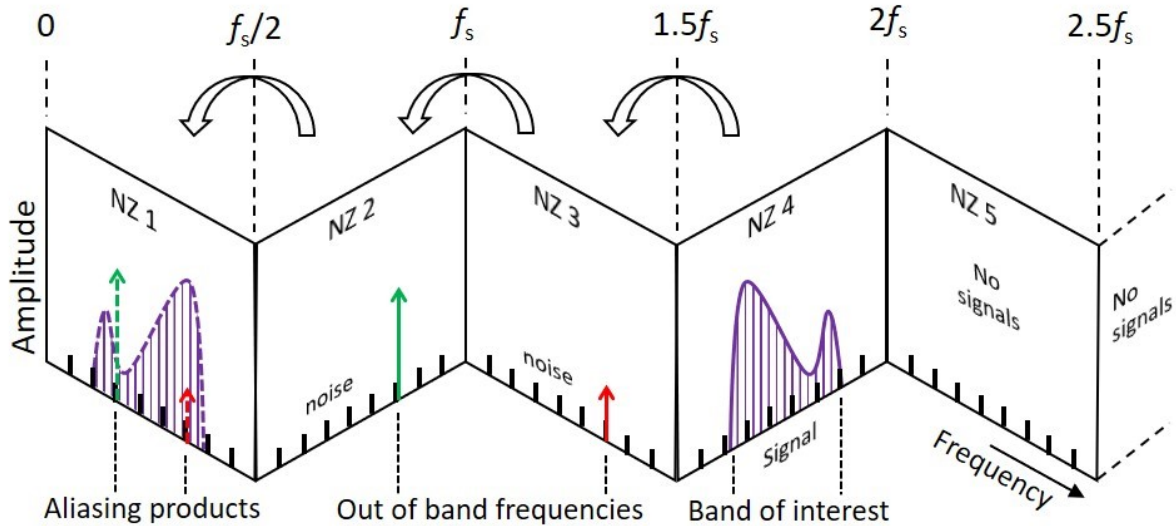


Fig. 4.7: Illustration of undersampling and aliasing with a fan-fold paper. Out of band frequencies and noise are folded back into the first Nyquist zone.

The horizontal edge represents the frequency axis that folds every $\frac{f_s}{2}$ and each sheet represents

a Nyquist zone. The vertical edge of the paper represents the amplitude of the signal. The signals are plotted along the frequency axis. In the illustration, the signal of interest is placed in the fourth NZ, and the interferers are in NZ two and three. The effect of sampling becomes clear by folding and collapsing the transparent paper into a single stack. This way, all signals from the different NZs, including noise, are superimposed upon each other. If the signal is limited to only one NZ, this is not a problem. If signals exist in more than one NZ, aliasing occurs, and the frequency components can no longer be separated. Undersampling can be used to save one or more RF down-conversion stages before the ADC. Despite these advantages, there are also negative aspects in practical applications. Even with a sharp, ideal filter placed at $f_c \pm 0.5f_{bw}$ the signal to noise ratio (SNR) of the original signal is not preserved with undersampling. Folding the spectrum will transfer all broadband noise into the first Nyquist zone, degrading the SNR of the original signal. According to [17, p. 48], the degradation D_{SNR} is:

$$D_{SNR} \approx 10\log_{10}(NZ) \text{ dB.} \quad (4.11)$$

The example in Fig. 4.7 shows the signal in NZ four, and thus the degradation of the SNR is already ≈ 6 dB.

4.4 Summary Conclusions on the A/D Conversion Process

1. A/D conversion will create alias signals when the Nyquist theorem is violated. If this happens due to nonlinear distortion within the ADC, these aliases cannot be removed by anti-aliasing low-pass filters in front of the ADC.
2. The frequencies of spurious signals can be predicted mathematically. These depend solely on the frequency of the input signal and the sampling frequency.
3. Systematic amplitude errors caused by pulse sampling are deterministic and can be corrected by hardware or software.
4. The amplitudes of nonlinear distortion products are difficult to predict since the exact distortion mechanism of an ADC is usually not known and must be determined by measurements.

5 Spectrum Analysis Using the FFT

The solution concept outlined in Subsection 1.3 is based on comparing amplitudes and frequencies in the output spectrum of an ADC. To decompose the discrete-time signals from an ADC into its frequency components, the fast Fourier transform (FFT), an algorithm for efficiently calculating the DFT, will be used [84, p. 1.5.3]. Due to the nature of the FFT, the output spectrum is not always a 100% exact representation of the sampled signal. For this reason, amplitude and frequency errors may occur [85]. Since an accurate frequency and amplitude measurement is critical to the success of the methods, the following Section analyzes the corresponding capabilities of the FFT.

An FFT can be regarded as a bank of parallel bandpass filters with a bandwidth depending on the sampling frequency f_s and the length N of the FFT [86]. The number of the individual filter curves is equivalent to the FFT resolution N . An individual filter is usually called a bin, and its bandwidth BW_{bin} is:

$$BW_{\text{bin}} = \frac{f_s}{N} . \quad (5.1)$$

Thus, a signal with the frequency f is placed at the center of a bin at the position m :

$$m = \frac{f}{BW_{\text{bin}}} = f \frac{N}{f_s} . \quad (5.2)$$

The result in the frequency domain is similar to looking at a continuous spectrum through N slits and is sometimes referred to as the picket-fence effect [85, p. 13]. A real-valued power spectrum from DC to $\frac{f_s}{2}$ is represented by m bins, with m incrementing from 0 to $\frac{N}{2} - 1$.

5.1 Scalloping Error

The magnitude response of an individual FFT filter curve is not flat but follows a $\frac{\sin(x)}{x}$ function [17, p. 138]. Therefore, the resulting overall amplitude response is a ripple function, as illustrated in Fig. 5.1. Consequently, if a sinusoidal signal moves up and down in frequency, there is a periodic amplitude variation known as scalloping error.

The error is the difference between the maximum and minimum responses of the FFT. Due to the frequency-dependent nature, the losses can only be accurately predicted if the FFT parameters and input signal frequency are known.

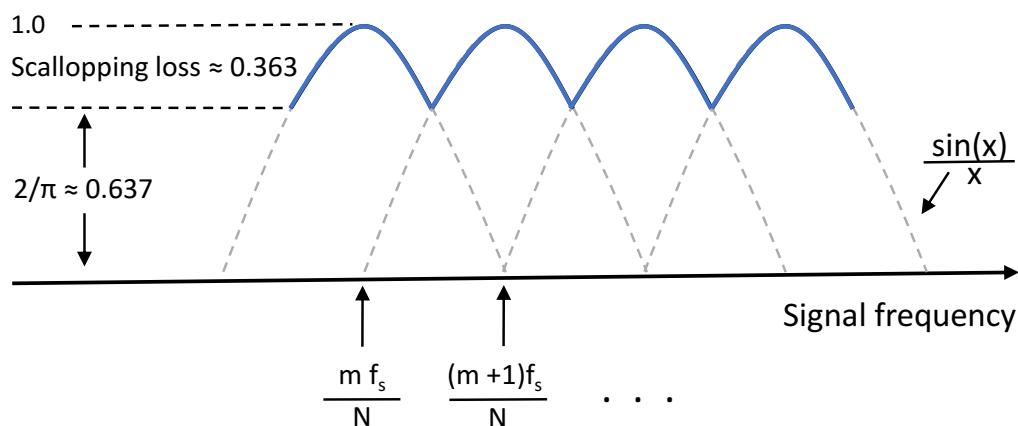


Fig. 5.1: Illustration of the scalloping loss caused by FFT amplitude ripple. The loss in the valleys in between the bins must be taken into account when evaluating the amplitudes of discrete frequencies. The illustration is redrawn after [17, p. 97].

5.2 Spectral Leakage

An FFT produces correct amplitude results only when the input data contains spectral energy that falls precisely into the middle of a bin and not in-between. According to (5.2), this is only the case when $f = m \frac{f_s}{N}$ and m is an integer. Such a constellation requires precise matching of the sampling frequency, input frequency, and FFT length. This technique is known as coherent sampling. Fig. 5.2 (a) shows a simulated FFT with two sinusoidal 0 dBm and -60 dBm signals. ©MATLAB [87] is used for calculating and plotting the results. The frequencies are such that all the energy is concentrated in the middle of a bin. With a random varying input frequency, this is rarely the case, and the energy will spill over into other FFT bins. This effect is known as spectral leakage or smearing, making it difficult to measure the exact frequency or amplitude from the FFT results. Fig. 5.2 (b) shows a worst-case scenario, where the 2.5 GHz signal is increased by only 76.3 kHz. It now falls precisely in between two bins. Thus, the energy is being smeared over a wide frequency range and completely obscures the weaker -60 dBm signal at 999.9084 MHz.

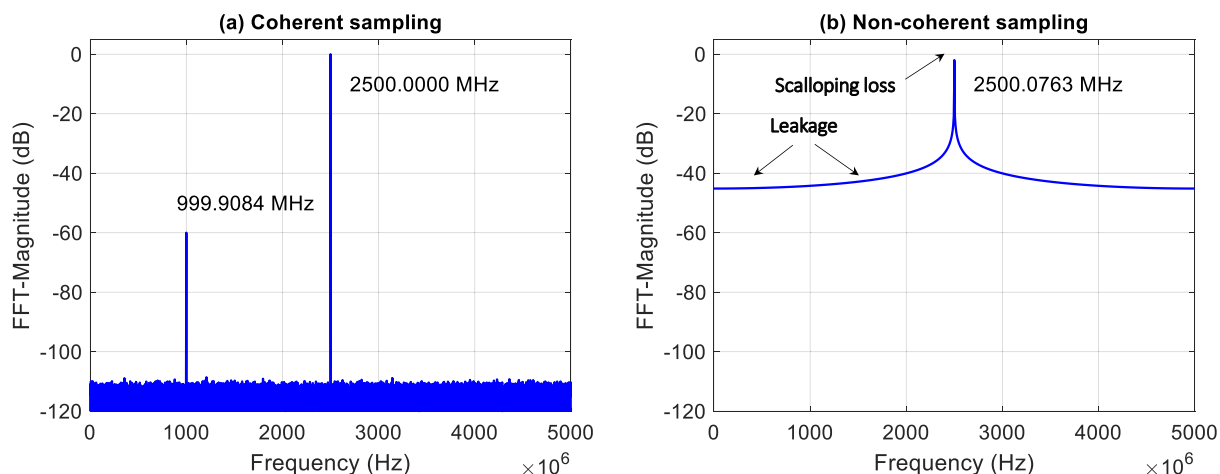


Fig. 5.2: Simulated FFT with 2^{16} data points and 10 GHz sampling frequency;

(a) Coherent sampling of a weak 999.9084 MHz and a strong 2500 MHz signal. All energy falls exactly into bin numbers $N \frac{f}{f_s} = 6553$ respectively 16384, therefore causing no leakage,

(b) Non-coherent sampling: The strong signal is now at 2500.0763 MHz. Its energy falls halfway between bins number 16384 and 16385, causing strong leakage and scalloping loss. The coherent sampled 999.9084-MHz signal is completely obscured.

The distribution of a signal's energy due to scalloping loss and smearing among several bins reduces the peak signal's amplitude which can be observed in Fig. 5.2 (b). This is not acceptable for applications where the FFT is used to determine the amplitude of unknown frequency components with reasonable accuracy. The accuracy can be considerably improved by pre-processing the sampled data, which is described in Section 5.3.

5.3 Windowing the Sampled Data

Spectral leakage is caused by the finite number of samples representing a time-continuous signal and the abrupt loss at the beginning and the end of each data block. Such disruptive amplitude changes in the time domain are transformed into many harmonic signals in the frequency domain. By smoothing the sharp, discontinuous transitions, the FFT's frequency and amplitude response can be improved considerably. This technique is called windowing and flattens the amplitudes at the beginning, and the end of the data block out to zero [17, p. 89]. This is achieved by multiplying the time-discrete samples with a window function. Many window functions with different characteristics are available for optimizing the amplitude and frequency

response of an FFT. Figure 5.3 shows the amplitude response of no window compared to the Hanning, and the Blackman-Harris window, two common but very different window functions.

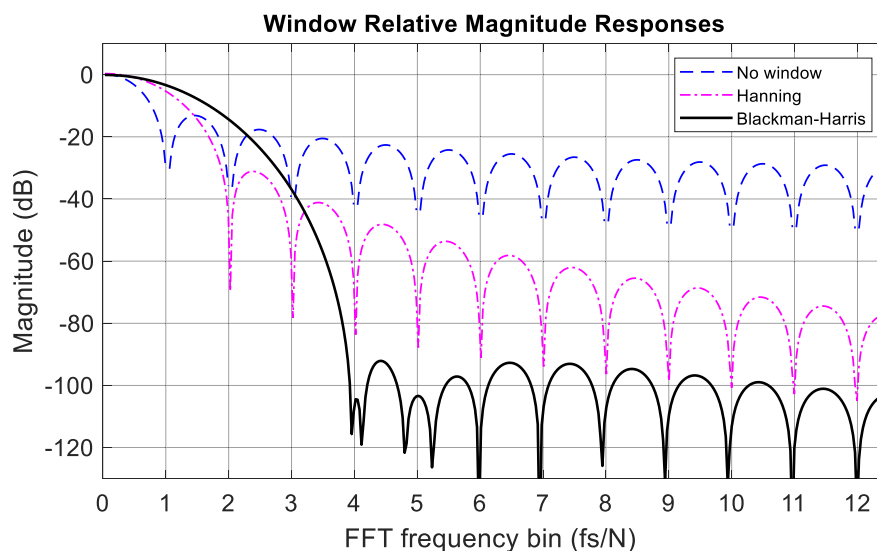


Fig. 5.3: Magnitude response of no window, the Hanning, and the Blackman-Harris window on a logarithmic scale. Only half of the filter response vs. frequency is shown. Window losses have been removed. The horizontal axis is normalized as units of bins.

The windows differ considerably in terms of frequency response. The common characteristic shows a main lobe that is one or more bins wide, followed by several periodically repeating sidelobes of decreasing magnitude. These sidelobes limit the dynamic range, and weak components may be obscured. Increasing the dynamic range by applying a window with better side-lobe suppression will result in a broader main lobe bandwidth. A broader main lobe means spreading the energy over more FFT bins, and the information about a signal's exact frequency becomes blurred. On the other hand, the scalloping loss is reduced as wider main lobes overlap more, flattening the amplitude response, as shown in Fig. 5.3. A comprehensive catalog of windowing functions and their figures of merit is given in [88, p. 55]. All windows, except the so-called rectangular and the flat-top window, introduce an amplitude error. This effect is known as processing loss or coherent power gain and must be taken into account when making accurate amplitude measurements [89]. This error is specific to the individual window function and can be corrected easily with a scaling factor in DSP. Like analog filters, window functions can be characterized by their frequency response. Table 5.1 lists some popular windowing functions and their typical characteristics, taken from [90].

Table 5.1: Frequency response of popular windowing functions. Data are taken from [90].

Window	Highest side lobe level (dB)	Processing loss (dB)	Scalloping loss (dB)	Worst-case processing loss (dB)	6-dB bandwidth (bins)	Half main lobe width (bins)
No window *	-13	0.00	3.92	3.92	1.21	1
Hanning *	-32	1.76	1.33	3.09	2.00	2
Hamming	-43	1.34	1.76	3.10	1.82	2
Four-term Blackman-Harris *	-92	3.00	0.83	3.83	2.72	4
Seven-term Blackman-Harris	-163	4.20	0.46	4.66	3.52	7

* Magnitude response see Fig. 5.3

The two Blackman-Harris windows exhibit the highest sidelobe suppression and are selected for further analysis. The improvement in spectral analysis of non-coherent sampled signals achieved with windowing is demonstrated in the simulation in Fig. 5.4. The signals are the same as in Fig. 5.2 (b), but in this case, the seven-term Blackman-Harris window (BH-7) is applied to the input data block. The result is a significant reduction of spectral leakage and a higher signal-to-noise ratio.

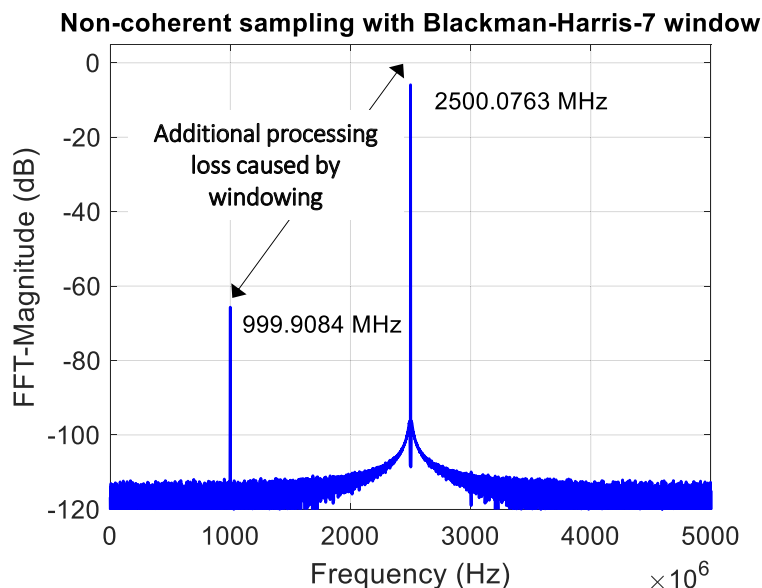


Fig. 5.4: Simulated non-coherent sampling of a windowed, noisy time signal. The FFT has 2^{16} data points, the sampling frequency is 10 GHz.

5.3.1 Selecting a Window Function

As highlighted in the previous Subsection, the time signals need to be windowed to improve the spectral resolution of the FFT. In receiver applications, the sidelobe suppression of the window must be greater than the dynamic range of the receiver to avoid possible interference from adjacent channels. The advantage of windowing in terms of selectivity and sidelobe suppression is exemplified in Fig. 5.5 using two Blackman-Harris (BH) windows created with [91].

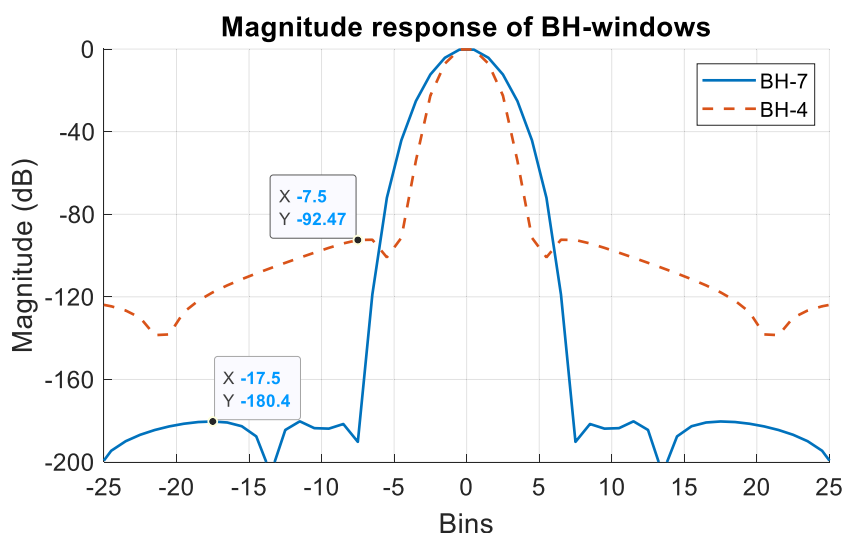


Fig. 5.5: Relative magnitude response of the BH-4 and BH-7 window vs. FFT-bins. The minimum sidelobe suppression is indicated by the X/Y labels.

The BH-4 window shows a superior selectivity, but its sidelobes are only suppressed by about ≈ 92 dB, which may already degrade a receiver's dynamic range. Therefore, the practical DSP implementations in this dissertation are carried out using the seven-term Blackman-Harris window, which provides much better sidelobe suppression of ≈ 180 dB.

Since the spurious suppression methods of this Thesis rely on the comparison of amplitude and frequency components of an FFT, a simulation is performed to determine the properties of the Blackman-Harris windows in this regard. Two sinusoidal signals, x_1 and x_2 , are sampled with $f_s = 106$ MHz, and an N-point FFT is calculated. The signals have an initial frequency $f_{in} = \frac{f_s}{4}$. Signal x_2 is increased in frequency until its level drops by 0.5 dB, 1 dB, or 3 dB compared to x_1 . The frequency difference between x_1 and x_2 is a measure of the selectivity of the BH-4 and BH-7 window functions. The simulation results are listed in Table 5.2.

Table 5.2: Amplitude vs. frequency response of the Blackman-Harris windows.

Amplitude	Blackman-Harris-4 window			Blackman-Harris-7 window		
	-0.5 dB	-1 dB	-3 dB	-0.5 dB	-1 dB	-3 dB
N = 2 ¹⁴	2.6 kHz	3.6 kHz	6.5 kHz	3.3 kHz	4.7 kHz	16.9 kHz
N = 2 ¹⁶	700 Hz	900 Hz	1.6 kHz	900 Hz	1.2 kHz	4.2 kHz
N = 2 ¹⁸	200 Hz	300 Hz	400 Hz	300 Hz	300 Hz	1.1 kHz

The BH-7 window shows a poorer selectivity due to its wider main lobe. This disadvantage can be compensated by a longer FFT if required. From the values given in Table 5.2, the minimum bin offset required to detect a 3 dB amplitude difference between two FFTs can be estimated. Assuming a sampling frequency of 106 MHz, an FFT length of $N = 2^{14}$ points, and a BH-7 window, the minimum frequency offset is $16.9 \text{ kHz} \times 2^{14} / 106 \text{ MHz} \approx 2.6$ bins.

5.4 Summary Conclusions on Errors in FFT Measurements

An overview of the errors and their sources when measuring a sinusoidal signal with an FFT is presented in Table 5.3.

Table 5.3: Errors introduced by FFT processing when measuring a sinusoidal signal.

FFT-error effect	Source of error	Sinusoidal signal error	Remark
Scalloping loss	Length of FFT	Incorrect Amplitude	frequency-dependent
Processing loss	Windowing	Incorrect Amplitude	constant
Leakage	Length of FFT, non-coherent sampling	Incorrect frequency	frequency-dependent

An in-depth analysis of possible errors affecting the accuracy when measuring amplitudes and frequencies with an FFT can be found in [89].

The suitability of the FFT for spectrum analysis and spurious detection can be summarized as follows:

1. Sufficiently accurate spectral measurements require an appropriate selection of the window type and FFT length to ensure the required amplitude and frequency resolution.
2. The most critical errors are leakage and scalloping loss since these are frequency-dependent and unpredictable for random signals. All other amplitude errors are constant and can be calibrated out in software.
3. Amplitude errors due to noise may occur when small signals close to the noise floor are measured using small FFT bandwidths. The uncertainty depends on the noise energy that is superimposed on the signal
4. For broadband spectrum monitoring, the International Telecommunication Union (ITU) requires an amplitude accuracy of ± 2 dB [3, p. 220], which can be achieved with the presented FFT measurement approach.

6 A New Spurious Suppression Technique

This Chapter introduces a novel technique for spurious signal suppression as the central contribution of this dissertation work. The underlying idea is that using a different A/D conversion parameter causes a signal to change its frequency or amplitude linearly in the frequency domain. Internally generated spurious signals, however, follow a different pattern because these depend on the sampling frequency or are caused by nonlinear distortion. This property of the A/D conversion process is used to detect spurious signals. For this purpose, the signal is digitized twice with two different A/D conversion parameters. The A/D conversion parameters considered in this work are either:

- The sampling frequency,
- the signal frequency,
- or the signal amplitude.

After A/D conversion, the two differently digitized time signals are transformed into the frequency domain using an FFT. The FFTs are normalized to the same frequency and amplitude resolution, theoretically resulting in identical spectral content. By comparing the spectra, false signals can now be detected. Spectral components that are not identical in both FFTs must necessarily be spurious signals generated by the A/D conversion process. These are therefore classified as unwanted artifacts and suppressed by subsequent digital signal processing.

This working principle and the three possible A/D conversion parameters allow the development of three different methods for spurious reduction. For simplicity and better readability, the methods are abbreviated and given short names.

The method based on a variation of:

- the sampling frequency is called the **DSF-method** (Different Sampling Frequency),
- the input frequency is called the **DIF-method** (Different Input Frequency),
- the signal amplitude is called the **DIA-method** (Different Input Amplitude).

The following Subsection describes how to obtain the two necessary sets of sampling data.

6.1 Data Acquisition with one or two ADCs

Implementing the methods requires a hardware structure that allows the acquisition of two differently sampled data sets. These can be obtained with a single ADC by sequentially sampling the signal with different A/D conversion parameters. Fig. 6.1 shows schematically how the three methods can be applied to the desired signal. A frequency conversion stage before the ADC allows its input frequency f_{ADC} to be shifted in relation to the LO frequency Δf_{LO} . The variable attenuation Δa is used to control the signal level of f_{ADC} , which is then digitized with a variable sampling clock frequency Δf_s .

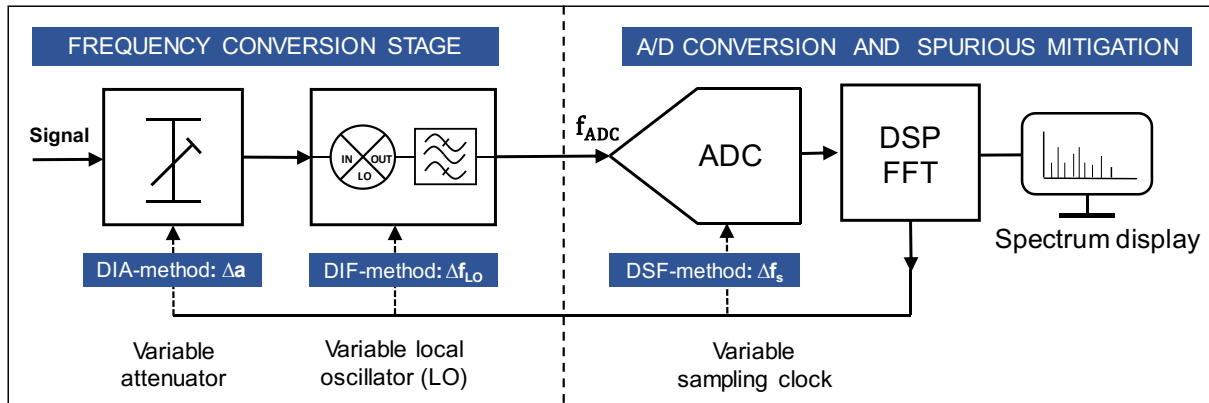


Fig. 6.1: A single ADC digitizer with frequency conversion and provisions for using the DIA-, DIF- and the DSF- spurious mitigation method.

The use of only one ADC device means that fewer components are required, and the same ADC distortion characteristics apply to both FFTs, allowing a ubiquitous spectral comparison. However, a major drawback of sequential sampling is that the input signals may change between the time-delayed snapshots, resulting in different spectral content. This is typically the case with pulsed or rapidly changing broadband modulated signals, making a meaningful comparison of the FFTs difficult.

Since the focus of this dissertation is on radio monitoring of modulated signals with high RTBW, an implementation of the methods with two parallel ADC is pursued. Thus no speed is lost, and the methods also work with rapidly changing signals. Similar distortion characteristics in both FFTs are achieved by using a dual-core ADC implemented on one chip. In the following two Sections for each of the methods, the working principle is elaborated in detail, using the two ADC approach.

6.2 The Different Sampling Frequency Method (DSF-method)

The DSF-method samples the same signal twice with different sampling frequencies. Fig. 6.2 shows the principle of operation. The signal is conditioned by splitting it into two paths by a power divider. Then it is A/D converted by two separate ADCs operating with different sampling frequencies, f_{s1} and f_{s2} . The resulting time signals are transformed into the frequency domain with an FFT. The difference in the sampling frequencies leads to different frequency scales of the resulting FFTs. Therefore, before comparing the spectra, FFT2 must be mathematically matched to achieve the same frequency resolution in both FFTs. If the two spectra are correctly aligned, a signal will appear at the same bin position in both FFTs. Now spurious signals can be detected by comparing the spectra bin by bin. Spectral components that are not identical in both FFTs must necessarily be interfering signals generated by the ADCs. These spectral components are classified as spurious signals and suppressed by subsequent digital signal processing (DSP). The following program description and implementation are done with ©MATLAB. MATLAB was chosen because it is very popular and combines computation and visualization with a powerful DSP toolbox.

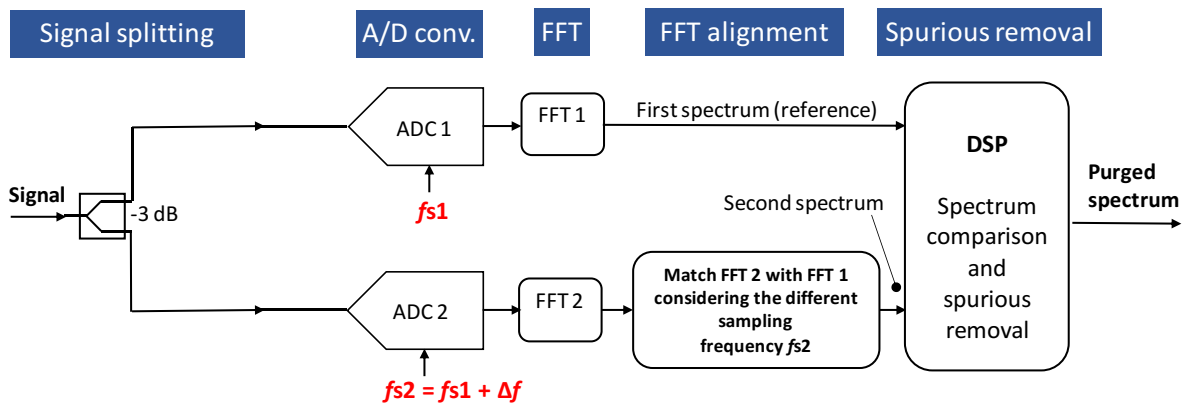


Fig. 6.2: The DSF-method uses two separate ADCs with different sampling frequencies to digitize the signal. Spurious are detected by comparing the aligned FFTs and removed by DSP.

To further illustrate the working principle, a distorted 30 MHz sinusoidal signal containing strong harmonics is assumed as an input signal. The ADCs sample the signal in parallel with 100 MHz and 103 MHz. Because of aliasing, some of the 30 MHz harmonics fall into the first Nyquist zone. Table 6.1 lists the frequencies of such HD2 to HD4 aliases, which are calculated using (4.9).

Table 6.1 Alias frequencies HD2 to HD4 of a distorted 30 MHz signal f , when sampling with two different sampling frequencies f_s .

f_s (MHz)	f (MHz)	HD2 (MHz)	HD3 (MHz)	HD4 (MHz)
100	30	40	10	20
103	30	43	13	17

Fig. 6.3 illustrates the sampled 30 MHz signals from Table 6.1 in the frequency domain. The harmonics are not visible because these are all ≥ 60 MHz and thus outside the first Nyquist zones, which end at 50 MHz resp. 51.5 MHz.

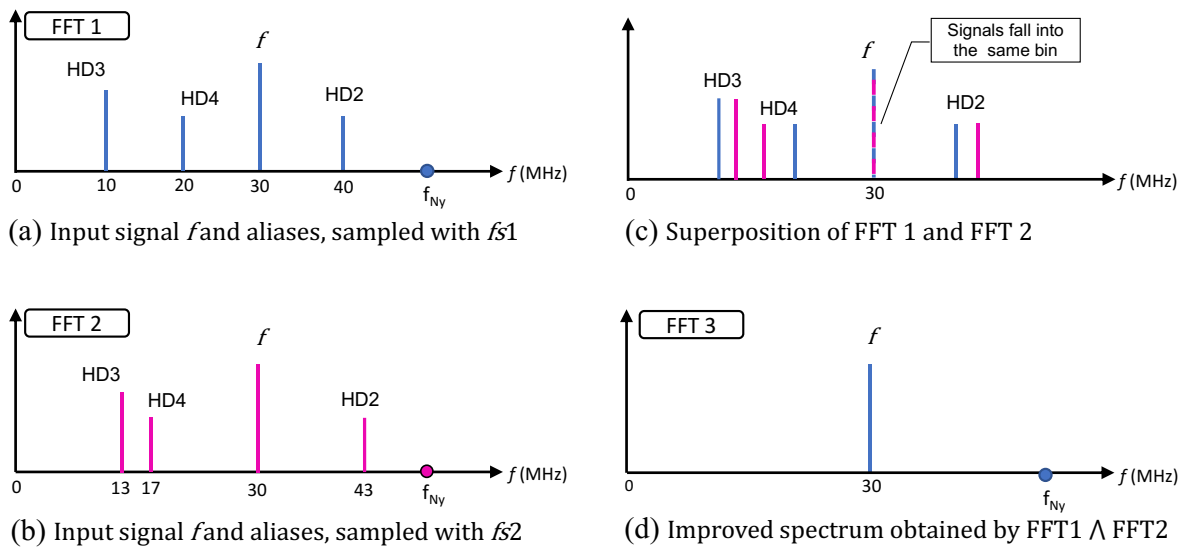


Fig. 6.3: Illustration of the DSF-method. The Nyquist frequencies are denoted by f_{Ny} ;
 (a) Signal f sampled with f_{s1} ,
 (b) Signal f sampled with f_{s2} ,
 (c) Spectra of (a) and (b) superimposed to illustrate emerging aliases,
 (d) Improved spectrum obtained by a logical AND operation of FFT 1 and FFT 2.

Alias signals resulting from harmonic distortion are removed in four steps:

- Digitize the signal with sampling frequencies f_{s1} and f_{s2}
- Calculate the reference spectrum FFT 1, Fig. 6.3 (a)
- Calculate FFT 2 considering the deviating sampling frequency f_{s2} , Fig. 6.3 (b)
- Calculate the purged spectrum FFT 3 by an AND operation and remove all signals from FFT 1 that are *not identical* in FFT 1 and FFT 2, Fig. 6.3 (d)

By superimposing FFT1 and FFT2, as shown in Fig. 6.3 (c), the deviating frequencies of the aliases caused by the different sampling frequencies are revealed. The prerequisite for successful spurious detection is that the frequency axes of the FFTs are correctly scaled and aligned. The following Subsection provides an example in MATLAB syntax of how this can be accomplished with digital signal processing.

6.2.1 Signal Flow of the DSF-Method

Fig. 6.4 presents an exemplary signal flow of the DSF-method using the MATLAB [92] syntax.

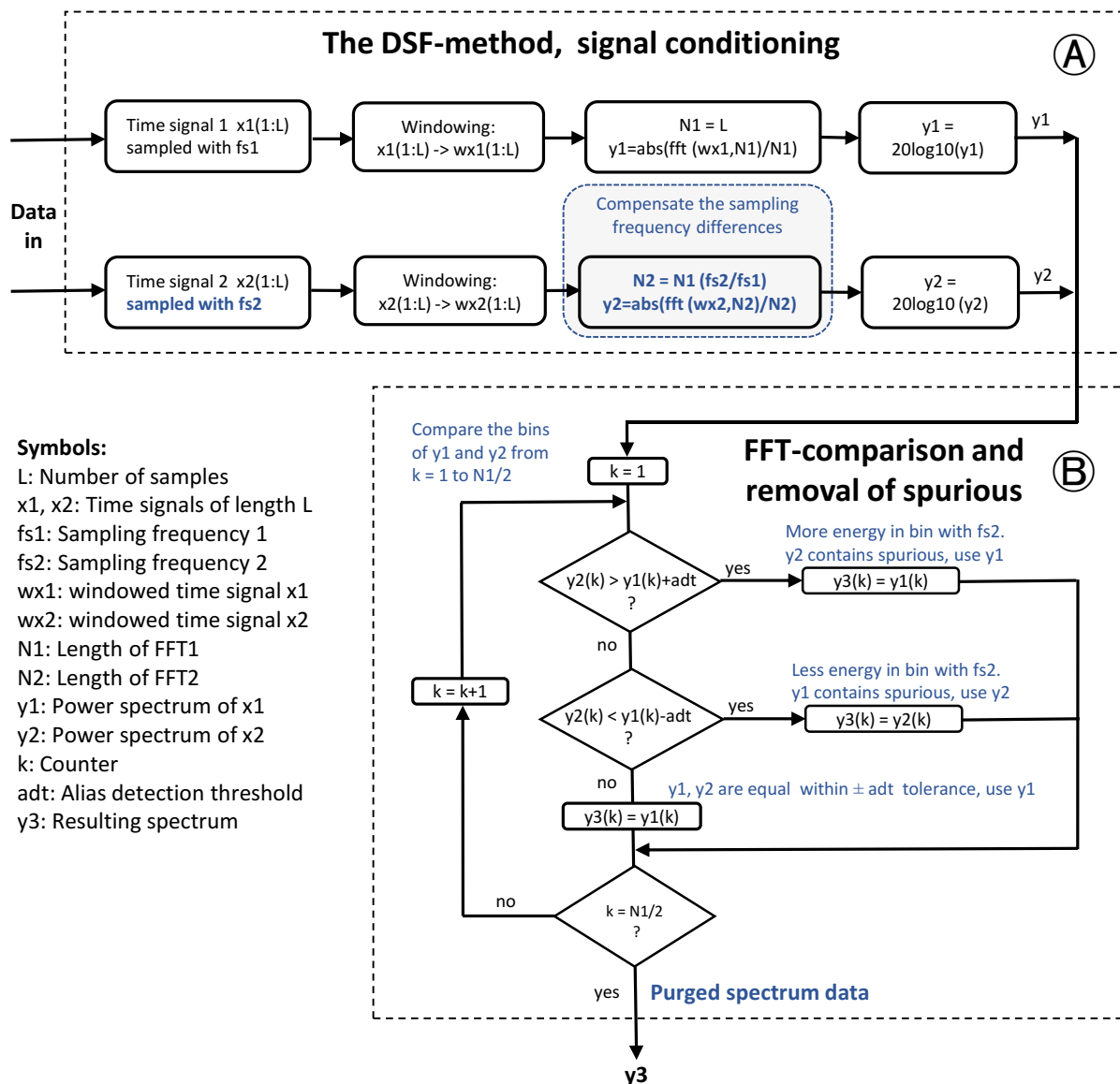


Fig. 6.4: DSP-signal flow of the DSF-method, consisting of two program blocks, (A) and (B).

The program consists of two main blocks – one for signal conditioning denoted as **(A)**, and another for FFT comparison and spurious removal marked as **(B)**. Block **(A)** performs the FFT, ensures that the frequency bins in both FFTs match precisely, and carries out a logarithmic scaling. Two vectors x_1 , and x_2 of length L , contain the real-valued ADC data sampled with different sampling frequencies f_{s1} and f_{s2} . After windowing, a one-sided power spectrum is calculated using the FFT. Equation (5.1) is used to achieve the same frequency resolution and bin width BW_{bin} in both FFTs. This is achieved by adjusting the length N_2 of FFT 2. Using $BW_{bin} = \frac{f_{s1}}{N_1} = \frac{f_{s2}}{N_2}$, we can solve for N_2 and get the length $N_2 = N_1 \left(\frac{f_{s2}}{f_{s1}} \right)$.

N_2 is now different from the number of samples L in wx_2 , and hence the length of wx_2 must be adjusted to match with L . MATLAB's built-in "*fft-function*" automatically takes care of that [93]. If the length of xw_2 is less than N_2 , then wx_2 is padded with trailing zeros to length N_2 . This technique is known as zero-padding [94], [95, p. 370]. If the length of wx_2 is greater than N_2 , then wx_2 is truncated to length N_2 . By this, both FFTs result in equal frequency resolution, and the signals are aligned at the same bin position despite different sampling frequencies. The following amplitude comparison of y_1 with y_2 is performed using a logarithmic power scale; therefore, the results are scaled logarithmically.

Block **(B)** compares the FFT amplitudes bin-wise, selects the correct value, and stores the purged spectrum data in the result vector y_3 . The spectrum is real-valued, so a comparison only needs to be done up to $\frac{N_1}{2}$ making the algorithm faster.

An alias detection threshold (adt) defines a tolerance window within which the amplitudes of y_1 and y_2 are considered equal. In this case, the reference spectrum y_1 is assumed to be correct and copied to y_3 . If the tolerance window is left, the algorithm decides on the smaller of the two values and copies it to y_3 . This decision is based on the assumption that a larger value is caused by an undesired superposition with alias signal energy, and therefore the smaller value is considered correct.

The following MATLAB code fragment shows an exemplary implementation of windowing, adjustment of the FFT length, and calculation of the logarithmic power spectra.

```

%% DSF-method, calculate FFT2 with the same frequency resolution as FFT1
...
L = 2^14; % number of time samples
fs1 = 106000000 - 2000; % compensate XO frequency offset
fs2 = 106250000 - 900;
N1 = L; % length of FFT1
N2 = ceil(N1*fs2/fs1); % adjust length of N2 considering fs2
signal_str_1 = query(tcpipObj1,'ACQ:SOUR1:DATA?'); % Capture ADC1 signal
x1 = str2num(signal_str_1(1,2:length(signal_str_1)-3));
...
win = create_window('blackmanharris7',N1); % window function by Morgan Prior [91]
xw1 = x1(:).*win.window; % window the time signal
xw2 = x2(:).*win.window;
y1 = abs(fft(xw1,N1)/N1); % calculate abs. power spectrum
y2 = abs(fft(xw2,N2)/N2);
y1 = 20*log10(y1) + cal1; % log (dBm) scaling and path calibration
y2 = 20*log10(y2) + cal2;
...

```

A MATLAB code fragment for comparing the power spectra in y_1 and y_2 and storing the result in y_3 looks like this:

```

%% compare y1 with y2 and store the lower value in y3, if outside the adt tolerance window.
% If inside tolerance window use y1 from the reference spectrum
...
adt = 3; % alias detection threshold
for k = 1:N1/2 % compare single sided spectrum only

    if y2(k) > y1(k) + adt
        y3(k) = y1(k); % amplitude in y2 is greater than y1+adt, use y1 from ref. spectrum

    elseif y2(k) < y1(k) - adt
        y3(k) = y2(k); % amplitude in y2 is less than y1-adt, use y2

    else
        y3(k) = y1(k); % y1 and y2 are equal +/- adt, use y1 from reference spectrum
    end

end
...

```

6.2.2 Sampling Frequency Offset for the DSF-Method

The difference in sampling frequencies Δf_s must be large enough to shift an alias signal distinctively into a different bin of the FFT. Otherwise, a successful detection is not possible. The bin-shift Δm resulting from a variation of the sampling frequency depends on the length of the FFT and the signal frequency. Using (5.2), Δm can be calculated by:

$$\Delta m = \left| N f_{in} \left(\frac{1}{f_s} - \frac{1}{f_s \pm \Delta f_s} \right) \right| \quad (6.1)$$

The diagram in Fig. 6.5 illustrates how decreasing the sampling frequency changes the bin allocation for different input frequencies. The graph is created using (6.1) and allows an estimation of the required frequency difference Δf_s to achieve a certain bin-shift Δm .

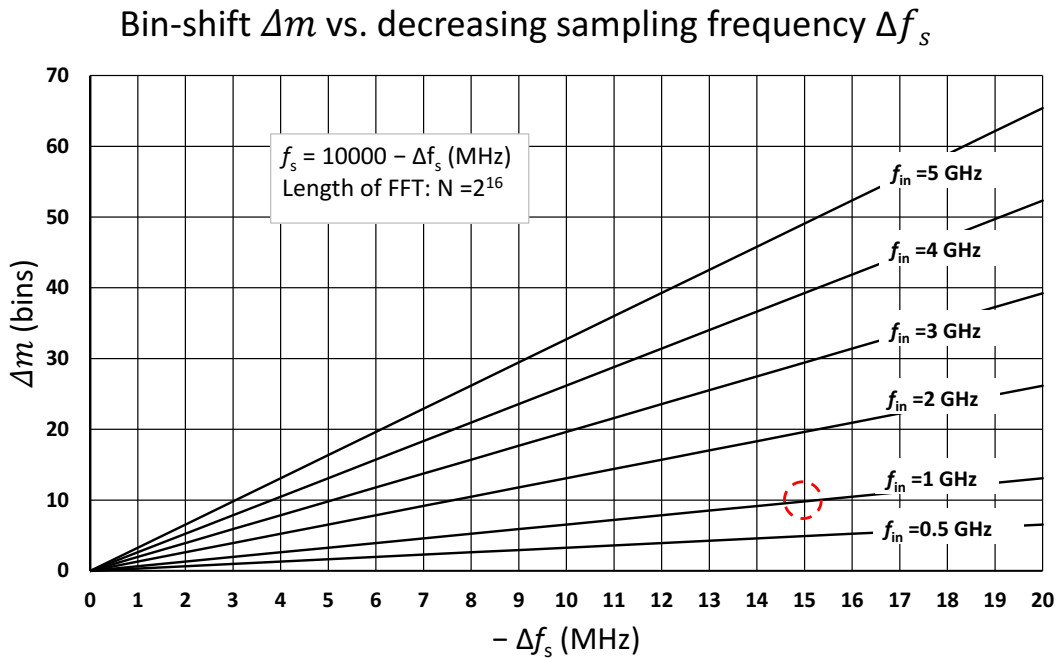


Fig. 6.5: Bin-shift Δm vs. sampling frequency variation Δf_s . FFT length is $N = 2^{16}$, the initial sampling frequency is $f_s = 10$ GHz. Parameter is the signal frequency f_{in} , ranging from 0.5 to 5 GHz.

The diagram indicates that higher signal frequencies react more sensitive to variations of the sampling frequency. Besides aperture jitter, this is another reason why the sampling clock must be very stable and is required to have a low phase noise to achieve a stable, high-resolution frequency measurement with an FFT.

6.2.3 Effectiveness and Limitations of the DSF-Method

The DFS-method removes undesired signals that are related to the sampling frequency. Generally, these are the aliases of a signal and its harmonics. Due to the principle of operation, the

method can also remove subharmonics or other artifacts related to the sampling clock. In an undersampling scenario, which is based on intentional aliasing, the method is not useful since, in this case, all desired signals are also removed. However, according to (4.9), the aliased signals, i.e., from the second Nyquist zone, have a constant frequency offset of $f_{s2} - f_{s1}$. If the spurious detection algorithm is extended and this frequency offset is compensated before comparing the FFTs, the DSF-method also works with undersampling. The DIF-method presented in the next Subsection shows how such a frequency offset compensation can be implemented.

Another limitation of the DSF-method arises for signals at the lower end of the spectrum. When f_{in} decreases, Δm decreases as well, and a higher Δf_s is necessary to achieve a certain bin-shift (see Fig. 6.5). This is obvious in the extreme case of a DC signal, which is always located in the first bin of the FFT, no matter what sampling frequency is used. Therefore, the DSF-method does not work for very low frequencies or very short FFTs. If a minimum bin shift Δm of 10 bins is desired in a system with $f_s = 10$ GHz, $\Delta f_s = 15$ MHz and $FFT = 2^{16}$, the lowest possible signal frequency can be estimated with the help of Fig. 6.5. With the conditions given above, the lowest working frequency is 1 GHz, marked by the dashed circle. All frequencies lower than that cannot achieve the required shift of 10 bins. An equation for determining the minimum working frequency f_{min} can be derived by re-arranging (6.1):

$$f_{min} \geq \frac{\Delta m}{N \left(\frac{1}{f_s - \Delta f_s} - \frac{1}{f_s} \right)}. \quad (6.2)$$

6.3 The Different Input Frequency Method (DIF-method)

The DIF-method detects spurious signals by analyzing their atypical movement on the frequency axis when shifting the input frequency. When the input frequency of a nonlinear system is changed, the harmonic frequencies resulting from the nonlinear distortion change by a multiple of the distortion order (3.3). This means harmonics move on the frequency axis by a factor of two, three, or more. Implementing the DSF-method requires additional hardware for a frequency conversion stage consisting of a mixer, a local oscillator, and adequate filtering. Such a configuration is similar to a single conversion superhert with broadband digital IF. Since the position of the RX band can now be freely selected, it is also possible to combine the DSF-

method and the frequency planning approach presented in Subsection 3.3.2. Fig. 6.6 illustrates the signal flow for the DIF-method with a frequency conversion stage in front of the ADCs. The frequency shift can be chosen by selecting the frequency difference of the local oscillators.

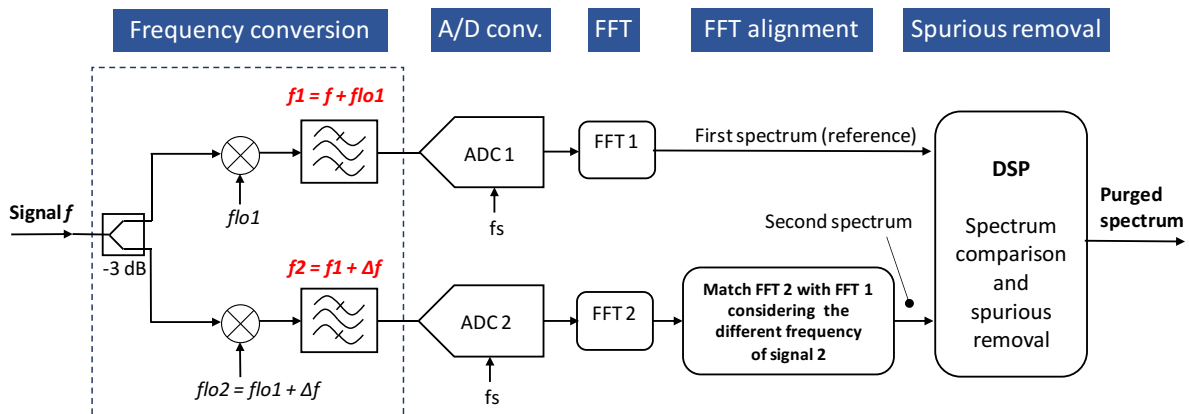


Fig. 6.6: The DIF method uses frequency conversion before the ADCs. The difference between the local oscillator frequencies f_{lo1} and f_{lo2} determine the frequency difference between the input signals.

The following example assumes a fundamental frequency of 3 MHz for f_1 and a frequency upshift of $\Delta f = 100$ kHz for f_2 . Table 6.2 illustrates the effect of the frequency shift on the harmonic frequencies.

Table 6.2 Harmonic frequencies HD2 to HD5 of a 3 MHz and a 3.1 MHz signal.

	HD2 (MHz)	HD3 (MHz)	HD4 (MHz)	HD5 (MHz)
$f_1 = 3.0$ MHz	6	9	12	15
$f_2 = f_1 + \Delta f = 3.1$ MHz	6.2	9.3	12.4	15.5

Fig. 6.7 illustrates the position of the frequencies on the horizontal axis. The frequency shift is $\Delta f = 100$ kHz.

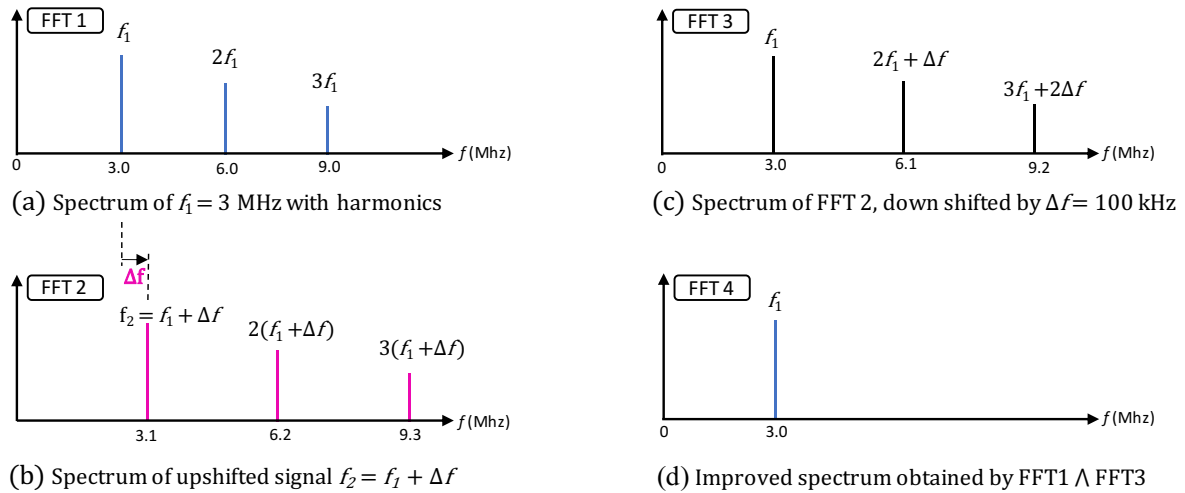


Fig. 6.7: Illustration of the DIF-method to reduce spurious caused by harmonic distortion;
 (a) FFT 1 of signal f_1 , with strong harmonic distortion,
 (b) FFT 2 of the same signal, upshifted by Δf . The harmonics are now spaced further apart,
 (c) FFT 2 mathematically downshifted by Δf . Signals are back in place; the harmonics are not,
 (d) Improved spectrum by executing a logical AND operation on spectra FFT 1 and FFT 3.

Spurious signals resulting from harmonic distortion are removed in six steps:

1. Prepare signal f_2 by shifting f_1 up by Δf .
2. Digitize signal f_1 with ADC 1 and signal f_2 with ADC 2.
3. Calculate FFT 1. The resulting spectrum is shown in Fig. 6.7 (a).
4. Calculate FFT 2. The resulting spectrum is shown in Fig. 6.7 (b).
5. Calculate FFT 3 by shifting the spectrum of FFT 2 down by Δf . Now the input signals are back in place, but the harmonics are at a different position than before, see Fig. 6.7 (c).
6. Calculate the purged FFT 4 by removing all signals that are not identical in FFT 1 and FFT 3, see Fig. 6.7 (d).

The next Subsection provides an example MATLAB program for performing these operations.

6.3.1 Signal Flow of the DIF-Method

The DSP-signal flow of the DIF-method is illustrated in Fig. 6.8. The data block x2 contains the upshifted version of the signal in x1. To minimize the error caused by scalloping loss and leakage, Δf is chosen so that the resulting bin-shift Δm is an integer number (6.3). After windowing the time signals, the two FFTs y1 and y2 are computed. The higher input frequency in x2 shifts all frequencies in y2 up by Δm bins. This frequency offset is compensated by mathematically shifting all bins in y2 down by Δm . The length of y2 is restored by appending Δm noise floor values (nf). Now, all valid signals appear at the same bin number, but the harmonics do not. A cleaned spectrum y3 can be calculated using the same “FFT-comparison and removal of spurious” algorithm, as shown in Fig. 6.4.

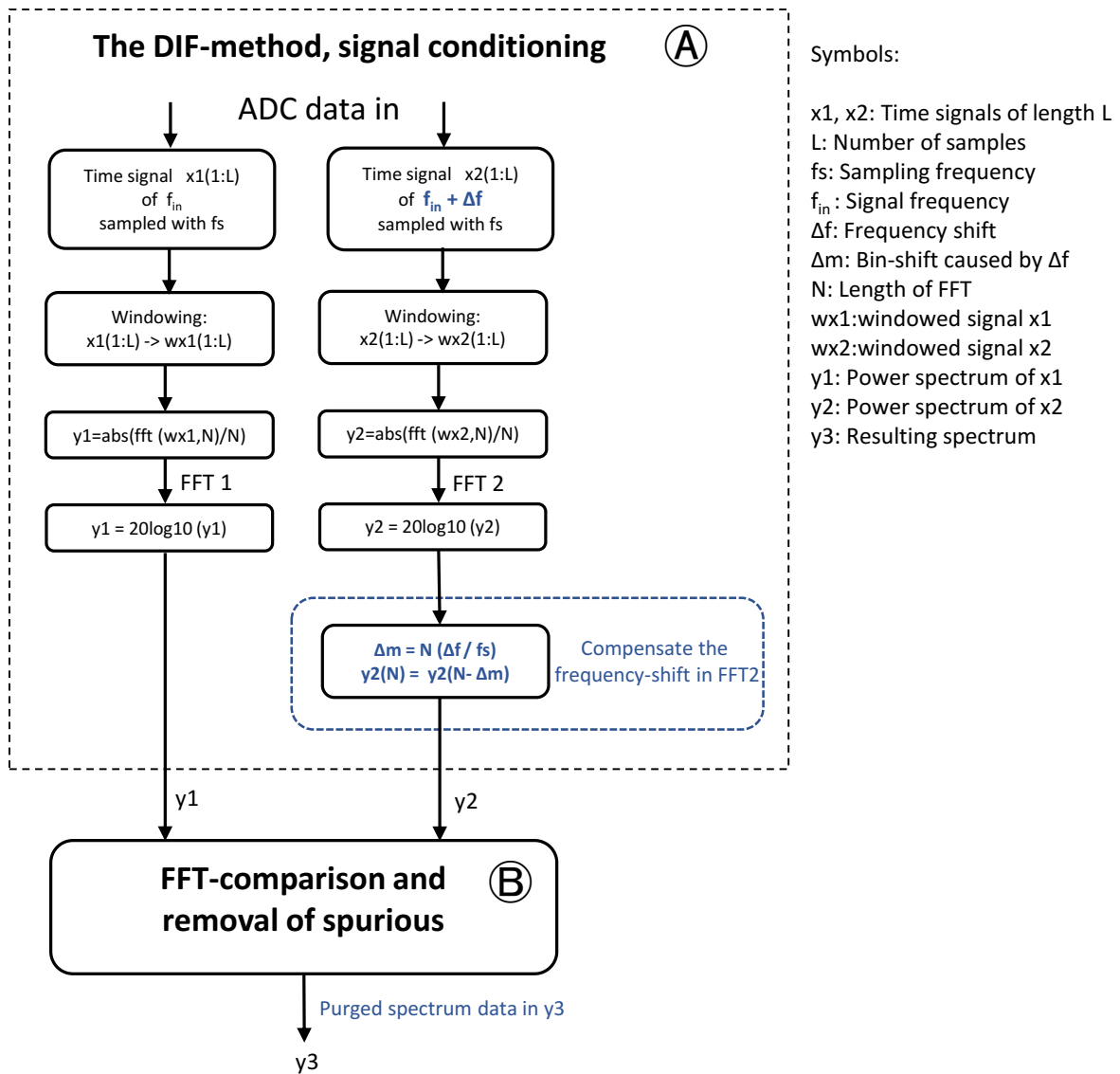


Fig. 6.8: Signal flow of the DIF-method. For details of block (B), refer to Fig. 6.4.

A MATLAB[®] code fragment showing the calculation of the logarithmic power spectrum and the compensation of the bin shift is given below.

```
%% calculate FFT2 and undo the frequency up-shift
...
fs= 106000000 - 2000;      % sampling frequency (Hz)
L = 2^14;                  % number of time samples
N = L;                     % length of FFT
binwidth = fs/N;          % refer to equation (5.1)
dm = 100;                  % bin shift by 100 bins
df = bandwidth*dm;        % calculate deltaf from no. of bins, 100 bins equal 646973 Hz
nf = -85;                  % System noise floor (dB)
...
y2 = abs (fft(xw2,N)/N);   % calculate FFT power spectrum
y2 = 20*log10(y2)+ cal1;   % log scaling (dBm), and magnitude calibration
...
%% undo the frequency up-shift by moving all bins dm-positions down
y2(1:dm) = [];             % delete lower bins from 1 to dm
yf(1:dm) = nf;             % create dm noise floor bins
y2 = horzcat (y2,yf);      % restore initial length by appending yf to y2
...
```

6.3.2 Choosing the Frequency Offset for the DIF-Method

Equation (5.2) can be used to calculate the required frequency shift Δf to achieve a certain bin offset Δm . With N being the length of the FFT, the frequency shift can be calculated as:

$$\Delta f = \Delta m \frac{f_s}{N} \quad (6.3)$$

For example, with a sampling rate $f_s = 10$ GHz and an FFT length of 2^{16} , a binshift of 20 bins is achieved by frequency shift Δf of:

$$\Delta f = 20 \frac{10^{10}}{2^{16}} \approx 3.518 \text{ MHz}$$

For the detection of harmonically related spurious, half of this frequency shift or less will be sufficient, as these will be offset by a multiple of their distortion order.

Frequency shifting might introduce amplitude errors caused by the amplitude vs. frequency response introduced by building blocks and filters preceding the ADC. It is therefore advisable to keep the frequency shift as small as possible. In practice, one chooses Δf in such a way that Δm is an integer number of bins. This gives a comparable situation in both FFTs because possible errors due to leakage or scalloping loss are equal and cancel out.

6.3.3 Effectiveness and Limitations of the DIF-Method

The DIF-method works well to detect undesired signals caused by a nonlinear distortion of the input frequency and its aliases. It does not have the limitation at very low frequencies that the DSF-method has. However, it cannot detect *odd-order* intermodulation distortion like IMD3, which is caused by the sum or difference of the signals. The reason is that the frequency spacing between the signals and the IMD products remains constant for this distortion type after a frequency shift. Therefore, undoing the frequency shift moves the IMD signals back to the original position. The mathematical proof is as follows: The *close in* IMD products resulting from the *difference* of two frequencies f_1 and f_2 or their multiples can be calculated by using (3.4):

$$f_{IM} = |nf_1 - f_2m|, \quad \text{with } n, m = 1, 2, 3, \dots \quad \text{and } n + m \geq 2. \quad (6.4)$$

The order of the distortion is given by $|n - m|$.

After shifting up both frequencies by $+\Delta f$ and digitizing again, the IMD frequencies are:

$$f_{IM_up} = |n(f_1 + \Delta f) - m(f_2 + \Delta f)|, \quad \text{with } n, m = 1, 2, 3, \dots \quad \text{and } n + m \geq 2. \quad (6.5)$$

Undoing the upshift moves the IMD products down to: $f_{IM_down} = f_{IM_up} - \Delta f$, which is equal to:

$$f_{IM_down} = |nf_1 + n\Delta f - mf_2 - m\Delta f - \Delta f|. \quad (6.6)$$

If the condition $f_{IM} = f_{IM_down}$ is fulfilled, the IMD products have moved back to their initial position, and the frequency shift cannot deliver a criterion for their identification. For this

non-working scenario, n and m can be calculated by using (6.4) and (6.6):

$$|nf_1 - mf_2| = |nf_1 + n\Delta f - mf_2 - m\Delta f - \Delta f|.$$

Now we can write: $0 = |n\Delta f - m\Delta f - \Delta f| = |\Delta f(n - m) - \Delta f|$, and

$$|\Delta f| = |\Delta f(n - m)|, \text{ which is true if } |n - m| = 1.$$

This means for all n and m satisfying $|n - m| = 1$, the method does *not* work. According to (3.4), these are the odd-order IMD-products like IMD3, IMD5, IMD7, ... and so on.

A similar calculation shows that the situation is different for the IMD products based on the sums of the frequencies $f_{IM} = |nf_1 + mf_2|$. Those are returning to their initial frequencies after a frequency shift only if $n + m = 1$. This is *not* a valid solution since n and m are integers and always ≥ 1 . In other words, all combinations of n and m produce a detectable frequency shift, and therefore the DIF method works for even-order IMD products.

6.4 The Different Input Amplitude Method (DIA-method)

The DIA method differs fundamentally from the DSF and DIF methods in that it detects interfering signals based on the amplitude characteristics rather than frequency. It takes advantage of the fact that the amplitude of harmonic and intermodulation distortion is a function of the signal's amplitude (3.2). The distortion is caused by the nonlinear transfer curve of the device under test, and the amplitude typically follows a quadratic, cubic, or even higher-order function. Thus, inserting a small, e.g., 3 dB attenuator in the signal path reduces the third-order distortion by 9 dB. This technique works well for analog systems like amplifiers and analog mixers and is used by measurement engineers to identify a distortion product and classify its order.

Table 6.3 illustrates how the amplitude of the IMD3 products changes when a 0-dBm two-tone signal is attenuated by 1 dB and by 3 dB, respectively.

Table 6.3 Example for intermodulation products IMD3 vs. input level.

ain (dBm)	0 (dBm)	-1 (dBm)	-3 (dBm)
IMD3	-20	-23	-29

To identify IMD products, the DIA-method samples a signal twice with slightly different input levels. The signal flow is shown in Fig. 6.9. In this example, the ADCs are running in parallel and sampling the signals with 100 MHz. ADC 2 receives the signal attenuated by Δa .

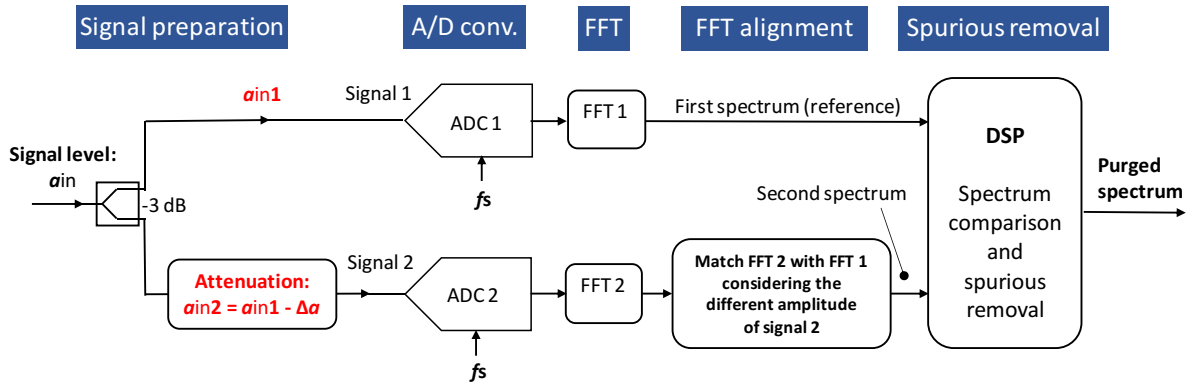


Fig. 6.9: The DIA-method uses different input signal levels to obtain two different data sets and reveal nonlinear distortion.

Detection and removal of the nonlinear distortion are illustrated in Figure 6.10 and performed in the following steps:

1. Prepare the signals by splitting ain with a power divider. Signal $ain1$ is directly connected to ADC1. Signal $ain2$ is a copy of $ain1$ attenuated by Δa and fed to ADC2.
2. Digitize signals $ain1$ and $ain2$ with ADC 1 and ADC 2.
3. Calculate FFT 1. See Fig. 6.10 (a).
4. Calculate FFT 2. See Fig. 6.10 (b).
5. Calculate FFT 3 by undoing the attenuation Δa in FFT 2. See Fig. 6.10 (c).
6. Calculate the purged spectrum FFT 4, considering only signals with identical amplitudes in FFT 1 and FFT 3. See Fig. 6.10 (d).

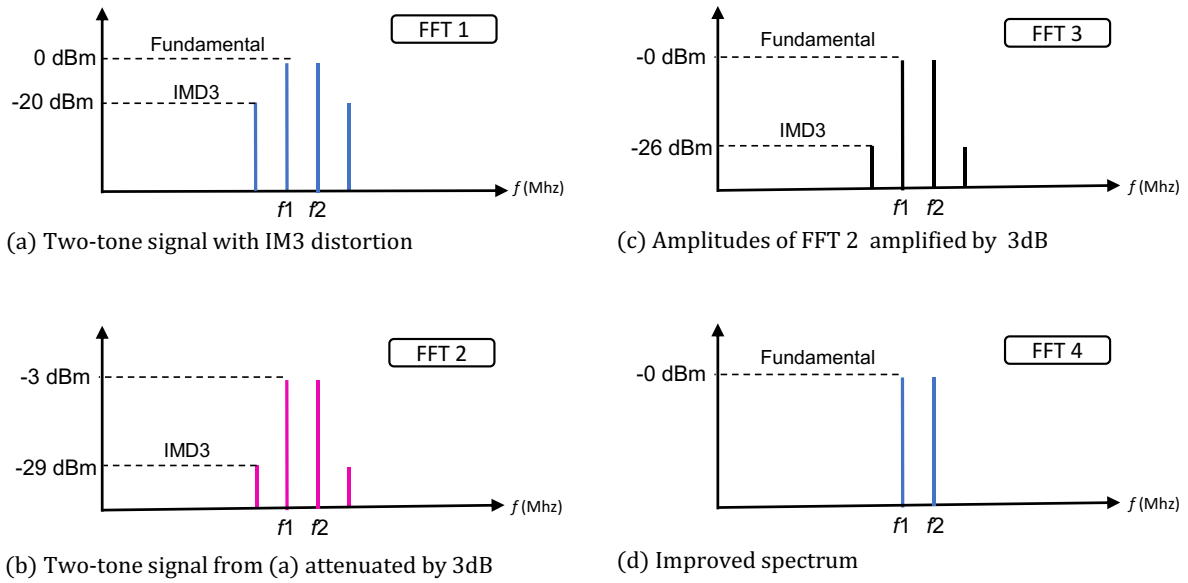


Fig. 6.10: Illustration of the DIA-method;

- (a) Initial two-tone signals with 0 dBm, IMD3 level is -20 dBm,
- (b) Two-tone signal attenuated by 3 dB, IMD3 level is now -29 dBm,
- (c) Spectrum of FFT 2 re-adjusted by +3 dB, the IMD3 level is now -26 dBm,
- (d) Improved FFT 4, using only signals with identical amplitudes in FFT 1 and FFT 3.

6.4.1 Signal Flow of the DIA-method

Figure 6.11 shows the signal flow for the DIA-method using the MATLAB syntax. The working principle is based on detecting nonlinear amplitude differences between the two FFTs. Signal x_2 is a by Δa (dB) attenuated version of x_1 and will therefore contain reduced nonlinear distortion content. Compensation of the attenuation is accomplished by adding the same amount in decibels to the logarithmic power spectrum y_2 in block (A). Since there is no frequency shift, there are no additional amplitude errors to be concerned about due to scalloping losses. Hence an amplitude comparator with a tolerance window of $\pm at$ (dB) is used for bin-wise comparison of the FFTs in block (B). Before starting the comparison, the result vector is loaded with the noise floor value of the system in dB. If the amplitudes of y_1 and y_2 match within the tolerance, y_1 is used as the result and copied to y_3 . If the amplitudes do not match, a spurious signal is assumed. In this case, y_3 is not changed, and the preloaded noise floor value remains in the result vector. In this way, the algorithm runs faster.

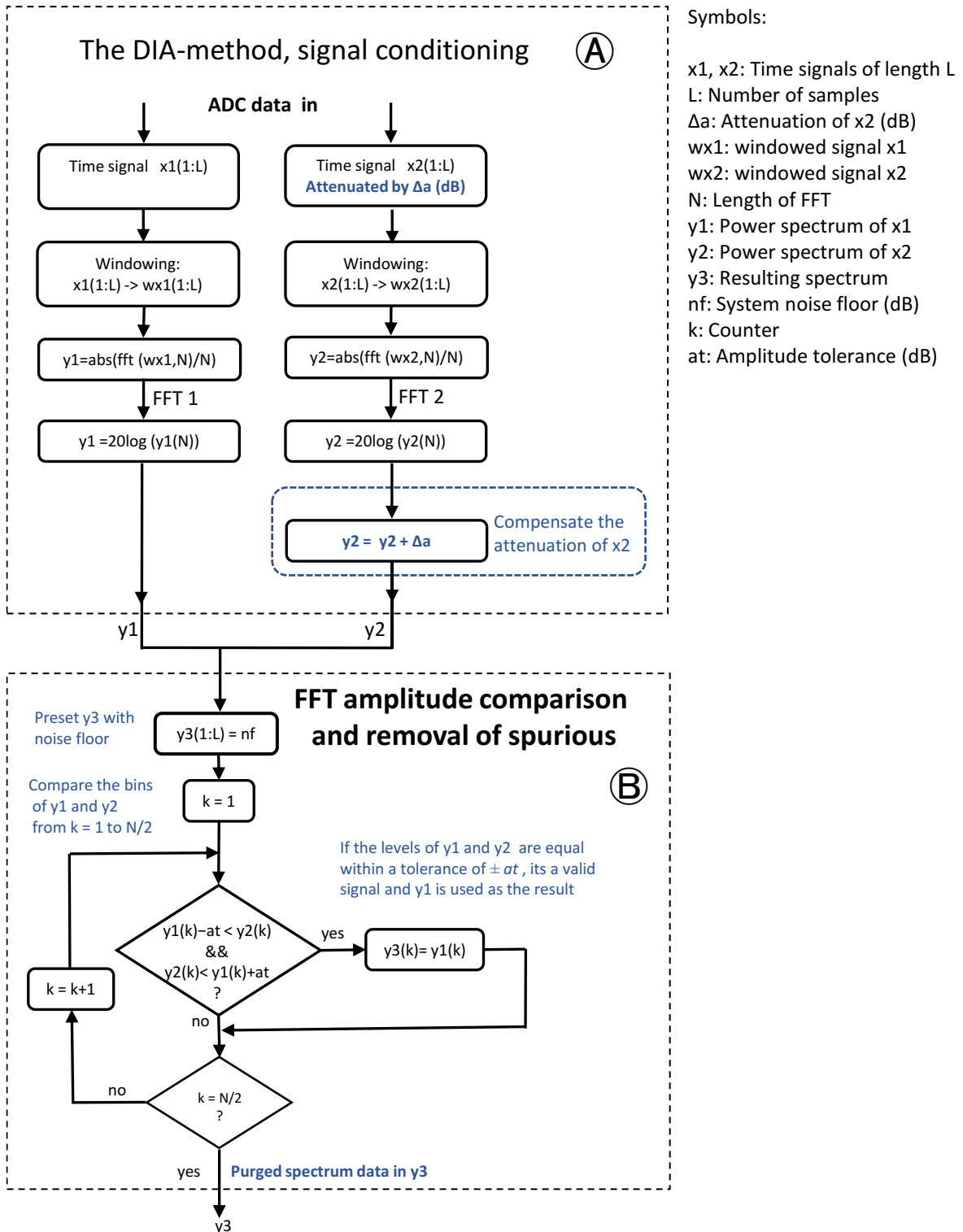


Fig. 6.11: The signal flow of the DIA-method.

6.4.2 Amplitude Difference for the DIA-Method

The necessary amplitude difference Δa between the two ADCs can be achieved either by amplification or attenuation in one of the signal paths. However, attenuation worsens the SNR, and amplification creates the potential risk of overdriving the ADC. In any case, the usable dynamic range is reduced by the amount of the chosen amplitude difference. It is, therefore, desirable to keep the difference as small as possible. On the other hand, a more significant variation has a more pronounced effect on the distortion products. For example, an amplitude difference of 1 dB results in a difference of 3 dB for the IM3 products. This expected amplitude difference of the spurs determines the required measurement accuracy. Section 5.5 shows that a measurement accuracy of ± 0.5 dB is about the best one can expect from the FFT approach. In addition, amplitude errors of the ADCs and differences in the RF paths must be taken into account, which can be estimated to be on the order of 2 dB or more. Therefore, an amplitude variation of 1 dB, resulting in a 3 dB IMD3 difference, should theoretically be sufficient for reliable operation. In the experiments performed in Chapter 7.2.3, an attenuation of 3 dB worked well, providing enough safety margin.

Possible errors in the frequency measurement are not decisive since these are the same in both ADCs and cancel each other out when compared.

6.4.3 Effectiveness and Limitations of the DIA-Method

The DIA method is based on amplitude measurements to detect the over-proportional growth of the distortion products with increasing signal amplitude. However, it became clear in Section 3.1 that ADCs behave fundamentally differently from analog systems, and the IMD level does not always follow a strict quadratic or cubic law. Therefore, the DIA-method may not work well for digital sampling systems using high-speed ADCs. For better classification, a series of spurious measurements are carried out with an AD9213 using the test bench from [7]. The results are summarized and plotted in Fig. 6.12.

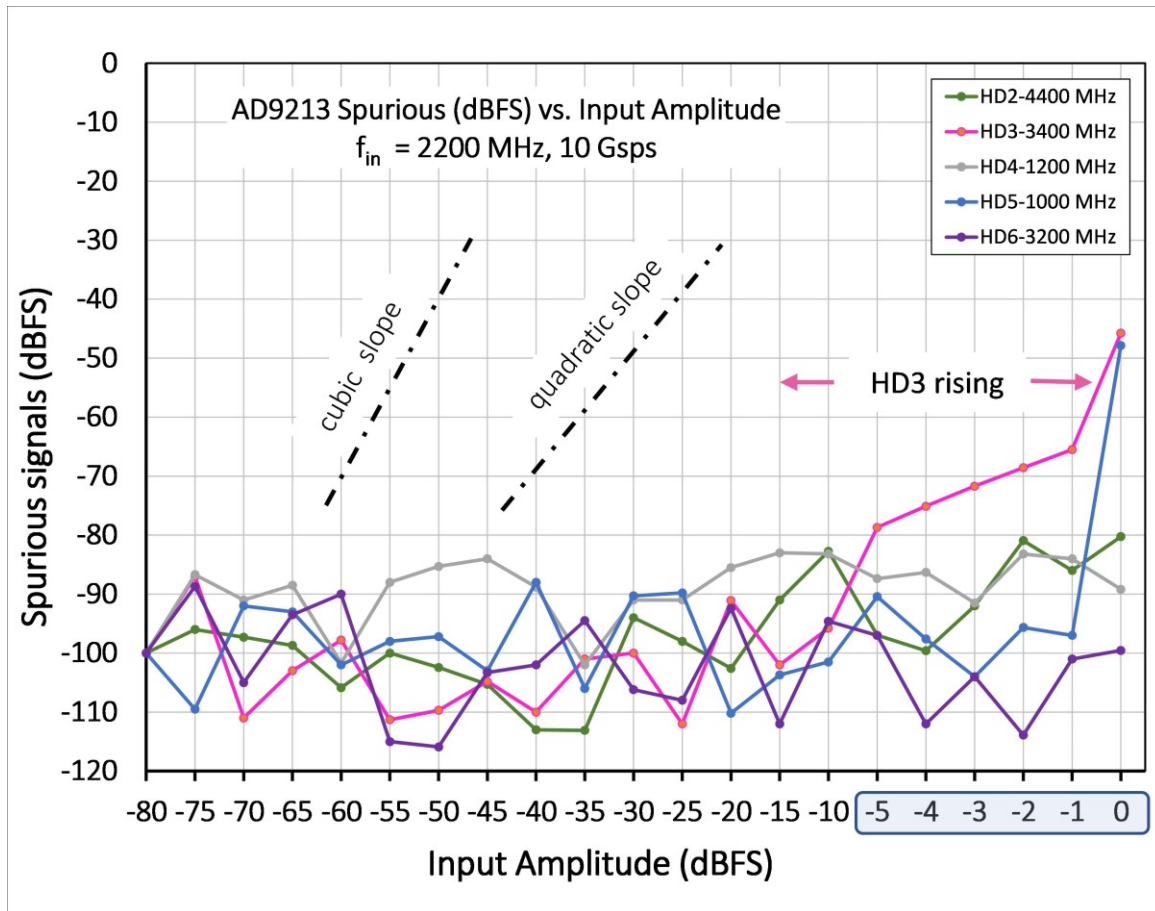


Fig. 6.12: The HD2 to HD6 spurious signals of an AD9213 vs. input amplitude measured with [7]. The signal frequency is 2.2 GHz, the sampling frequency is 10 GHz. For enhanced resolution, the scale from -5 dBFS to 0 dBFS is stretched to 1 dB steps.

All major distortion products remain approximately constant over a wide range of input values. Only the HD3 distortion increases monotonically from about -15 dBFS upwards. Therefore, the effectiveness of the DIA-method is doubtful for small signal levels, at least for the ADC technology considered here. For levels above -15 dB and the HD3 distortion, it might work. If nonlinear amplifiers or mixers cause noticeable distortion products before the sampling stage, the method can still be helpful since these tend to behave more according to the textbook. Further experimental verification of the DIA-method using actual ADCs is presented in Section 7.2.

Another conclusion that emerges from the measurements is that a direct RF-sampling receiver using this type of A/D converter should use some form of level control to feed a large enough signal to the ADC to maximize its dynamic range.

6.5 Boundary Conditions for Spurious Mitigation

The methods described in Section 6.2 to Section 6.4 are subject to the following boundary conditions:

1. The methods assume identical desired signals in the spectra to be compared. Therefore, the two ADC approach has an advantage over the one ADC approach for frequency agile signals. The two parallel ADCs must be synchronized to sample the signals at the same time instant.
2. Using two separate ADCs with very different characteristics would result in unequal distortion products, which are difficult to identify by spectral comparison. This is best avoided with a dual-channel ADC, where both devices are implemented on the same chip to ensure a high degree of uniformity of the A/D transfer characteristics.
3. The A/D conversion parameters should only be changed to such an extent that a clearly discernible effect is achieved on the spurious signals. If the amplitude or frequency changes are too extensive, the ADC's current working range might be left. As a result, difficult to predict influences on the amplitude non-linearities or the frequency response of an ADC may occur. A comparison of the two spectra would then no longer make sense.
4. The resolution of the FFT and the window function must be selected in such a way that a clear differentiation of the spectral lines is possible. Furthermore, unavoidable frequency and amplitude errors must be taken into account by using tolerance windows in subsequent signal processing.

7 Evaluation of the Spurious Suppression Methods

In this Chapter, the developed methods are examined for their effectiveness using simulations and practical experiments with signal generators and antenna signals to answer the following questions:

1. How much suppression of spurious signals can be achieved?
2. Which method is suited best to suppress a particular type of spurious signals (alias, harmonics, intermodulation)?
3. Can the methods also remove fast-changing, modulated broadband signals?
4. What is the influence of the methods on the SFDR and the system noise figure?
5. What are the limitations of the methods?

7.1 Computer Simulations

All three methods are first implemented as simulations using [©]MATLAB. The signals used for the simulations are distorted and undistorted sinusoidal signals, with and without modulation. The description of the working principles is based on the MATLAB syntax. All simulations are performed with a signal length of 2^{16} . For better comparison with the results of the practical tests described in Section 7.2., sampling frequencies in the range of 100 MHz are used. The difference between the sampling frequencies of 100 MHz and 103 MHz was deliberately chosen to be very large (3 MHz) in order to make the influence of the sampling frequency on the spurious signals more visible. Based on the theoretical considerations in Chapter 6, one can assume that the methods will work for simple sinusoidal signals. For this reason, additional signal scenarios are chosen, intended to show the limitations of the methods better. These are, for example, modulated signals or frequency combinations that overlap or do not permit a simple escape strategy when shifting the input frequency or the frequency of the sampling clock.

7.1.1 Signal Generation

Testing the methods with simulations requires a suitable signal scenario. This scenario is created by adding one or more time-sampled sinusoidal signals with selectable frequencies and

amplitudes. The resulting signal can either be distorted by a non-linear amplifier or band-limited with a low-pass filter. Fig. 7.1 shows the basic signal flow and the computation of the test signals.

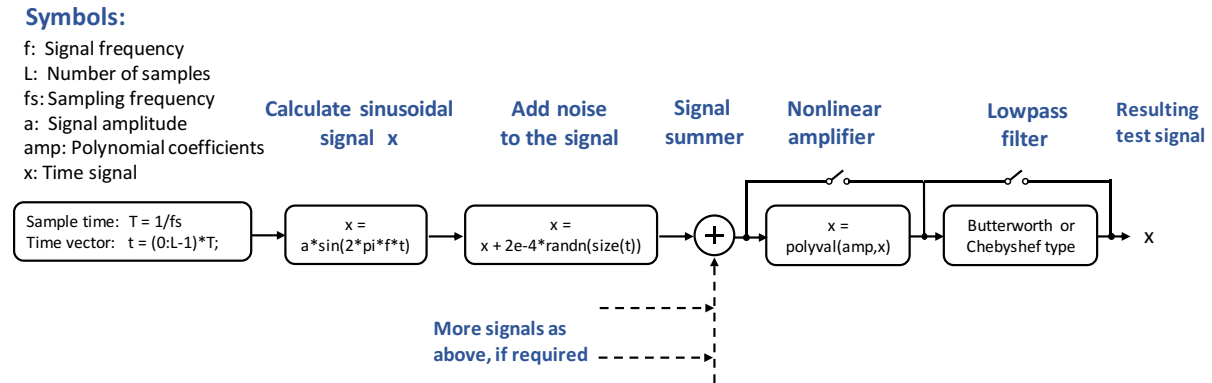


Fig. 7.1: The signal flow for generating a multi-tone signal scenario using MATLAB.

A sinusoidal function is used to calculate amplitude samples at time intervals of the sampling rate. Some noise is superimposed on the signal to limit the dynamic range to about 110 dB. This noise level achieves a display range similar to a practical receiver. If needed, the signal can be optionally passed through a nonlinear amplifier to create harmonic and intermodulation distortion. The signal can be bandlimited by an n-term Butterworth or Chebyshev lowpass filter. The result is a real-valued data block of the length L, stored in the vector x. It contains the time samples of a noisy, distorted, lowpass filtered sinusoidal signal f_s sampled with frequency f_s . Several such signals with randomly varying amplitude, frequency, and phase are generated and summed up for multitone testing.

The test signal algorithm is verified by generating an undistorted, noisy, low-pass filtered two-tone signal. It is analyzed with MATLAB's function "*dsp.SpectrumAnalyzer*" [96]. The resulting spectral plot is shown in Fig. 7.2. The frequencies and levels are as expected. The amplitude roll-off at ≈ 50 MHz is due to the low-pass filter. The visual representation shows the expected two-tone spectrum free of distortion. The test signal algorithm is therefore considered suitable for the following tests.

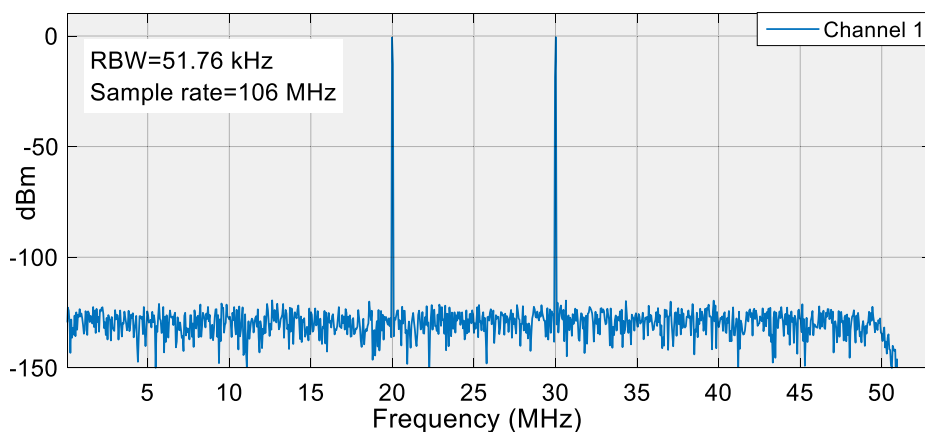


Fig. 7.2: A two-tone 0 dBm test signal at 20 MHz and 30 MHz, analyzed with MATLAB's spectrum analyzer function. The signal is passed through a 6-pass Butterworth low-pass filter with a cutoff frequency of 50 MHz. Frequencies and levels of the test signal appear as expected.

7.1.2 Simulation of the DSF-Method

The following simulations of the DSF-method assume a setup with two separate ADCs sampling the signal with a frequency of 100 MHz in the reference channel (FFT1) and 103 MHz in the second channel (FFT2). The alias detection threshold (adt) is set to 3 dB.

a) DSF-method simulation with a three-tone signal:

This simulation uses a three-tone signal with an unfavorable frequency combination. The characteristics of the test signal are as follows:

Signals	Frequency (MHz)	Level (dBm)	Modulation	Distortion	AAF
f1	30	0	no	yes	no
f2	10	-95	no	no	no
f3	43	-95	no	no	no

Since no anti-aliasing filter (AAF) is used, this oversampling scenario provokes alias generation. The frequencies are chosen in such a way that a worst-case scenario results. With the given sampling frequencies, strong HD2 and HD3 aliases of the 30 MHz signal exist at 10 MHz and 43 MHz. These always fall on top of one of the weak signals no matter which of the two sampling frequencies is used. This circumstance is not very likely in a real-world scenario but may sometimes happen in a congested RF environment. Spectrum plots of the four relevant spectra are shown in Fig. 7.3.

The sequence of the workflow is *clockwise* from Fig. 7.3 (a) to (d). In order to better compare the original spectrum (a) with the result (d), these were arranged on top of each other.

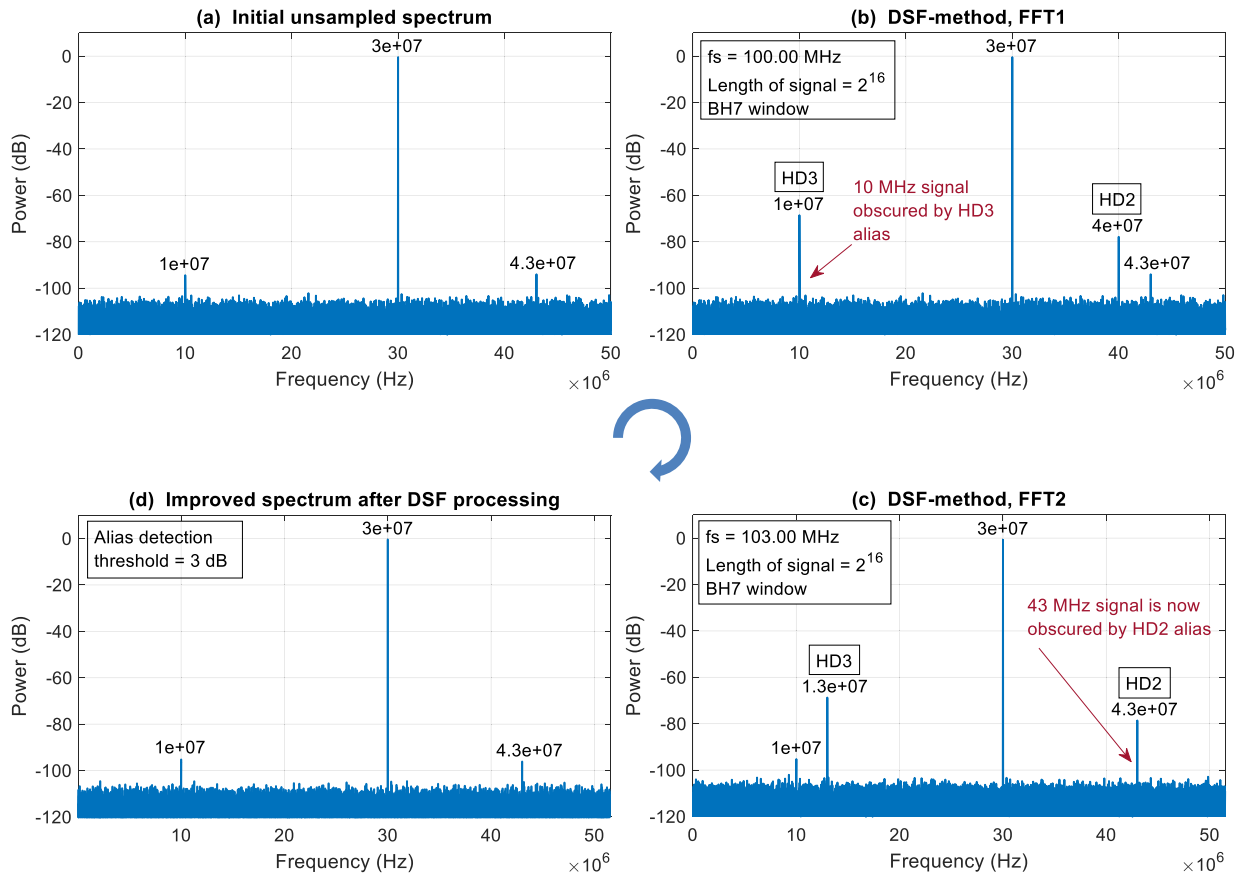


Fig. 7.3: DSF-method simulation with a three-tone sinusoidal signal;
 (a) Visualisation of the test signals f_1 , f_2 , and f_3 in the frequency domain,
 (b) Test signals sampled with 100 MHz,
 (c) Test signals sampled with 103 MHz,
 (d) Improved spectrum after DSF processing with removed aliases.

Fig. 7.3 (a) illustrates the unsampled three-ton test signal on the frequency axis. The spectrum of this signal, sampled with 100 MHz, is depicted in Fig. 7.3 (b). The strong HD3 alias at 10 MHz obscures the desired signal, which is also at 10 MHz. Fig. 7.3(c) shows the same signal sampled with 103 MHz. Now the desired signal at 43 MHz is obscured by a strong HD2 alias. The improved spectrum after DSF processing is shown in Fig. 7.3 (d). Comparing Fig. 7.3 (a) with Fig. 7.3 (d) shows that the aliases resulting from the sampling process can be completely removed. The small, desired signals at 10 MHz and 43 MHz are recovered, although their frequencies are chosen very unfavorably. It can be stated that the DSF method can effectively remove alias signals and recover desired signals previously masked by an alias.

b) DSF-method simulation with a broadband FM signal:

The test is performed with a 30.5 MHz broadband FM signal with a frequency deviation of 500 kHz, modulated with 10 kHz, passed through a nonlinear amplifier. The sampling frequencies are again 100 MHz and 103 MHz. The test signal has the following characteristics:

Signal	Frequency (MHz)	Level (dBm)	Modulation	Distortion	AAF
f1	30.5	0	FM	yes	no

According to Carson's bandwidth rule [97], this creates a ≈ 1 MHz wide signal that ranges from 30 MHz to 31 MHz and thus occupies $\approx 2\%$ of the Nyquist bandwidth. The plots of the four relevant spectra are shown in Fig. 7.4 below. The ≈ 2 MHz and ≈ 3 MHz wide alias frequency bands visible in Fig. 7.4 (b) result from nonlinear distortion and the absence of an anti-aliasing filter.

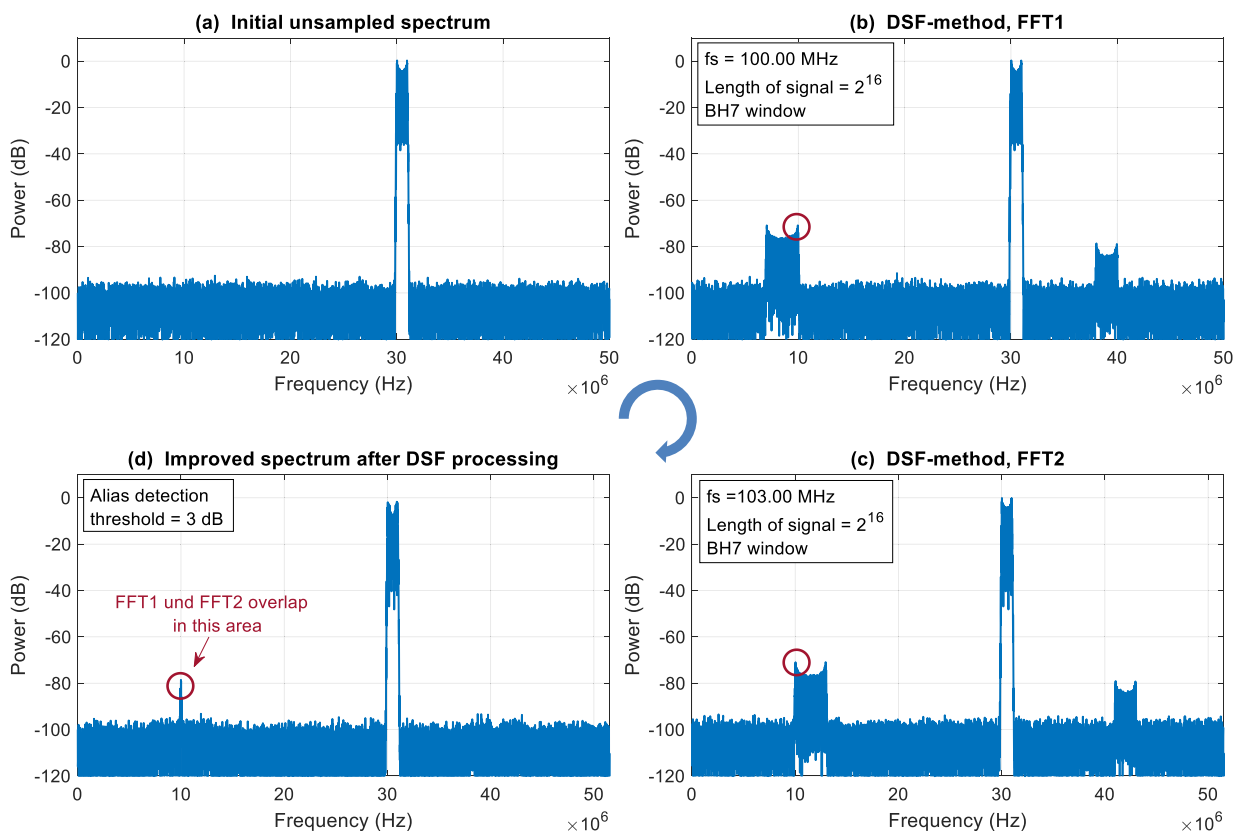


Fig. 7.4: DSF-method simulation with a distorted 30.5 MHz broadband FM signal;
 (a) Visualisation of the test signal f1 in the frequency domain,
 (b) FFT of the signal sampled with 100 MHz,
 (c) FFT of the signal sampled with 103 MHz,
 (d) Improved spectrum after processing with the DSF-method.

Fig. 7.4 (d) shows the improved spectrum with a remaining artifact at 10 MHz which is not entirely suppressed. It is caused by the slight overlap of the HD3 alias frequency bands in FFT1 and FFT2 at 10 MHz, indicated by the red circles. The 3 MHz difference of the sampling frequencies is insufficient to separate the slightly more than three megahertz wide HD3 alias bands. This simulation shows that the frequency shift for the DSF-method must be large enough to separate the possible aliases of broadband signals.

7.1.3 Simulation of the DIF-Method

The following DIF-method simulations are performed with a sampling frequency of 100 MHz for both analog signals and a bin up-shift of 600 bins, corresponding to a frequency shift of $\Delta f = 600 \times 10^8 \times 2^{16} = 915527$ Hz for the second channel.

a) DIF-method simulation with a two-tone signal:

A distorted two-tone signal is passed through a nonlinear amplifier. An anti-aliasing filter is omitted to provoke aliasing. The characteristics of the test signals f1 and f2 are as follows:

Signals	Frequency (MHz)	Level (dBm)	Modulation	Distortion	AAF
f1	15	0	no	yes	no
f2	16	0	no	yes	no

Spectrum plots of the four spectra of the DIF-method are presented in Fig. 7.5 (a) to (d). Fig. 7.5 (b) shows various IM-products, harmonics, and aliases resulting from nonlinear distortion and the sampling process. The resulting spectrum after processing with the DIF-method is depicted in Fig. 7.5 (d). It is considerably cleaner, but as expected, the close-in IMD3 products are still visible.

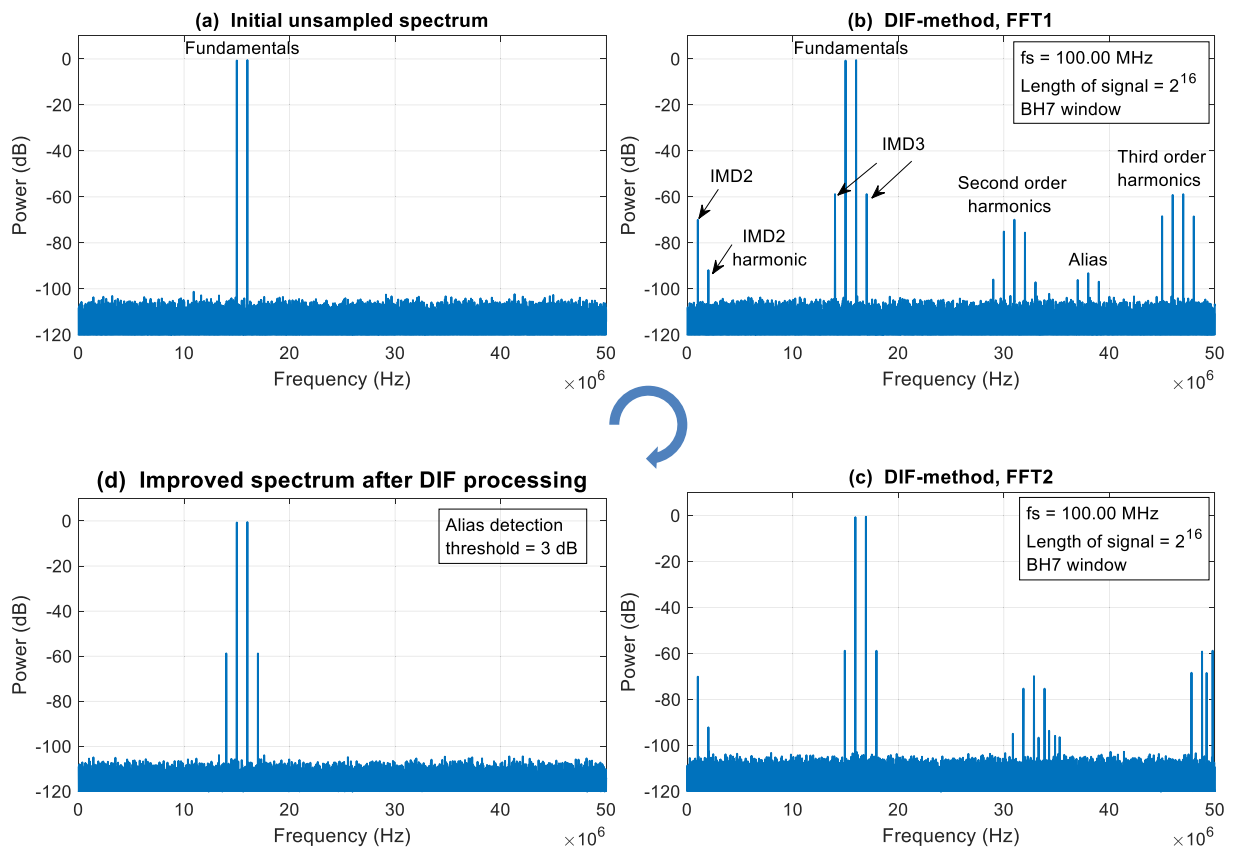


Fig. 7.5: DIF-method simulation with a distorted two-tone signal;
 (a) Visualisation of the test signals f_1 and f_2 in the frequency domain,
 (b) FFT1 of the sampled signal, showing intermodulation, harmonics, and alias frequencies,
 (c) FFT2 of the signal upshifted by 600 bins resp. 915527 Hz and sampled again,
 (d) Improved spectrum after processing with the DIF-method. IMD3 is not removed.

The DIF-method is well suited to remove all kinds of alias signals which result from violating the sampling theorem. It is not relevant whether the signals are externally fed or caused by ADC internal distortion. However, odd-order intermodulation products cannot be detected and removed for reasons outlined in Subsection 6.3.2. It also does not work with undersampling architectures because it suppresses the required alias signals.

For a better understanding and visualization of the previous simulations, the spectrum of the unsampled test signal and a plot of the FFT2 was shown. For reasons of space, these two graphs are not shown for further simulations since these only represent the defined signals graphically and do not provide relevant, additional information.

b) DIF-method simulation with a broadband FM signal:

This simulation is performed using a 30.5 MHz broadband FM signal with a frequency deviation of 500 kHz, modulated with 10 kHz, passed through a nonlinear amplifier. The resulting 1 MHz wide test signal has the following characteristics:

Signal	Frequency (MHz)	Level (dBm)	Modulation	Distortion	AAF
f1	30.5	0	FM	yes	no

Fig. 7.6 shows the sampled broadband FM signal and the resulting spectrum plots.

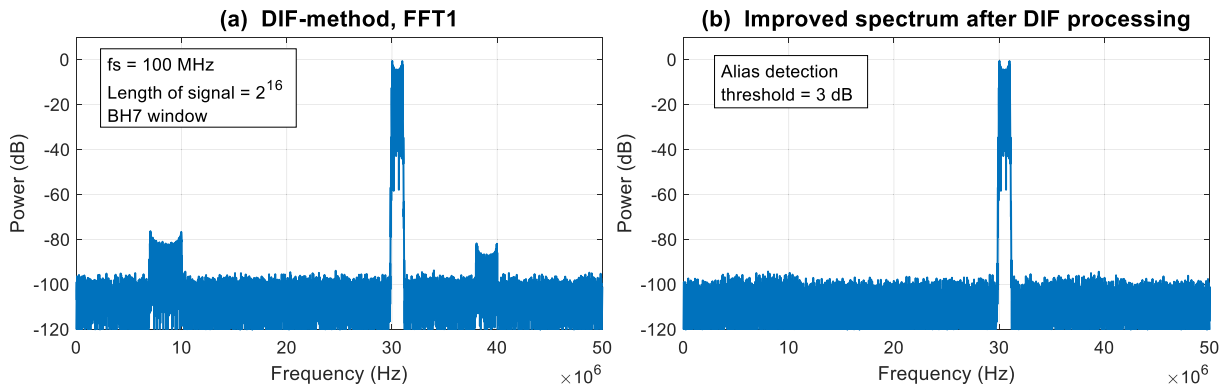


Fig. 7.6: DIF-method simulation with a 1 MHz wide 30.5 MHz broadband FM signal;
 (a) FFT of the sampled signal,
 (b) Improved spectrum after processing with the DIF-method.

The alias frequency bands are successfully removed. The DIF-method works well for narrow- and broadband signals as long as the interfering frequency bands in FFT1 and FFT2 do not overlap. Similar to the DSF-method, for very broad band signals, the frequency shift must be large enough to separate signal components suppress alias frequencies successfully.

7.1.4 Simulation of the DIA-Method

The following simulations of the DIA method are performed with a 3 dB attenuation in the second channel and a nonlinear amplifier to roughly simulate the distortion of the test signals by an ADC. The distortion characteristics of a real ADC are similar but, in practice, depending on its operating principle and the hardware implementation of the device.

a) DIA-method simulation with a two-tone signal:

First, a distorted two-tone signal is used to determine if IMD3 products and harmonics can be successfully suppressed. The characteristics of the test signal are as follows:

Signals	Frequency (MHz)	Level (dBm)	Modulation	Distortion	AAF
f1	15	0	no	yes	no
f2	16	0	no	yes	no

The resulting spectrum of the sampled two-tone signal is depicted in Fig. 7.7 below.

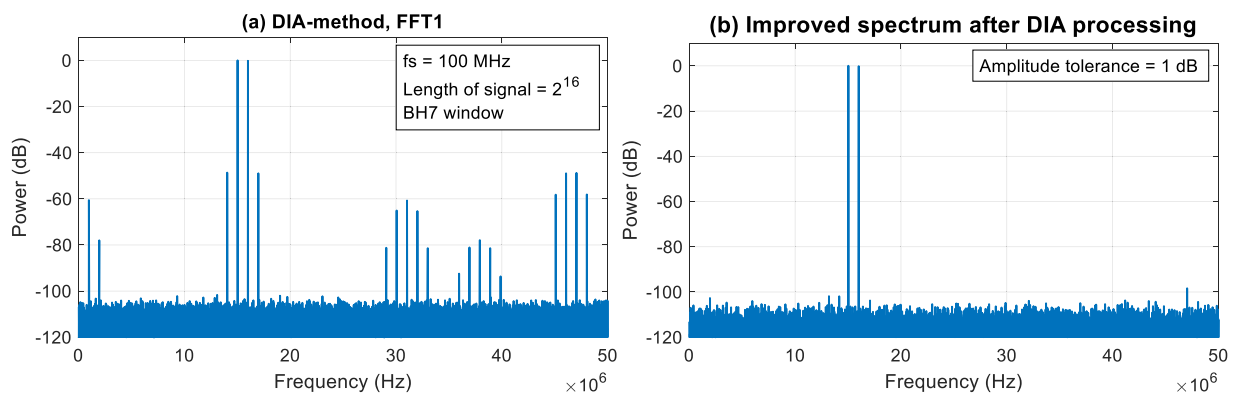


Fig. 7.7: DIA-method simulation of a distorted two-tone signal at 15 MHz and 16 MHz;
 (a) FFT of the sampled signal, showing intermodulation, harmonics, and alias frequencies,
 (b) Improved spectrum after processing with the DIA-method.

The improved spectrum in Fig. 7.7 (b) shows that the DIA-method can successfully remove the IMD3 products and all harmonic signals resulting from a non-linear analog system.

b) DIA-method simulation, undersampling of a two-tone signal:

A distorted two-tone signal positioned in the second Nyquist zone is used to simulate an under-sampling scenario. The characteristics of the test signals are as follows:

Signals	Frequency (MHz)	Level (dBm)	Modulation	Distortion	AAF
f1	65	0	no	yes	no
f2	66	0	no	yes	no

With a sampling frequency of 100 MHz, the wanted signals are expected to appear in the first Nyquist zone at 35 MHz and 34 MHz. Figure 7.8 (a) shows that this is the case and depicts the two-tone signal and its alias and distortion products in the first Nyquist zone. The resulting spectrum after DIA-processing is shown in Fig. 7.8 (b).

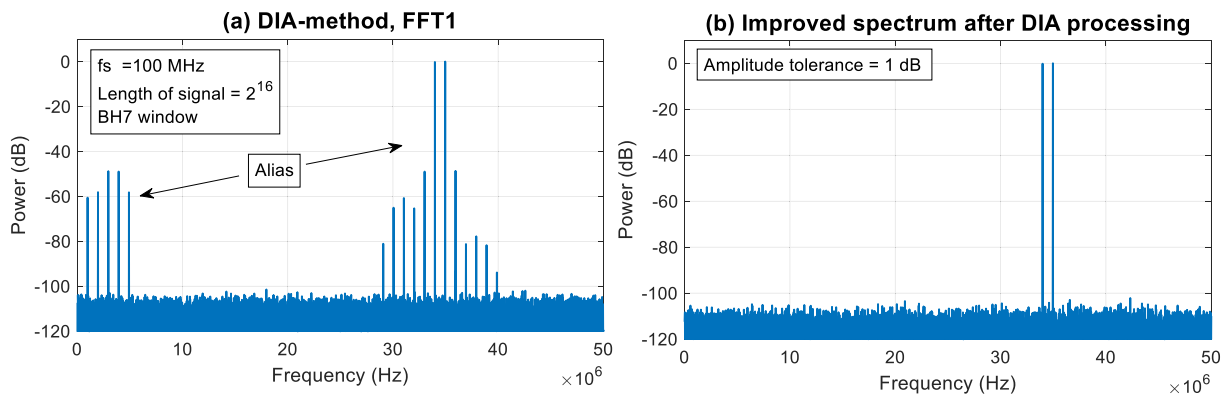


Fig. 7.8: DIA-method, simulating undersampling of a distorted two-tone signal (65 MHz and 66 MHz);
 (a) Initial spectrum and
 (b) Improved spectrum after processing with the DIA-method.

The DIA-method is effective in detecting and removing higher-order distortion and odd-order intermodulation. It also works for undersampling applications.

c) DIA-method simulation with a broadband FM signal:

A 2 MHz wide modulated 10 MHz FM signal is passed through a nonlinear amplifier to provoke harmonics. The characteristics of the test signal are as follows:

Signal	Frequency (MHz)	Level (dBm)	Modulation	Distortion	AAF
f1	10	0	FM	yes	no

Fig. 7.9 (a) shows the sampled broadband FM signal, and Fig. 7.9 (b) depicts the resulting spectrum after DIA-processing.

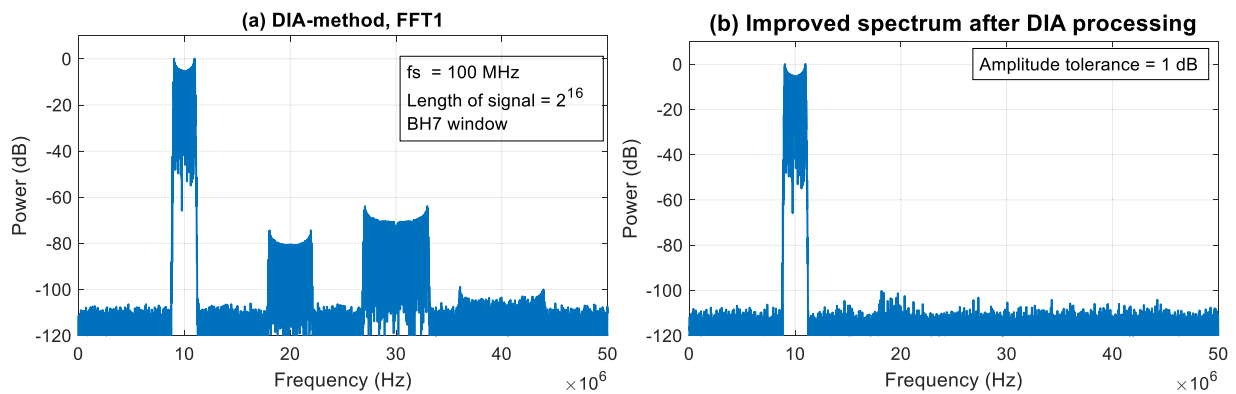


Fig. 7.9: DIA-method simulation with a distorted 2 MHz broad 10 MHz FM signal;
 (a) FM signal and its harmonics centered around 20 MHz, 30 MHz, and 40 MHz,
 (b) Improved spectrum after DIA-processing.

In this simulation, the DIA-method can remove most of the harmonic distortion of a broadband FM signal. However, some artifacts below -100 dB around 18 MHz can still be seen. These can be mitigated either by increasing the FFT resolution to, for example, 2^{18} points, which results in better frequency selectivity and thus better suppression for neighboring frequencies. Another possibility is to increase Δa to, e.g., 6 dB which leads to a more pronounced amplitude variation of the distortion products, which are then easier to distinguish and suppress. Such an improvement would either be associated with a longer processing time for the FFT or a higher noise figure of the system due to the increased attenuation.

It can be concluded that the DIA-method works very well in the simulations for all types of nonlinear distortion. However, since the amplitude distortion depends on the ADCs, it is difficult to predict to what extent these simulations can be transferred to practice. Therefore the DIA-method is further investigated experimentally with actual ADCs in Sections 7.2 and 7.3.

7.1.5 Dense Spectrum Simulation

As frequency selectivity of the FFT has turned out to be a performance-critical parameter, a heavy load simulation using the DIF-method is presented in Fig. 7.10. The goal is to generate a densely populated frequency spectrum and determine how many random signals the FFT can resolve and whether signals are lost by processing with the DIF method. The signals are generated with random amplitudes from -80 dBm to -3 dBm, frequencies from 0.1 MHz to 50 MHz, and phase angles from 0 to 359 degrees. After DIF-processing, all spectral lines in the resulting FFT with a level > -85 dB are counted with the help of a level detection algorithm [98] and compared to the number of input signals. The difference is a measure of the FFT's ability to resolve individual frequencies in a congested signal environment. The selectivity expressed as the -6 dB bandwidth of the Blackman-Harris 7 window can be calculated by using the values from Table 5.1. In the following simulation, the bandwidth is equal to $2 \times 3.52 \times 106 \text{ MHz} / 2^{18} \approx 2.85 \text{ kHz}$. A simulation with 4500 randomly generated signals with a spacing of at least 10 kHz shows that all signals can be successfully resolved and recovered after processing with the DIF-method.

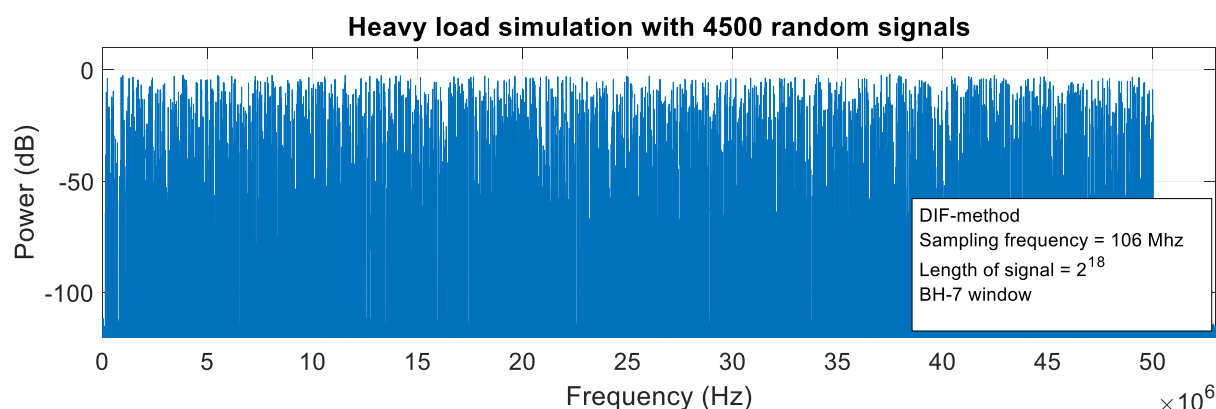


Fig. 7.10: FFT of 4500 simulated random sinusoidal signals with a spacing of $\geq 10 \text{ kHz}$ sampled with 106 MHz . The FFT length is 2^{18} . The time signal is windowed with a BH-7 window.

If the restriction of a minimum distance of 10 kHz is removed and the number of random signals is steadily increased, more and more are lost from 200 signals upwards. Fig. 7.11 shows the ratio of detected signals versus the number of input signals in percent. With 1000 signals, the detection rate is reduced to about 95% and falls to approximately 75% for 10 000 signals.

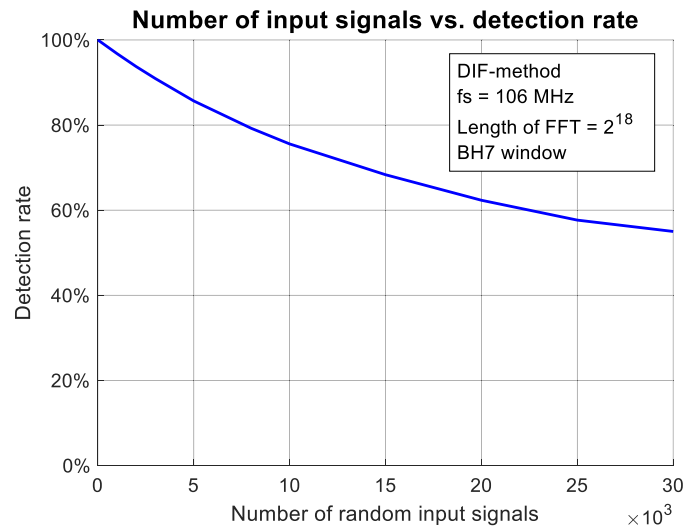


Fig. 7.11: Detection rate of an FFT as a function of the number of randomly generated sinusoidal signals with no minimum frequency spacing. The simulation is performed using the DIF- algorithm with the parameters denoted in the legend.

The reason for this is that as the number of signals randomly populating a limited frequency range increases, more and more signals occasionally fall on top of each other in the same FFT bin. Saturating the spectrum with random frequencies reduces the probability of accurately resolving the individual signals with an FFT. This behavior is not different from multi-channel analog receivers with conventional IF filtering because it too cannot distinguish between adjacent signals that fall in the same communication channel. The loss of signals is primarily caused by the limited frequency resolution of the FFT. This circumstance must be taken into account when using the spurious suppression methods in very dense spectra. Signals that are superimposed in the same channel cannot be separated.

7.2 Laboratory Tests

This Section aims to determine if practical measurements with actual ADCs match the simulation results in a laboratory environment and how effective the spurious suppression works in practice. For this purpose, measurements are performed with signals from RF generators. In addition, it will be investigated if there are any disturbing side effects resulting from the practical implementation.

Since the spurious suppression is performed in the digital domain using the sampled time signals, the working principle is independent of the absolute sampling frequency. Therefore, the test setup is scaled down from the intended 10 GHz range by a factor of 100. In this way, all signals are shifted to the 100 MHz range, where affordable measurement equipment and A/D converter boards are available without compromising the experimental results. The SFDR and SNR specifications of the 100 MHz ADCs were deliberately chosen to be worse than the state-of-the-art would allow. In this way, the reduced SFDR and SNR data of a current GSPS ADCs can be better represented with an ADC working in the 100 MHz range that would otherwise be “too good”. With such non-optimal ADCs, the spurious reduction methods can be demonstrated more clearly. Two ‘Red Pitaya STEM LAB 125-10’ digitizer boards [99] shown in Fig. 7.12 are used for the measurements. The A/D part consists of a dual-channel AD9608 ADC [100], a ‘Xilinx Zynq SoC’ with FPGA, and other building blocks as indicated in Fig. 7.13.

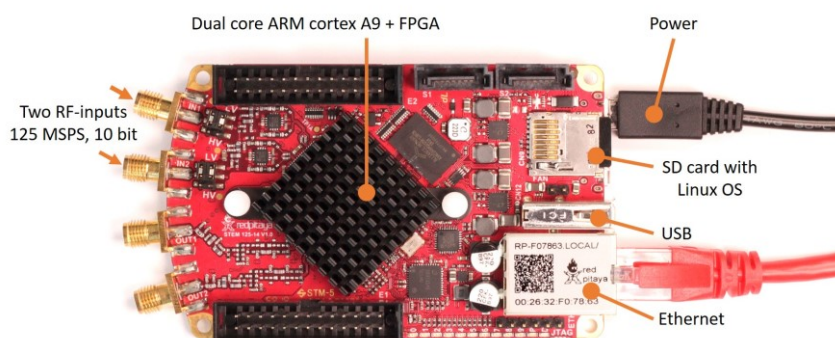


Fig. 7.12: The STEM LAB 125-10 board [99]. The picture was taken from [101] and annotated.

The analog input bandwidth of the AD9608 is 650 MHz; it has a resolution of 10-bit and a maximum sampling rate of 125 MSPS. The SNR is ≈ 62 dBFS, and the SFDR is ≈ 85 dBc.

The corresponding specifications of an AD9213 GSPS ADC are ≈ 56 dBFS for the SNR and ≈ 72 dB for the SFDR. Thus, despite the sampling frequencies differing by a factor of 100, there is rough equality of these ADC data. Interestingly, the price also differs by a factor of 100.

For this dissertation work, two STEM LAB 125-10 boards were mounted in an aluminum housing. The original 125 MHz sampling frequency was modified by replacing the clock oscillators with ones that work at 106 MHz and 106.25 MHz [102]. Thus, experiments with the DSF-method and a sampling frequency difference of 250 kHz are possible. An attempt to feed the boards with clocks from external signal generators was abandoned because too much noise was coupled into the ADCs, generating unwanted signals in the output spectrum. The simplified schematic in Fig. 7.13 shows that the test signals are fed to the four ADCs either via a signal combiner (connector “IN”) or separately. The digitizer boards are interfaced to a personal computer (PC) via Ethernet (ETH) and a universal serial bus (USB) interface provided by a single-chip microcomputer. Time synchronous sampling of the ADCs can either be triggered via the USB interface from MATLAB or by a manual push button on the ADC enclosure.

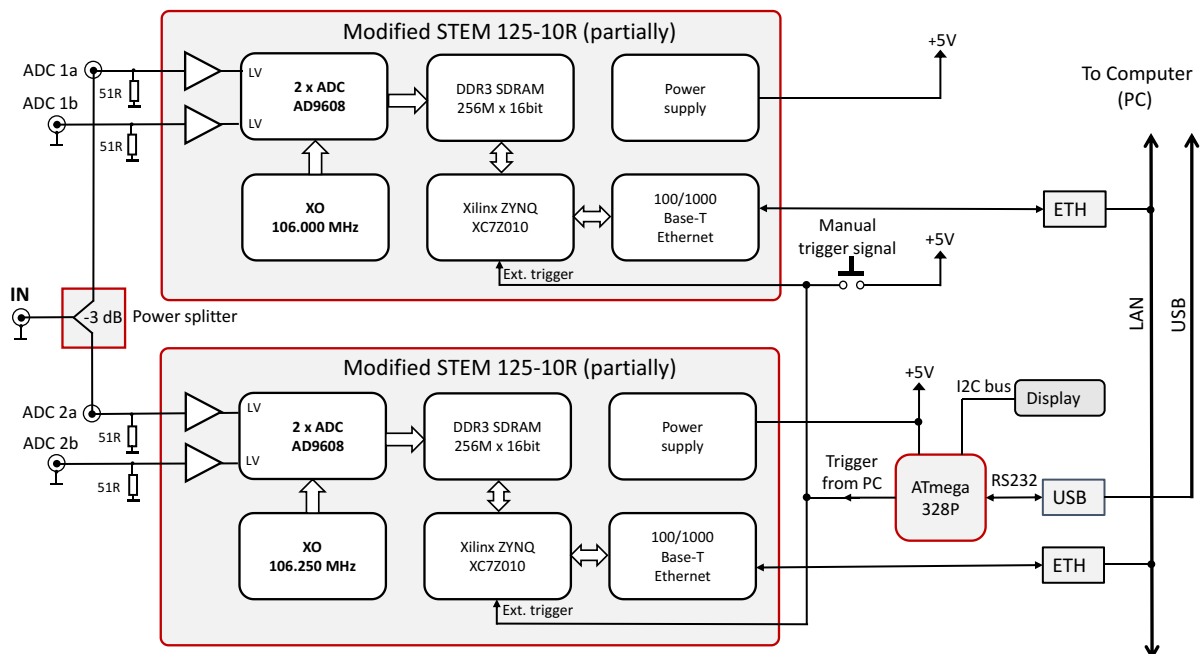


Fig. 7.13: Simplified schematic of the data acquisition setup with two STEM 125-10R boards. The clock oscillators are modified in frequency; the boards are interfaced to a PC via Ethernet and USB.

A photo of the test setup is shown in Fig. 7.14. Test signals are created with two RF generators and a two-channel arbitrary waveform generator by combining the signals with an 8-port power combiner. The signals are verified with a spectrum analyzer [103] and routed to the ADC housing with coaxial cables. The ADC boards are connected to a local area network which forwards the captured ADC data to the PC via an SCPI server application. Due to the buffer on the acquisition boards, the maximum number of ADC samples is limited to 2^{14} per trigger event. Signal processing for spurious reduction is performed in the PC using the MATLAB algorithms outlined in Chapter 6.

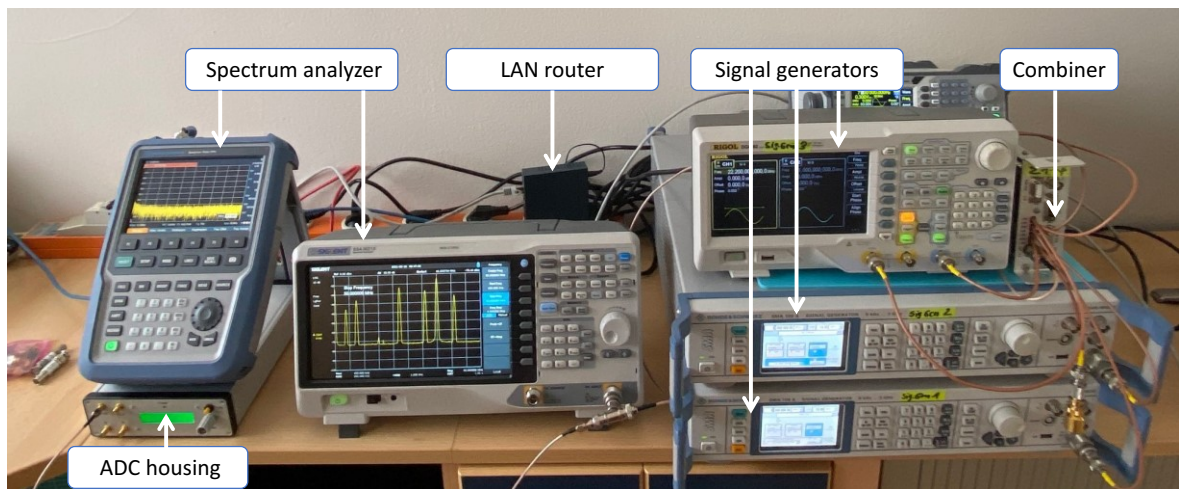


Fig. 7.14: Photograph of the testbench with the ADC housing and some measurement equipment.

7.2.1 Laboratory Test of the DSF-Method

The following tests are carried out with fixed sampling frequencies of 106 MHz and 106.25 MHz, an FFT length of 2^{14} , and a BH-7 window. The lowest operating frequency for this setup is determined using (6.2) and the minimum bin shift from Table 5.2.

$$f_{\min} = 2^{14} \times 2.6 / \left(\frac{1}{106} \text{ MHz} - \frac{1}{106.25} \text{ MHz} \right) \approx 7.14 \text{ MHz.}$$

This lower frequency limit is taken into account by selecting all test frequencies ≥ 16 MHz to ensure a sufficient safety margin for the DSF method. It should be noted that the ADC devices on the two ADC boards are from different production lots and therefore have some variation in level accuracy and distortion characteristics.

a) DSF-method test with a strong, distorted single tone signal:

The test signal is a strong, single-tone sinusoidal signal from a signal generator with some harmonic content. The characteristics are as follows:

Signal	Frequency (MHz)	Level (dBm)	Modulation	Harmonics	AAF
f1	16	≈ 0 dBm	no	< -60 dBm	no

Fig. 7.15 shows the test signal on a spectrum analyzer.

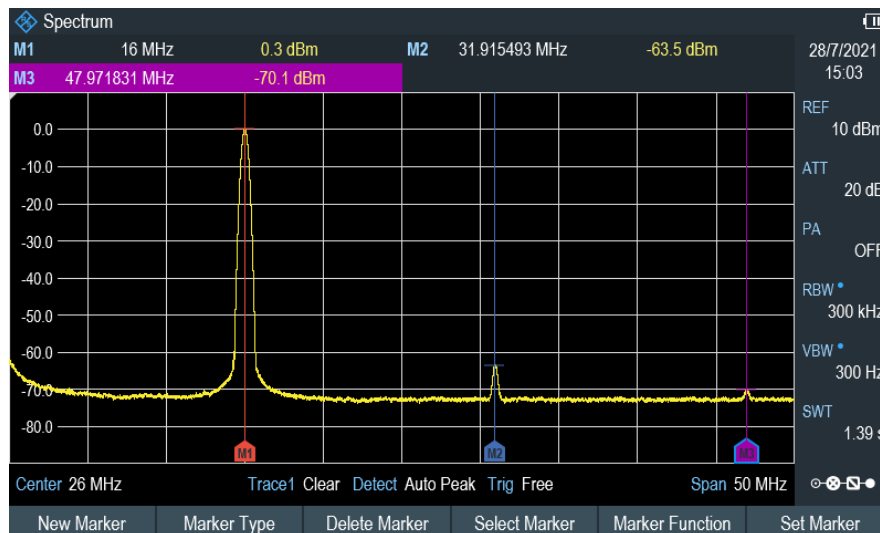


Fig. 7.15: Spectrum analyzer screenshot of the 16 MHz, 0 dBm test signal marked by M1.

The analyzer screenshot spans the first Nyquist zone up to 52 MHz. The fundamental of the generator signal is marked with M1; its harmonics are visible at 32 MHz (M2) and 48 MHz (M3). Fig. 7.16 (a) and Fig. 7.16 (b) show the FFTs of the test signal digitized by two AD9608 ADCs, sampling with 106 MHz and 106.25 MHz. Due to the strong 0 dBm signal, the A/D conversion increases the HD2 and HD3 harmonics and generates additional aliases.

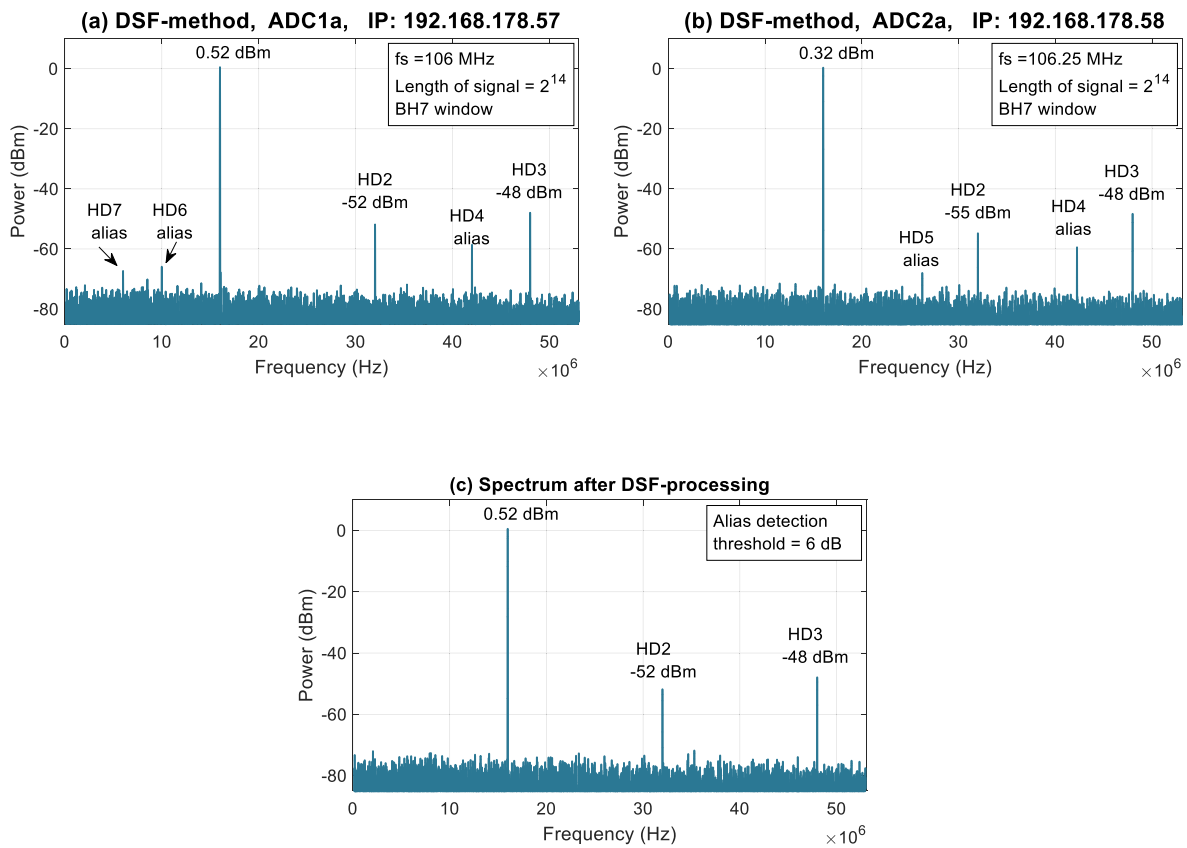


Fig. 7.16: DSF-method test with a 16 MHz signal sampled with;
 (a) 106 MHz,
 (b) 106.25 MHz,
 (c) Improved spectrum after DSF processing, alias signals are removed.

Comparing Fig. 7.16 (a) with Fig. 7.16 (b), it is noticeable that the amplitudes of the distortion products differ by several dB because the ADCs have manufacturing tolerances.

The resulting improved spectrum after DSF processing is shown in Fig. 7.16 (c). The harmonic distortion introduced by the ADC is still visible. This is to be expected since the DSF-method does not remove the harmonic distortion. However, all alias signals are completely removed and pushed into the noise floor.

b) DSF-method test with an unfavorable three-tone signal:

This test is performed with a three-tone signal comparable to the simulation in Subsection 7.1.2. It consists of two weak and one strong signal. The frequencies are chosen to create a worst-case scenario where the alias of the strong signal deliberately covers one of the weak desired signals. The characteristics of the test signals are as follows:

Signal	Frequency (MHz)	Level (dBm)	Modulation	Harmonics	AAF
f1	30	≈ 9	no	< -45 dBm	no
f2	46.25	≈ -60	no	no	no
f3	16	≈ -60	no	no	no

A spectrum analyzer screenshot of the combined test signals f1 to f3 taken at the input of the ADCs is shown in Fig. 7.17.

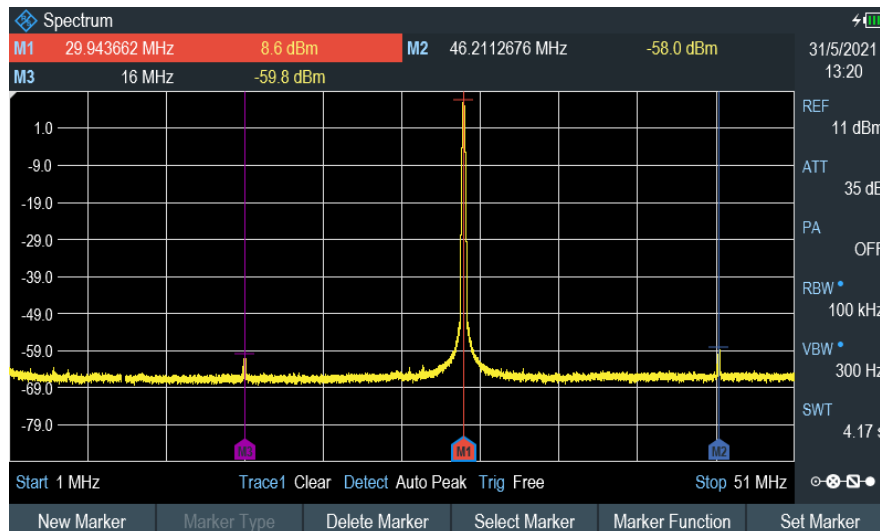


Fig. 7.17: Spectrum analyzer screenshot of the three-tone test signal. The markers indicate a strong signal at 30 MHz (M1) and two weak signals at 16 MHz (M3) and 46.25 MHz (M2).

Fig. 7.18 (a) shows the spectrum of the signals digitized with 106 MHz. The -44 dBm HD3 alias at 16 MHz covers the desired weak signal f3. Close to the desired signal f2, a -40 dBm HD2 alias resulting from the strong signal is visible at 46 MHz.

Fig. 7.18 (b) shows the spectrum of the signal sampled with 106.25 MHz. The HD2 alias now obscures the weak signal f2. The HD3 alias has moved to 16.25 MHz and uncovers the desired signal f3. The resulting, improved spectrum after DSF-processing is shown in Fig. 7.18 (c) below.

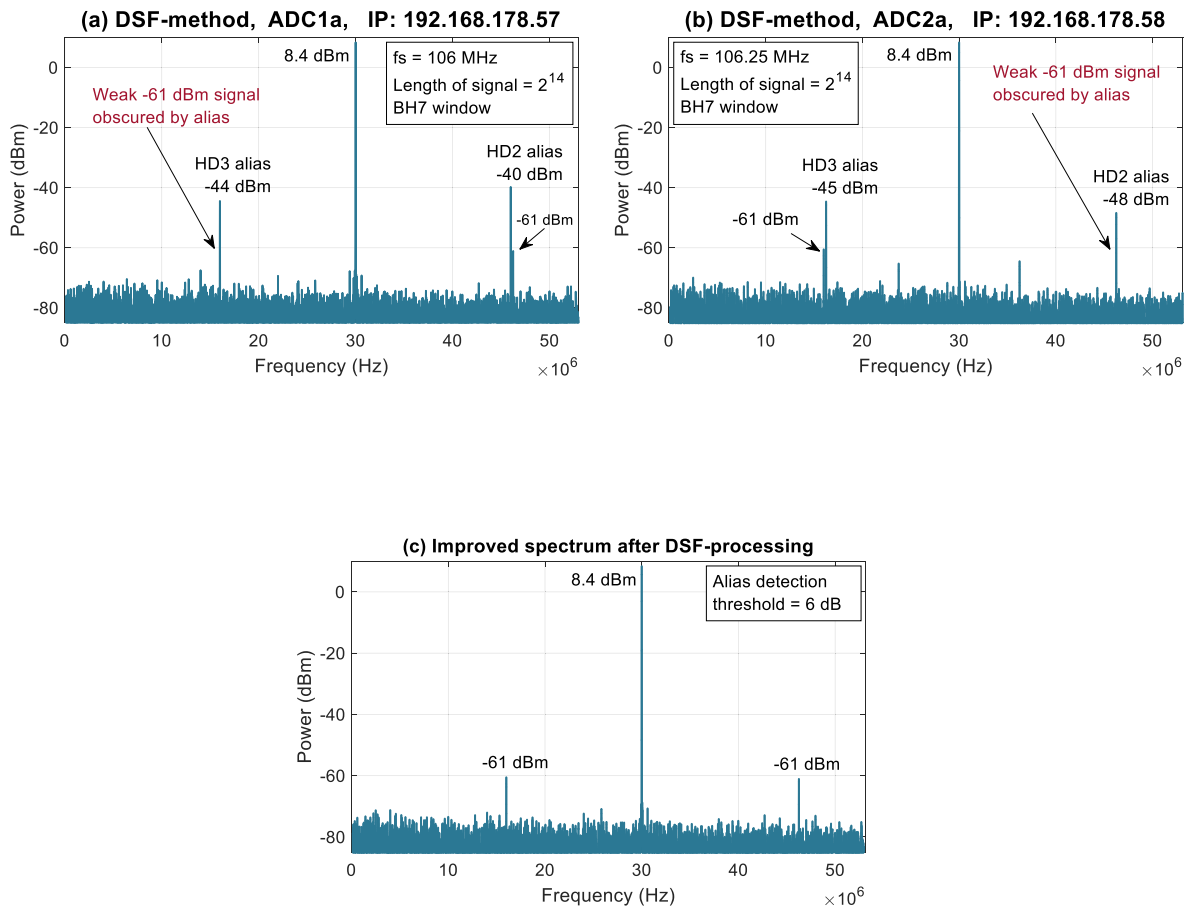


Fig. 7.18: DSF-method test with a three-tone signal sampled with;
 (a) 106 MHz,
 (b) 106.25 MHz,
 (c) Improved spectrum after DSF processing, the alias signals are removed.

The DSF-method successfully removes aliases of a single carrier and uncovers weak signals previously not visible. The suppression of alias signals when comparing Fig. 7.18 (a) with Fig. 7.18 (c) is at least 30 dB.

c) DSF-method test with a broadband FM signal:

The test signal is a 30.5 MHz FM-modulated carrier. Its FM deviation is 100 kHz, and its modulation frequency is 1 kHz. With these settings, the -3 dB bandwidth of the signal is approximately 300 kHz. The characteristics of the test signal are as follows:

Signal	Frequency (MHz)	Level (dBm)	Modulation	Harmonics	AAF
f1	30.5	≈ 9	FM	≈ -46 dBm	no

The close-in spectrum of the FM test signal on a spectrum analyzer is shown in Fig. 7.19.

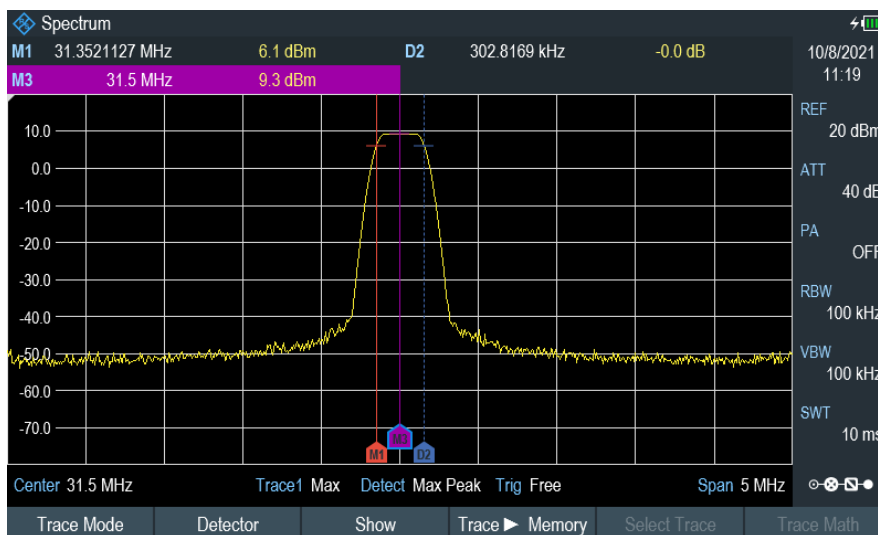


Fig. 7.19: Spectrum analyzer screenshot of an FM modulated 31.5 MHz test signal. The markers M1 and D2 indicate the 3 dB bandwidth of the signal.

The following Fig. 7.20 shows the FFT spectra of the broadband FM signal digitized with two different sampling frequencies.

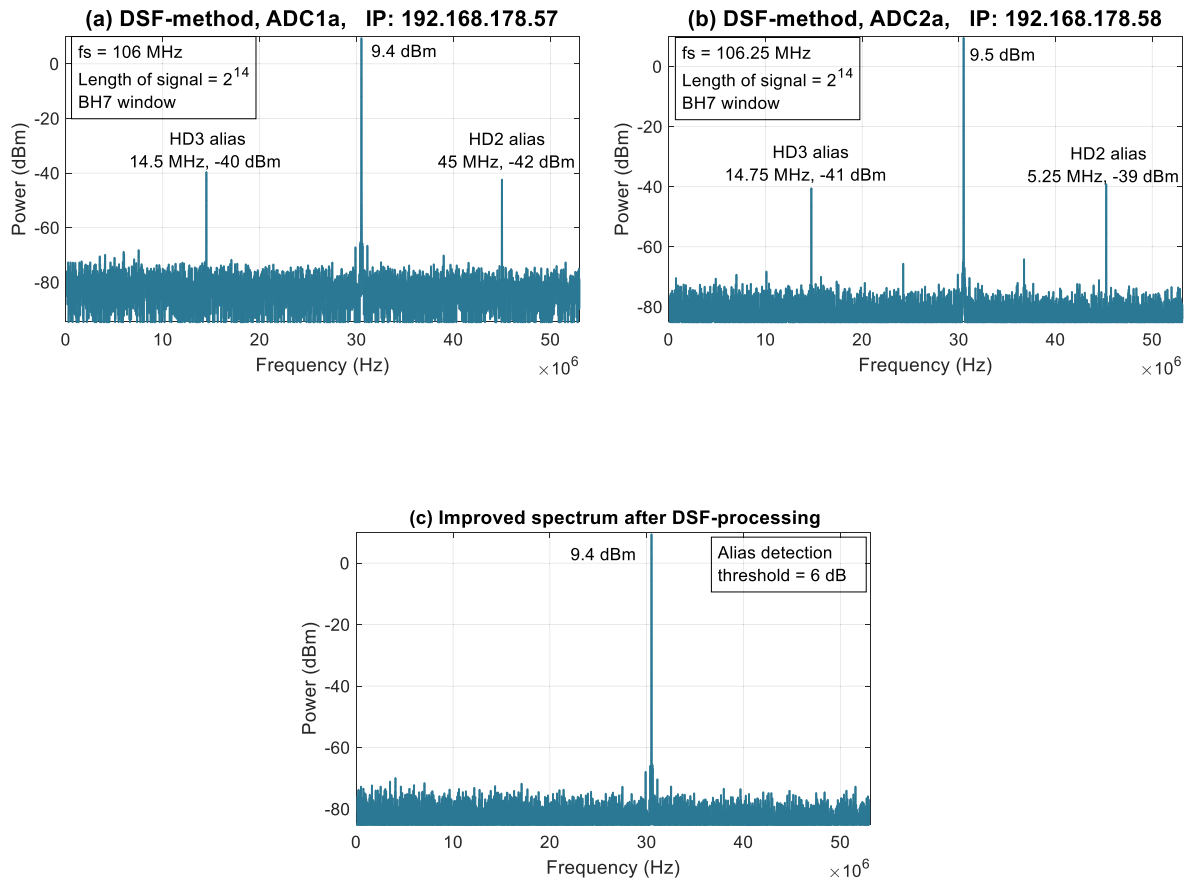


Fig. 7.20: DSF-method test with a 30.5 MHz broadband FM signal sampled with;
 (a) 106 MHz, creating an HD3 alias at 14.5 MHz and an HD2 alias at 45 MHz,
 (b) 106.25 MHz, creating an HD3 alias at 14.75 MHz and an HD2 alias at 45.25 MHz,
 (c) Improved spectrum after DSF processing; the alias signals are removed.

The resulting improved spectrum after DSF processing is shown in Fig. 7.20 (c). The DSF-method can effectively remove the alias of a broadband FM signal. The SFDR improvement of the spectrum in Fig. 7.20 (a) when compared with Fig. 7.20 (c) is >30 dB. The small signals close to the carrier are not removed; these are spurious of the signal generator and “belong” to the signal.

7.2.2 Laboratory Test of the DIF-Method

a) DIF-method test with a moderate level, single tone signal:

This basic test uses a single-tone 0 dBm signal with harmonic content. The sampling frequency is 106 MHz, and the bin shift is 50 bins, equal to ≈ 323.486 kHz. The bin shift is achieved by setting the signal generator to the required frequencies and sampling the signal again with the same ADC. The characteristics of the test signal are as follows:

Signal	Frequency (MHz)	Level (dBm)	Modulation	Harmonics	AAF
f1	15	≈ 0	no	< -55 dBm	no

A spectrum analyzer screenshot of the unmodulated test signal is shown in Fig. 7.21 below.



Fig. 7.21: Spectrum analyzer screenshot of the single-tone test signal. Marker M1 indicates the fundamental signal at 15 MHz.

Fig. 7.22 shows the four spectra obtained during DIF processing. The ADC distorts the fundamental signal and generates internal harmonics and aliases of the harmonics.

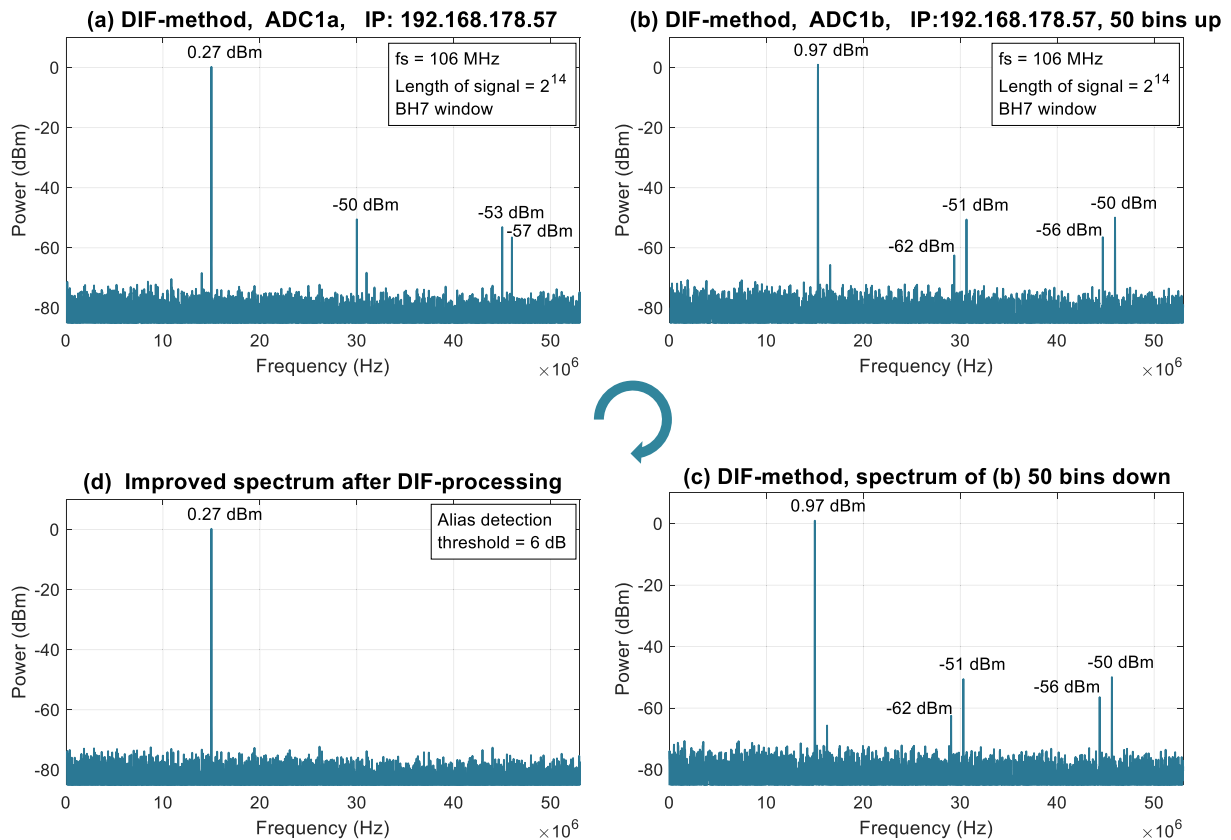


Fig. 7.22: Test of the DIF method with a single-tone signal using a dual-core ADC;
 (a) ADC1a, the initial spectrum of the test signal,
 (b) ADC1b, the spectrum of the test signal upshifted by ≈ 323.5 kHz,
 (c) Spectrum of (b) mathematically downshifted by 50 bins,
 (d) Improved two-tone spectrum after processing with the DIF-method.

The harmonics and alias components are pushed into the noise. When comparing the spectrum of Fig. 7.22 (a) with Fig. 7.22 (d), an improvement of the SFDR of > 20 dB can be observed.

b) DIF-method test with a strong two-tone signal.

This test is performed to investigate to what extent odd-order intermodulation products can be removed with the DIF-method. Two signals with the following characteristics are used:

Signal	Frequency (MHz)	Level (dBm)	Modulation	Harmonics	AAF
f1	15	≈ 4	no	≈ -45 dBm	no
f2	16	≈ 4	no	≈ -48 dBm	no

The spectrum analyzer screenshot in Fig. 7.23 shows the spectrum of the test signal.

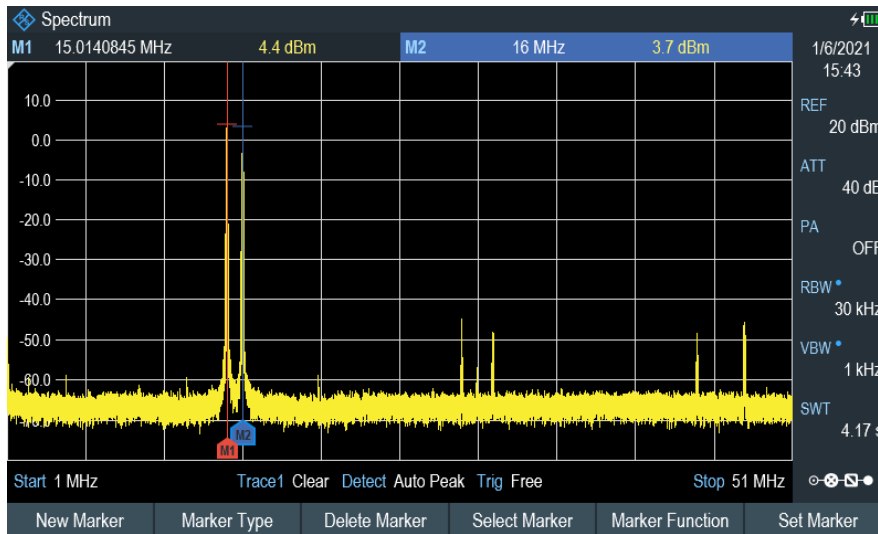


Fig. 7.23: A spectrum analyzer screenshot of the two-tone test signal and its harmonics.

Fig. 7.24 presents the first two spectra obtained during DIF processing.

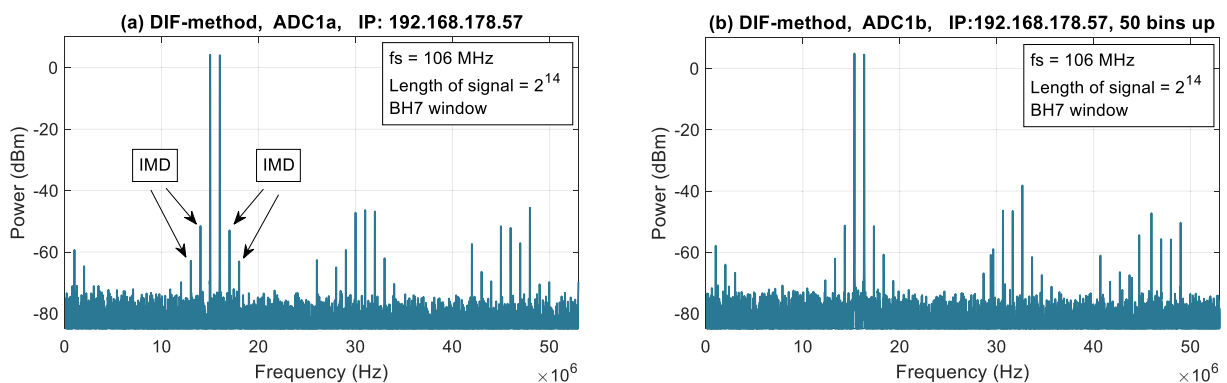


Fig. 7.24: Test of the DIF-method with a two-tone signal using a dual-core ADC;
 (a) Initial spectrum of the test signals,
 (b) Spectrum of the test signals upshifted by 50 bins.

The mathematically downshifted spectrum and the purged spectrum are shown in Fig. 7.25.

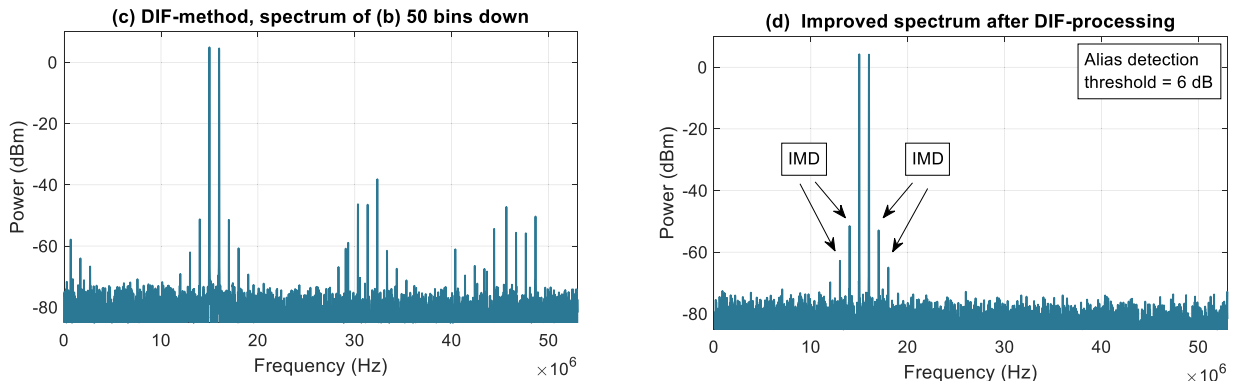


Fig. 7.25: Test of the DIF-method with a two-tone signal using a dual-core ADC;
 (c) Spectrum of the test signals downshifted by 50 bins,
 (d) Improved two-tone spectrum after processing with the DIF-method.

The resulting spectrum in Fig. 7.24 (d) looks much cleaner compared to Fig. 7.24 (a), but as expected, the DIF-method cannot remove odd-order IMD products like IMD3, IMD5, and higher. The SFDR improvement regarding all other spurious products is >30 dB.

7.2.3 Laboratory Test of the DIA-Method

The measurements on the AD9213 in Subsection 6.3.2 indicate that the DIA method may not work at low signal levels. The AD9608 used in the experiments has a more pronounced dependency of the SFDR from the input level than the AD9213, as illustrated in Fig. 7.26.

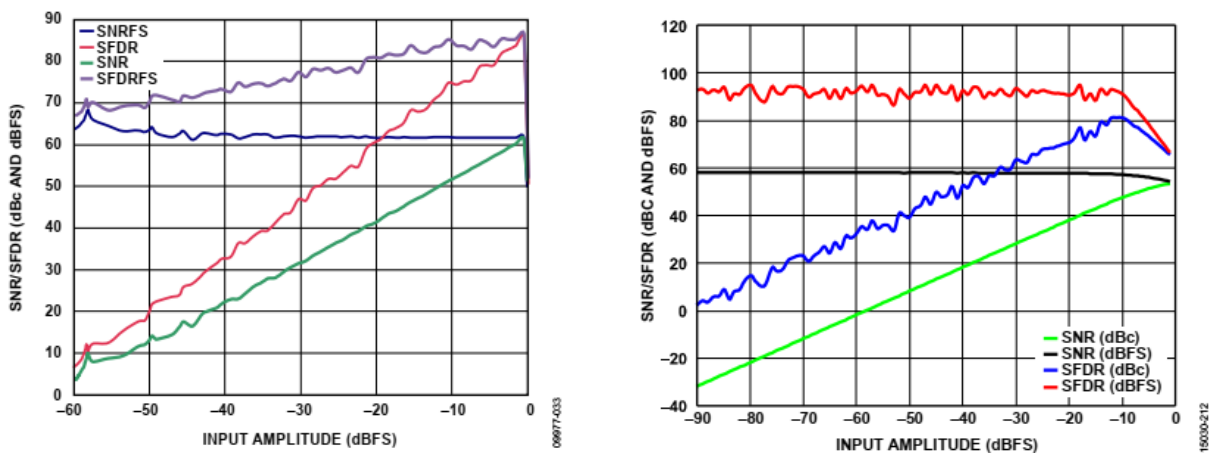


Fig. 7.26: SFDR graphs of (a) the AD9608 and (b) the AD9213 versus input amplitude. Graphics are taken from the datasheets [100] and [8].

Therefore, it is expected that the AD9608 will show better spurious suppression properties with the DIA-method than the AD9213. For the tests, the signal attenuation Δa for the second FFT is set to 3dB. The amplitude tolerance window at for the comparison algorithm is set to 1.5 dB.

a) DIA-method test with a high-level signal:

This test investigates the effectiveness of the DIA- method using a strong signal. The characteristics of test signals are as follows:

Signal	Frequency (MHz)	Level (dBm)	Modulation	Harmonics	AAF
f1	15	≈ 10 dBm	no	< -60 dB	no

The test signal spectrum with the 10 dBm fundamental frequency at 15 MHz (marker M1) is depicted in Fig. 7.27.

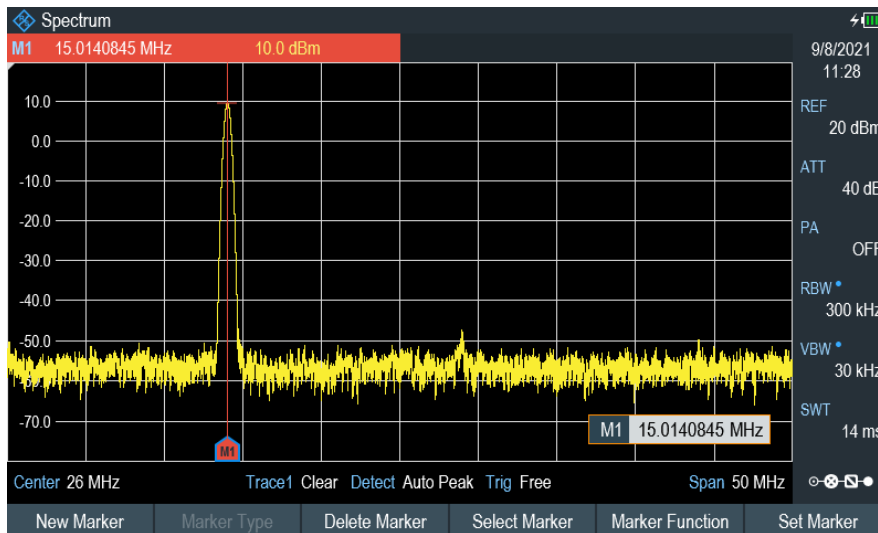


Fig. 7.27: Spectralanalyzer screenshot of the single-tone test signal.

Figure 7.28 (a) shows the FFT of the test signal obtained with ADC1a. The signal is distorted with a second harmonic HD2 at $-48,33$ dBc and a third harmonic HD3 at -55.86 dBc. The second FFT in Figure 7.28 (b) shows the signal attenuated by 3 dB and sampled with ACD1b. Due to the reduced signal level, HD2 is now 56.46 dBc, and HD3 is 66.34 dBc. Thus, the 3 dB

signal attenuation has reduced the level of HD2 by 8.13 dB and HD3 by 10.48 dB relative to the carrier. The amplitude variation is greater than the 6 dB or 9 dB one would expect from an analog amplifier and is caused by the distortion mechanisms of the AD9608. The observed level variation is large enough to be clearly detected by the comparison algorithm. The improved spectrum is shown in Figure 7.28 (d).

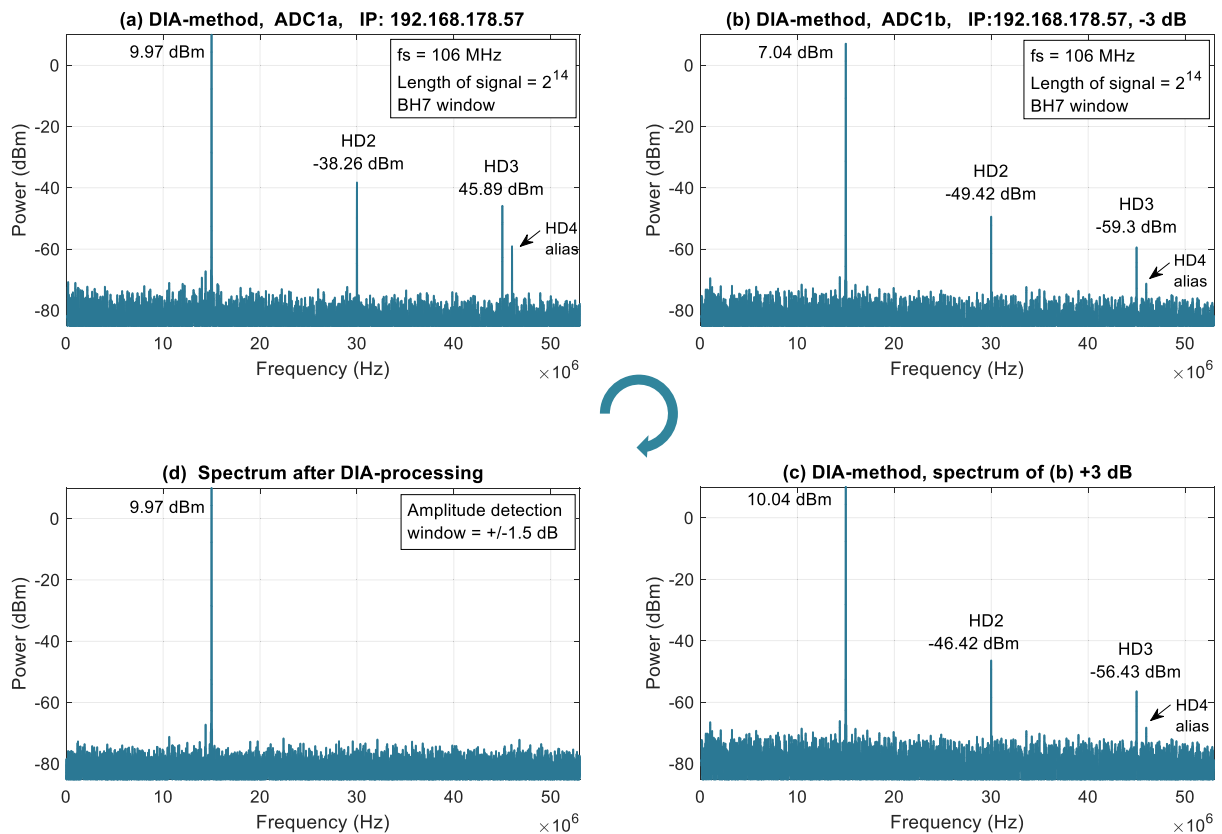


Fig. 7.28: Testing the DIA-method with a single-tone signal using a dual-core ADC;
 (a) Spectrum of the initial test signal,
 (b) Spectrum of the attenuated test signal (FFT2),
 (c) Amplitude of FFT2 mathematically increased by 3 dB,
 (d) Improved spectrum after processing with the DIA-method.

The experiment shows that the DIA-method can effectively remove harmonic distortion using the nonlinear transfer characteristic of an ADC.

b) DIA-method test with a strong two-tone signal:

The following test is performed to investigate to what extent intermodulation products can be removed using the DIA-method. A 5 dBm, clean, low-pass-filtered two-tone signal is used as a

stimulus. The characteristics of the signals are listed below:

Signal	Frequency (MHz)	Level (dBm)	Modulation	Harmonics	LPF
f1	15	≈ 5	no	< -60 dBm	25 MHz
f2	16	≈ 5	no	< -60 dBm	25 MHz

The spectrum of the two-tone test signal is depicted in Figure 7.29.

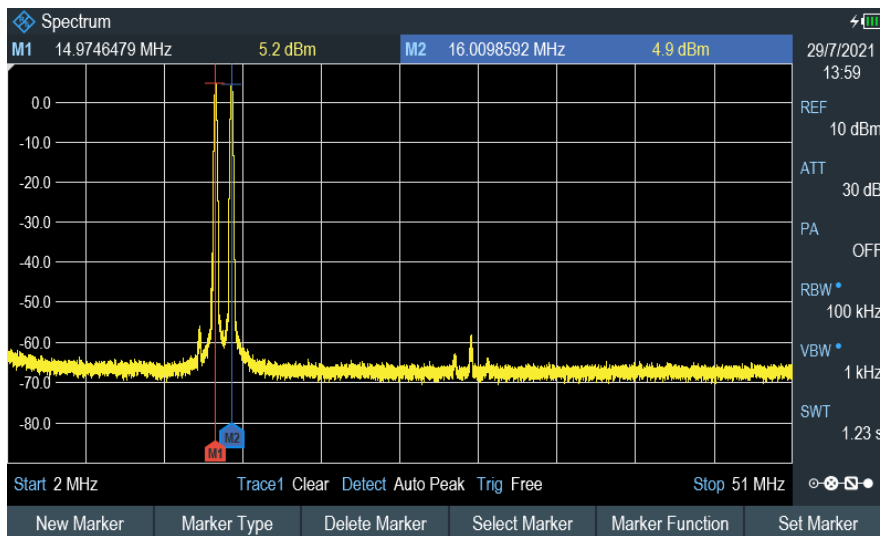


Fig. 7.29: Spectral analyzer screenshot of the low-pass filtered two-tone test signal.

The initial and the attenuated signal spectrum are shown in Figure 7.30 (a) and (b). The ADC creates intermodulation products and harmonics.

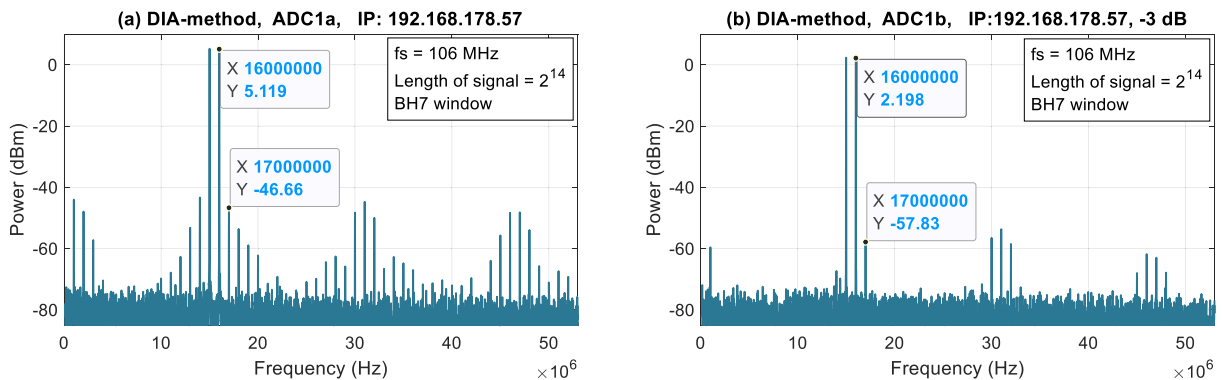


Fig. 7.30: Testing the DIA-method with a two-tone signal and a dual-core ADC;
 (a) Spectrum of the initial test signal,
 (b) Spectrum of the attenuated test signal (FFT2).

The FFT of the two-tone test signal in Figure 7.30 (a) shows noticeable third-order intermodulation approximately 51 dB below the test tones. As can be seen from Fig. 7.30 (b), a signal attenuation of 3 dB reduces IMD3 by approx. 11 dB, which is sufficient for the DIA-method to distinguish a desired signal from distortion.

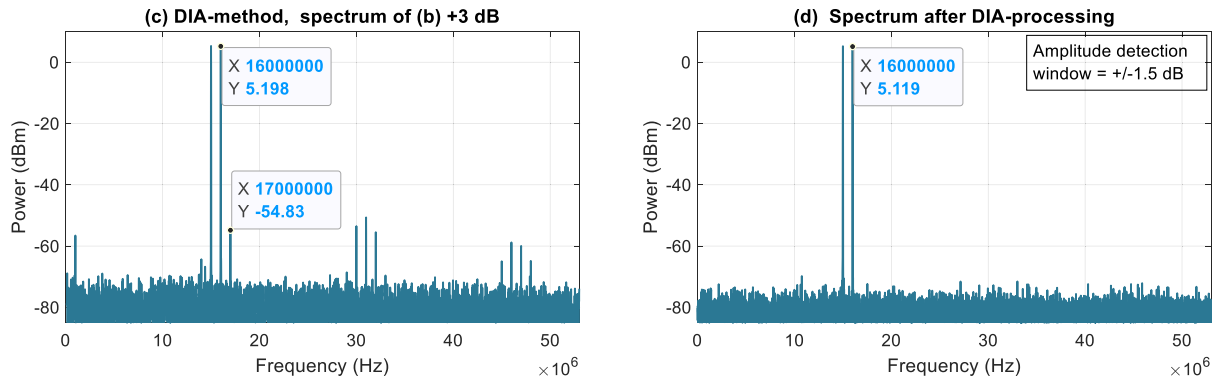


Fig. 7.31: Testing the DIA-method with a two-tone signal and a dual-core ADC;
 (c) Amplitude of FFT2 mathematically increased by 3 dB,
 (d) Improved spectrum after processing with the DIA-method.

The improved spectrum in Figure 7.31 (d) shows that the DIA-method can remove harmonic distortion, alias, and intermodulation products. The suppression of unwanted signals is >30 dB.

Remark:

If a small desired signal is covered by a strong intermodulation product that follows the 3 dB rule, the detection algorithm will assume distortion and remove the underlying desired signal as well. This corruption of the original spectrum is an undesirable property and limitation of the DIA-method and may occur whenever a strong, dominating ADC artifact sits on top of a weak desired signal.

c) DIA-method test with a broadband AM signal:

Since the DIA-method is based on amplitude measurements, a test is carried out with an amplitude modulated carrier signal to investigate if the amplitude modulation affects the spurious detection. The modulation depth of the signal is 100%, so the modulation sidebands are 3 dB below the carrier. The modulation frequency is set to 50 kHz to place sidebands outside the

filter bandwidth of the FFT. The characteristics of the test signal are as follows:

Signal	Frequency (MHz)	Level (dBm)	Modulation	Harmonics	LPF
f1	16	≈ 3 dBm	100% AM	< -60 dBm	25 MHz

The close-in spectrum of the test signal is shown in Fig. 7.32.

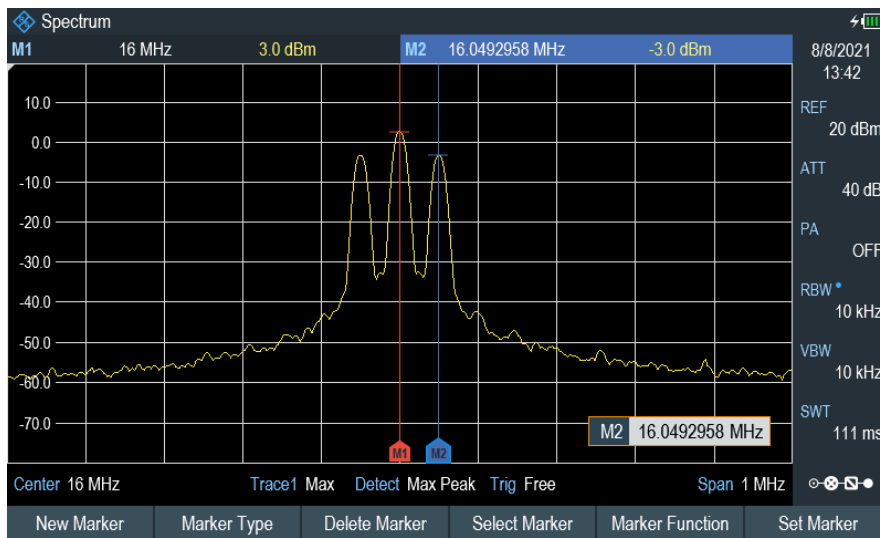


Fig. 7.32: Close-in spectrum of the AM modulated 16 MHz carrier signal.

The four spectra resulting from DIA-processing are shown in Fig. 7.33 and Fig. 7.34. The ADC produces harmonic signals at 32 MHz and 48 MHz.

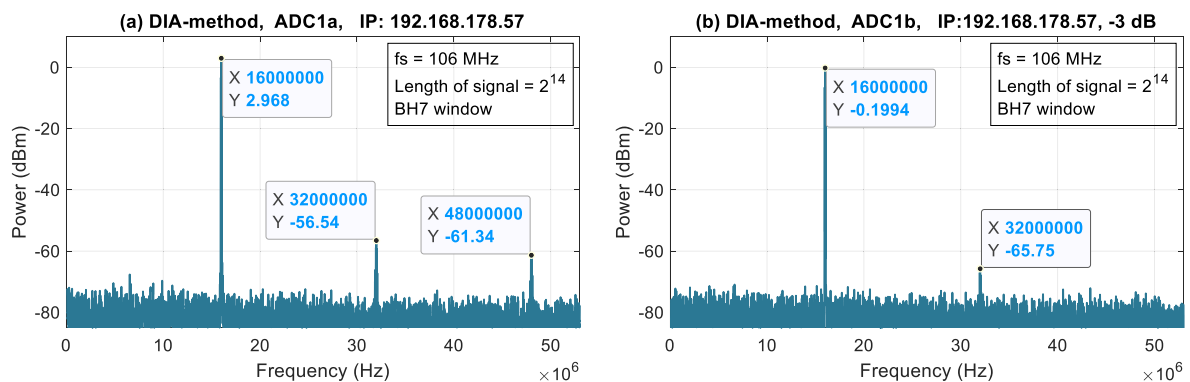


Fig. 7.33: Test of the DIA method with a 16 MHz AM modulated signal;
 (a) Spectrum of the initial test signal with ADC harmonics,
 (b) Spectrum of the attenuated test signal (FFT2) with reduced harmonics.

The improved spectrum after DIA-processing is shown in Fig. 7.34 (d) below.

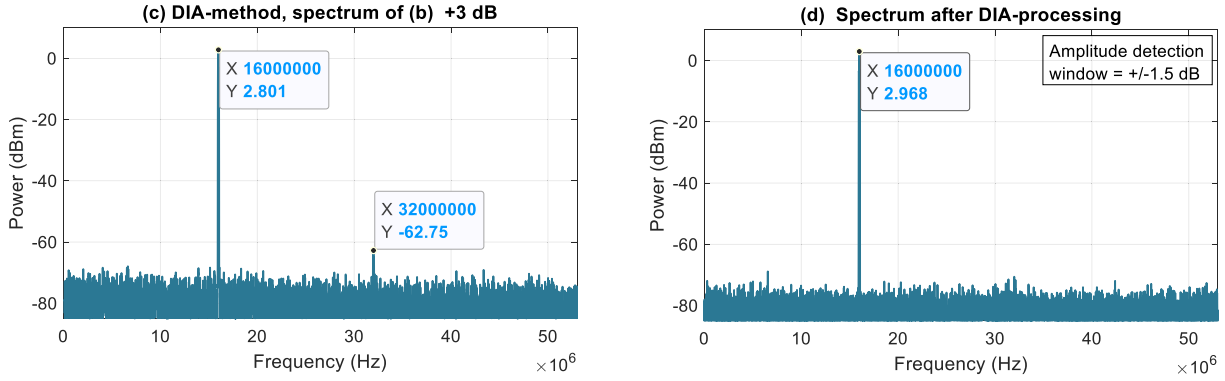


Fig. 7.34: Test of the DIA method with a 16 MHz AM modulated signal;
 (c) Amplitude of FFT2 mathematically increased by 3 dB,
 (d) Improved spectrum after processing with the DIA-method.

The comparison of Fig. 7.33 (a) with Fig. 7.34 (d) shows that the DIA-method has completely removed the harmonics of the AM signal. The suppression of the harmonic distortion is at least 20 dB. Since the signals are sampled with a dual-core ADC at the same time instance, the amplitude variation of the AM signal is present in both FFTs simultaneously. Therefore, the AM modulation does not affect the effectiveness of the DIA method.

d) DIA-method test: Undersampling, two-tone signal.

The following test represents an undersampling scenario with a medium-level, two-tone test signal placed in the second Nyquist zone. The characteristics of the signal are as follows:

Signal	Frequency (MHz)	Level (dBm)	Modulation	Harmonics	AAF
f1	75	≈ -10 dBm	no	< -45 dB	no
f2	76	≈ -10 dBm	no	< -45 dB	no

The spectrum of the two-tone test signal is shown in Fig. 7.35.

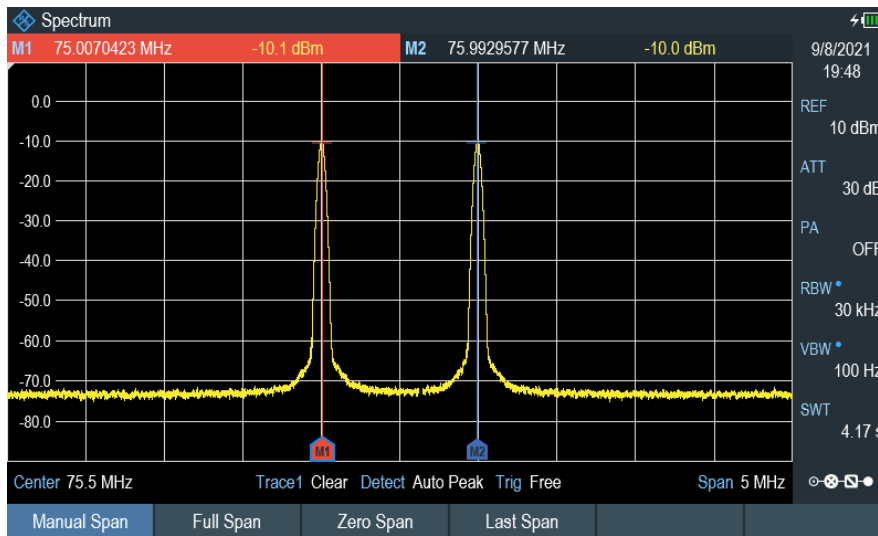


Fig. 7.35: Spectrum analyzer screenshot of the 75 MHz and 76 MHz two-tone test signal for the undersampling test.

Fig. 7.36 shows the spectra obtained after A/D conversion with a dual-core ADC. Aliasing transfers the signals to 29 MHz and 30 MHz. Due to the 3 dB attenuation prior to A/D conversion, the spectrum in Fig. 7.36 (b) shows reduced intermodulation products.

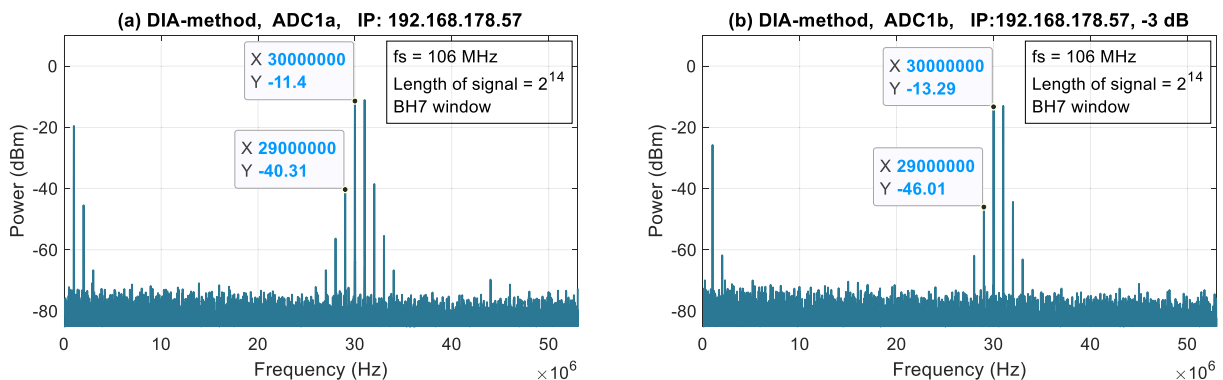


Fig. 7.36: Test of the DIA-method with an undersampled two-tone signal at 75 MHz and 76 MHz;
 (a) Spectrum of the initial test signal aliased into the first Nyquist zone,
 (b) Spectrum of the attenuated test signal (FFT2).

Fig. 7.37 (c) shows the mathematically amplified (3 dB) spectrum from Fig. 7.36 (b). Undersampling has shifted the signals and the intermodulation products to the first Nyquist zone at 31 MHz and 30 MHz. First-order mixing products of the harmonics of the fundamentals are visible at the low end of the spectrum. The improved spectrum is shown in Fig. 7.37 (d).

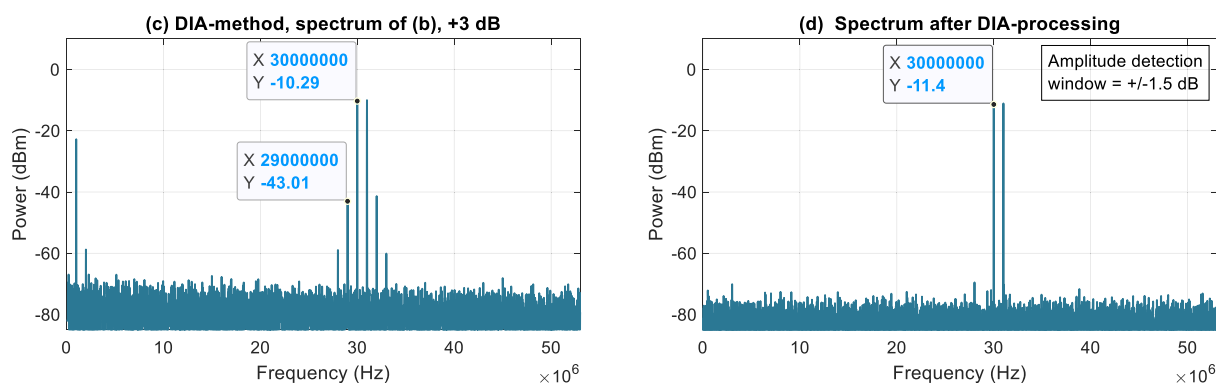


Fig. 7.37: Test of the DIA-method with an undersampled two-tone signal at 75 MHz and 76 MHz;
 (c) Amplitude of FFT2 mathematically increased by 3 dB,
 (d) Improved spectrum after processing with the DIA-method.

The result shows that the DIA-method also works in undersampling scenarios and removes most of the distortion products. When comparing Fig. 7.36 (a) with Fig. 7.37 (d), a reduction of spurious signals by more than 25 dB is observed.

In summary, it can be stated that the DIA-method is very effective as it has the potential to remove spurious signals generated by nonlinear distortion like harmonics and aliases of harmonics. It is the only method that works with undersampling and can also remove odd-order intermodulation products. However, suitable distortion characteristics of the ADC must allow the use of the method. The DNL and INL error characteristics of a particular ADC may limit the usefulness of the method.

7.3 Measurements With Antenna Signals

In this Section, the DSF and DIA method is tested using RF signals from a 2×15 m long dipole antenna. The ADC boards from Section 7.2 are used for testing. This setup allows a broadband display from DC to 53 MHz. Receiving small radio signals from an antenna requires a driver amplifier to overcome the comparatively high noise level of the ADC. The required gain of the amplifier was estimated by measuring the maximum RF level at the antenna. The strongest signals were observed in the evening hours and sometimes reached values of more than -25 dBm, as indicated by the red circle on the spectrum analyzer screenshot. Refer to Fig. 7.38.

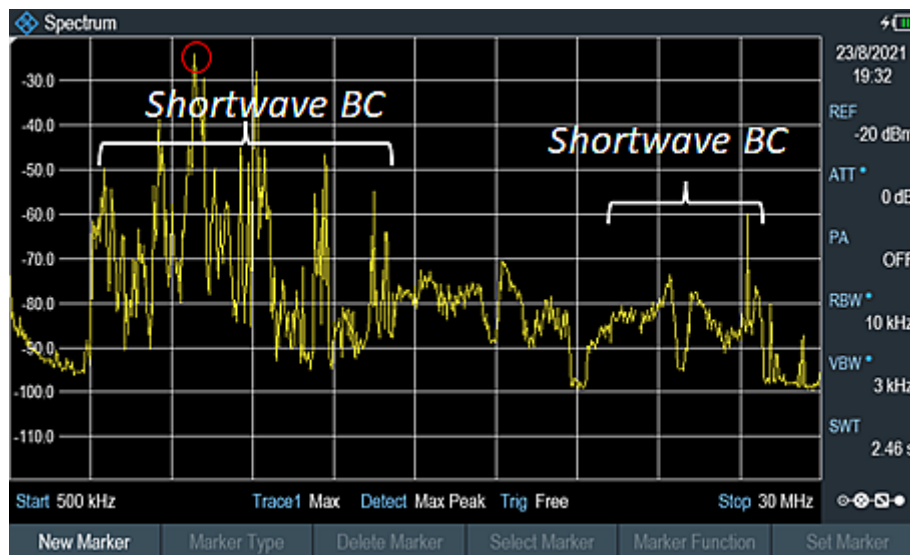


Fig. 7.38: Strong shortwave broadcast (BC) signals from a dipole antenna, recorded with a spectrum analyzer. The frequency axis ranges from 500 kHz to 30 MHz.

These signals can add up depending on their phase relation and thus reach even higher sum levels with broadband processing. Therefore, the driver amplifier must not exceed a gain of 30 dB in order not to overload the ADC with its maximum input amplitude of 10 dBm. Accordingly, a low-noise, low-distortion driver amplifier (DRV) with a gain of 28 dB was developed. This amplifier achieves a noise figure of ≈ 4 dB and a third-order output intercept point (OIP3) of ≈ 41 dBm, and a -3 dB bandwidth of ≈ 100 MHz. It comprises four cascaded Norton amplifier (LNA) stages. These use high-current BFG235A RF transistors in common-base topology with magnetically coupled “noiseless feedback” to provide a low noise figure and a high dynamic range. The concept is illustrated in Figure 7.39.

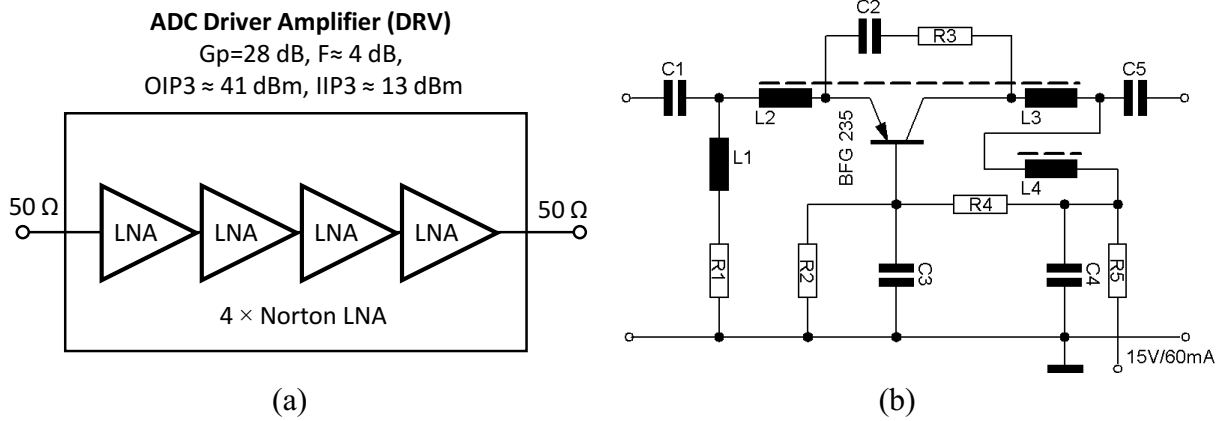


Fig. 7.39: (a) The driver amplifier (DRV) consists of four cascaded Norton amplifier (LNA) stages, (b) Circuit diagram of a single Norton amplifier stage.

The influence of the driver amplifier on the system's dynamic range is determined by measuring the total power of noise and distortion (Pnd) in the Nyquist band with - and without the amplifier before the ADC. A MATLAB program was written to calculate the Pnd values by summing the power of all bins in the Nyquist band. The obtained results are shown in Fig. 7.40.

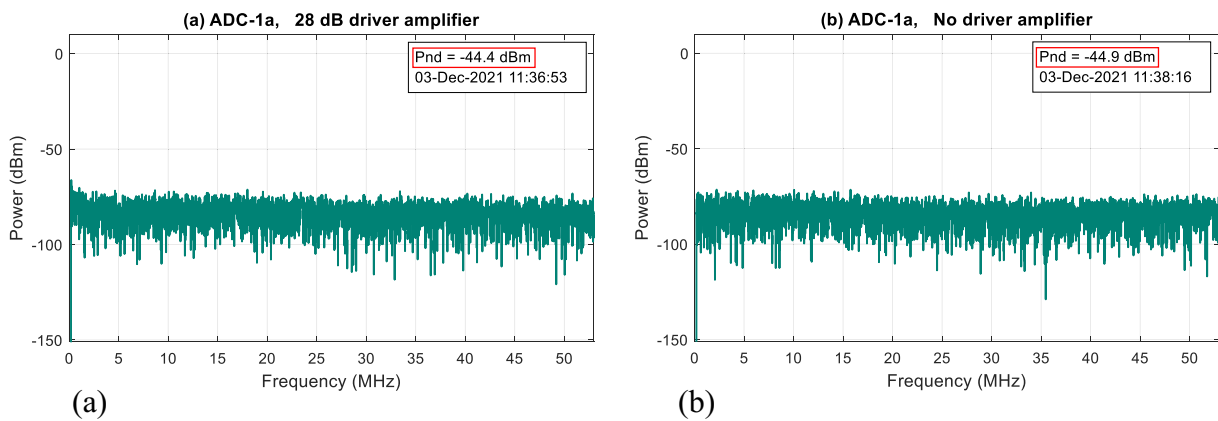


Fig. 7.40: The total power of noise and distortion (Pnd) of the FFT in the Nyquist band: (a) Pnd with the 28 dB driver amplifier, (b) Pnd without the driver amplifier.

The noise energy is distributed over 2^{14} FFT bins, so the displayed average noise level (DANL) can be calculated from the Pnd value by:

$$\text{DANL} = \text{Pnd} - 10 \log\left(\frac{2^{14}}{2}\right) = \text{Pnd} - 39.13 \text{ dBm}.$$

Therefore, the DANL of the stand-alone ADC is: $-44.9 \text{ dBm} - 39.13 \text{ dBm} = -84.03 \text{ dBm}$.

Adding the amplifier in front of the ADC raises the DANL to:

$-44.4 \text{ dBm} - 39.13 \text{ dBm} = -83.53 \text{ dBm}$. This 0.5 dB loss of dynamic range is due to the noise contribution of the amplifier. Given the noise-limited dynamic range of the ADC of about 90 dB, this reduction of 0.5 dB seems tolerable.

7.3.1 Setup for the Antenna Measurements

The test setup is illustrated in Fig. 7.41. The antenna signal and optionally an interference signal from a signal generator are fed into the receive path via a -3 dB power splitter. After passing through an optional 50 MHz low-pass filter, the signal is amplified by 28 dB and fed through another -3 dB power divider into the ADC boards for A/D conversion and subsequent signal processing. The second output of the power divider is connected to an EB500[®] monitoring receiver which allows comparison of the processed FFT with the receiver's spectrum display.

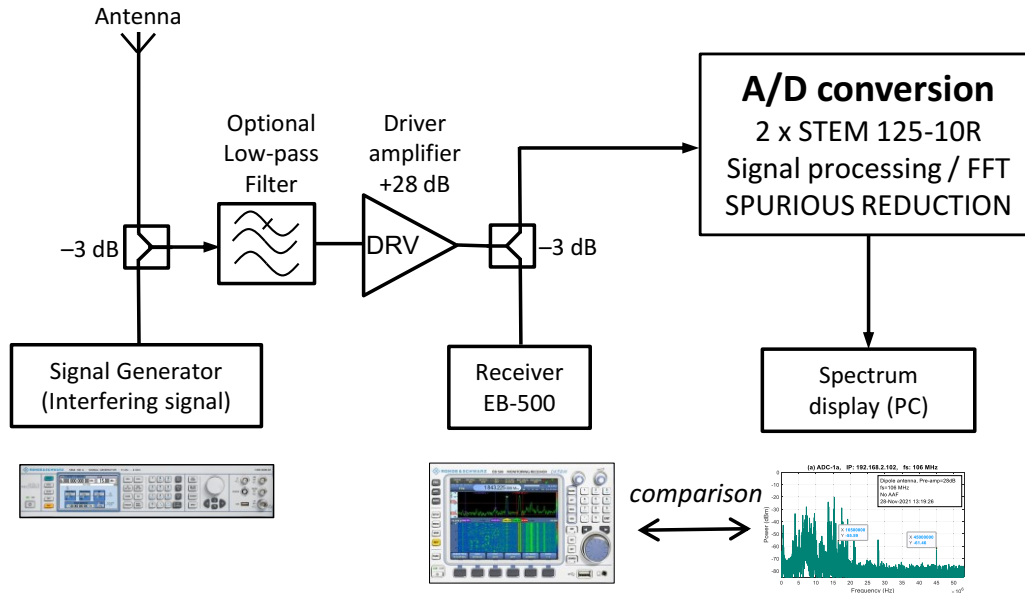


Fig. 7.41: The basic scheme of the test setup for antenna measurements. The combined signals from the antenna and a signal generator are amplified by a driver amplifier (DRV) and digitized by two STEM 125-10R boards. An EB500 spectrum monitoring receiver allows signal verification and comparison with the processed ADC data.

7.3.2 Antenna Measurements With the DSF-Method

The following experiment demonstrates the display of a densely populated RF spectrum over the entire Nyquist bandwidth of the ADC and the suppression of alias products using the DSF-method. No low-pass filter (anti-aliasing filter) is used so that signals outside the first Nyquist zone >53 MHz (for example, FM broadcast stations) can also reach the ADC input and provoke aliasing. Additionally, a strong 61 MHz interfering signal from the signal generator is combined with the antenna signals. Fig. 7.42 depicts the FFT of this signal. A densely occupied spectrum with many broadcast and amateur radio stations can be observed. Based on the sampling frequency of 106 MHz, two exemplary alias frequencies have been identified and are highlighted with X/Y coordinates. The 16.5 MHz signal is an alias from a strong 89.5 MHz FM station ($f_s - 89.5$ MHz); whereas the 45 MHz signal is an alias from the 61 MHz generator signal ($f_s - 61$ MHz).

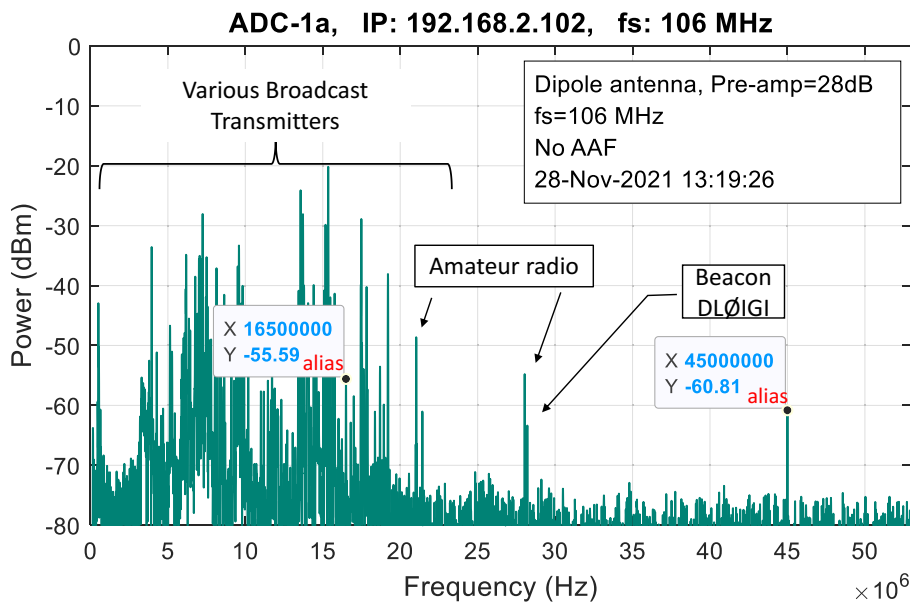


Fig. 7.42: The signal spectrum at the antenna. Many broadcast and amateur radio stations are visible. Two alias signals appear at 16.5 MHz and 45 MHz and are marked with the X/Y values.

These alias signals should not be present in a narrowband monitoring receiver with RF-preselection, which was verified with the EB500. Fig. 7.43 shows the antenna signal on the receiver's spectrum display. Since the maximum bandwidth is limited to 20 MHz, the center frequency is set to ≈ 37 MHz to display the 45 MHz alias frequency. Due to the receiver's FFT-averaging function being turned on, the displayed noise level is lower than the FFT display in Figure 7.42.

The DLØIGI beacon at 28.206 MHz (marker 1) and an amateur radio station next to it can be seen on the left side of the display. In contrast to the FFT display in Figure 7.42, the monitoring receiver does not show any signal in the 45 MHz range (marker 2).



Fig. 7.43: Screenshot of a 20 MHz wide spectrum on the EB500 monitoring receiver, showing the weak DLØIGI radio beacon at 28.205 MHz (marker1) and the amateur radio station at 28.030 MHz. No signal is present in the 45 MHz range (marker 2).

It is evident that the 45 MHz signal is an alias caused by the AD9608. A similar test was performed with the 16.5 MHz signal, which was also found to be an alias.

Next, the DSF method is applied to remove the alias signals from the spectrum display. The improved spectrum after DSF-processing is shown in Fig. 7.44. All signals are still visible, but the alias frequencies at 16.5 MHz and 45 MHz are successfully removed.

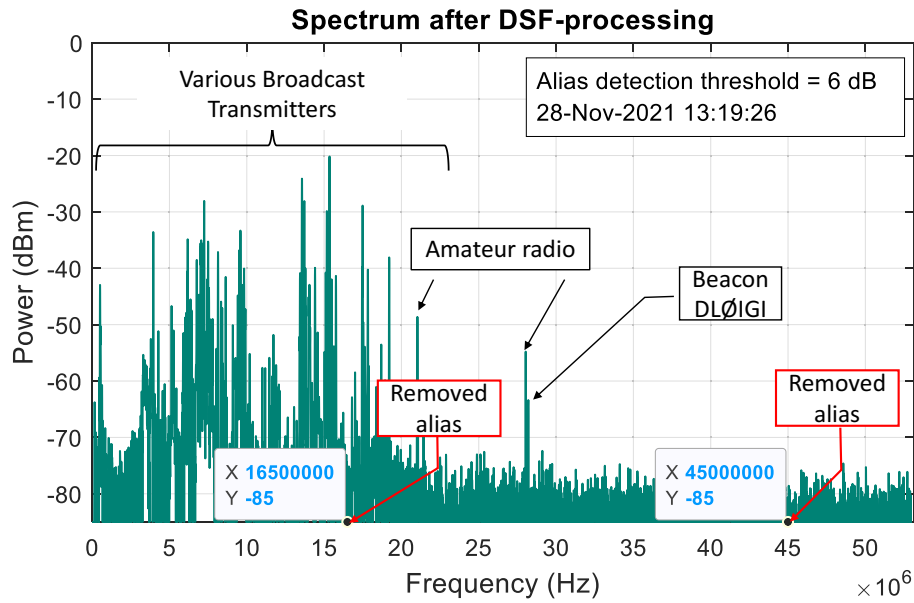


Fig. 7.44: Improved antenna signal spectrum after spurious suppression with the DSF-method. The alias signals at 16.5 MHz and 45 MHz are removed.

For better visualization, the suppressed signals are mathematically extracted in the DSF algorithm and shown separately in Fig. 7.45.

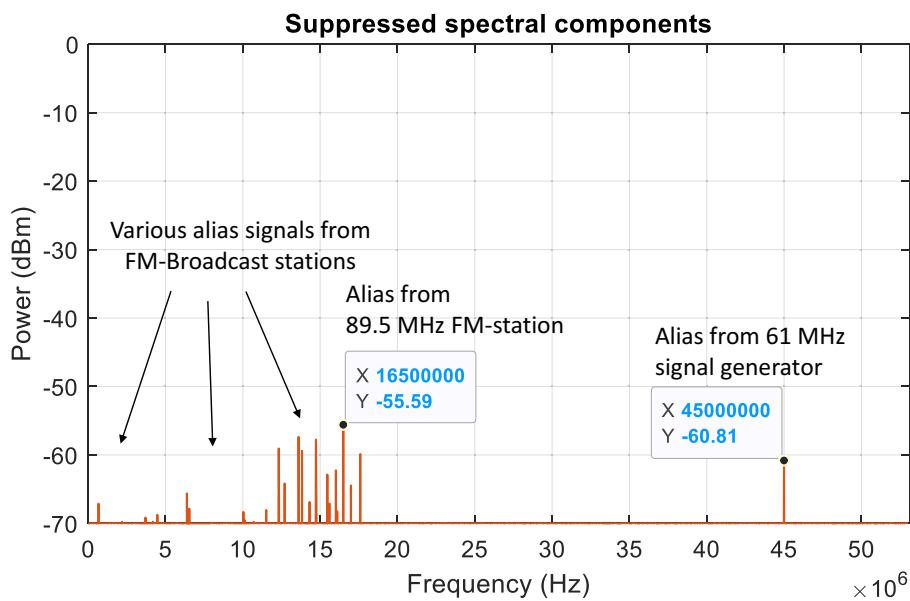


Fig. 7.45: The spectral components > -70 dBm that are removed by DSF-processing.

The program has removed a number of prominent aliases. Apart from the generator signal, these are obviously caused by strong FM transmitters in the second Nyquist zone. With a sampling frequency of 106 MHz and the FM signals populating the frequency range from 87.5 MHz to 108 MHz, the alias frequencies $f_{\text{alias}} = |f_{\text{signal}} - f_{\text{sampling}}|$ appear from 0 MHz to 18.5 MHz. To verify that these signals are indeed aliases of FM broadcast transmissions, a 50 MHz low-pass filter was switched into the receive path. The attenuation of the FM signals removed all spurious signals from the display, confirming that it was aliases.

In conclusion, the DSF method successfully works with antenna signals over the entire Nyquist bandwidth of the ADC and effectively eliminates alias signals.

7.3.3 Antenna Measurements With the DIA-method

The following experiment demonstrates the suppression of nonlinear distortion using the DIA-method. A 50 MHz low-pass filter prevents aliasing, and a strong 11 MHz interfering signal from the signal generator is combined with the amplified antenna signal. The FFT in Fig. 7.46 shows a densely occupied spectrum with many broadcast and amateur radio stations. Due to the strong 11 MHz interferer, the ADC creates a second-order harmonic at 22 MHz.

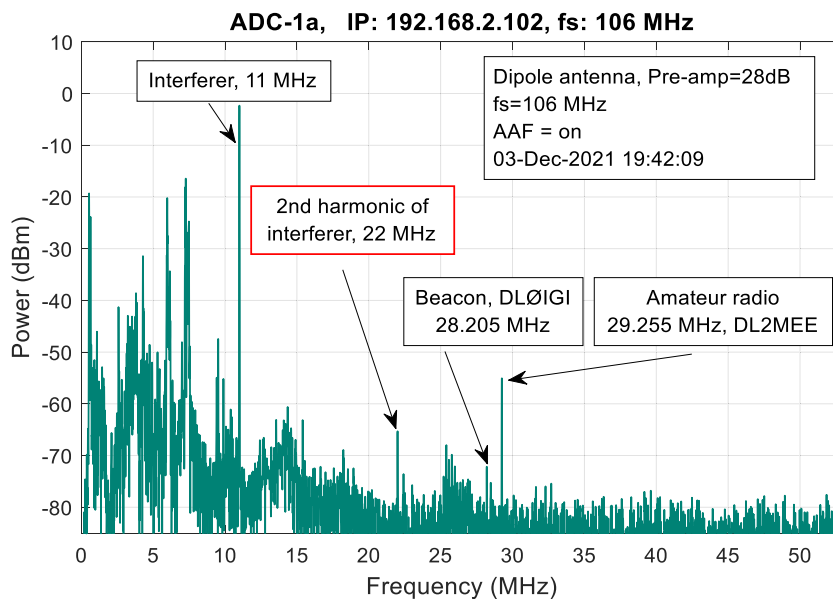


Fig. 7.46: Antenna signal spectrum. Numerous broadcast and amateur radio stations are visible. The strong 11 MHz interferer creates second-order harmonic distortion at 22 MHz.

After DIA-processing, the second-order harmonic caused by the interferer is removed. The improved spectrum is shown in Fig. 7.47.

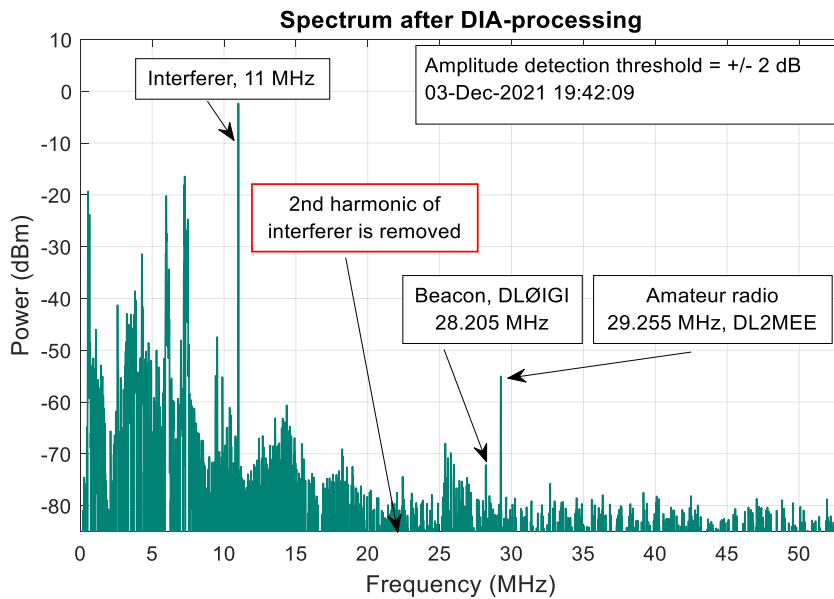


Fig. 7.47: Antenna signal spectrum after spurious suppression using the DIA-method. The second-order harmonic distortion at 22 MHz is successfully removed.

Fig. 7.48 shows an EB500 screenshot of the 10m shortwave band for reference. Comparison with the processed spectrum in Fig. 7.47 shows that the signals at 28.205 MHz and 29.255 MHz agree. The DIA-method has removed distortion but did not corrupt the original signal.

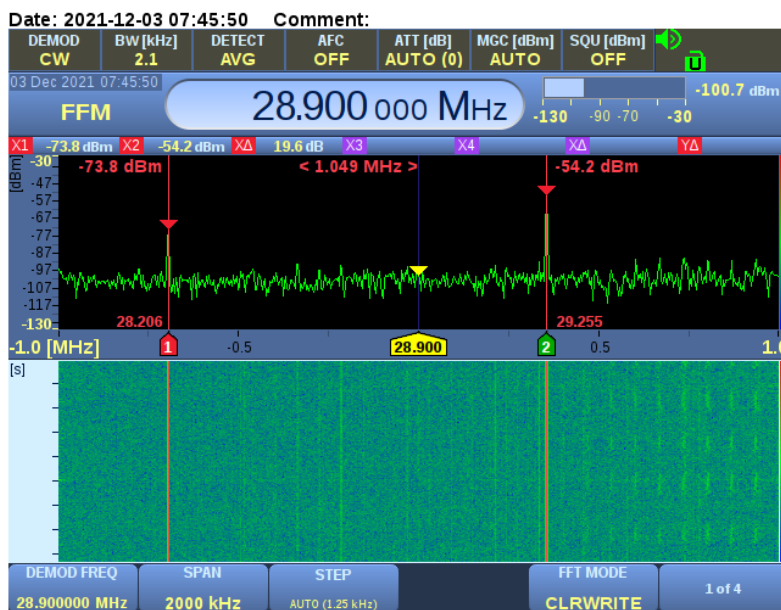


Fig. 7.48: An EB500 screenshot of a 28.9 MHz \pm 1 MHz frequency range. The beacon is visible at marker1; the amateur radio station is at marker2.

In summary, practical measurements with the ADCs show that the DSF method also works successfully with real antenna signals.

7.4 Effects of Spurious Suppression on Noise and Distortion

The effect of the spurious reduction methods on the noise and distortion characteristics of a processed signal is examined in the following Section, using the hardware setup depicted in Fig. 7.41. Since the signal processing is similar for all three spurious reduction methods, the results are considered transferable. Therefore, the evaluation is performed using the DSF method as an example, with the alias detection threshold set to 6 dB.

The **Signal-to-Interference ratio, including Noise And Distortion (SINAD)**, is used as a metric to study the effects of spurious reduction on noise and distortion. A clean sinusoidal stimulus from a signal generator and a MATLAB algorithm is used to calculate the total power of the FFT spectrum by summing up all signal, noise, and distortion components (P_{snd}). Next, the DC component and the signal's fundamental frequency are mathematically removed, and the remaining power of noise and distortion (P_{nd}) is calculated. From these two values, the SINAD ratio of the FFT is determined as [19, p. 620]:

$$\text{SINAD} = \left(\frac{P_{\text{snd}}}{P_{\text{nd}}} \right) \text{ dB} . \quad (7.1)$$

The practical test is performed with a 41.44 MHz single-tone stimulus of ≈ 9 dBm (-1 dBFS) passed through an 8-pole bandpass filter to suppress generator harmonics and synthesizer spurious. The unprocessed spectrum depicted in Fig. 7.49 (a) shows the 41.44 MHz fundamental and the associated alias signals caused by internal ADC distortion. The SINAD ratio of the unprocessed signal, marked with a red box, is 46.5 dB. After DSF processing, Fig. 7.49 (b), the spectrum shows an improved SINAD value of 55.4 dB (red box).

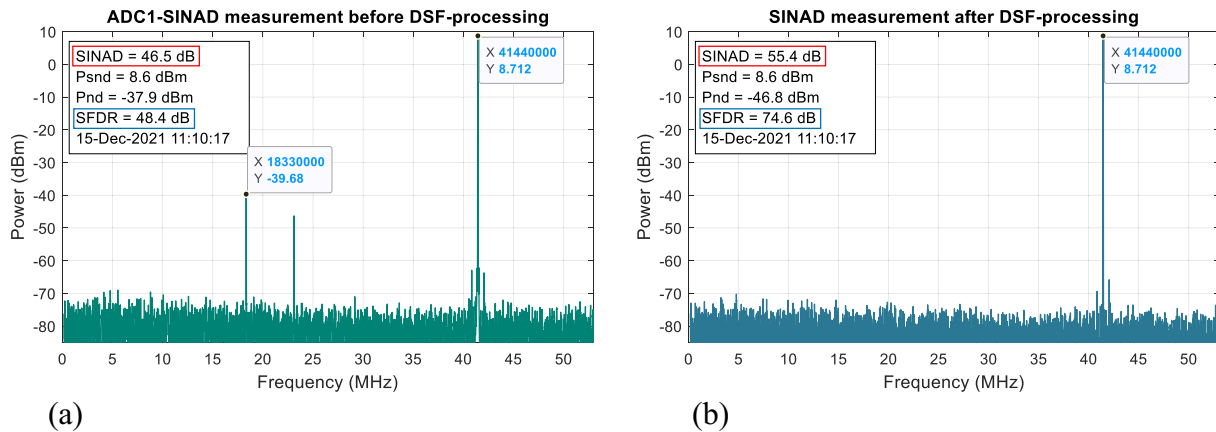


Fig. 7.49: SINAD and SFDR values of a 41.44 MHz signal before and after DSF-processing;
 (a) Unprocessed signal with spurs, SINAD = 46.5 dB, SFDR = 48.4 dB,
 (b) DSF-processed signal with removed spurs, SINAD = 55.4 dB, SFDR = 74.6 dB.

Removal of the spurious signals has reduced Pnd from -37.9 dBm to -46.8 dBm. Thus, according to (7.1), the SINAD value increases from 46.6 dB to 55.4 dB, an improvement of 8.8 dB. The reduction of the alias signals enhances the spurious-free dynamic range (blue boxes) by: 74.6 dB -48.4 dB = 26.2 dB.

7.4.1 Effect on the System Noise Level

In this Subsection, the influence of the DSF-method on the overall system noise level is investigated. Without any signal, only the broadband noise of the ADCs is present in the output spectrum. The calculated total power of noise and distortion (Pnd) of both FFTs is depicted in Fig. 7.50 (a) and Fig. 7.50 (b). The values of -43.9 dBm, respectively -44.2 dBm agree within 0.3 dB. The difference is due to the hardware tolerances of the ADCs, the test setup, and the amplitude fluctuations of the broadband noise. The SINAD value is 0 dB because no signals are present.

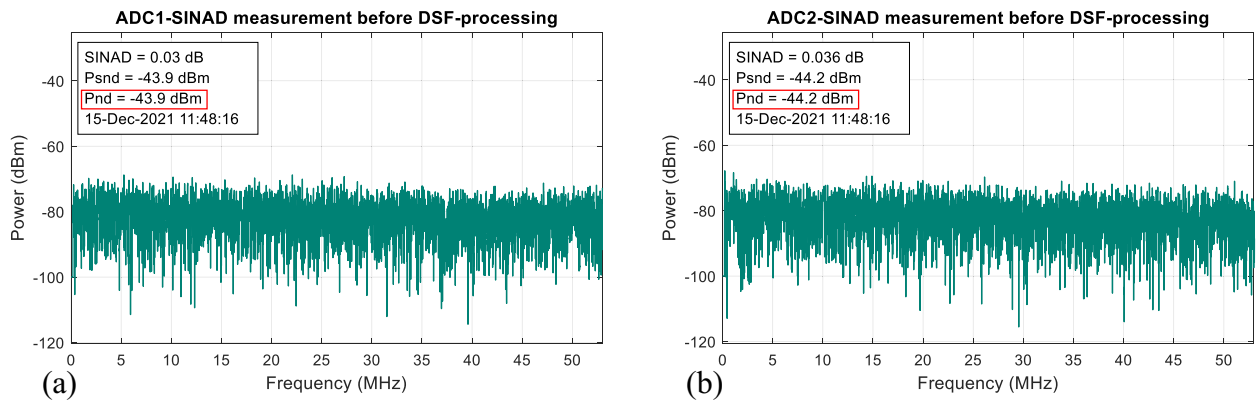


Fig. 7.50: The total power of noise and distortion (Pnd) of both ADCs with no signals applied; (a) ADC1, unprocessed noise spectrum, Pnd = -43.9 dBm, (b) ADC2, unprocessed noise spectrum, Pnd = -44.2 dBm.

The displayed average noise level (DANL) of the unprocessed spectrum of Fig. 7.50 (a) is:

$$\text{DANL} = \text{Pnd} - 10 \log\left(\frac{N}{2}\right) = -43.9 - 10 \log\left(\frac{2^{14}}{2}\right) \approx -83 \text{ dBm}.$$

After DSF-processing, the resulting spectrum looks as depicted in Figure 7.51. Compared to Figure 7.50 (a), Pnd is reduced by 1.9 dB to -45.8 dBm and DANL has improved accordingly to -84.9 dBm.

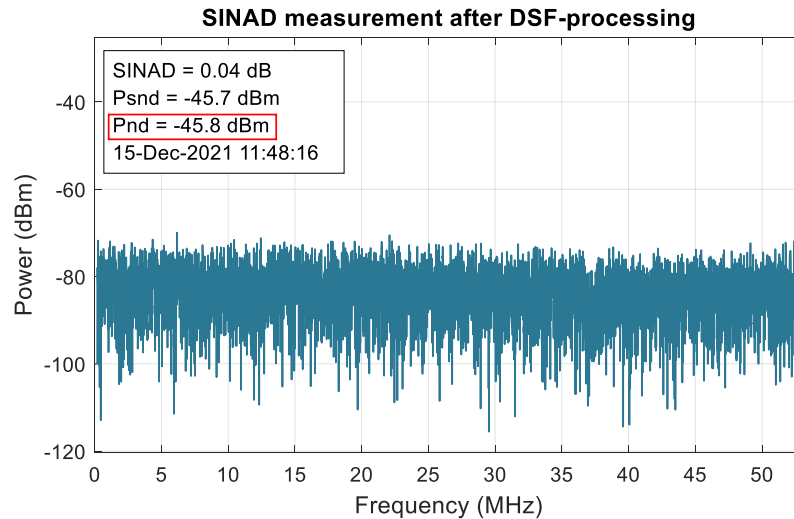


Fig. 7.51: Noise spectrum after DSF-processing. Pnd is reduced to -45.8 dBm.

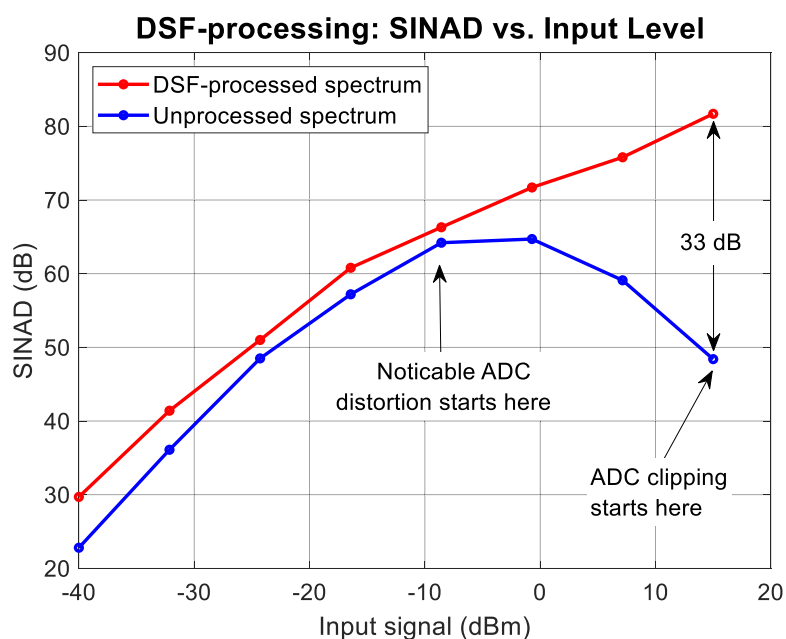
This enhancement can be explained as follows: The noise spectra shown in Fig. 7.50 (a) and Fig. 7.50 (b) are not correlated because the noise originates from two separate, independent integrated circuits (ADCs). Nevertheless, the total energy of the two FFTs is roughly the same

as the devices are similar, and the noise energy is integrated over the entire Nyquist bandwidth of more than 50 MHz. However, the amplitudes in a specific, corresponding frequency bin of the FFTs, at a certain time instant, are not the same, as the noise amplitudes fluctuate uncorrelated with time. If the amplitude difference in these bins exceeds the alias detection threshold (denoted as adt in Figure 6.3 of the DSF-algorithm), the superposition of a spurious signal is assumed. In this case, the lower of the two values is taken. This mechanism systematically reduces the noise floor to the lower of the two FFTs. Thus, the total energy of the processed spectrum decreases, and the resulting P_{nd} value is lower.

In summary, the DSF-method reduces the power of noise and distortion from an FFT by removing possibly existing spurious components. Thus, SFDR and SINAD are generally improved. How much improvement can be achieved depends on the signal levels and the distortion characteristics of the ADC. Higher ADC distortion levels result in more improvement.

Minimal spurious signals that differ only a few dB from the fluctuating noise floor cannot be removed because these are indistinguishable from noise.

Next, a series of SINAD measurements is carried out with the AD9608 using the DSF method and a 30 MHz signal to evaluate the effectiveness of alias reduction as a function of the ADC signal level. A diagram of the measurement results is shown in Fig. 7.52. Fig.



7.52: SINAD vs. input level of the AD9608 with a 30 MHz signal and the DSF method. $adt = 6$ dB.

The SINAD value of the processed spectrum (red line) is generally higher than that of the unprocessed spectrum (blue line) for the reasons stated above. The improvement is small over a wide range of input amplitudes as there are no spurious to remove. At higher input levels, the ADCs start to generate distortion, and upcoming spurious signals are mitigated. Therefore, continuous SINAD improvement is observed up to a maximum of ≈ 33 dB over an input range of approximately 25 dB. Once the ADCs start clipping, the analog values are no longer encoded correctly, and extreme amounts of uncorrelated distortion occur. The FFT comparison leads to erroneous results, and the suppression of spurious signals is then no longer possible.

Finally, it can be stated that the spurious mitigation methods do not worsen the signal-to-noise ratio of a spectrum. This result is to be expected since the working principle does not add energy to the spectrum but only removes it if spurs are detected.

8 Technical Results and Key Findings

This Chapter summarizes the main technical results found in simulations and tests.

Key results found during testing:

1. The DSF-method is suitable for mitigating aliases resulting from external signals or internal ADC distortion.
2. The DIF-method requires additional hardware for a frequency conversion stage. It is well suited for removing spurious signals related to harmonic distortion and aliases thereof.
3. The DIA-method can mitigate all kinds of distortion except the alias of the fundamental. The effectiveness depends on the distortion characteristics of the ADC.
4. An SFDR improvement of more than 20 dB can be achieved with either method.
5. The systems noise floor is not increased by applying the methods.
6. The DIF- and DIA-method work over the entire Nyquist bandwidth.
7. Only the DIA-method can suppress odd-order intermodulation and works with under-sampling.
8. A higher-resolution FFT improves the frequency resolution and thus the ability to distinguish spurious from desired signals.
9. The windowing process of the time signals is essential for sufficient frequency selectivity and sidelobe suppression.
10. The effects of frequency leakage and amplitude errors introduced by the ADCs, FFT, and windowing must be considered by using tolerance windows in DSP.
11. The mathematical alignment process of the FFTs has no noticeable effect on the frequency or amplitude accuracy.

12. The simple, fast amplitude comparison algorithms developed for this dissertation work have proven to be effective.
13. The probability of intercept (POI) for short signals can be configured; it depends on the sampling frequency and length of the sampled sequence.

Limitations found during testing:

1. The DSF- and DIF-method are based on shifting spurious signals on the frequency axis. The spurious suppression will suffer when the shifted spurious overlap with the original signal. Therefore, a sufficient frequency offset is required to separate the frequencies.
2. In a densely populated spectrum, the effectiveness of the methods is limited by the frequency resolution of the FFT since narrow-spaced signals may fall into the same FFT bin. In this case, the FFT resolution must be enhanced.
3. The effectiveness of the DIA-method depends on the amplitude distortion characteristics of the ADC. For successful detection, the amplitude of the spurious signals must follow a nonlinear, monotonic function.
4. If a strong nonlinear spur superimposes the energy of a weak desired signal in the same frequency bin, the DIA method will remove the spur together with the desired signal.
5. Depending on the selected sampling parameters, the DSF method has a lower operating frequency limit (6.2).
6. The DIA-method is based on an amplitude comparison of two FFTs. Therefore, to achieve optimal results, the different amplitude responses of the two ADC channels must be calibrated out.

9 Summary Conclusions and Future Work

Modern wireless communication leads to increasingly broadband signals and a steady expansion of the frequency spectrum used. Monitoring and regulating the frequency spectrum requires radio receivers with high bandwidth and a high dynamic range. Today's broadband monitoring receivers have a much poorer dynamic range than traditional sweeping superhet designs, especially when their real-time bandwidth exceeds several hundred megahertz. An examination of the available receiver architectures shows that none is available today that solves this dilemma with reasonable technical effort. Direct sampling of the RF signals with giga samples per second ADCs (GSPS ADCs) could solve the bandwidth problem, but it has a serious drawback. The dynamic range of such RF-sampling architectures is limited by the spurious-free dynamic range (SFDR) of the analog-to-digital converter stage. The achievable SFDR is only in the range of about 65 dBFS due to internally generated spurious signals.

A market review of commercially available GSPS ADCs and measurements on a high-end, state-of-the-art device made it clear that another way to improve the SFDR must be found. In the literature, several approaches have already been published over the years to address this problem. Most focus on the improvement of the ADC hardware, frequency dithering, or better frequency planning. In addition, a few digital signal processing (DSP) methods have been presented, but these are not widely used. There is room for improvement in this area.

As stated in Section 1.2, the objective of this dissertation was to develop a technique to improve the bandwidth and dynamic range of a broadband monitoring receiver by reducing ADC spurious signals. The goals set were:

- An SFDR improvement of more than 20 dB,
- Functional across the entire Nyquist bandwidth of an ADC,
- Applicable with commercial-off-the-shelf A/D converters.

The above objectives have been achieved by developing a novel technique for spurious suppression using a unique combination of two separate ADCs and digital signal processing.

The baseline of the methods brought forward is to digitize a signal in parallel with two separate ADCs using different A/D conversion parameters such as the sampling frequency, the signal frequency, or the signal amplitude.

The analysis of the A/D conversion process shows that the amplitudes and frequencies of spurious signals depend on the A/D conversion parameters and behave differently from the desired signals. This fact is used to detect and remove erroneous signals by digital signal processing.

By performing a fast Fourier transform (FFT) on the ADC data obtained with different A/D conversion parameters and comparing the frequencies and amplitudes of the spectra, false signals can be revealed. Spectral components that are not identical in both FFTs must necessarily be artifacts generated by the ADCs. These are subtracted by digital signal processing, resulting in a set of purged frequency data with improved spurious-free dynamic range.

The main part of this dissertation deals with the development of three separate methods applying different A/D conversion parameters. For this purpose, either a **Different Sampling Frequency** (DSF-method), a **Different Input Frequency** (DIF-method), or a **Different Input Amplitude** (DIA-method) is used to perform the A/D conversion.

The theoretical part describes the working principle of the methods, including aspects such as the origin of ADC spurious signals, FFT resolution, amplitude accuracy, and error analysis. An exemplary DSP signal flow and a MATLAB implementation conclude this part. The practical part evaluates the performance by simulations and experiments with two ADC boards sampling in the hundred megahertz range. Signals from signal generators and an antenna are used as stimuli.

In conclusion, all three methods have proven to be effective in simulations, laboratory tests, and with antenna signals. All types of spurious signals, such as aliases, harmonics, and intermodulation distortion, can be suppressed by one of the methods, but no method alone is capable of removing all types of spurious. The variable A/D conversion parameter determines which type of spurious can be suppressed. Table 9.1 shows the relationship between the A/D conversion parameters and the ability to detect spurious signals. For details, refer to Chapter 6 and Chapter 8.

Table 9.1: Suitability of the spurious reduction methods vs. origin of spurious signals.

Method	Spur detection principle	A/D conv. parameter	Spurious reduction method effective against:				
			Alias of fundamental	Alias of Harmonics	Harmonics of fundamental	Odd order IMD	Even order IMD
DSF	Frequency difference	Sampling clock	Yes	Yes	No	No	No
DIF	Frequency difference	Input frequency	No	Yes	Yes	No	Yes
DIA	Amplitude difference	Input amplitude	No	Yes	Yes	Yes	Yes

In general, the spurious signals are attenuated by at least 20 dB and, in most cases, suppressed below the noise floor. Thus, the spurious-free dynamic range of the current 10 GSPS ADCs can be typically improved from approximately 65 dB to 85 dB. Further analysis and measurements showed that applying the methods does not increase the noise level of the FFT.

Two of the methods, the DIF- and DIA-method, work over the entire Nyquist bandwidth of modern, commercial-off-the-shelf ADCs, thus allowing 5 GHz real-time bandwidth with improved SFDR.

However, the presented approach cannot solve the shortcomings of the ADC hardware and prevent the generation of spurious signals, but it can mitigate them at the expense of multiple sampling and signal processing overhead.

In a very dense spectrum, in which desired and spurious signals overlap in wide ranges, the DSF and DIF methods reach their limits. The suppression suffers from the fact that a reliable separation of the spectral components is no longer possible.

In summary, the new spurious mitigation approach presented in this dissertation can significantly improve A/D conversion performance for many signal scenarios by virtually eliminating internally generated distortion and aliasing. Extensive simulations and tests were carried out to evaluate the performance, and the resulting measurement results were provided. The operating principle can be applied to all A/D conversion methods, as it works independently of the data conversion technique used.

Future work could potentially improve the concept further and should focus on two areas:

1. Improving the detection of spurious signals:

Detection could be improved by using a third ADC and applying two of the methods to the signal at the same time. This way, three different data sets containing more information become available, and intelligent comparison algorithms could better detect and distinguish spurious from desired signals.

In this dissertation, a real-valued, single-sided power spectrum is used for determining the frequency and magnitude of signals in the frequency domain. The detection of spurious signals could possibly be improved if the phase angle of the signals is also taken into account.

2. Improving the spectral analysis technique:

The methods presented in this Thesis perform spectral analysis using an FFT and windowing of the time signal with a 7-term Blackman-Harris window. Instead, more advanced filter bank algorithms with polyphase filters [104] could improve the selectivity and accuracy of the spectral analysis, leading to better frequency resolution and spurious signal detection.

10 Appendix

10.1 The ADC Test Setup

For testing purposes, two "Red Pitaya STEM LAB 125-10" boards [99], each equipped with a dual-core AD9608 ADC [100], were mounted in the aluminum housing shown in Fig. 10.1 (a). As part of this work, the original 125 MHz ADC clock oscillators were replaced with ones that work at 106 MHz and 106.25 MHz [102], to enable experiments with the DSF method. Figure 10.1 (b) depicts the 106 MHz replacement oscillator. The low voltage, high impedance input ports of the STEM LAB boards were terminated with 51-Ohm resistors to match the impedance with other system components. A Power splitter, a 50 MHz low-pass filter, a single-chip microcomputer providing the USB interface, and a status display are also part of the assembly, shown in Fig. 10.1 (c).

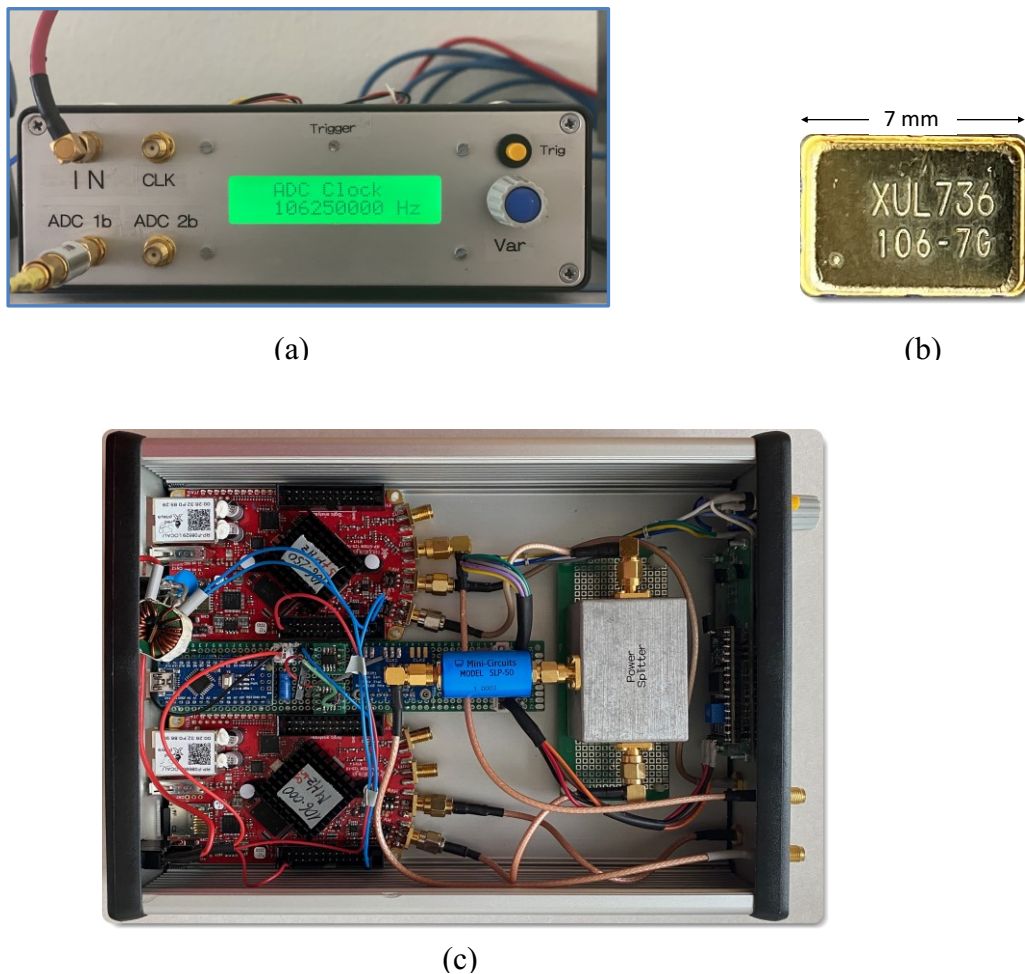


Fig. 10.1: Picture of the ADC test setup;
 (a) ADC housing, front view, RF-connectors, display, trigger button,
 (b) the 106 MHz replacement clock oscillator,
 (c) interior view with two ADC boards, power splitter, μ -processor, and low-pass filter.

10.2 Test Signal Generation

Two RF generators [105] and a dual output arbitrary waveform generator [106] provide the test signals, as illustrated in Fig. 10.2. An 8-port power combiner [107] with 23 dB port to port isolation sums up the signals and reduces generator intermodulation. If required, the test signals can be filtered by a low-pass filter [108] and attenuated by a variable step attenuator (R&S DPSP) or several fixed-value RF attenuators [109]. The integrity of the signals is verified with an R&S FPH spectrum analyzer and an R&S NRVS power meter [110], equipped with an NRV-Z51 power sensor.

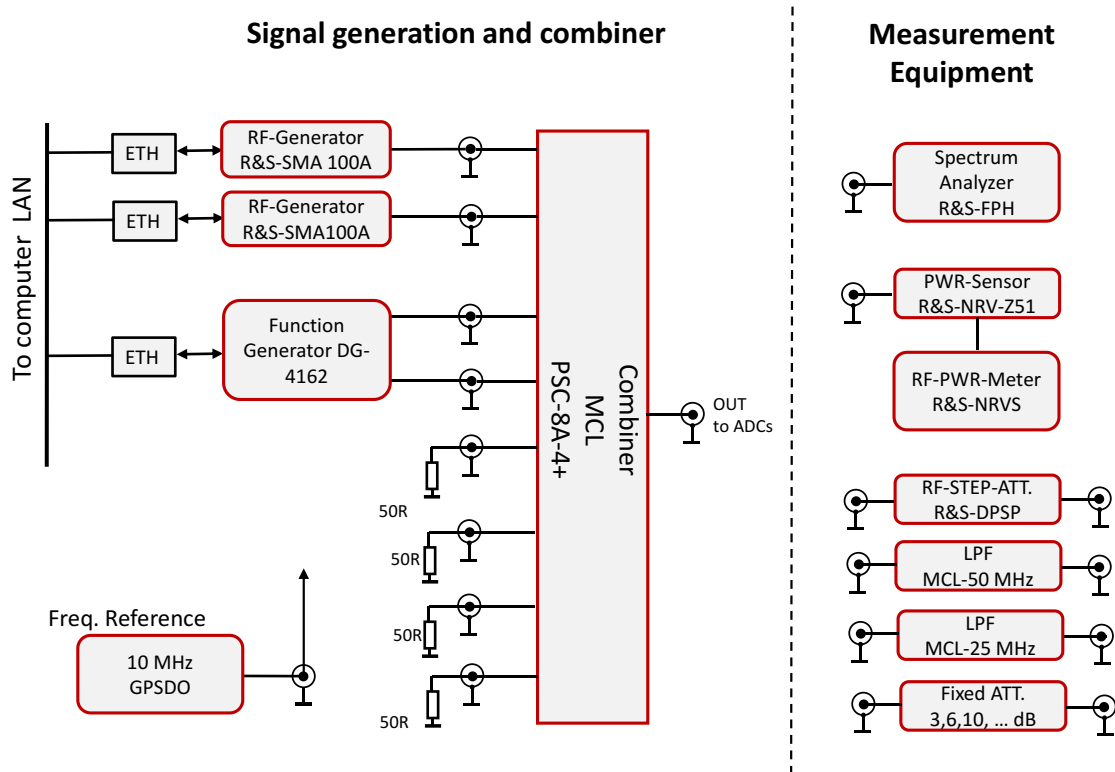


Fig. 10.2: Block diagram of the test signal generation and additional measurement equipment.

Amplitude measurement uncertainties have been estimated to be approximately ± 1 dB for the AD-conversion setup and another ± 1 dB for the test signal generation. The signal generator frequencies are referenced to a GPS-controlled 10 MHz standard. An offset correction in the software compensates for the frequency errors of the ADC clock oscillators (less than 2 kHz) since the STEM LAB board does not offer the possibility to lock it to an external reference.

10.3 Test Accessories

The following pictures show some test instruments and accessories used for this dissertation.

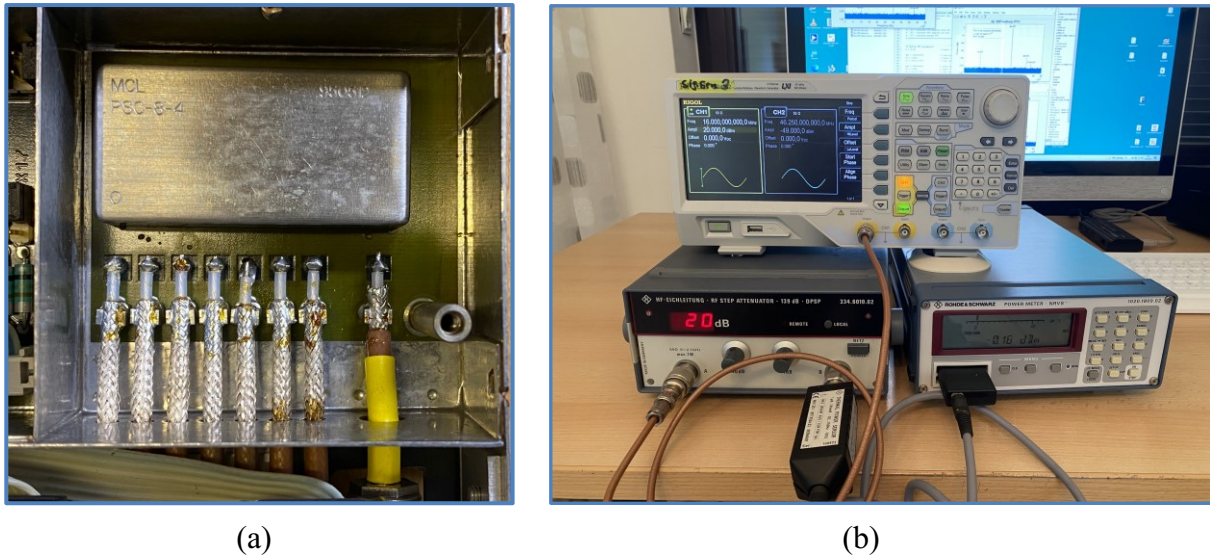


Fig. 10.3: (a) The 8-port signal combiner, (b) Dual arbitrary waveform generator (top), step attenuator (left), power meter (right) and power sensor (front).

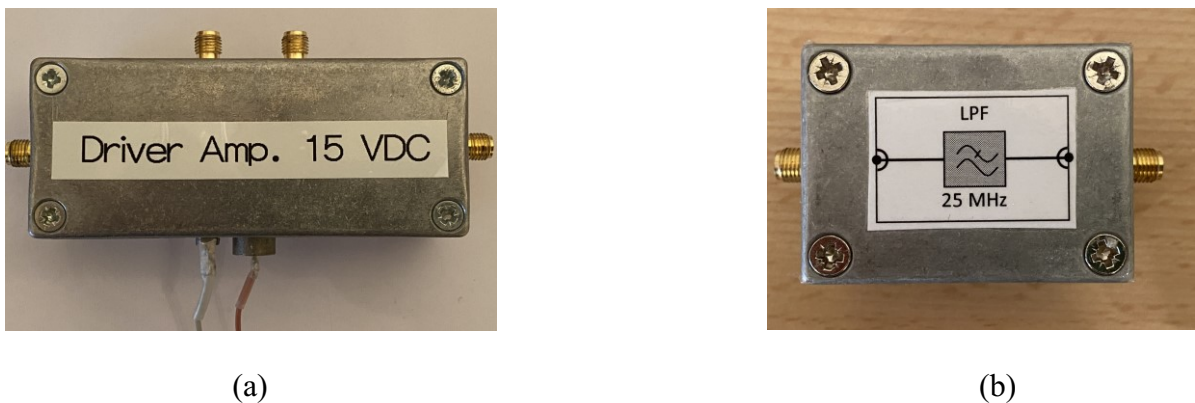


Fig. 10.4: (a) Picture of the Norton driver amplifier, (b) 25 MHz lowpass filter.

11 Abbreviations

5G	Wireless standard for 5th generation of mobile networks
AAF	Anti-aliasing filter
ADC	Analog-to-digital converter
A/D	Analog-to-digital
AGC	Automatic gain control
BH	Blackman-Harris (window)
BPF	Bandpass filter
COTS	Commercial of-the-shelf
COMINT	Communications intelligence
dBFS	Decibels full scale
DC	Direct current
DFT	Discrete Fourier Transform
DIV	Power divider
DNL	Differential nonlinearity (error)
DRV	Driver amplifier
ELINT	Electronic intelligence
ETH	Ethernet
FFT	Fast Fourier transform
FOM	Figure of merit
FPGA	Field Programmable Gate Array
FS	Full scale
GPS	Global positioning system
GSPS	Giga samples per second
HD _n	Harmonic distortion of order n
HF	High frequency
IF	Intermediate frequency
ITU	International Telecommunication Union
INL	Integral nonlinearity (error)
I/Q	In phase / quadrature phase
IMD	Intermodulation distortion
IMR	Image reject mixer
IP ₂ , IP ₃	Intercept point second order, third order

Abbreviations

LAN	Local area network
LNA	Low-noise Amplifier
LO	Local oscillator
LPF	Low-pass filter
LSB	Least significant bit
LTE	Wireless standard for 4th generation of mobile networks
MSB	Most significant bit
MSPS	Mega samples per second
NCO	Numerically controlled oscillator
NF	Noise figure
NSD	Noise spectral density
NZ	Nyquist zone
PC	Personal computer
POI	Probability of intercept
RF	Radio frequency
RTBW	Real time bandwidth
Rx	Radio receiver
SCPI	Standard Commands for Programmable Instruments
SFDR	Spurious-free dynamic range
SHA	Sample and hold amplifier
SIGINT	Signals intelligence
SINAD	Signal to noise and distortion (ratio)
SNR	Signal to noise ratio
Spurs	Short for spurious signals
Superhet	Short for superheterodyne receiver
Tx	Radio transmitter
USB	Universal serial bus
WiGig	Wireless network protocol (IEEE 802.111ay)

12 References

- [1] Department Of Defense, "Electromagnetic Spectrum Superiority Strategy," October 2020. [Online]. Available: https://media.defense.gov/2020/Oct/29/2002525927/-1/-1/0/ELECTROMAGNETIC_SPECTRUM_SUPERIORITY_STRATEGY.PDF. [Accessed 14 August 2021].
- [2] United States Government Accountability Office, "NTIA Planning and Processes Need Strengthening to Promote the Efficient Use of Spectrum by Federal Agencies," 2011. [Online]. Available: <https://www.gao.gov/assets/gao-11-352.pdf>. [Accessed 23 October 2021].
- [3] International Telecommunication Union, Handbook Spectrum Monitoring, Geneva: ITU Radiocommunication Bureau, 2011.
- [4] Keysight Technologies, "Real-Time Spectrum Analyzer (RTSA)," Product Brochure, Dec 2017. [Online]. Available: <https://www.keysight.com/at/de/assets/7018-03791/technical-overviews/5991-1748.pdf>. [Accessed 13 August 2021].
- [5] Rohde & Schwarz GmbH & Co. KG, "R&S@FSW SIGNAL AND SPECTRUM ANALYZER," [Online]. Available: https://www.rohde-schwarz.com/de/produkt/fsw-produkt-startseite_63493-11793.html. [Accessed 14 August 2021].
- [6] T. Neu, "Direct RF conversion: From vision to reality," May 2015. [Online]. Available: https://www.ti.com/lit/wp/slyy068/slyy068.pdf?ts=1622801266717&ref_url=https%253A%252F%252Fwww.google.de%252F. [Accessed 4 June 2021].
- [7] Analog Devices, Inc., "AD9213 Remote Hardware Evaluation Tool," Softwareprogram. [Online]. Available: http://labs.analog.com/remoteeval/#tool_pid=AD9213Remote&tab=fft. [Accessed 20 12 2020].
- [8] Analog Devices, Inc., "AD9213, 12-Bit, 6 GSPS/10.25 GSPS, JESD204B, RF Analog-to-Digital Converter," Datasheet Rev. A, 2020. [Online]. Available: <https://www.analog.com/media/en/technical-documentation/data-sheets/AD9213.pdf>. [Accessed 15 August 2021].
- [9] Analog Devices Inc., "High Speed A/D Converters >10 MSPS," 2021. [Online]. Available: <https://www.analog.com/en/parametricsearch/10826#/>. [Accessed 28 March 2021].
- [10] Texas Instruments, Inc., "High-speed ADCs(>10MSPS)," 2021. [Online]. Available: <https://www.ti.com/data-converters/adc-circuit/high-speed/products.html>. [Accessed 28 March 2021].
- [11] J. J. Fahie, A History of Wireless Telegraphy, 2nd ed. revised, New York: DODD, MEAD AND CO., 1901.
- [12] V. J. Phillips, Early radio wave detectors, London and New York: Institution of Electrical Engineers, 1980.

References

- [13] L. Levy, "Système de transmission électrique à distance, applicable particulièrement à la télégraphie et téléphonie sans fil". France Patent FR493660A, 19 Aug. 1919.
- [14] E. H. Armstrong, "Method of Receiving High Frequency Oscillations". USA Patent US1342885, 8 Jun. 1920.
- [15] R. A. Fessenden, "Wireless Signaling". USA Patent 706,740, 12 Aug. 1902.
- [16] I. Bronstein and K. Semendjajev, Taschenbuch der Mathematik, 13 ed., Frankfurt/Main: Harri Deutsch, 1973.
- [17] R. D. Lyons, Understanding Digital Signal Processing, 3rd ed., Upper Saddle River, NJ: Prentice Hall, 2011.
- [18] Texas Instruments Inc., "LMX8410L High-Performance Mixer With Integrated Synthesizer," Datasheet Nov. 2018. [Online]. Available: https://www.ti.com/lit/ds/symlink/lmx8410l.pdf?ts=1629005849790&ref_url=https%253A%252F%252Fwww.ti.com%252Fproduct%252FLMX8410L. [Accessed 15 August 2021].
- [19] U. Rohde, J. Whitaker and H. Zahnd, Communications Receivers, Principles and Design, Fourth Edition, 4 ed., New York: McGraw-Hill Education, 2017.
- [20] D. Smith, Digital Signal Processing Technology: Essentials of the Communications Revolution, Newington, CT USA: The American Radio Relay League, Inc., 2001.
- [21] U. L. Rohde, *R&S-XK4100 Transceiver, own receiver measurements*, Upper Saddle River, NJ, U.S.A., 2018.
- [22] ICOM Inc. Japan, "ICOM shortwave transceiver, IC-7851," Product Brochure, [Online]. Available: https://www.icomjapan.com/lineup/products/IC-7851/?open=1#detail_content. [Accessed 15 12 2021].
- [23] Rohde & Schwarz GmbH & Co. KG, "Communication systems," Product Brochure. [Online]. Available: https://www.rohde-schwarz.com/us/product/ek4100a-d-productstartpage_63493-10135.html. [Accessed 27 10 2021].
- [24] F. C. Travis, R. Getz, D. Pu and A. M. Wyglinski, "Software-Defined Radio for Engineers", Norwood, MA 02062, USA: Artech House Publishers, 2018.
- [25] K.-w. Nam, "Direct Down-Conversion System with I/Q Correction," Texas Instruments, Application note slwu085, 2013. [Online]. Available: <https://www.ti.com/lit/ug/slwu085/slwu085.pdf>. [Accessed 06 10 2020].
- [26] Analog Devices Inc., "AD9371, Integrated Dual RF Transceiver with Observation Path," Datasheet Rev. B, 2016-2017. [Online]. Available: <https://www.analog.com/media/en/technical-documentation/data-sheets/AD9371.pdf>. [Accessed 15 August 2021].
- [27] R. Raman and S. Svitek, "DC Offsets in Direct-Conversion Receivers: Characterization and Implications," *IEEE microwave magazine*, pp. 76-86, Sept. 2005.

References

- [28] A. Mashhour, W. Domino and N. Beamish, "On the Direct Conversion Receiver -- A Tutorial," *Microwave Journal*, vol. 44, no. 6, pp. 114-128, 1 Jun 2001.
- [29] A. Alagan, "Direct conversion receiver for radio communication systems," *IEEE Potentials*, pp. 33-35, January 2006.
- [30] Texas Instruments, Inc., "Designing 4- to 12-GHz Direct Conversion Receiver With LMX8410L IQDemodulator," Application note, SNAA329–April 2019. [Online]. Available: https://www.ti.com/lit/an/snaa329/snaa329.pdf?ts=1629101729679&ref_url=https%253A%252F%252Fwww.google.de%252F.
- [31] M. Valkama, M. Renfors and V. Koivunen, "Advanced methods for I/Q imbalance compensation in communication receivers.," *IEEE Transactions on Signal Processing* 49(10):2335 - 2344, Nov. 2001.
- [32] U. L. Rohde, "Digital HF Radio: a Sampling of Techniques," *Ham Radio Magazine*, pp. 18-42, April 1985.
- [33] J. I. Mitola, *Software Radio Architecture, Object-Oriented Approaches to Wireless Systems Engineering*, New York: John Wiley & Sons, Inc., 2000.
- [34] Rohde & Schwarz GmbH & Co. KG, "R&S®EB500 Monitoring receiver," [Online]. Available: https://www.rohde-schwarz.com/products/aerospace-defense-security/desktop-and-rack-mount-single-channel/rs-eb500-monitoring-receiver_63493-11225.html?change_c=true. [Accessed 14 August 2021].
- [35] Narda Safety Test Solutions, "SignalShark® 3320, Real-Time Remote Analyzer," Product Brochure. [Online]. Available: <https://www.atecorp.com/atecorp/media/pdfs/data-sheets/narda-signalshark-3320-real-time-remote-analyzer.pdf?ext=.pdf>. [Accessed 15 August 2021].
- [36] IZT GmbH, Product Information, "R5010 Wideband Receiver," 2019. [Online]. Available: <https://www.izt-labs.de/izt/media/IZT-R5010-Wideband-Receiver.pdf>. [Accessed 14 August 2021].
- [37] FlexRadio Systems, "FLEX-6700 HF/50MHz Transceiver," Product Brochure 2020. [Online]. Available: https://edge.flexradio.com/www/uploads/20201120233459/FLEX-6700_Brochure-202011.pdf. [Accessed 15 August 2021].
- [38] CommsAudit, "VHF - UHF Wideband Digital Receiver," [Online]. Available: <https://www.commsaudit.com/product/ca7852-receiver/>. [Accessed 15 August 2020].
- [39] L. Wu, "Optimierung des Signal-Rausch-Abstands von AD-Wandlern," 2010. [Online]. Available: <https://www.all-electronics.de/wp-content/uploads/migrated/article-pdf/87551/ei10-11-050.pdf>. [Accessed 30 10 2021].
- [40] R. R. Cornwell Jerry, "Conquering Your Electronic Countermeasures and Surveillance Design Challenges," 20 01 2016. [Online]. Available: <https://www.analog.com/en/education/education-library/webcasts/conquering-your-electronic-countermeasures.html>. [Accessed 31 10 2020].

References

- [41] National Security Agency Central Security Service, "Signals Intelligence, what is SIGINT," [Online]. Available: <https://www.nsa.gov/what-we-do/signals-intelligence/>. [Accessed 1 July 2021].
- [42] Rohde & Schwarz GmbH & Co. KG, "R&S®ESMD Wideband Monitoring Receiver," [Online]. Available: https://www.rohde-schwarz.com/products/aerospace-defense-security/desktop-and-rack-mount-single-channel/rs-esmd-wideband-monitoring-receiver_63493-9558.html?change_c=true. [Accessed 14 August 2021].
- [43] U. L. Rohde, "Next Generation Networks: Software Defined Radio - Emerging Trends," in *Sir J C Bose Memorial Lecture Event, December 02 2016*, Hyderabad, 2016.
- [44] C. Vogel and H. Johannson, "Time-Interleaved Analog-To-Digital Converters: Status and Future Directions," in *2006 IEEE International Symposium on Circuits and Systems*, Kos, Greece, 21-24 May 2006.
- [45] Texas Instruments Inc. Application Report SLAA 617, *Maximizing SFDR Performance in the GSPS ADC: Spur Sources and Methods of Mitigation*, December 2015.
- [46] Rohde & Schwarz GmbH & Co. KG, Press release, "Rohde-Schwarz-launches-high-performance-elint-receiver," 16 9 2020. [Online]. Available: https://www.rohde-schwarz.com/de/unternehmen/news-und-presse/all-news/rohde-schwarz-launches-high-performance-elint-receiver-pressemitteilungen-detailseite_229356-918848.html. [Accessed 8 11 2020].
- [47] Keysight Technologies, "X-Series Signal Analyzers," [Online]. Available: <https://www.keysight.com/us/en/products/spectrum-analyzers-signal-analyzers/x-series-signal-analyzers.html>. [Accessed 16 August 2021].
- [48] B. Manz, "Technology Survey: A Sampling of Radar ESM and ELINT Receivers – JED, December 2019," *Journal of Electromagnetic Dominance*, [Online]. Available: <https://www.jedonline.com/2020/05/20/technology-survey-a-sampling-of-radar-esm-and-elint-receivers-jed-december-2019/>. [Accessed 1 July 2021].
- [49] Linear Technology Cooperation, *LTC2208, Datasheet 16-Bit, 130Msps ADC*, Milpitas, CA, USA, 2005.
- [50] P. Delos, "A Review of Wideband RF Receiver Architecture Options," 2017. [Online]. Available: <https://www.analog.com/en/technical-articles/a-review-of-wideband-rf-receiver-architecture-options.html#>. [Accessed 4 June 2021].
- [51] T. Neu, "Microwaves&RF-High-Speed Converters Provide Direct Conversion at C-Band," 17 August 2017. [Online]. Available: <https://www.mwrf.com/markets/defense/article/21848588/highspeed-converters-provide-direct-conversion-at-cband>. [Accessed 02 May 2021].
- [52] X. Lin, "Spurs Analysis in the RF Sampling ADC, Application Report SLAA824," February 2018. [Online]. Available: https://www.ti.com/lit/an/slaa824/slaa824.pdf?ts=1622801636713&ref_url=https%253A%252F%252Fwww.google.com%252F. [Accessed 4 June 2021].

References

- [53] W. Kester, Data Conversion Handbook (Analog Devices, Inc.), Burlington, MA, USA: Elsevier, 2005.
- [54] The American Radio Relay League, The ARRL Handbook For Radio Communications, Ninety-Fourth Edition, Newington, U.S.A.: ARRL, the national association for Amateur Radio, 2017.
- [55] Microchip Technology, Inc., "ADC Differential Non-linearity," Microchip Developer Help 2021, [Online]. Available: <https://microchipdeveloper.com/adc:adc-differential-nonlinearity>. [Accessed 17 November 2021].
- [56] Maxim Integrated Products, Inc., "INL/DNL MEASUREMENTS FOR TYPES OF HIGH-SPEED ANALOG-TO-DIGITAL CONVERTERS (ADCS)," Application note, an 283, 2001. [Online]. Available: <http://www.maximintegrated.com/an283>. [Accessed 27 March 2021].
- [57] S. Arar, "Quantization Noise and Amplitude Quantization Error in ADCs," EETech Media, LLC., 22 April 2019. [Online]. Available: <https://www.allaboutcircuits.com/technical-articles/quantization-nois-amplitude-quantization-error-analog-to-digital-converters/>. [Accessed 14 July 2021].
- [58] E. T. Red, Arbeitsbuch für den HF-Techniker, München: Franzis-Verlag GmbH, 1986.
- [59] W. Bennet, "Spectra of Quantized Signals," BELL SYSTEM TECHNICAL JOURNAL July 1948. [Online]. Available: <http://oldweb.mit.bme.hu/books/quantization/papers/Bennett.pdf>. [Accessed 16 August 2021].
- [60] Analog Devices Inc., "VisualAnalog™ Converter Evaluation Tool, Version 1.9.48.1," 2005-2018. [Online]. Available: <https://www.analog.com/en/design-center/interactive-design-tools/visualanalog.html>.
- [61] U. Rohde, E. Rubiola and J. Whitaker, "Microwave and Wireless Synthesizers:Theorie and Design", 2 ed., Hoboken, NJ, U.S.A.: John Wiley & Sons, Inc., 2021.
- [62] P. Horowitz and W. Hill, The Art of Electronics, Third Edition, New York, USA: Cambridge University Press, 2015.
- [63] I. Beavers, "Noise Spectral Density:A New ADC Metric?," Technical Article, 2017. [Online]. Available: <https://www.analog.com/media/en/technical-documentation/tech-articles/Noise-Spectral-Density-A-New-ADC-Metric.pdf>. [Accessed 16 August 2021].
- [64] Fujitsu Microelectronics America, Inc, "56GSa/s 8-bit Analog-to-Digital Converter," Product Brochure 2010. [Online]. Available: https://www.fujitsu.com/downloads/MICRO/fma/pdf/56G_ADC_FactSheet.pdf. [Accessed 22 April 2021].
- [65] B. Murmann, ""ADC Performance Survey 1997-2020"," 2 8 2020. [Online]. Available: <http://web.stanford.edu/~murmman/adcsurvey.html>. [Accessed 19 12 2020].
- [66] R. Schreier and G. C. Temes, Understanding Delta-Sigma Data Converters, New York: Wiley & Sons, Inc.,Publication, 2005.

References

- [67] Analog Devices Inc., "RF-Converters Japan," [Online]. Available: <https://www.analog.com/-/media/analog/en/technologies/rf-converters/ad9213-new.png?h=192&w=275&la=ja>. [Accessed 22 01 2021].
- [68] Keysight Technologies, "CXA X-Series Signal Analyzer, N900A," Datasheet 2018. [Online]. Available: <https://www.keysight.com/de/de/assets/7018-02222/datasheets/5990-4327.pdf>. [Accessed 07 November 2021].
- [69] P. Nikaeen, *Dissertation: DIGITAL COMPENSATION OF DYNAMIC ACQUISITION ERRORS AT THE FRONT-END OF ADCS*, Department of electrical engineering, Stanford University U.S.A, 2008.
- [70] S. Xi, "Analyzing and Solving Fixed Frequency Spur Issues in High Precision ADC Signal Chains," *Analog Dialouge-51*, 04 April 2017.
- [71] A. Smith, "High Sensitivity Receiver Applications Benefit from Unique Features in 16-Bit 130MSPS ADC," *Design Solutions 44, Linear Technology*, pp. 1-3, Oct. 2005.
- [72] Maxim Integrated Products, Inc., "FREQUENCY PLANNING AND EVALUATING TOOL, Application Note 1106," 1 Oct. 2002. [Online]. Available: <https://www.maximintegrated.com/en/design/technical-documents/app-notes/1/1106.html>. [Accessed 29 March 2021].
- [73] Texas Instruments Inc., "RF-Sampling Frequency Planner, Analog Filter, and DDC Excel™ Calculator," Texas Instruments Inc. USA, 19 OCT 2017. [Online]. Available: <https://www.ti.com/tool/FREQ-DDC-FILTER-CALC>. [Accessed 27 JAN 2021].
- [74] Analog Devices, Inc., "Frequency Folding Tool," Analog Devices Inc., Software program 2021. [Online]. Available: <https://www.analog.com/en/design-center/interactive-design-tools/frequency-folding-tool.html>. [Accessed 29 March 2021].
- [75] M. Valkama et al, "Advanced Digital Signal Processing Techniques for Compensation of Nonlinear Distortion in Wideband Multicarrier Radio Receivers," *IEEE TRANSACTIONS ON MICROWAVE THEORY AND TECHNIQUES*, VOL. 54, NO. 6, pp. 2356-2364, June 2006.
- [76] M. Grimm, *Dissertation: Dirty RF Signal Processing for Mitigation of Receiver Front-end Non-linearity*, Ilmenau: University of Technology Ilmenau, urn:nbn:de:gbv:ilm1-2014000134, 2014.
- [77] M. Allen, "Nonlinear Distortion in Wideband Radio Receivers and Analog-to-Digital Converters: Modeling and Digital Suppression", Tampere: Tampere University of Technology. Publication; Vol. 1329, 2015.
- [78] C. Kikkert and B. A., "REDUCING DISTORTION IN MICROWAVE ANALOGUE TO DIGITAL CONVERTERS," James Cook University, Townsville, Qld., Australia, 4811, 2000.
- [79] P. Jackson and W. O'Reilly, "Reducing Spurious Signals: A Critical Requirement for the Warfighter," Precision Receivers, PRI, Inc. 4111 Rutledge Ln, Marshall, VA 20115, 2021. [Online]. Available: <http://precisionreceivers.com/wp-content/uploads/2020/09/PRI-White-Paper-1.pdf>. [Accessed 06 May 2021].

References

- [80] S. H. Mnene, *An Introduction to Digital Signal Processing: A Focus on Implementation*, Aalborg, Denmark: River Publishers, 2008.
- [81] J. James, *A Student's Guide to Fourier Transforms with Applications in Physics and Engineering*, Third Edition, Cambridge, UK: University Press, 2011.
- [82] O. Jamin, *Broadband Direct RF Digitization Receivers*, Springer International Publishing, Switzerland, 2014.
- [83] S. W. Smith, *Digital Signal Processing, A practical Guide for Engineers and Scientists*, 200 Wheeler Road, Burlington MA 01803: Elsevier Science, 2003.
- [84] V. K. Madiseti and D. B. Williams, "Digital Signal Processing Handbook", Atlanta, Georgia U.S.A.: CRC Press LLC, 1999.
- [85] M. Cerna and A. F. Harvey, "The Fundamentals of FFT-Based Signal Analysis and Measurement, National Instruments, Application Note 041," July 2000. [Online]. Available: https://www.sjsu.edu/people/burford.furman/docs/me120/FFT_tutorial_NI.pdf. [Accessed 29 March 2021].
- [86] R. Lyons, "Reducing FFT Scalloping Loss Errors Without Multiplication," *IEEE SIGNAL PROCESSING MAGAZINE* [112], p. 1, March 2011.
- [87] MATLAB:2020, *Version: 2020a Update 4(9.8.0.1417392)*, Massachusetts U.S.A.: The Mathworks Inc., 2020.
- [88] F. J. Harris, "On the Use of Windows for Harmonic Analysis with the Discrete Fourier Transform," *PROCEEDINGS OF THE IEEE, VOL. 66, NO. 1*, pp. 51-83, January 1978.
- [89] S. Scholl, "Exact Signal Measurements using FFT Analysis,," [Online]. Available: https://kluedo.uni-kl.de/frontdoor/deliver/index/docId/4293/file/exact_fft_measurements.pdf. [Accessed 31 March 2021].
- [90] L. Chioye, "Choose The Right FFT Window Function When Evaluating Precision ADCs," 12 November 2013. [Online]. Available: <https://www.electronicdesign.com/technologies/analog/article/21798689/choose-the-right-fft-window-function-when-evaluating-precision-adcs>. [Accessed 21 02 2020].
- [91] M. Prior, "Create Windows for use with FFT functions," 10 Feb. 2015. [Online]. Available: https://github.com/Matlab-Toolbox/create_window. [Accessed 13 March 2021].
- [92] The Mathworks Inc., "Matlab,," [Online]. Available: www.mathworks.com. [Accessed 18 11 2020].
- [93] The Mathworks Inc., "Fast Fourier transform," Program documentation, [Online]. Available: <https://de.mathworks.com/help/matlab/ref/fft.html>. [Accessed 26 June 2021].

- [94] Hochschule Karlsruhe, Systemtheorie Online, "FREQUENZAUFÖSUNG DER DFT– ZERO-PADDING," [Online]. Available: <https://www.eit.hs-karlsruhe.de/mesysto/teil-b-zeitdiskrete-signale-und-systeme/diskrete-fourier-transformation/frequenzaufloesung-der-diskreten-fourier-transformation-zero-padding.html>. [Accessed 15 August 2021].
- [95] D. G. Manolakis and V. K. Ingle, Applied Digital Signal Processing, Cambridge UK: Cambridge University Press, 2011.
- [96] The MathWorks, Inc., "Display frequency spectrum of time-domain signals," Help Center, dsp.SpectrumAnalyzer, 2021. [Online]. Available: <https://de.mathworks.com/help/dsp/ref/dsp.spectrumanalyzer-system-object.html>. [Accessed 3 April 2021].
- [97] General Services Administration, Information Technology Service, "FEDERAL STANDARD, Telecommunications: GLOSSARY OF TELECOMMUNICATION TERMS," National Technical Information Service, 5285 Port Royal Road, Springfield, VA 22161, 7 August 1996. [Online]. Available: <https://www.its.blrdoc.gov/fs-1037/fs-1037c.htm>. [Accessed 27 May 2021].
- [98] N. Yoder, "peakfinder(x0, sel, thresh, extrema, includeEndpoints, interpolate) version 2.0.2.0," 2021. [Online]. Available: <https://de.mathworks.com/matlabcentral/fileexchange/25500-peakfinder-x0-sel-thresh-extrema-includeendpoints-interpolate>. [Accessed 12 June 2021].
- [99] Red Pitaya d.d., "RED PITAYA STEMLAB BOARD," [Online]. Available: <https://redpitaya.com/stemlab-125-10/>. [Accessed 22 May 2021].
- [100] Analog Devices Inc., "AD9608, 10-Bit, 125/105 MSPS, 1.8 V Dual Analog-to-Digital Converter," Datasheet Rev. C, 2011-2015. [Online]. Available: <https://www.analog.com/media/en/technical-documentation/data-sheets/AD9608.pdf>. [Accessed 15 August 2021].
- [101] R. P. d.o.o., "Connect to Red Pitaya," 2021. [Online]. Available: <https://redpitaya.readthedocs.io/en/latest/quickStart/first.html?highlight=connect>. [Accessed 17 11 2021].
- [102] Renesas Electronics Corporation, Tokyo, Japan, Datasheet, "XL Family of Low Phase Noise Quartz-based PLL Oscillators," 19 January 2021. [Online]. Available: <https://www.renesas.com/us/en/document/dst/xl-family-low-phase-noise-quartz-based-pll-oscillators-datasheet>. [Accessed 13 June 2021].
- [103] Rohde & Schwarz GmbH & Co. KG, "R&S®SPECTRUM RIDER FPH HANDHELD SPECTRUM ANALYZER," [Online]. Available: https://www.rohde-schwarz.com/products/test-and-measurement/handheld/rs-spectrum-rider-fph-handheld-spectrum-analyzer_63493-147712.html?change_c=true. [Accessed 15 June 2021].
- [104] The MathWorks, Inc., "High Resolution Spectral Analysis," 2021. [Online]. Available: <https://de.mathworks.com/help/dsp/ug/high-resolution-spectral-analysis.html>. [Accessed 30 June 2021].

References

- [105] Rohde & Schwarz GmbH & Co. KG, Product Brochure, "R&S®SMA100A Signal Generator," [Online]. Available: https://www.rohde-schwarz.com/de/produkt/sma100a-produkt-startseite_63493-7566.html. [Accessed 22 May 2021].
- [106] Rigol Technologies, Inc., "DG4000 SERIES, Arbitrary Waveform Generators," Product Brochure. [Online]. Available: <https://www.rigolna.com/products/waveform-generators/dg4000/>. [Accessed 23 May 2021].
- [107] Mini-Circuits, Inc., "PSC-8A-4+, Power Splitter/Combiner," [Online]. Available: <https://www.minicircuits.com/pdfs/PSC-8A-4+.pdf>. [Accessed 22 May 2021].
- [108] Mini-Circuits, Inc., "SLP-50, Coaxial Low Pass Filter DC - 48 MHz," [Online]. Available: <https://www.minicircuits.com/pdfs/SLP-50.pdf>. [Accessed 22 May 2021].
- [109] Mini-Circuits, Inc., "SMA Fixed Attenuator, SMA-ATT-3, DC to 6000 MHz," [Online]. Available: <https://www.minicircuits.com/pdfs/VAT-3+.pdf>. [Accessed 22 May 2021].
- [110] Rohde & Schwarz GmbH & Co. KG, "R&S®NRVS Power Meter," [Online]. Available: https://www.rohde-schwarz.com/us/product/nrvs-productstartpage_63493-8479.html?change_c=true. [Accessed 15 June 2021].